TECHNISCHE UNIVERSITÄT WIEN
Vienna | Austria

DISSERTATION

Model-based control of the transverse strip shape and position in a hot-dip galvanizing line

Ausgeführt zum Zwecke der Erlangung des akademischen Grades eines
Doktors der technischen Wissenschaften (Dr. techn.)

unter der Leitung von
Univ.-Prof. Dipl.-Ing. Dr. techn. Andreas Kugi
E376
Institut für Automatisierungs- und Regelungstechnik

eingereicht an der
Technischen Universität Wien
Fakultät für Elektrotechnik und Informationstechnik

von
Martin Saxinger
Matrikelnummer: 0656768

Wien, Dezember 2020

Studiendekan:	Univ.-Prof. Dr.-Ing. Wolfgang Gawlik
Betreuer:	Univ.-Prof. Dipl.-Ing. Dr. techn. Andreas Kugi
Tag des Rigorosums:	04. Dezember 2020
Prüfungsvorsitzender:	Univ.-Prof. Dr.-Ing. Wolfgang Gawlik
Erster Gutachter:	Prof. S.O. Reza Moheimani, BSc, MEngSc, PhD
Zweiter Gutachter:	Associate Prof. Dr.-Ing. Wolfgang Kemmetmüller

Vorwort

Diese Arbeit entstand im Rahmen meiner Tätigkeit als wissenschaftlicher Mitarbeiter im CD-Labor für „Modellbasierte Prozessregelung in der Stahlindustrie“ am Institut für Automatisierungs- und Regelungstechnik (ACIN) der Technischen Universität Wien. Ich bedanke mich für die finanzielle Unterstützung durch das Bundesministerium für Digitalisierung und Wirtschaftsstandort und die Nationalstiftung für Forschung, Technologie und Entwicklung, die Christian Doppler Forschungsgesellschaft sowie durch die voestalpine Stahl GmbH.

Mein ganz besonderer Dank gebührt an erster Stelle Univ.-Prof. Dipl.-Ing. Dr.techn. Andreas Kugi für die hervorragende Betreuung der Arbeit. Die Diskussionen mit Prof. Kugi fanden üblicherweise in der wöchentlichen „CD-Labor Besprechung“ statt, welche ein regelmäßiger Bestandteil des CD-Labors war. Im Besonderen danke ich auch Associate Prof. Dipl.-Ing. Dr.techn. Andreas Steinböck, der mich in zahlreichen Diskussionen mit Rat und Tat unterstützt hat.

Auch meinen CD-Labor Kollegen Dipl.-Ing. Lukas Marko und Dipl.-Ing. Dr.techn. Michael Baumgart gebührt ein herzlicher Dank für die gemeinsame Zusammenarbeit im Projekt Feuerverzinken. Gerne erinnere ich mich auch an unsere Fahrten zur voestalpine Stahl GmbH und die zahlreichen fachlichen Gespräche. Für die Unterstützung beim Aufbau des Laborversuchs danke ich Dipl.-Ing. Andreas Ettl, Dipl.-Ing. Ulrich Knechtelsdorfer und Dipl.-Ing. Christoph Orth. Ein besonderer Dank gilt Dipl.-Ing. Georg Stadler für den unermüdlichen LaTeX Support. In guter Erinnerung werde ich auch alle anderen Kolleginnen und Kollegen am ACIN behalten.

Auf Seiten der voestalpine Stahl GmbH gilt mein großer Dank Dipl.-Ing. Peter Kerschbaummayr, Dipl.-Ing. Josef Nigl und Dipl.-Ing. Andreas Eder für die große Hilfsbereitschaft, die tatkräftige Unterstützung und die flotte Umsetzung unserer Vorhaben.

Meiner Familie danke ich herzlichst für das Vertrauen, das Ermöglichen meiner Ausbildung und die Unterstützung meiner Entscheidungen.

Abstract

Hot-dip galvanizing is the state-of-the-art technology to produce zinc coats on steel strips. For quality reasons, the steel industry has to guarantee a required minimum coating thickness at any lateral position of the strip. The primary objective of this process is to establish a zinc layer with a defined uniform thickness. In this way, the zinc consumption and thus the operating costs of the plant can be significantly reduced without violating the coating thickness requirement. One condition to achieve a homogeneous zinc layer is a uniform air gap between the strip and the gas wiping dies, where excess liquid zinc is blown off. Hence, a flat transverse strip profile at the gas wiping dies is required. However, the steel strips processed in such plants often exhibit unknown but usually only slowly varying residual curvatures which entail transverse flatness defects of the strip. In addition, vibrations of the strip at the gas wiping dies must be suppressed to keep the air gaps constant. Persistently exciting vibrations of the strip are frequently encountered in hot-dip galvanizing lines. These vibrations typically exhibit a dominant sinusoidal or sometimes multi-harmonic shape. The underlying excitation process, the frequency, the amplitude, and the phase are generally unknown. Clearly, flatness defects and superimposed strip vibrations at the gas wiping dies cause non-uniform and time-varying air gaps and hence an inhomogeneous zinc coating thickness.

In modern hot-dip galvanizing lines, electromagnetic actuators are used for contactless vibration and shape control of the transverse strip shape. In the considered application, the control input (force of electromagnetic actuators), the sensor output (measured transverse strip displacements near the electromagnets), and the system output to be controlled (transverse strip displacement at the gas wiping dies) are usually located at different positions along the strip, which makes the overall control task quite challenging. In addition, the disturbance input (source of multi-harmonic periodic excitation) is also located at an unknown position. State-of-the-art control algorithms realize an approximately flat strip

profile only at the height of the displacement sensors but it is unfeasible to mount distance sensors directly at the gas wiping dies. Moreover, a persistently exciting disturbance cannot be fully suppressed by the state-of-the-art control algorithms (not even at the measured positions). This usually entails a time-varying flatness defect with non-zero mean at the gas wiping dies, which in turn brings along a suboptimal zinc coating thickness.

In this thesis, model-based methods are developed to improve the homogeneity and accuracy of the zinc coating thickness compared to state-of-the-art methods. To this end, a dynamical model of the motion and elastic deformation of the steel strip in an industrial hot-dip galvanizing line is derived that captures the most important physical effects, e.g., the flatness defects in the strip, the electromagnetic forces, and the transverse loads of impinging air cooling jets. The underlying partial differential equations are derived via Hamilton's principle for systems of changing mass. The Galerkin weighted residual method is employed for spatial discretization. The domain of the strip is divided into finite elements, where local ansatz functions are used. A tailored time integration scheme for structural mechanics problems is applied to perform time-efficient transient simulations. The model is validated for both steady-state and dynamic cases with measurements from the industrial hot-dip galvanizing line for different test strips.

The mathematical model serves as a basis for the design of a feedforward controller of the transverse strip profile at the position of the gas wiping dies. For this, an estimator of the flatness defects is designed and validated for different test strips and settings of the plant. Using the validated mathematical model, a simulation study is conducted to compare the state-of-the-art control method (flat strip profile at the electromagnets) with the developed feedforward controller (flat strip profile at the gas wiping dies). Furthermore, the influence of the vertical distance between the gas wiping dies and the electromagnets on the control performance is analyzed in detail.

In order to suppress persistently exciting disturbances at the position of the gas wiping dies, a control concept is developed that consists of a linear quadratic regulator (LQR) combined with a disturbance feedforward concept based on the theory of invariant manifolds and an extended Kalman filter (EKF). The proposed control strategy is successfully validated by means of an experimental test rig that mimics the essential properties of the industrial hot-dip galvanizing line. To this end, custom-made electromagnetic actuators are used to exert forces on the strip. The desired electromagnetic control force is realized in a pure feedforward mode, where neither a force sensor nor a displacement sensor for measuring the air gap between the strip and the magnetic core are required. Finally, measurement results of the control concept, which demonstrate the excellent performance to suppress persistently exciting disturbances, are presented for the experimental test rig.

Kurzzusammenfassung

Kontinuierliches Feuerverzinken ist eine Standardtechnologie zur Herstellung von verzinkten Stahlbändern. Zur Erfüllung der Produktqualitätsansprüche muss die Stahlindustrie eine erforderliche Mindestdicke der Zinkschicht an jeder beliebigen Querposition des Bandes garantieren. Das primäre Ziel dieses Prozesses ist das Aufbringen einer Zinkschicht mit einer definierten gleichmäßigen Dicke. In diesem Fall können der Zinkverbrauch und daher auch die Betriebskosten der Anlage deutlich reduziert werden, ohne dass die Anforderung bezüglich der erforderlichen Zinkschichtdicke verletzt wird. Eine maßgebliche Bedingung zur Aufbringung einer homogenen Zinkschicht ist ein gleichmäßiger Luftspalt zwischen dem Band und der Luftabstreifdüse, mit welcher überschüssiges, am Band haftendes Zink, abgeblasen wird. Dazu wird ein möglichst flaches Bandprofil in der Abstreifdüse benötigt. Tatsächlich weisen die zu verzinkenden Bänder in solchen Anlagen häufig unbekannte, jedoch meist nur langsam variierende plastische Vorverformungen auf, welche zu Ebenheitsfehlern des Bandes führen. Treten unerwünschte Bandschwingungen in der Luftabstreifdüse auf, so führt dies zu einer zusätzlichen zeitlichen Variation des Luftspaltes. In Feuerverzinkungsanlagen werden oftmals Bandschwingungen beobachtet, die über einen externen Mechanismus permanent angeregt werden. Solche Bandschwingungen haben typischerweise eine ausgeprägte Sinusform, es können aber auch Oberwellen überlagert sein. Der zugrundeliegende Mechanismus zur Anregung, die Frequenz, die Amplitude und die Phase der Schwingung sind dabei unbekannt. Plastische Vorverformungen und Bandschwingungen führen typischerweise zu ungleichmäßigen und zeitlich variierenden Luftspalten in der Luftabstreifdüse und damit in weiterer Folge zu einer inhomogenen Zinkschichtdicke.

Moderne Feuerverzinkungsanlagen sind mit mehreren Elektromagnetaktuatoren ausgestattet, welche zur kontaktlosen Schwingungsdämpfung und zur Regelung der transversalen Bandform verwendet werden. Genau genommen befinden sich in der betrachteten Anwendung der Steuereingang (Kräfte der Elektromagnete),

der Messausgang (gemessene transversale Bandauslenkung in der Nähe der Elektromagnete) und der zu regelnde Ausgang (Bandauslenkung in der Abstreifdüse) normalerweise an unterschiedlichen Positionen entlang des Bandes. Dies führt auf ein komplexes regelungstechnisches Problem. Zusätzlich befindet sich auch der Störeingang (Quelle der periodischen Bandschwingung) an einer anderen Position. Herkömmliche Regelalgorithmen realisieren ein annähernd flaches Bandprofil auf Höhe der Abstandssensoren. Eine direkte Montage von Abstandssensoren auf der Luftabstreifdüse ist jedoch nicht möglich. Periodisch angeregte Bandschwingungen können von solchen Regelalgorithmen nicht vollständig unterdrückt werden (auch nicht auf der Höhe der Abstandssensoren). Dies führt dazu, dass typischerweise ein zeitlich variierender und nicht mittelwertfreier Ebenheitsdefekt an der Abstreifdüse verbleibt, welcher eine suboptimale Zinkschichtdicke zur Folge hat.

In dieser Arbeit werden modellbasierte Methoden entwickelt, die im Vergleich zu existierenden Methoden zu einer weiteren Verbesserung der Zinkschichtdickenhomogenität und -genauigkeit führen sollen. Zu diesem Zweck wird ein dynamisches Modell der Bewegung und elastischen Deformation eines Stahlbandes in einer Feuerverzinkungsanlage entwickelt. Die wichtigsten physikalischen Einflussgrößen, wie z. B. die plastische Vorverformung des Bandes, die Kräfte der Elektromagnete und die Strömungskräfte durch die Luftkühler werden berücksichtigt. Die zugrundeliegenden Differentialgleichungen folgen aus dem Hamiltonschen Prinzip für offene Systeme mit veränderlicher Masse. Zur örtlichen Diskretisierung kommt die Galerkin-Methode der gewichteten Residuen zum Einsatz, wobei das Rechengebiet mithilfe von lokalen Ansatzfunktionen in finite Elemente diskretisiert wird. Transiente Simulationen werden mit einem speziellen Zeitintegrationsverfahren durchgeführt, welches für strukturmechanische Systeme entwickelt wurde. Das Bandmodell wird mithilfe von Messungen in quasistatischen und dynamischen Szenarien validiert. Die Messungen dazu wurden an der industriellen Feuerverzinkungsanlage für verschiedene Testbänder durchgeführt.

Das mathematische Modell wird für die Entwicklung einer Vorsteuerung des transversalen Bandprofils bei der Luftabstreifdüse verwendet. Dazu wird ein Schätzer der Ebenheitsdefekte entworfen und mithilfe von verschiedenen Testbändern und Einstellungen der Anlage validiert. Mithilfe des validierten Bandmodells wird eine Simulationsstudie durchgeführt, um die derzeitige Standardmethode (flaches Bandprofil bei den Elektromagneten) mit der entwickelten Vorsteuerung (flaches Bandprofil bei der Luftabstreifdüse) zu vergleichen. Des Weiteren wird der Einfluss des vertikalen Abstands zwischen der Luftabstreifdüse und den Elektromagneten auf die Ergebnisse der Vorsteuerung detailliert untersucht.

Zur Unterdrückung von periodisch angeregten Bandschwingungen wird ein Regelungskonzept entworfen, welches aus einem linear-quadratischen Regler in Kombination mit einer Störgrößenvorsteuerung und einem erweiterten Kalman-Filter besteht. Die Störgrößenvorsteuerung basiert auf der Theorie der invarianten Mannigfaltigkeiten. Das entwickelte Regelungskonzept wird dabei erfolgreich mithilfe eines experimentellen Versuchsaufbaus validiert, mit welchem die wesentlichen

Eigenschaften des Feuerverzinkungsprozesses nachgebildet werden können. Zum Aufbringen der Kraft werden selbst entwickelte elektromagnetische Aktuatoren verwendet. Die gewünschte elektromagnetische Kraft wird mithilfe einer reinen Vorsteuerung realisiert, d. h., es werden weder ein Kraftsensor noch ein Abstandssensor zur Messung des Luftspalts zwischen Band und Magnetkern verwendet.

Contents

List of symbols

Abbreviations

BR	Bottom roll
CR	Correction roll
FF	Feedforward control
SR	Stabilization roll
TR	Tower roll

Variables (Latin symbols)

A	Extensional stiffness
D	Bending stiffness
E	Young's modulus
I	Index set
J	Performance indicator
L	Strip length
M	Thickness-integrated moment
N	Thickness-integrated force
$N_{xx,\mathrm{L}}$	Tensile load at the tower roll
O	Inertial coordinate system
O^{g}, O^{s}	Local coordinate systems
R	Weighting factor for the control input (LQR)
$\bar{R}$	Variance for the EKF
T_{s}	Sampling time
V	Bulk velocity of the strip

X	Hermite polynomial
Y	Legendre polynomial
b	Strip width
e, f	Indices of a finite element
f_{mag}, f_{s}	Forces
g	Gravitational acceleration
h	Strip thickness
h_{Zn}	Zinc coating thickness
i_{c}	Current in electromagnetic coil
i_{off}	Offset current
k	Time index
m	No. of lateral finite elements (out-of-plane system)
$\bar{m}_{\mathrm{pot}}$	Accumulated mass inertia of zinc pot
n	No. of longitudinal finite elements
n_{x}	No. of Hermite polynomials
n_{y}	No. of Legendre polynomials
p	Degree of polynomial (residual curvature)
p_{clr}	Supply pressure of a cooling element
q	Distributed load in transverse direction
t	Time
u, v, w	Strip displacements
u_k	Control input at the time instant kT_{s} (electromagnetic force)
$w_{\mathrm{gwd}}(y)$, $w_{\mathrm{mag}}(y)$	Transverse strip profiles
$w_{\mathrm{mean}}^{\mathrm{g,s}}$	Mean displacement between gas wiping dies and strip stabilizer
$w_{\mathrm{mean}}^{\mathrm{s}}$	Mean displacement of strip stabilizer
w_{tow}^{l}	Measured transverse strip displacement at the tower sensor l
x, y, z	Cartesian coordinates
x_{mag}, x_{gwd}, x_{tow}	Vertical positions of the respective devices
x_{pot}	Filling level of the zinc pot
z_{CR}	Displacement of the correction roll
$\mathbf{A}$, $\mathbf{b}$, $\mathbf{G}_{\mathrm{d}}$,$\mathbf{h}_{\mathrm{p}}$	Continuous-time state-space description of Euler-Bernoulli beam model
$\mathbf{A}_{\mathrm{d}}$	Continuous-time state-space description of disturbance model
$\mathbf{I}$	Identity matrix
$\mathbf{Q}$	Weighting matrix for the states (LQR)
$\bar{\mathbf{Q}}$	Covariance matrix for the EKF
$\mathbf{f}_{\mathrm{mag}}$	Vector of electromagnetic forces

$\mathbf{k}_{\mathrm{x}}$, $\mathbf{k}_{\mathrm{w}}$	Feedback gains
$\mathbf{p}$	Position offset
$\mathbf{q}$	Relative position offset
$\mathbf{t}$	Vector of Galerkin coefficients
$\mathbf{u}$	Strip profile mode
$\mathbf{v}$	Mode of electromagnetic forces
$\mathbf{w}_{\mathrm{gwd}}$	Discretized strip profile at the gas wiping dies, system output to be controlled
$\mathbf{w}_{\mathrm{mag}}$	Strip displacements at the electromagnets
$\mathbf{y}_{\mathrm{gwd}}$	Equidistant grid in lateral direction
$\mathbf{y}_{\mathrm{mag}}$	Lateral positions of electromagnets
$\mathbf{y}_{p}$	Vector of basis functions for residual curvature

Variables (Greek symbols)

Γ	Boundary
Δ	Step size / difference
Δx	Vertical distance between gas wiping dies and electromagnets
Ω	Domain
α	Viscous damping factor
β	Kelvin-Voigt damping factor
$\bar{\gamma}$, $\bar{\beta}$	Parameters associated with the numerical quadrature
δ	Air gap
ϵ^0, γ_{xy}^0	Membrane strains
ϵ^1, γ_{xy}^1	Bending strains
$\epsilon^{\mathrm{r},0}$	Residual membrane strain in the strip
$\epsilon^{\mathrm{r},1}$	Residual curvature of the strip
$\epsilon_{yy}^{\mathrm{c},l}$	Polynomial coefficient l of the residual curvature
ι	No. of cooling elements
κ	No. of pairs of electromagnets
λ	No. of equidistant grid points in the vector $\mathbf{y}_{\mathrm{gwd}}$
μ	No. of tower sensors
ν	Poisson's ratio
ρ	Density
σ	Singular value
υ	No. of harmonics of the disturbance
$\varphi^{\mathrm{g,s}}$	Skew angle between gas wiping dies and strip stabilizer
φ^{s}	Skew angle of electromagnetic stabilizer

ω_d	Fundamental frequency of the disturbance
$\boldsymbol{\Gamma}_\mathrm{gwd}$, $\boldsymbol{\Delta}_\mathrm{gwd}$, $\boldsymbol{\Gamma}_\mathrm{mag}$, $\boldsymbol{\Delta}_\mathrm{mag}$	Sensitivities determined from the strip model
$\boldsymbol{\Phi}$, $\boldsymbol{\Omega}$	Sensitivity related to a variation of the position offset
$\boldsymbol{\Phi}_\mathrm{d}$	Discrete-time state-space description of disturbance model
$\boldsymbol{\Phi}_\mathrm{s}$, $\boldsymbol{\gamma}$, $\boldsymbol{\Delta}$,$\boldsymbol{\sigma}$	Discrete-time state-space description of Euler-Bernoulli beam model
$\boldsymbol{\Psi}$	Vector of basis functions used for Galerkin method
$\boldsymbol{\varepsilon}_{yy}^{\mathrm{r},1}$	Polynomial coefficients of the residual curvature

Sub/superscripts and diacritics

clr	Cooling element
d	Disturbance
gwd	Gas wiping dies
lsr	Laser distance sensor
m	Position of electromagnet (experimental test rig)
mag	Electromagnets
max	Maximum value
mean	Mean value
off	Offset
pot	Zinc pot
r	Position of rejection (experimental test rig)
s	Position of distance sensor (experimental test rig)
tow	Tower sensors
xx, yy	Normal components
xy	Shear component
b	Bottom side
des	Desired value
e	Inertial coordinate system of experimental test rig
g	Local coordinate system of gas wiping dies
s	Local coordinate system of electromagnetic stabilizer
t	Top side
$\star$	Optimal value
$*$	Predicted value
$\breve{\ }$	In-plane system
$\tilde{\ }$	Out-of-plane system
$\dot{\ }$	Time derivative
$\hat{\ }$	Estimated quantity
$\bar{\ }$	Weighting function / model used for observer design

CHAPTER 1

Introduction

Although the hot-dip galvanizing process was developed decades ago, the quality demands on zinc-coated steel strips are still increasing. This brings along that the application of advanced automation and control technologies is getting more and more important.

This work focuses on the optimization of the coating process in an industrial hot-dip galvanizing line, i.e., the objective is to improve the homogeneity of the zinc coating thickness. In this context, it is important to know that the product standard for zinc-coated steel strips defines the required minimum thickness of the zinc coating in the range of $60\,\mathrm{g/m^2}$ to $350\,\mathrm{g/m^2}$ [1]. The homogeneity of the coating thickness in the lateral direction is of minor importance. To achieve the minimum coating thickness in a hot-dip galvanizing process, typically large parts of the strip have to be processed with a thicker zinc coating compared to the required one. However, if a homogeneous coating thickness can be realized, e.g., with the methods developed in this work, the average coating thickness and thus the zinc consumption can be reduced. This also significantly reduces the operating costs because zinc is an expensive metal.

To describe the complexity of the hot-dip galvanizing process and especially the mechanism behind the coating process, Section 1.1 gives an overview of an industrial processing line.

1.1 Continuous hot-dip galvanizing lines

Figure 1.1 shows parts of an industrial hot-dip galvanizing line of voestalpine Stahl GmbH, Linz, Austria. The coils of steel strips to be processed in this plant have lengths of about 2000 m, their thicknesses and widths range from 0.6 mm to

2.0 mm and 0.8 m to 1.8 m, respectively. The typical production capacity of the plant is 400 000 t/yr [1].

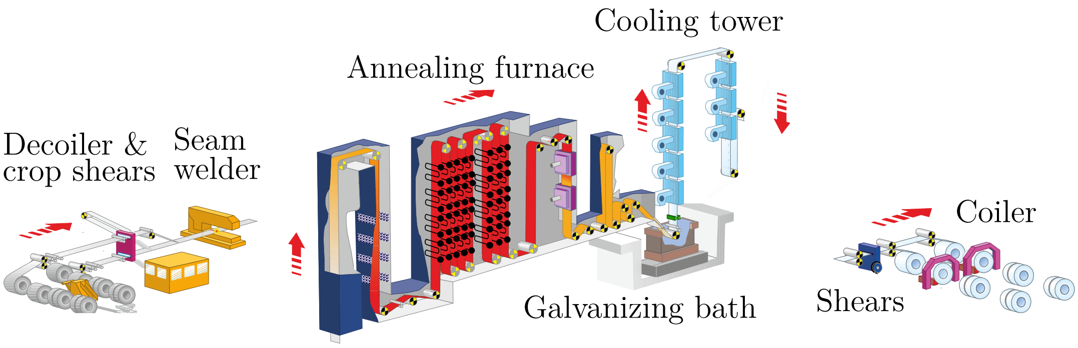

(a) Incoming coils of steel strips.

(b) Section between annealing furnace and cooling tower.

(c) Outgoing coils of zinc-coated steel strips.

Figure 1.1: Overview of an industrial hot-dip galvanizing line of voestalpine (© voestalpine Stahl GmbH).

1.1.1 Industrial processing of zinc-coated steel strips

Continuous hot-dip galvanizing lines are designed for a non-stop production of zinc-coated steel strips, see Fig. 1.1. Different process steps have to be carried out in order to ensure a proper strip processing. As shown in Fig. 1.1a, coils of steel strips to be coated are delivered to the plant. The strip is decoiled and both ends of the strip are cropped by shears. The trailing edge of one coil is welded together with the leading edge of the following coil in the seam welder. The strip enters an entry looper (also known as strip accumulator), which is used to decouple the strip velocities in the different sections of the galvanizing line. In this way, the bulk velocity of the strip in the section between the annealing furnace and the cooling tower, see Fig. 1.1b, can be kept nearly constant or is only slowly varying. The velocity of the strip in this section can be varied from 1 m/s to 2 m/s. After a heat treatment of the strip in the annealing furnace to control its mechanical properties, e.g., the strength and deformability, the strip enters the galvanizing section. This section ranges from the zinc pot to the radiometric gauges of the zinc coating thickness. The zinc layer is added in this plant section, which will be described in detail in Section 1.1.2. Finally, as shown in Fig. 1.1c, the strip passes the shears for cutting the strip into its final length and it is again coiled.

1.1.2 Hot-dip galvanizing section

For a typical industrial hot-dip galvanizing line, Fig. 1.2 shows the strip section between the galvanizing bath and the radiometric gauges of the zinc coating thickness. The photograph in Fig. 1.3 shows the area near the gas wiping dies.

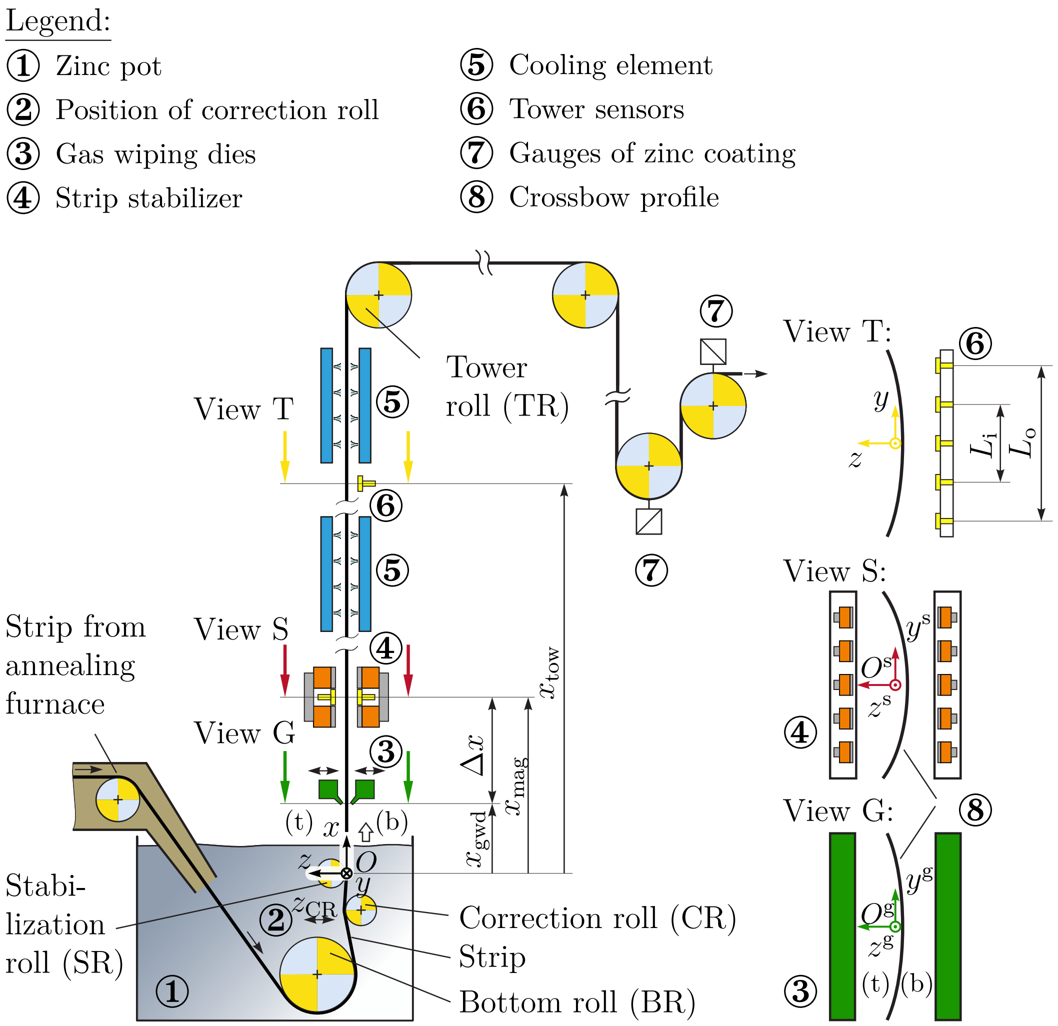

Figure 1.2: Industrial hot-dip galvanizing line equipped with an electromagnetic stabilizer.

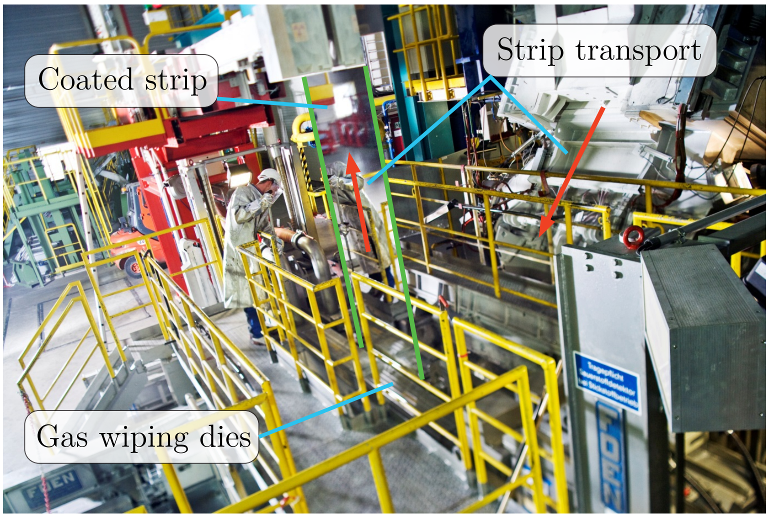

Figure 1.3: Production of a zinc-coated steel strip using a hot-dip galvanizing bath (© voestalpine Stahl GmbH).

The zinc coating is added to the steel strip in a pot of molten zinc ①, which has a temperature of approximately 460 °C. Excessive zinc is blown off by the gas wiping dies ③ positioned above the zinc pot. The remaining zinc layer solidifies in the cooling tower before the strip gets in contact with the tower roll. To this end, the cooling elements in the tower ⑤ generate a continuous flow of cooling air over the surface of the strip. To process a homogeneous zinc coating thickness, the supply pressure in the gas wiping dies has to be constant and the distances between the strip and the gas wiping dies (strip-to-nozzle distances) have to be uniform in lateral direction. The influence of the strip-to-nozzle distances on the homogeneity of the final zinc coating thickness was analyzed and reported in the literature, see, e.g., [2, 3]. It is known that the thickness of the zinc-coating layer decreases with an increasing supply pressure in the gas wiping dies and a decreasing strip-to-nozzle distance. Clearly, the profile of the zinc coating thickness at the bottom side (marked with (b) in Fig. 1.2) is correlated with the transverse strip profile at the gas wiping dies. A negative correlation appears for the zinc coating thickness at the top side (t) of the strip. In practice, the supply pressure in the gas wiping dies is calculated using a mathematical coating-weight model that takes into account the nominal strip-to-nozzle distance [2]. Hence, a flat transverse strip profile at the gas wiping dies is a prerequisite to achieve a homogeneous zinc coating thickness. Downstream radiometric gauges ⑦ of the zinc coating thickness are employed to monitor the lateral coating profiles on the top and the bottom side of the strip. However, the radiometric gauges entail a significant transport delay because they are positioned far away from the gas wiping dies [4].

The strip is exposed to thermal treatment in the upstream annealing furnace

Mode	Name	CR	G	S
	Even	✗	✓	✓
	Skew	✗	✓	✓
	Crossbow	✓	✗	✓
	Relevant higher-order modes	✗	✗	✓

Table 1.1: Profile modes of the steady-state strip displacement at the gas wiping dies and suitable actuators for their compensation: CR - correction roll, G - gas wiping dies, S - electromagnetic strip stabilizer.

and numerous plastic bending deformations at the deflection rolls of the galvanizing line, see, e.g., [5]. After a history of plastic deformations at different temperatures, see Fig. 1.1, the incoming strip typically exhibits unknown residual curvatures and flatness defects.

In normal production, the conditions in the upstream annealing process vary only slowly [6, 7]. Because usually only elastic deformations of the strip occur in the section between the stabilization roll and the tower roll, the residual curvatures of the strip are constant in this section. By this line of reasoning, the residual curvatures of the strip can be assumed to be uniform in longitudinal direction, i.e., the residual curvatures are only functions of the time t and the coordinate y. Typical flatness defects are the so-called crossbow ⑧ and coil-set, which describe non-zero curvatures of the strip in lateral and longitudinal direction, respectively [8, 9]. Table 1.1 gives an overview of typical flatness defects along the lateral direction (profile modes) at the gas wiping dies. Generally, the transverse strip displacement profile is composed of more than one mode. For instance, a coil-set can cause a shift of the transverse strip displacement at the gas wiping dies (even profile mode). Different actuators in the hot-dip galvanizing line can be used to compensate the single profile modes.

In practice, the three-roll tension leveler in the zinc pot is used to reduce the crossbow mode of the transverse strip profile at the position of the gas wiping dies by an elasto-plastic deformation of the strip [10]. For this purpose, the position z_{CR} of the correction roll ② can be adapted, see Fig. 1.2 and Tab. 1.1. The influence of the position z_{CR} of the correction roll on the residual curvatures of a strip is analyzed in detail in [11]. Other profile modes cannot be suppressed by the tension leveler. However, the even and skew profile modes can be considered by adjusting the position and the tilt angle of the gas wiping dies, see Tab. 1.1. In practice, the measured zinc coatings are used as feedback to find the optimal position adjustments of the correction roll and the gas wiping dies. The zinc coating measurements are used as feedback because it is unfeasible to install sensors that measure the transverse strip displacement directly at the gas wiping dies, mainly due to design and thermal reasons. Generally, the adaption process for the correction roll and the gas wiping dies must be slow because of the significant transport delay of the zinc-coating measurements.

Transverse vibrations of the strip are frequently encountered in hot-dip galvanizing lines. Such vibrations entail fluctuations in the strip-to-nozzle distances and are thus unwanted. They result in a deterioration of the homogeneity of the zinc-coating thickness of the final product. Vibrations of the strip are mostly unavoidable and are caused by different sources, e.g., eccentricities of the zinc pot rolls or air jets of the cooling elements in the tower [12]. Taking into account the multiple rolls and actuators along the plant, maintaining a specific tensile load in the strip is known to be a difficult control task. Fluctuations of the strip tension can also lead to transverse strip vibrations. Eccentric rolls in the zinc pot or eccentric touch rolls in a short distance above the gas wiping dies constitute a main source of vibrations [13, 14]. Such touch rolls are sometimes used in older hot-dip galvanizing lines, where an electromagnetic strip stabilizer is not available.

In modern plants, strip stabilizers ④, which are equipped with electromagnetic actuators and displacement sensors, are located above the gas wiping dies and utilized for vibration damping and control of the transverse strip displacement [4, 15–17]. The displacement sensors are usually located near the electromagnets. However, an ideal collocation between the sensor-acuator pairs is often unfeasible, mainly due to space restrictions. In some cases, the electromagnetic stabilizers are mechanically connected to the gas wiping dies, where linear actuators adjust the alignment of the stabilizer relative to the gas wiping dies. For constructional reasons, a vertical distance $\Delta x = x_{\mathrm{mag}} - x_{\mathrm{gwd}} > 0$ between the gas wiping dies and the strip stabilizer is unavoidable, see Fig. 1.2. The stabilizer is equipped with multiple pairs of electromagnets, which are arranged in lateral direction, see Fig. 1.2. Every electromagnet includes a distance sensor for measuring its pole-shoe-to-strip distance (air gap).

In practice, decentralized PID controllers are used for every electromagnetic actuator pair. These controllers use the currents of the electromagnets as control inputs [18]. The actuators are typically used to control the transverse strip positions at the strip stabilizer. This control task is simplified by the fact that the positions to be controlled are measured. The reduction of strip vibrations and flatness defects at the displacement sensors results in an improved homogeneity of the final zinc-coating thickness [18]. In general, strip stabilizers have the potential to compensate all relevant strip profile modes at the gas wiping dies, see Tab. 1.1. The required force levels and the number of actuators (pairs of electromagnets) in lateral direction limit the order of the highest strip profile mode that can be controlled.

1.1.2.1 Three-roll tension leveler in the zinc pot

In the zinc pot, the strip is subject to high temperatures and tension. It is guided by the three-roll tension leveler as shown in Fig. 1.4. Depending on different conditions, e.g., the geometry of the tension leveler and the position z_{CR} of the correction roll, the strip passes the stabilization roll either at a contact point or it wraps around the stabilization roll. The geometric dimensions and vertical distances of the tension leveler are small enough to assume that the curvature of the strip is zero in lateral direction, i.e., a crossbow cannot develop inside the zinc pot [19].

The considered coordinate systems are all located in the lateral center plane of the strip. The inertial coordinate system $Oxyz$ is located at the height of the stabilization roll as outlined in Fig. 1.4. The x-axis in Fig. 1.4 defines the so-called ideal pass line of the strip, i.e., the vertical line between the vertex of the stabilization roll and the vertex of the tower roll. Note that due to the influence of gravity, the tensile load $N_{xx,\mathrm{BR}}$ at the bottom roll is approximately ten percent lower than the tensile load $N_{xx,\mathrm{L}}$ at the tower roll.

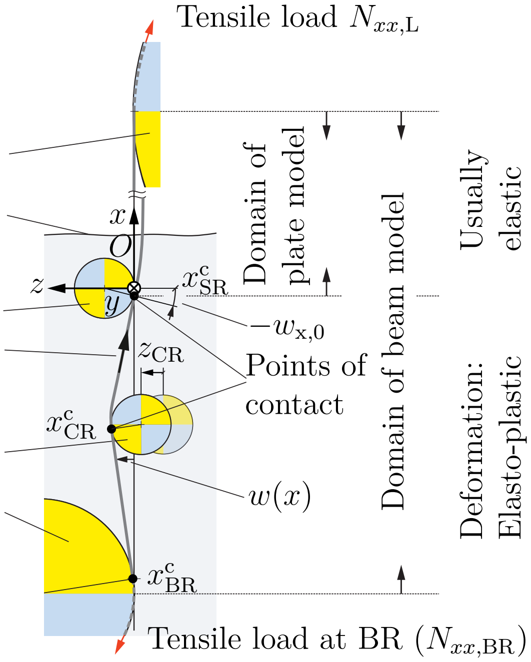

Figure 1.4: Roll configuration in the zinc pot.

1.1.2.2 Gas wiping dies and electromagnetic strip stabilizer

The gas wiping dies and the strip stabilizer are located above the stabilization roll at the adjustable and known distances x_{gwd} and x_{mag}, respectively, cf. Fig. 1.2.

The gas wiping dies and the electromagnetic actuators can be freely positioned relative to the strip in their horizontal planes (y-z-plane), see also Fig. 1.6. However, mainly to save time and costs, only a coarse geometric calibration is conducted during installation and maintenance of the plant. This means that the horizontal positions of these devices with respect to the inertial coordinate system are not accurately known. Hence, additional local coordinate systems are utilized for the gas wiping dies and the electromagnetic actuators and marked with the superscripts s and g, respectively.

Figure 1.6a shows the local coordinate system $O^{\mathrm{s}}x^{\mathrm{s}}y^{\mathrm{s}}z^{\mathrm{s}}$ at the position x_{mag} of the strip stabilizer, which exhibits $\kappa = 5$ pairs of electromagnets. The function $w^{\mathrm{s}}_{\mathrm{mag}}(y)$ represents the local strip profile at the height x_{mag} of the displacement sensors. Figure 1.5 outlines an electromagnet of the strip stabilizer, which is used in the considered hot-dip galvanizing line. Here, the displacement sensor is located in the center of the U-shaped core, cf. [18, 20].

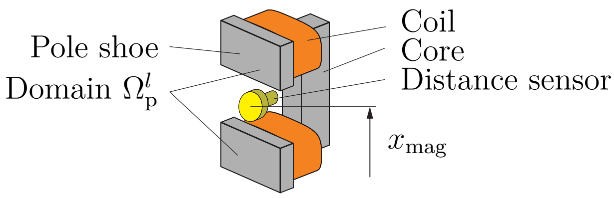

Figure 1.5: Electromagnet with pole shoes and U-shaped core [20].

The vectors $\boldsymbol{\delta}^{\mathrm{t}} \in \mathbb{R}^{\kappa}$ and $\boldsymbol{\delta}^{\mathrm{b}} \in \mathbb{R}^{\kappa}$ contain the measured air gaps between the strip and the respective pole shoes of the electromagnetic actuators at the top (t) and bottom (b) side of the strip. The relation $\Delta z_{\mathrm{mag}} = \delta^{\mathrm{t},l} + \delta^{\mathrm{b},l} + h$ holds for $l \in \{1, \ldots, \kappa\}$, see Fig. 1.6a, where h is the strip thickness and Δz_{mag} denotes the pole-shoe-to-pole-shoe distance of two vis-à-vis electromagnets. The vector $\mathbf{w}^{\mathrm{s}}_{\mathrm{mag}} = \frac{\boldsymbol{\delta}^{\mathrm{b}} - \boldsymbol{\delta}^{\mathrm{t}}}{2}$ contains the deflections of the strip along the direction z^{s} with respect to the local coordinate system of the electromagnetic stabilizer. For $\mathbf{w}^{\mathrm{s}}_{\mathrm{mag}} = \mathbf{0}$, all measured points of the strip are located in the plane $z^{\mathrm{s}} = 0$. The mean displacement $w^{\mathrm{s}}_{\mathrm{mean}}$ and the skew angle φ^{s} indicated in Fig. 1.6a are unknown and therefore have to be estimated.

Figure 1.6b shows the local coordinate system $O^{\mathrm{g}}x^{\mathrm{g}}y^{\mathrm{g}}z^{\mathrm{g}}$ at the position x_{gwd} of the gas wiping dies. The quantities $w^{\mathrm{g,s}}_{\mathrm{mean}}$ and $\varphi^{\mathrm{g,s}}$ in Fig. 1.6b denote the mean deflection and skew angle between the local coordinate system $O^{\mathrm{g}}x^{\mathrm{g}}y^{\mathrm{g}}z^{\mathrm{g}}$ of the gas wiping dies and the local coordinate system $O^{\mathrm{s}}x^{\mathrm{s}}y^{\mathrm{s}}z^{\mathrm{s}}$ of the strip stabilizer. Since the angles φ^{s} and $\varphi^{\mathrm{g,s}}$ are both very small, a small-angle approximation can be performed, i.e. $\cos(\varphi^{\mathrm{s}}) \approx 1$, $\cos(\varphi^{\mathrm{g,s}}) \approx 1$, $\sin(\varphi^{\mathrm{s}}) \approx \varphi^{\mathrm{s}}$, and $\sin(\varphi^{\mathrm{g,s}}) \approx \varphi^{\mathrm{g,s}}$. This infers that the lateral positions of the electromagnets are the same in the local and inertial coordinate system, i.e. $y^{\mathrm{s},l}_{\mathrm{mag}} = y^{l}_{\mathrm{mag}}$. The measured local strip displacements $\mathbf{w}^{\mathrm{s}}_{\mathrm{mag}}$ at the strip stabilizer are transformed into the inertial coordinate system utilizing

$$\mathbf{w}_{\mathrm{mag}} = \mathbf{w}^{\mathrm{s}}_{\mathrm{mag}} + \mathbf{\Phi}\mathbf{p}, \tag{1.1}$$

with the matrix $\mathbf{\Phi} = [\mathbf{1}, \mathbf{y}_{\mathrm{mag}}] \in \mathbb{R}^{\kappa \times 2}$, the lateral positions of the electromagnets

$$\mathbf{y}^{\mathrm{T}}_{\mathrm{mag}} = \left[y^{1}_{\mathrm{mag}}, \ldots, y^{\kappa}_{\mathrm{mag}}\right], \tag{1.2}$$

and the vector $\mathbf{p}^{\mathrm{T}} = [w^{\mathrm{s}}_{\mathrm{mean}}, \varphi^{\mathrm{s}}]$ of unknown quantities.

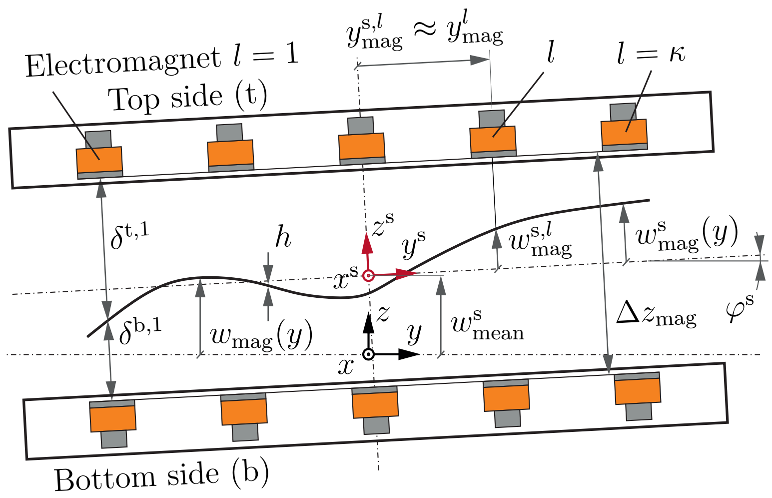

(a) Electromagnetic stabilizer with $\kappa = 5$ pairs of electromagnets.

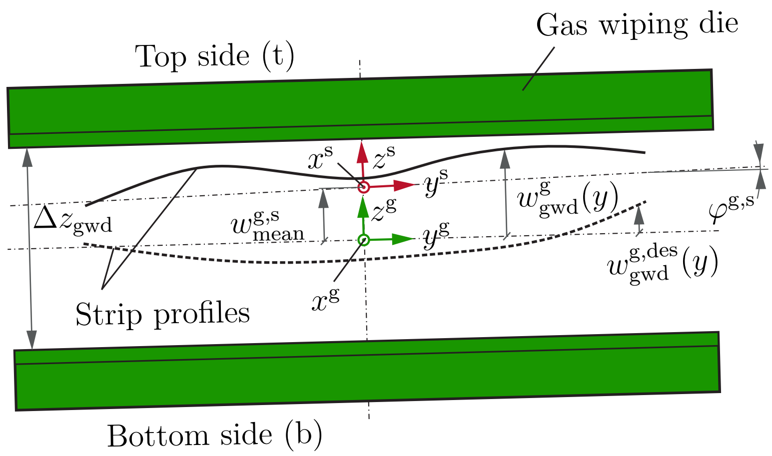

(b) Gas wiping dies.

Figure 1.6: Sketch showing inertial and local coordinate systems of the actuators.

In Fig. 1.6b, the mean deflection $w^{\mathrm{g,s}}_{\mathrm{mean}}$ and the skew angle $\varphi^{\mathrm{g,s}}$ between the coordinate systems $O^{\mathrm{g}}x^{\mathrm{g}}y^{\mathrm{g}}z^{\mathrm{g}}$ and $O^{\mathrm{s}}x^{\mathrm{s}}y^{\mathrm{s}}z^{\mathrm{s}}$ are measured with sufficient accuracy.

The functions $w^{\mathrm{g}}_{\mathrm{gwd}}(y)$ and $w^{\mathrm{g,des}}_{\mathrm{gwd}}(y)$ are the actual and the desired local transverse strip profiles, respectively, at the gas wiping dies. The vector

$$\mathbf{y}^{\mathrm{T}}_{\mathrm{gwd}} = \left[-\frac{b}{2}, -\frac{b}{2} + \frac{b}{\lambda - 1}, \dots, \frac{b}{2} - \frac{b}{\lambda - 1}, \frac{b}{2}\right], \tag{1.3}$$

with $\mathbf{y}_{\mathrm{gwd}} \in \mathbb{R}^{\lambda}$ and $\lambda \gg \kappa$, contains equidistant grid points over the width b of the strip. Values of the corresponding transverse strip profiles at the points $\mathbf{y}_{\mathrm{gwd}}$ are assembled in the vectors $\mathbf{w}^{\mathrm{g}}_{\mathrm{gwd}}$ and $\mathbf{w}^{\mathrm{g,des}}_{\mathrm{gwd}}$. The transverse strip displacement $\mathbf{w}_{\mathrm{gwd}}$ at the gas wiping dies transformed into the inertial coordinate system $Oxyz$ reads as

$$\mathbf{w}_{\mathrm{gwd}} = \mathbf{w}^{\mathrm{g}}_{\mathrm{gwd}} + \mathbf{\Omega}(\mathbf{p} - \mathbf{q}), \tag{1.4}$$

with $\mathbf{\Omega} = [\mathbf{1}, \mathbf{y}_{\mathrm{gwd}}] \in \mathbb{R}^{\lambda \times 2}$ and $\mathbf{q}^{\mathrm{T}} = [w^{\mathrm{g,s}}_{\mathrm{mean}}, \varphi^{\mathrm{g,s}}]$. The vector $\mathbf{w}^{\mathrm{g}}_{\mathrm{gwd}}$ contains the transverse strip displacements at the gas wiping dies expressed in the local coordinate system $O^{\mathrm{g}}x^{\mathrm{g}}y^{\mathrm{g}}z^{\mathrm{g}}$.

1.1.2.3 Cooling elements

Air coolers consisting of multiple cooling elements span over a wide range in the tower of the plant, cf. Fig. 1.2. They continuously reduce the temperature of the coated strip to ensure a solidified zinc layer at the tower roll. This prevents a deposition of liquid zinc particles at the tower roll and surface defects of the strip. A single cooling element is shown in Fig. 1.7. The heat dissipation of a cooling element can be controlled via the fan speed of its blower.

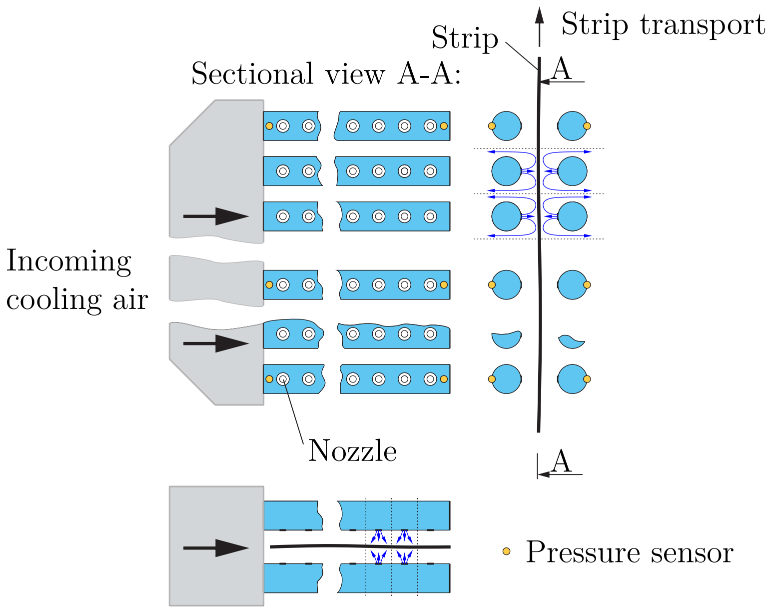

Figure 1.7: Sktech of a cooling element supplied by an air blower.

1.1.2.4 Radiometric gauges of the zinc coating weight

The coating thicknesses on both sides of the strip are measured by radiometric gauges after the zinc is completely solidified. In fact, the measurement equipment is located more than 50 m downstream of the gas wiping dies. This yields a significant transport delay between the currently realized coating thickness at the gas wiping dies and its downstream measurement. This delay also depends on the bulk velocity V of the strip. Since the sensor units traverse in lateral direction, the current zinc-coating thickness is measured at discrete points in a zigzag pattern as shown in Fig. 1.8. Moreover, the top and bottom sensor are not synchronized, see Fig. 1.8. Consequently, they can only measure the time-delayed coating profiles, where the average profiles correlate to the steady-state flatness defects of the strip. Hence, these measurements can only be used as feedback for steady-state control concepts.

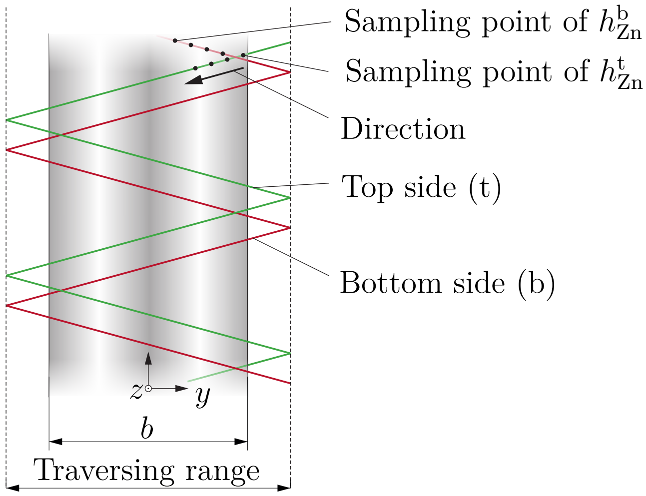

Figure 1.8: Zigzag pattern representing the measurement path of the traversing radiometric gauges. The strip is fixed in this illustration.

1.1.3 Current problems at the industrial plant

This section describes the unresolved challenges in the hot-dip galvanizing process, which should be addressed in this work. The following measurements were performed at an industrial hot-dip galvanizing line of voestalpine Stahl GmbH in Linz, Austria, see also [1].

1.1.3.1 Stability problems caused by the air coolers

Experience over the years has shown that air cooling jets in the tower can jeopardize the stability of the strip motion, in particular when broader and thinner strips are processed. Furthermore, in special situations unintended vibrations of the strip can be induced or the strip may even collide with the nozzles of a cooling element. In particular, the tensile load, the strip thickness, and the pressure in the supply duct of the air coolers have to be adjusted properly in order to avoid these issues.

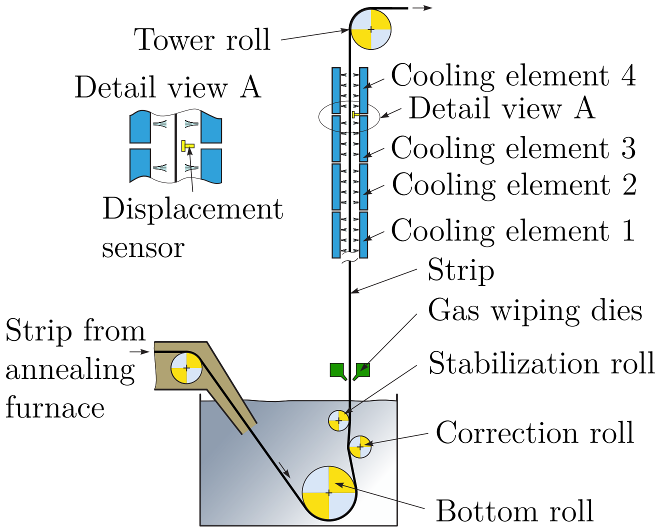

(a) Hot-dip galvanizing line without a strip stabilizer.

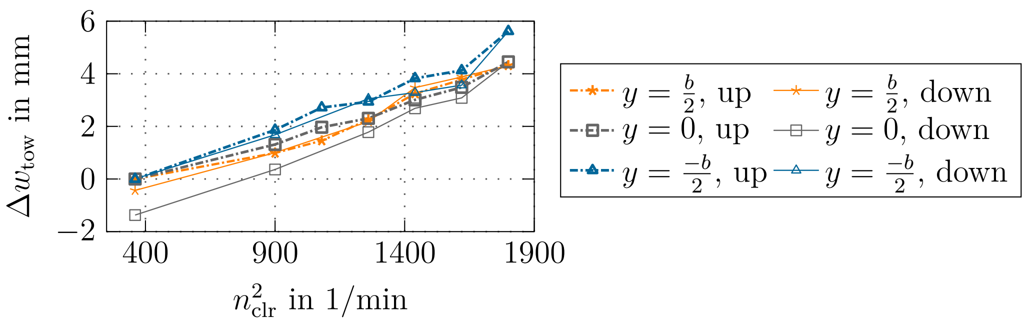

(b) Relative transverse displacement Δw_{tow} of the strip for multiple sensor positions: up - increasing fan speed n^2_{clr} of cooler 2, down - decreasing fan speed n^2_{clr} of cooler 2.

Figure 1.9: Experiment conducted in the industrial hot-dip galvanizing line.

In an experiment, three eddy current displacement sensors, see Fig. 1.9a, were used to examine the interaction between the fan speed of the air cooler and the relative transverse displacement of the strip. The sensors were mounted between the cooling elements 3 and 4. Two of them were located at the outer edges of the strip at the positions $y = -b/2$ and $y = b/2$. The third sensor was positioned in the middle of the strip at $y = 0$. The fan speed n^2_{clr} of cooler 2 was varied for this experiment, all other fan speeds n^1_{clr}, n^3_{clr}, and n^4_{clr} and the most relevant parameters of the plant were held constant during the experiment. Figure 1.9b shows the measured relationship between the transverse displacement Δw_{tow} of the strip and the fan speed n_{clr}^2 for both increasing and decreasing fan speeds. The transverse displacement Δw_{tow} of every sensor is measured relative to its initial position. The displacements Δw_{tow} for increasing fan speeds (up) are designated with bold dash-dotted lines, whereas decreasing fan speeds (down) are highlighted with thin solid lines. The fan speed was kept constant at a certain level for a short period of time. The averaged measurements are highlighted with markers. The results clearly demonstrate that the transverse strip displacement is influenced by the fan speed of the air blower. Although a stable strip pass is necessary for the safe operation of the processing line, no systematic investigations of the influence of the cooler air jets on the stability of the strip are reported in the literature.

1.1.3.2 The transverse strip profile at the gas wiping dies

Modern hot-dip galvanizing lines are often equipped with electromagnetic strip stabilizers. The unavoidable and non-zero vertical distance Δx, see Fig. 1.2, and the absence of sensors measuring the transverse strip profile at the gas wiping dies make it very challenging to control the transverse strip profile at the gas wiping dies. Clearly, this control problem would be trivial for $\Delta x = 0$. Usually, an approximately flat strip profile at the position of the electromagnetic stabilizer is realized by commanding zero set-points to the subordinate PID position controllers. For a non-zero crossbow of the strip, e.g., caused by an improper position of the correction roll, and despite the approximately flat strip profile at the stabilizer, a crossbow can still remain at the gas wiping dies. This problem is also addressed by the manufacturer of the strip stabilizer [18]. Figure 1.10 shows the measurement results of an experiment conducted in the industrial hot-dip galvanizing line, where a polynomial curve of order 9 was fitted. For this experiment, a traversing laser distance sensor was temporarily assembled right above the gas wiping dies to measure the steady-state transverse strip profile w_{lsr}. The vertical distance between the nozzle slit and the sensor was approximately 300 mm. This sensor traverses similar to the trajectory shown in Fig. 1.8 and cannot be used in normal production. Using the zero strip position set-points shown in Fig. 1.10a, the measured zinc coating thickness is still not optimal and could be improved. In practice, active position control of the electromagnetic strip stabilizer using zero set-points can reduce but usually not completely suppress the crossbow at the gas wiping dies. The vertical distance Δx between the strip stabilizer and the gas wiping dies significantly influences the improvement of the flatness at the gas wiping dies. Basically, the shorter Δx is, the better is the uniformity of the nozzle-to-strip distance (air gap) in the gas wiping dies. Generally, the zero set-points are used for the position controllers at the electromagnets because the optimal position set-points are unknown [18]. These optimal set-points would ensure the best homogeneity of the lateral zinc coating thickness. Figure 1.10b shows the measurement results after an optimization of the coating thickness, where the set-point values of the position controllers were manually tuned. This yields an almost flat transverse strip profile at the gas wiping dies. Despite this possibility to improve the homogeneity of the coating, a systematic approach for the compensation of lateral flatness defects at the gas wiping dies is not used in practice.

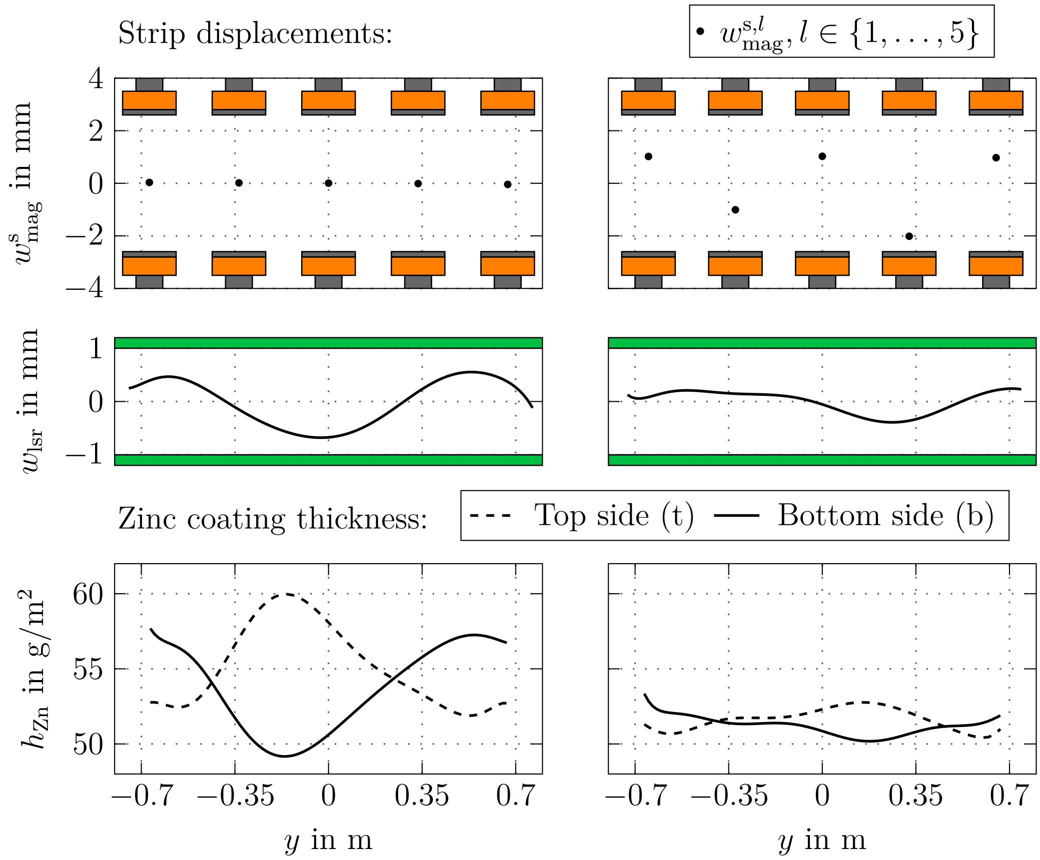

(a) Standard method using zero set-points for the position controllers.

(b) Manually adjusted set-point values for the position controllers to optimize the processed coating thickness.

Figure 1.10: Experiment conducted in an industrial hot-dip galvanizing line to manually improve the zinc coating thickness using the position control of the electromagnetic strip stabilizer ($\Delta x = 1.2\,\mathrm{m}$).

1.1.3.3 Eccentric rolls in the zinc pot

The rolls of the tension leveler in the zinc pot define boundary conditions for the moving strip. An eccentricity of the correction or the stabilization roll is frequently observed, which usually results in a persistent harmonic (sometimes multi-harmonic) excitation of the strip. There are various (sometimes unknown) reasons for such eccentricities, e.g., wear of the bearings of a roll (the bearings are submerged in liquid zinc), roll bending caused by a non-uniform thermal expansion, or the non-uniform deposition of metal particles on the roll surface. Such a roll eccentricity shows up in the characteristic amplitude spectrum of the transverse strip displacement given in Fig. 1.11b. In this case, the dominating frequency of the spectrum precisely coincides with the rotating frequency of the correction roll. In general, either the stabilization roll or the correction roll, which have a similar diameter, cause these disturbances. In the conducted experiments, the bottom roll, which has a large diameter, was never observed as a source of the disturbances.

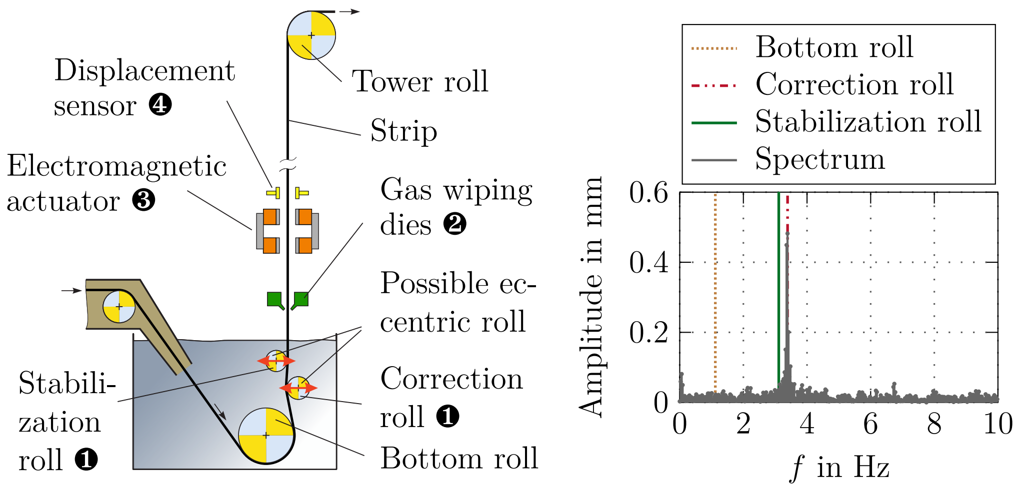

(a) Plant with eccentric pot rolls.

(b) Typical single-sided amplitude spectrum.

Figure 1.11: Frequency spectrum of the transverse strip displacement measured at the position ❹ in an industrial hot-dip galvanizing line. The vibration is caused by an eccentric pot roll at the position ❶.

Randomly excited vibrations of the strip can be reasonably damped by ordinary PID controllers. However, this is usually not the case for persistently exciting vibrations, e.g., caused by an eccentric pot roll. Since the mechanism behind the (multi-)harmonic disturbances and the exact excitation process are unknown, it is reasonable to expect that this disturbance acts at a specific point on the strip, is periodic, has a constant and unknown (fundamental) frequency, and an unknown amplitude and phase. Moreover, the number of harmonics to be considered in the disturbance model depends on the typical frequency spectrum of the specific application, see, e.g., Fig. 1.11b.

Remark: The assumption of the constant (fundamental) frequency does not constitute a significant restriction for this specific application. In industrial hot-dip galvanizing lines, strips are welded together to maintain a continuous operation of the processing line. For quality reasons, the bulk velocity of the strips remains almost constant and is only allowed to be slowly changed if a welded joint traverses the plant. Since roll eccentricities are a typical source for the harmonic disturbances, also the disturbance frequency remains constant for most of the times and changes only slowly in transition periods. A slow change of the (fundamental) frequency can be well captured by the control method presented in this work.

In contrast to the advanced strip stabilizer shown in the Figs. 1.5 and 1.6a, many devices are available on the market where the sensor-actuator pairs are not perfectly collocated. Hence, a situation can occur where the disturbance input (❶, persistent multi-harmonic disturbance), the control input (❸, electromagnetic forces), the sensor output (❹, displacement sensor), and the system output (❷, strip displacement in the gas wiping dies) are all located at different positions along the strip, see Fig. 1.11a. For such a configuration, vibration control in the system output is a very challenging task.

1.2 Objectives of this work

In this work, model-based control approaches are pursued to address the challenges described in Section 1.1.3. To this end, it is necessary to develop a sufficiently accurate dynamical model of the strip in an industrial hot-dip galvanizing line. However, not all of the developed control concepts can be directly tested in the industrial plant. Some of them are evaluated using an experimental test rig that mimics a scenario from the industrial hot-dip galvanizing line [21, 22]. This experimental test rig was designed to study different control concepts and the impact of various actuator and sensor positions. Experiments conducted on the test rig served as the basis for an implementation of the proposed methods in the industrial plant. Moreover, a finite-element model of the strip shape was developed that can be easily adapted to the dimensions of an industrial hot-dip galvanizing line or the experimental test rig.

The objectives can be summarized as follows:

- *Systematic investigation of the steady-state and dynamic behavior of the strip in the industrial hot-dip galvanizing line*
  A suitable mechanical model of the transverse strip shape should be derived that takes into account the most influential effects of the different devices in the plant, e.g, the electromagnetic forces or the transverse loads due to the cooling elements (cf. Section 1.1.3.1), and the deformation history of the strip. The complexity of the model should be kept as low as possible and the model has to be validated with measurements from the plant.

- *Optimal compensation of flatness defects at the gas wiping dies*
  An optimization-based feedforward control concept should be developed

to improve the uniformity of the air gaps in the gas wiping dies in case of non-zero flatness defects of the strip (cf. Section 1.1.3.2). This optimal compensation method should be based on a model-based estimator of the flatness defects and a model-based feedforward controller of the transverse strip profile at the gas wiping dies. The estimator should be validated for different scenarios with measurements from the plant. A detailed analysis of the feedforward control concept should be performed.

- *Active rejection control of unknown multi-harmonic disturbances at an unmeasured position of the strip*
  A method for the suppression of an exogenous multi-harmonic periodic disturbance at an arbitrary position of a steel strip should be developed (cf. Section 1.1.3.3). In the considered experimental test rig, the disturbance input, the displacement sensor, the electromagnetic actuator, and the controlled system output (cf. the gas wiping dies) are all located at different positions. The electromagnetic actuator should operate in a pure feedforward mode. The developed control method should be validated on the experimental test rig.

1.3 State of the art and new contributions of this work

In this section, the state of the art in systems analysis and control concepts for hot-dip galvanizing lines is discussed and ideas from recent literature are presented. Section 1.3.1 gives an overview of available mathematical models used for similar applications. Section 1.3.2 describes the literature related to modeling and control of the industrial hot-dip galvanizing line. In Section 1.3.3, possible control concepts for the active rejection of unknown periodic disturbances suitable for the experimental test rig scenario are discussed.

The research presented in this thesis is mainly based on works that were already published in journals or presented at conferences. The corresponding references are given in the following.

Mathematical modeling

[23] M. Saxinger, A. Steinboeck, M. Baumgart, and A. Kugi, “Dynamical model of axially moving steel strips”, *IFAC-PapersOnLine*, vol. 49, no. 20, pp. 190–195, 2016.

[24] M. Saxinger, A. Steinboeck, M. Baumgart, P. Kerschbaummayr, and A. Kugi, “Influence of air cooling jets on the steady-state shape of strips in hot dip galvanizing lines”, *IFAC-PapersOnLine*, vol. 28, no. 17, pp. 143–148, 2015.

[25] M. Saxinger, A. Steinboeck, L. Marko, M. Baumgart, and A. Kugi, “Nonlinear dynamical model of an axially moving steel strip in a surface coating plant (in German)”, *at-Automatisierungstechnik*, vol. 65, no. 8, pp. 546–560, 2017, (best paper award).

[26] M. Saxinger, A. Steinboeck, M. Baumgart, and A. Kugi, “Nichtlineares Bewegungsmodell für ein Stahlband in einer Oberflächenbeschichtungsanlage”, in *Tagungsband GMA-Fachausschuss 1.30 "Modellbildung, Identifikation und Simulation in der Automatisierungstechnik"*, Anif/Salzburg, Austria, 2016, pp. 46–67.

[27] M. Baumgart, A. Steinboeck, M. Saxinger, and A. Kugi, “Elasto-plastic bending of steel strip in a hot-dip galvanizing line”, in *Proceedings of the 3rd Polish Congress of Mechanics (PCM) and 21st International Conference on Computer Methods in Mechanics (CMM)*, Gdansk, Poland, 2015, pp. 55–56.

[19] M. Baumgart, A. Steinboeck, M. Saxinger, and A. Kugi, “Elasto-plastic bending of steel strip in a hot-dip galvanizing line”, *Acta Mechanica*, vol. 228, no. 7, pp. 2455–2470, 2017.

[17] L. Marko, M. Saxinger, A. Steinboeck, and A. Kugi, “Magnetic actuator design for strip stabilizers in hot dip galvanizing lines”, in *Proceedings of the IEEE Industry Applications Society Annual Meeting*, Portland, Oregon, USA, 2018, pp. 1–9.

[20] L. Marko, M. Saxinger, A. Steinboeck, and A. Kugi, “Magnetic actuator design for strip stabilizers in hot-dip galvanizing lines: Examining rules and basic tradeoffs”, *IEEE Industry Applications Magazine*, vol. 26, no. 2, pp. 54–63, 2020.

Control concepts

[28] M. Saxinger, L. Marko, A. Steinboeck, and A. Kugi, “Active rejection control for unknown harmonic disturbances of the transverse deflection of steel strips with control input, system output, sensor output, and disturbance input at different positions”, *Mechatronics*, vol. 56, pp. 73–86, 2018, (best paper award).

[29] M. Saxinger, L. Marko, A. Steinboeck, and A. Kugi, “Non-collocated position control of steel strip with electromagnetic rejection of unknown multi-harmonic disturbances”, *IFAC-PapersOnLine*, vol. 52, no. 15, pp. 430–435, 2019, (best young author award).

[30] M. Saxinger, L. Marko, A. Steinboeck, and A. Kugi, “Feedforward control of the transverse strip profile in hot-dip galvanizing lines”, *Journal of Process Control*, vol. 92, pp. 35–49, 2020.

1.3.1 Dynamic strip models and suitable solvers

Axially moving shallow structures (e.g. steel strips) are usually encountered in different engineering applications. The widths of the strips range from a few millimeters in magnetic tape data storage systems to more than one meter in production facilities of the paper, foil, and steel industry. In these production facilities, strip vibrations may influence the stability of the production process. Such strip vibrations often deteriorate the quality of the processed goods. Sophisticated dynamic models can accurately describe the strip vibrations. In practice, accurate models of the transverse strip displacements are required for plant design and reliability or safety reasons. Moreover, many control engineering tasks are related to the control of axially moving structures, where models are used for model-based controller and observer design. For the latter purpose, the complexity of the model has to be kept at a low level. In practice, co-simulations are often used for the controller design, where the different subsystems of the coupled problem are simulated in a distributed manner. As an example, the mechanical subsystem (strip model) can be solved using Ansys, whereas the controller and the observer calculations are executed in Matlab. The mutual data exchange occurs at discrete points in time. However, the application of commercially available finite-element software in an industrial plant is often difficult or expensive, especially if it is intended for permanent online simulation of the model. In such situations, tailored models have to be developed. In order to keep the computational load low, it is desirable to use low-dimensional and if possible linear models. Moreover, the main influencing effects, e.g., the residual curvatures of the strip in a hot-dip galvanizing line, have to be considered to provide sufficiently accurate models.

A considerable number of mechanical models are reported in the literature. Each of them is tailored to a specific application scenario. A mechanical model for dynamic responses of an axially moving membrane without considering the bending stiffness and the residual curvatures is presented in [31, 32]. The length-to-width ratios of the considered membranes are assumed to be small. Hence, global basis functions are utilized in the form of Legendre polynomials and trigonometric functions. Furthermore, the interaction between in-plane and out-of-plane motion was neglected. This decoupling leads to a geometrically linear problem, which was solved with the generalized-α method for solving linear systems in the field of structural dynamics [33]. An implicit time integration method tailored to nonlinear structural dynamic problems is published in [34]. In [35], this implicit time integration scheme is extended to account for numerical dissipation of high frequency modes. Moreover, the Newton-Raphson method is augmented by a line search method in special situations [35]. The so-called modified generalized-α method has some similarities to the generalized-α method [35].

In this work, a mechanical model is developed to describe the dynamics of an axially moving steel strip in an industrial hot-dip galvanizing line. The length-to-width ratio of the strip is substantially larger compared to other works [31, 32].

Moreover, the model has to consider the geometrical nonlinearity, the bending stiffness of the strip, and the influence due to residual curvatures of the strip. The assumptions of the Kirchhoff-Love plate theory are utilized [36]. The mechanical plate model is derived based on Hamilton's principle for systems of changing mass [37, 38]. The spatial discretization into finite elements is conducted using the Galerkin weighted residual method. The strip section between the last pot roll and the tower roll is partitioned into an arbitrary number of finite elements in longitudinal and lateral direction by utilizing local basis functions in the form of Hermite and Legendre polynomials. Both the number of the finite elements and the order of the local basis functions influence the accuracy of the model. The transient simulations of the geometrically nonlinear model are carried out with a method based on the works reported in [34, 35]. The steady-state solutions of the nonlinear model are obtained by means of the Newton-Raphson method. This model serves as a basis for all model-based methods developed in this work.

1.3.2 Hot-dip galvanizing line

The literature survey in Section 1.3.2.1 gives an overview of works that are related to the analysis of the steady-state and the dynamic behavior of strips in hot-dip galvanizing lines. In Section 1.3.2.2, works from the literature are presented which are related to the position control of the transverse strip profile with an electromagnetic strip stabilizer.

1.3.2.1 Models used for analyses

An accurate mathematical model has to capture the most important influencing effects on the strip shape. In the literature, works that describe the steady-state and dynamic behavior of the strip in an industrial hot-dip galvanizing line in a systematic way are very rare, if not absent. Therefore, a physics-based model had to be derived that can be used to study the influence of different devices or conditions on the strip shape, i.e., the forces applied by the electromagnetic actuators, the pressure load exerted by the air jets in the cooling section, the unknown residual curvature of the strip, the boundary conditions at the supporting rolls, and the influence of the zinc pot.

The electromagnetic forces can be computed based on a finite-element model, which depends on the measured coil currents and the measured pole-shoe-to-strip distances, cf. Fig. 1.5. A magnetic coupling between neighboring actuators is frequently observed in hot-dip galvanizing lines. In [20], this effect was analyzed in detail based on the finite-element model. The mathematical model was validated by in-situ measurements conducted in an industrial plant and a simple method was proposed to approximately decouple the neighboring electromagnets [20]. This decoupling strategy is also implemented in the considered hot-dip galvanizing line.

Remark: High temperatures and dust consisting of metal particles near the zinc pot constitute harsh conditions for the electromagnetic stabilizer. To prevent failures of the sensors and actuators, they are typically placed in a housing with heat shields, mechanical protection, and active air cooling. Despite the protection of the sensor-actuator pairs against overheating, increased temperatures usually influence the magnetic properties (BH-curve) of the magnetic cores. This applies also to the steel strip and thus influences the electromagnetic force exerted on the strip, see also [20]. However, the longitudinal temperature profile of a strip in an industrial hot-dip galvanizing line is known and can be taken into account. In general, there are two possibilities for considering the temperature influence on the electromagnetic forces. First, the finite-element model can be used for up-front computations of the quasi-static electromagnetic forces, which are computed as a function of different coil currents, air gaps, and strip thicknesses. The results are stored in a look-up table. Clearly, the finite-element model has to take into account the dependence of the BH-curve of the steel strip on the temperature. Note that the influence of the temperature on the BH-curve is well investigated for different materials [39]. As a second method, the quasi-static electromagnetic forces can be directly measured using a dedicated test rig. For this, the electromagnetic forces have to be measured for the different coil currents, air gaps, strip thicknesses, and strip temperatures. Such a test rig has to be equipped with a force sensor, a specimen heating device, and a controller for the specimen temperature.

An analysis is performed to study the influence of the air jets of a cooling element in Fig. 1.7 on the steady-state shape and on the stability of the strip. To this end, the nonlinear force characteristic of a single nozzle is measured by means of a laboratory-scale flow simulator. The approach differs from conventional methods where usually CFD simulations are employed. Based on the force characteristic of the cooling elements, a stability analysis is conducted to assess the calculated equilibrium points. The influence of different types of boundary conditions is evaluated for different tensile loads at the tower roll, strip thicknesses, and fan speeds of the blower.

The unknown residual curvature (crossbow) of the strip above the stabilization roll mainly depends on the position z_{CR} of the correction roll. A crossbow cannot develop near the tension leveler, see Section 1.1.2.1. Hence, the resultant bending line of the strip in Fig. 1.4 can be approximately captured with an elasto-plastic beam model on the domain between the bottom and the tower roll [19, 27]. Clearly, the assumption of a zero crossbow is questionable for the domain between the stabilization roll and the tower roll. However, it turned out that the influence of the non-zero crossbow above the stabilization roll on the residual curvature at the stabilization roll is almost negligible [19]. Based on this beam model, a feedforward control concept to adjust the transverse position of the gas wiping dies was successfully implemented and validated in an industrial hot-dip galvanizing line [19]. The calculated quantities, e.g., the residual curvature and the boundary conditions at the stabilization roll, serve as input parameters for the elastic plate model capturing the domain between the stabilization roll and the tower roll.

The beam model is used to calculate the plastic deformation state for different test strips. Applying these parameters to the plate model, the impact of the geometrical nonlinearity on the transverse strip displacements is analyzed in the case of a faulty air cooler. The influence of the geometrical nonlinearity on both the steady-state and the dynamic behavior of the strip is investigated in detail. The simulation studies are performed for different boundary conditions at the tower roll. Moreover, it is analyzed whether the geometrical nonlinearity of the model is negligible. In principle, the beam model of the bending line can be used for an online calculation of the residual curvature of the strip [19]. However, the method requires accurate measurements of the positions and diameters of the rolls of the tension leveler, which are often not available. Therefore, another model-based approach is developed in this work to estimate the uncertain residual curvature of the incoming strip. This model-based estimator takes into account the nominal parameters of the current production, the measured strip displacements at the electromagnets, and the currently applied electromagnetic forces. The method is validated using the additional displacement sensors in the tower located more than 30 m downstream of the gas wiping dies, see also Fig. 1.2. The validation is carried out for several scenarios, e.g., for different strip dimensions, various positions z_{CR} of the correction roll, and various electromagnetic forces. Besides the direct validation via extra displacement measurements, it will be shown that also the measured zinc coating thickness is clearly correlated with the computed transverse strip profile at the gas wiping dies.

The dynamic model of the strip shape is also successfully validated with free vibration experiments for different initial displacements at the electromagnets. To this end, the extra displacement sensors in the tower are employed. In contrast to the steady-state case, the damping effect of the zinc pot has to be taken into account. This effect is analyzed in detail with measurements conducted for different configurations of the plant (with and without a zinc pot).

1.3.2.2 Position control of the transverse strip profile

Different methods exist to improve the homogeneity of the processed zinc coating thickness. For industrial hot-dip galvanizing lines not equipped with electromagnetic stabilizers, a few zinc coating controllers can be found in the literature, see, e.g., [40–45]. Such a coating controller is usually employed to regulate the even and skew modes of the zinc coating thickness by adjusting the position and the tilt angle of the gas wiping dies, the pressure in the supply duct of the nozzle, and the nozzle-to-nozzle distance of the gas wiping dies. These control approaches allow only a very slow adjustment of the zinc coating thickness because of the delayed downstream measurement. The influence of a non-zero crossbow and higher-order transverse profile modes on the final zinc coating cannot be suppressed at all by these existing control concepts. In [40], the concept of skew control is successfully used to adaptively improve the homogeneity of the zinc coating thickness. In [41, 42], a synthesis method is reported that uses a nonlinear long-term model and a linear short-term model of the coating process. Based on both models, a coating weight controller was developed and successfully tested in a hot-dip galvanizing line. In [43], a multivariable approach is proposed to control the zinc coating thickness, where a model of the coating process is used. Another controller of this type is reported in [44]. It adjusts the supply pressure in the gas wiping dies and their horizontal and vertical positions. A different approach using a neural network-based zinc coating controller is proposed in [45]. There, a feedforward approach is used to define the strip-to-nozzle distance in the gas wiping dies and the supply pressure in the nozzle in case of a fast change of the processing conditions. An additional feedback controller is employed to regulate the supply pressure in the nozzle under steady-state conditions. Since the influence of a crossbow on the zinc coating thickness cannot be suppressed by these controllers, the position z_{CR} of the correction roll, see also Fig. 1.2, has to be manually tuned by an operator to limit the crossbow. Usually, the operator looks at the measured zinc coating profiles and manually corrects the position z_{CR} of the correction roll to minimize the inhomogeneity of the zinc coating thickness.

Newer plants are often equipped with electromagnetic stabilizers. They are typically used to rectify flatness defects in strips to improve the homogeneity of the lateral zinc profiles. In addition, the measurement of the zinc coating can still be used to optimize the homogeneity of the zinc coating thickness. However, the significant transport delay cannot be avoided in this case. A systematic indirect optimization of the homogeneity by means of a flattened strip profile at the gas wiping dies is challenging and only possible with an accurate mathematical model of the strip shape and a model-based feedforward control of the transverse strip profile at the gas wiping dies. Note that the real transverse strip profile at the gas wiping dies cannot be measured. Works that address the optimization of the zinc coating profile in an industrial hot-dip galvanizing line equipped with an electromagnetic stabilizer are rare. In [4], the electromagnetic stabilizer is utilized for both active vibration damping and the control of a uniform lateral zinc coating profile. The measured coating profile is decomposed into constant (even) and linear (skew) components, which are used to correct the position and the tilt angle of the gas wiping dies. The crossbow component is suppressed by strip position control using the electromagnetic actuators. However, because of the time-delayed measurements of the zinc coating thickness, the control loop is tuned to respond slowly.

To avoid a control loop that uses the time-delayed zinc coating measurements, see, e.g., [4], a model-based feedforward control concept for the strip flatness in the gas wiping dies is proposed in this work. Clearly, a model-based approach requires knowledge of the nominal parameters of the current production and the estimated residual curvature of the incoming strip. The feedforward position controller is developed to directly flatten the transverse strip profile at the gas wiping dies (or to adjust a desired transverse strip profile at this position). In this case, the homogeneity of the zinc coating thickness is indirectly optimized. Furthermore, this method does not depend on time-delayed measurements.

A sensitivity matrix is derived from the mathematical model to describe the relation between the control input (forces of the electromagnets) and the discretized transverse strip profile at the gas wiping dies. A singular value decomposition of this sensitivity matrix is used to compensate individual strip profile modes at the gas wiping dies by selecting appropriate forces of the electromagnets. Clearly, the choice of the profile modes to be compensated is a trade-off between the achievable flatness of the strip and the limitations of the electromagnetic forces (and hence the strip deflection at the electromagnets). Since the time-delayed measurements of the zinc coating thickness are not used by the developed feedforward controller, it can quickly react to fast changes of the processing conditions. The feedforward controller computes the required set-points for the strip position controllers realized by the electromagnetic stabilizer. Based on the validated plant model, a simulation study is conducted to test the performance of the proposed feedforward controller for various residual curvatures of the strip. Furthermore, the influence of Δx, see also Fig. 1.2, on the feedforward controller is analyzed in detail. The results are compared to the standard control method, where an approximately flat strip profile is realized at the electromagnets.

Because the computed position set-points for an optimal compensation of the flatness defect at the gas wiping dies are realized by the position controllers of the electromagnetic strip stabilizer, a modification of the existing control structure is not required. Moreover, a costly investment in additional sensors is not necessary since the proposed method uses only nominal production parameters and available measurements. The extra displacement sensors in the tower are only used to validate the estimator.

1.3.3 Experimental test rig

In the first place, the PID controllers of the strip stabilizer are also used for active damping control. More advanced control algorithms, e.g., positive position feedback as reported in [46] or passive damping and boundary control as described in [47], are also recommended for vibration damping in industrial hot-dip galvanizing lines.

Active vibration control of flexible structures such as strings, beams, plates, and shells has been a vivid field of research in the recent decades, see, e.g., [48, 49]. Many of these control approaches require a collocation of the sensor-actuator pair. In [50], an electromagnetic suspension system is described which is used for non-contact processing and vibration damping of tubular steel beams.

Recently, a vibration control approach for a clamped-clamped beam using a multi positive feedback control was reported in [51]. In certain applications, however, collocation of sensor-actuator pairs cannot be realized, e.g., due to limited installation space. Especially for systems with low structural damping, e.g., thin steel strips, it is difficult to achieve a stable control loop in the presence of non-collocated sensor-actuator configurations, see, e.g., [52]. Nevertheless, active vibration control with non-collocated sensor-actuator configuration has been reported in a few publications, see, e.g., [53–55]. H_2, H_∞, and μ-synthesis methods are employed for the synthesis of optimal and robust controllers. The performance of such controllers is guaranteed as reported in [56]. In [57], a review of H_∞ and μ-synthesis methods can be found. Here, systems with collocated and non-collocated sensor-actuator pairs are described for active vibration damping in flexible structures such as beams and plates. Furthermore, LQR and LQG methods are also used for active vibration damping in flexible beam structures, see, e.g., [49].

Persistently exciting disturbances are a frequently observed phenomenon in devices with rotating parts. The best solution would be to remove the root cause of the disturbance itself. If this is not possible, the difficulty of suppressing persistently exciting disturbances depends on the structure of the considered system. The suppression of a purely sinusoidal disturbance at a position that coincides with the position of a collocated sensor-actuator pair is a relatively simple problem. In this case, disturbance rejection control can be realized without a mathematical model of the system. There are different publications addressing the so-called filtered-X LMS method for minimizing the least mean square of a measured quantity (error signal), see, e.g., [58, 59]. An overview of narrow-band disturbance rejection methods in the case of a known disturbance frequency can be found in [60, 61]. An overview of disturbance rejection control for both known and unknown disturbance frequencies is given in [62]. Many of these methods can only suppress the disturbance at a position which is measured. In [63], a disturbance rejection controller is reported for a known frequency. Here, a purely sinusoidal disturbance in an optical disc drive due to an eccentricity of the disc is considered. The disturbance is suppressed by an add-on controller which augments the existing feedback controller. This approach was extended in [64] to deal with a purely sinusoidal disturbance with a non-zero mean. The frequency of the disturbance is estimated by means of an additional adaption algorithm. Another method for the frequency estimation was reported in [65]. In [66], a method for adaptive disturbance rejection in a MIMO system is reported. Moreover, a compensator using an adaptive internal model for the suppression of sinusoidal disturbances based on measurements of a tracking error is reported in [67]. In [68], a nonlinear disturbance observer is proposed, where the disturbance is persistently excited by a linear exogenous system. The disturbance observer design is independent of the controller design. The states of the nonlinear system are assumed to be known. This control approach is used in a robotics application. In [69], an approach to solve an output regulation problem for a linear distributed-parameter system is presented. Here, a so-called dual observer is implemented and the system outputs to be controlled are not measured. By means of a simulation study, the method is tested for the suppression of a sinusoidal disturbance with a known frequency at a certain position of an Euler-Bernoulli beam with a concentrated force acting as system input.

A part of this work deals with the suppression of an unmeasured transverse multi-harmonic vibration of the strip with a constant tensile load. The vibration is suppressed at an arbitrary position (e.g., the gas wiping dies). It is caused by an unknown multi-harmonic persistently exciting disturbance (with an unknown frequency) which acts at one end of the strip. Custom-made electromagnetic actuators are used to apply the desired force without measuring the air gaps between the strip and the cores. The inverse quasi-static force characteristics of the electromagnet is evaluated to apply the desired force. A direct measurement of the electromagnetic force exerted on the strip is thus not required. Note that a direct measurement of the force is difficult and usually not possible in the industrial plant, cf. [70]. The states of the strip and the disturbance are estimated by an extended Kalman filter [71], which uses only a single displacement sensor as a measurement output. The electromagnetic actuator (at a distinct position) acts as a control input. In the proposed control method, an optimal state controller is augmented by an additional controller for disturbance rejection. The latter is based on the theory of invariant manifolds [72–74]. In general, a single actuator allows the suppression of a disturbance at a single position of the strip. Nominal parameters of the steel strip, e.g., strip dimensions, mechanical parameters, tensile load, and the boundary conditions at the strip edges are known with sufficient accuracy. This is also true for the electromagnetic force characteristics of the actuator. The feasibility and robustness of the developed control concept are demonstrated on the experimental test rig.

1.4 Structure of this thesis

The work is structured as follows: In Chapter 2, a mathematical plate model of the axially moving strip in an industrial hot-dip galvanizing line is derived. A suitable time integration method for the calculation of transient solutions is presented. The force characteristics of both the electromagnetic actuators and the cooling elements are analyzed. The plastic deformation history of a test strip is calculated based on the beam model of the bending line and the outcomes are compared to the results calculated with the plate model. In Chapter 3, the impact of the geometric nonlinearity is analyzed depending on different boundary conditions of the strip. Moreover, the impact of the cooling elements on the stability of the strip is studied. Finally, the dynamic model is validated based on free vibration experiments conducted in the industrial plant. A block diagram of the proposed control concept for industrial hot-dip galvanizing lines is presented in Chapter 4. Based on the mathematical plate model, the estimator of the residual curvature of the strip is developed and validated. The model outputs are compared to measurement results from the industrial plant. Chapter 4 is also concerned with the design and analysis of a feedforward controller of the transverse strip profile at the gas wiping dies. In Chapter 5, a method for the suppression of unknown multi-harmonic disturbances at an arbitrary position of a steel strip is derived and tested on the experimental test rig. Two different versions of the extended Kalman filter are developed: (i) an EKF based on the exact (explicit) discrete-time model, and (ii) an EKF based on an implicit Euler discretization. Measurement results from both versions of the disturbance rejection control concept are shown. In Chapter 6, final conclusions are drawn and the transfer of the developed control concepts to the industrial hot-dip galvanizing line is discussed.

CHAPTER 2

Mathematical modeling

This chapter is significantly based on the author's publications [17, 19, 20, 23–25, 27, 30].

2.1 Dynamic model of the axially moving strip

Figure 2.1 shows the axially moving steel strip in the section between the pot and the tower roll. Here, $(x, y) \in \Omega = (0, L) \times (-b/2, b/2)$ defines the (undeformed) middle plane of the strip and Γ its boundary. A point of the strip undergoes the local deflections $\grave{u}(x, y, z)$, $\grave{v}(x, y, z)$, and $\grave{w}(x, y, z)$ in the directions x, y, and z, respectively. The strip is supported by the pot roll (typically the stabilization roll) at the boundary $x = 0$ and by the tower roll at the boundary $x = L$. A uniform thickness h, a uniform mass density ρ, and a constant axial bulk velocity V are assumed. The dead load of the strip is considered, where the gravitational acceleration g acts in negative direction x. External viscous damping, i.e., air resistance at the strip surface, is considered via the damping coefficient c. Internal material damping, e.g., due to a viscoelastic material behavior of the strip, is also taken into account. Forces acting on the strip, e.g., due to the electromagnetic actuators (q_{mag}), the air jets of the cooling elements (q_{clr}), or the inertia of liquid zinc in the pot (q_{pot}), can be considered by the transverse distributed load $q = q(x, y, t)$. Also, an additional unknown but uniform transverse load q_{p} is included, which will be useful in the design of an extended Kalman filter (process noise).

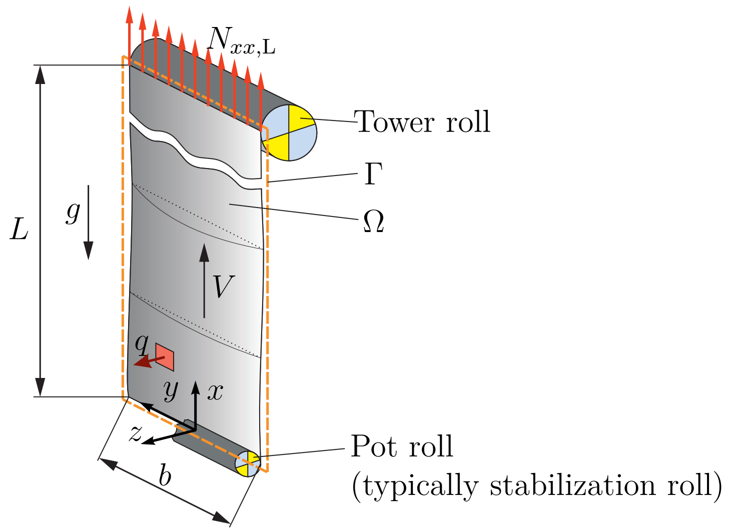

Figure 2.1: Section of the strip in the hot-dip galvanizing line between pot and tower roll.

2.1.1 Electromagnetic forces

An electromagnetic actuator consists of a pair of electromagnets at the top side (t) and the bottom side (b) of the strip. This setup allows to exert forces on both sides of the strip, i.e., positive and negative forces along z^{s}, see Fig. 1.6a. The operation of the electromagnetic circuit is assumed to be quasi-static. Hence, the total electromagnetic force applied by the actuator pair l to the strip can be written in the form

$$f^l_{\mathrm{mag}} = f^l_{\mathrm{mag}}\left(i^{\mathrm{t},l}_{\mathrm{c}}, i^{\mathrm{b},l}_{\mathrm{c}}, \delta^{\mathrm{t},l}, \delta^{\mathrm{b},l}\right) \tag{2.1}$$

depending on measured quantities. Here, $i^{\mathrm{t},l}_{\mathrm{c}}$ and $i^{\mathrm{b},l}_{\mathrm{c}}$ denote the currents in the top and bottom coil, respectively, and $\delta^{\mathrm{t},l}$ and $\delta^{\mathrm{b},l}$ are the air gaps of the actuator, see also Fig. 1.6a. Measurements of the coil currents and the air gaps are provided by the automation system of the electromagnetic stabilizer. Note that f^l_{mag} also depends on the temperature of the strip and on the BH-curve of the core. Figure 2.2a shows the calculated magnetic flux density in the middle plane of the strip for a scenario with maximum coil currents and a typical strip in a setup with three actuators. In this scenario, the computational domain was chosen to be $1\,\mathrm{m} \times 1\,\mathrm{m}$ large and the middle magnet was positioned in the center of the strip. Obviously, a high saturation occurs in the vicinity of each pole shoe. Figure 2.2b shows the related force density distribution. According to Fig. 2.2b, it is justified to assume that the force distribution is limited to the domain Ω^l_{p} of the pole shoes, see [20].

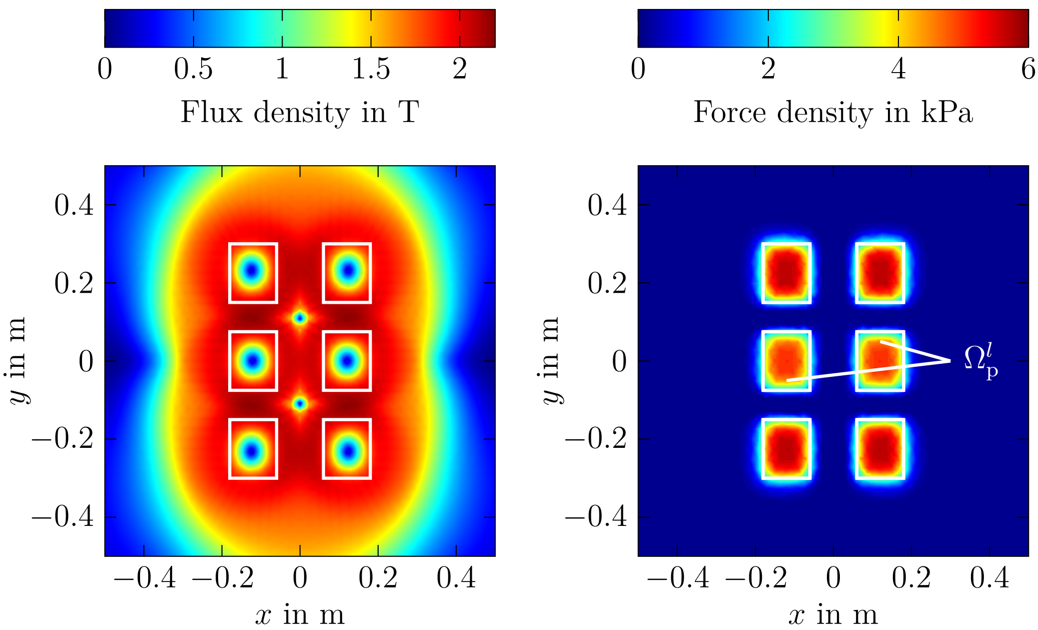

(a) Magnetic flux distribution.

(b) Force density distribution.

Figure 2.2: Typical flux and force density distribution for three U-shaped cores, where the white lines indicate the contours of the pole shoes. The coils of both outer magnets and the vis-à-vis magnet of the middle magnet pair are subject to the same maximum current [17].

Figure 2.3 depicts the typical force characteristics of an electromagnetic actuator pair l for $l = 2, \dots, \kappa - 1$ and $l = 1, \kappa$ for three strip thicknesses h. The actuators $l = 1, \kappa$ are always positioned in the vicinity of the strip edges, which is why their electromagnetic force characteristics are attenuated compared to the other actuators $l = 2, \dots, \kappa - 1$, see Fig. 2.3. This effect is mainly caused by a reduction of the electromagnetic fluxes [20]. Several functions f_{mag} were determined by a finite-element model (FEM) for different strip materials, strip thicknesses, and BH-curves. The results are stored in look-up tables. The evaluation of such a look-up table for the given material of the strip (BH-curve) by using the measured coil currents and air gaps gives the estimated electromagnetic forces $\hat{f}_{\mathrm{mag}}$ with low computational effort. Using κ electromagnetic actuators, the estimated forces are assembled in the vector $\hat{\mathbf{f}}_{\mathrm{mag}}$.

According to the results of the FEM analysis, the distributed load $q_{\mathrm{mag}}^{l}(x, y, t)$ related to the electromagnetic actuator l can be assumed to be homogeneous over the domain Ω_{p}^{l}, see also Fig. 2.2b. The parameters x_{p} and y_{p} define the dimensions of the pole shoe in the direction x and y, respectively. Hence, the total force f_{mag}^{l} of the electromagnet $l \in \{1, \dots, \kappa\}$ leads to a distributed load in

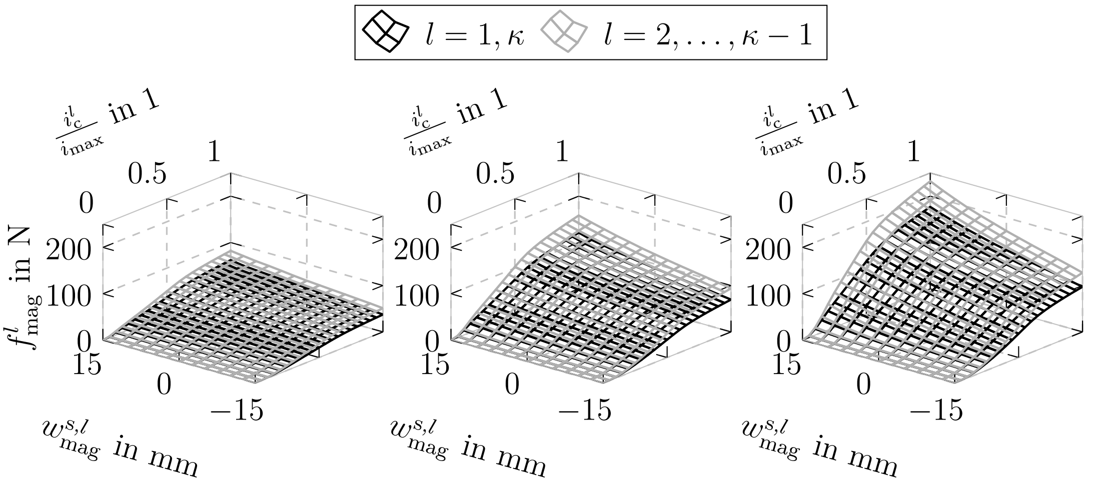

(a) $h = 0.5\,\mathrm{mm}$ (b) $h = 1\,\mathrm{mm}$ (c) $h = 1.5\,\mathrm{mm}$

Figure 2.3: Typical electromagnetic force characteristics for different strip thicknesses h depending on the local strip displacement $w_{\mathrm{mag}}^{\mathrm{s},l}$ and the normalized coil currents $i_{\mathrm{c}}^l / i_{\mathrm{max}}$.

the form

$$q_{\mathrm{mag}}(x, y) = \begin{cases} q_{\mathrm{mag}}^l = \frac{f_{\mathrm{mag}}^l}{2x_{\mathrm{p}}y_{\mathrm{p}}} & \text{for} \quad (x, y) \in \Omega_{\mathrm{p}}^l \wedge l \in \{1, \dots, \kappa\} \\ 0 & \text{else.} \end{cases} \tag{2.2}$$

2.1.2 Pressure load caused by the cooling elements

The cooling air is supplied by a blower to the cooling element. For this blower, the relation between fan speed and pressure is analyzed. Then, an experimental flow simulator is employed to measure the force caused by an impinging air jet of a single nozzle. Finally, a semi-empirical relation is derived for the resultant transverse load on the strip as a function of known quantities.

2.1.2.1 Relation between fan speed and pressure

Measurements conducted in an industrial hot-dip galvanizing line revealed a clear correlation between the relative supply pressure p_{clr} of the cooling elements and the fan speed n_{clr} of the respective air blower. All pipes of the cooling element shown in Fig. 1.7 are supplied by the air blower from one side. An experimental cooler test run was performed to study the pressure distribution inside a cooling element. Twelve pressure sensors were installed at different positions of the cooling element. The sensor positions are highlighted as yellow points in Fig. 1.7. For the maximum fan speed of the blower ($n_{\mathrm{clr,max}} \approx 1800\,1/\mathrm{min}$), the pressure difference inside the cooling element was less than 2.25 mbar at a pressure level of about

$p_{\mathrm{clr}} = 40\,\mathrm{mbar}$. Hence, the pressure nonuniformity inside a cooling element can be considered as negligible. A semi-empirical relation of the form

$$p_{\mathrm{clr}} = c_1 n_{\mathrm{clr}} + c_2 n_{\mathrm{clr}}^2 \tag{2.3}$$

is used to describe the characteristics between fan speed n_{clr} and pressure p_{clr}. The unknown parameters are determined by means of a least-squares approximation ($c_1 = 1.6785 \cdot 10^{-4}\,\mathrm{mbar\,min}$, $c_2 = 1.1847 \cdot 10^{-5}\,\mathrm{mbar\,min}^2$). A flow simulator was designed to study the pressure load of an impinging nozzle jet on the strip surface.

2.1.2.2 Flow simulator

Because of the negligible pressure difference inside the pipes of a cooling element shown in Fig. 2.4a, the air flow through all nozzles is approximately the same. Moreover, the flow conditions after the fluid leaves the nozzle are quite similar for all nozzles. This assumption is supported by the geometry of the cooling element, where the fluid can only escape to the rear side. For the analysis of the force characteristic, an experimental flow simulator equipped with three nozzles was designed and built, see Fig. 2.4b. The mechanism of the impinging jet force on a plate was analyzed for different distances δ_{clr} between the nozzle outlet and the plate and different relative pipe pressures p_{clr}. Various design aspects were taken into consideration. First of all, the area of the application surface of the force equals the associated area of the strip at the real cooling element. Furthermore, the diameter of the pipe used in the flow simulator is equal to the real cooling pipe and the lateral distance between neighboring nozzles is the same as in the industrial plant. The vertical distance L_{p} between the single pipes is equal to the depth of the flow simulator. Hence, the channel for the back-flow is also similar to the real cooling element. To take into account interactions between streams of neighboring nozzles, a pipe segment with at least three nozzles was used. Friction along the wall of the simulator can be neglected because of the low fluid velocity at the wall.

Figure 2.5a shows the measured force f_{s} exerted on the plate area A_{s} as a function of the pressure p_{clr} depending on the distance δ_{clr}. An interesting feature is shown in Fig. 2.5b: In normal operating situations ($\delta_{\mathrm{clr}} > 1\,\mathrm{cm}$), the distance δ_{clr} has no influence on the air flow rate $\dot{V}_{\mathrm{s}}$. For this analysis, the distance δ_{clr} was varied from 0 to L_{w}.

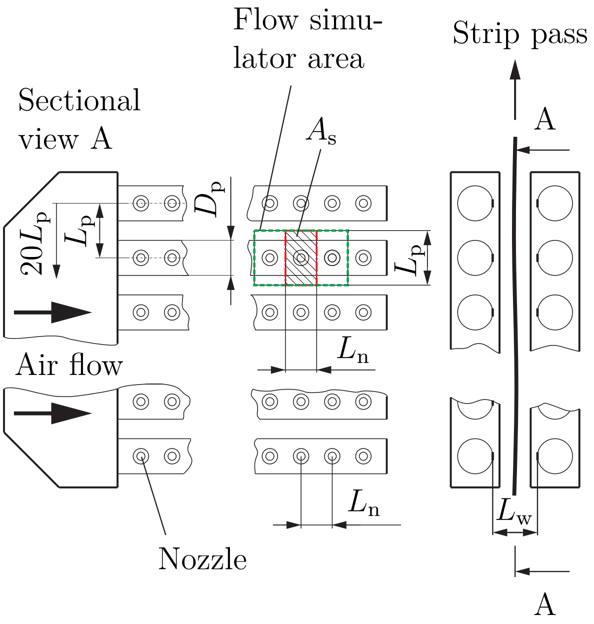

(a) Sketch of a cooling element.

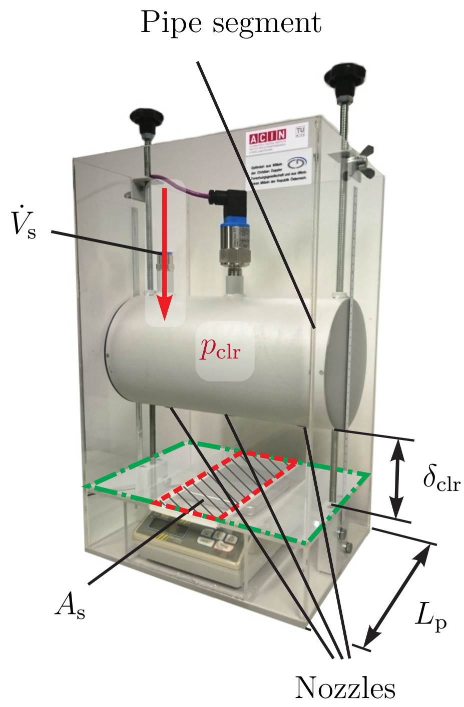

(b) Photograph of the flow simulator.

Figure 2.4: The concept of an experimental flow simulator. The flow simulator area is highlighted with dashed lines. All nozzle outlets have the diameter $D_n = 17.5\,\mathrm{mm}$. The dimensions are as follows: $D_p = 168.3\,\mathrm{mm}$, $L_p = 250\,\mathrm{mm}$, $L_n = 110\,\mathrm{mm}$, and $L_w = 250\,\mathrm{mm}$.

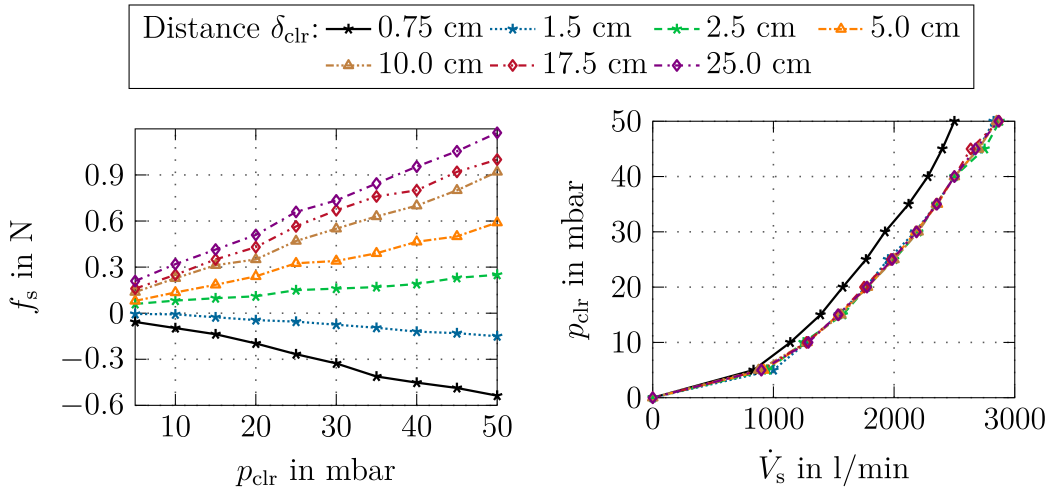

(a) Force of an impinging nozzle jet f_{s}.

(b) The flow rate $\dot{V}_{\mathrm{s}}$ is affected by δ_{clr} only at small distances < 1 cm.

Figure 2.5: Measurements of the flow simulator depending on the distance δ_{clr}.

2.1.2.3 Cooling elements

To transfer the results of the flow simulator to the nozzles of the industrial plant, the transverse strip displacement $w = \delta^{\mathrm{b}}_{\mathrm{clr}} - L_{\mathrm{w}}/2$ is introduced, see Fig. 2.4 for details. The quantity $\delta^{\mathrm{b}}_{\mathrm{clr}}$ denotes the distance between the strip and the nozzle outlet at the bottom side of the strip. Based on the measurement results, in particular Fig. 2.5a, a semi-empirical relation of the form

$$f^{\mathrm{b}}_{\mathrm{s}}(p_{\mathrm{clr}}, w) = \left(p_{\mathrm{clr}} + c_3 p^2_{\mathrm{clr}}\right)\left(c_4 e^{-c_5 w} + c_6 w + c_7\right) \tag{2.4}$$

can be identified with the constant parameters $c_3 = -2.897 \cdot 10^{-5}\,1/\mathrm{Pa}$, $c_4 = -1.645 \cdot 10^{-6}\,\mathrm{m}^2$, $c_5 = 43.944\,1/\mathrm{m}$, $c_6 = 4.086 \cdot 10^{-4}\,\mathrm{m}$, and $c_7 = 2.179 \cdot 10^{-4}\,\mathrm{m}^2$. The corresponding force characteristics of a single nozzle is shown in Fig. 2.6. In a similar way, the transverse strip displacement $w = -\delta^{\mathrm{t}}_{\mathrm{clr}} + L_{\mathrm{w}}/2$, with the distance $\delta^{\mathrm{t}}_{\mathrm{clr}}$ between the strip and the nozzle outlet at the top side of the strip, can be introduced. For a nozzle pair consisting of two vis-à-vis nozzles (cf. the considered industrial plant), the resulting pressure load on the area A_{s} is then obtained in the form

$$q_{\mathrm{clr}}(p_{\mathrm{clr}}, w) = \frac{f^{\mathrm{b}}_{\mathrm{s}}(p_{\mathrm{clr}}, w + w_{\mathrm{off}}) - f^{\mathrm{t}}_{\mathrm{s}}(p_{\mathrm{clr}}, -w - w_{\mathrm{off}})}{A_{\mathrm{s}}}, \tag{2.5}$$

where w_{off} is a constant transverse offset of the strip, see also Fig. 2.7. Assume an industrial hot-dip galvanizing line equipped with ι cooling elements. The transverse distributed load $q^l_{\mathrm{clr}}\left(p^l_{\mathrm{clr}}, w\right)$, which is defined in the domain $\Omega^l_{\mathrm{clr}} \subset \Omega$, is exerted on the strip by the cooling element l with $l = 1, \ldots, \iota$. For instance, $\Omega^1_{\mathrm{clr}} = [L_{\mathrm{a}}, L_{\mathrm{a}} + L_{\mathrm{c}}] \times (-b/2, b/2)$ defines the domain of cooler 1.

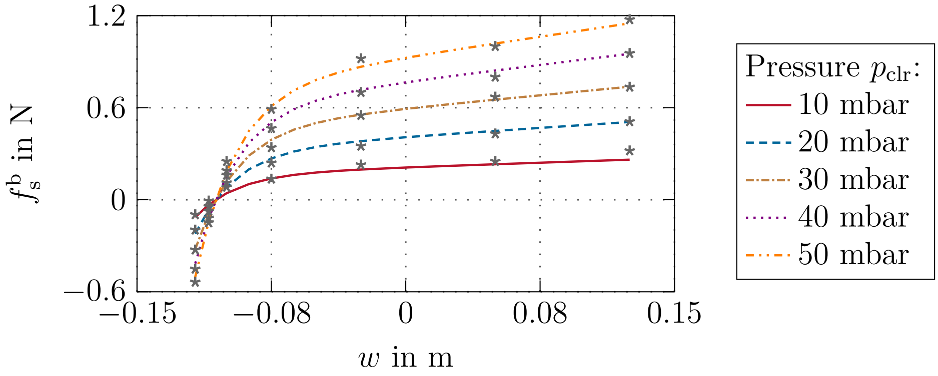

Figure 2.6: Force of an impinging nozzle jet f_s depending on the supply pressure p_{clr} in the pipe. Measured data points are highlighted by markers.

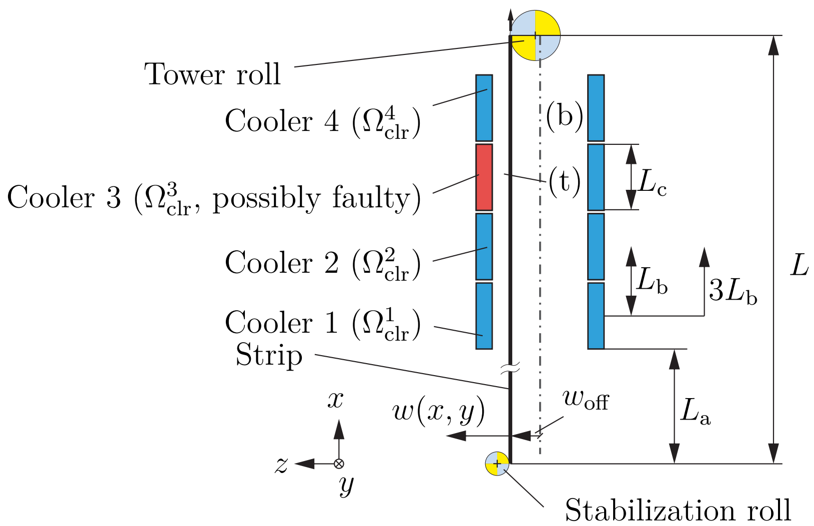

Figure 2.7: Industrial plant equipped with four coolers. The cooler dimensions are defined by $L_a = 34.1\,\mathrm{m}$, $L_b = 5.2\,\mathrm{m}$, and $L_c = 5\,\mathrm{m}$. For the simulation study in Section 3.1.2, one half of cooler 3 is assumed to be faulty.

In the following, the dynamic model of the strip shape is derived using the assumptions of the Kirchhoff-Love plate theory [36]. Let $u(x, y)$, $v(x, y)$, and $w(x, y)$ denote the local displacements of a point in the middle plane of the strip and assume that the transverse deflection $\mathring{w}$ of an arbitrary point of the strip is independent of z.

2.1.3 Hamilton's principle

Hamilton's principle is often used to derive the equations of motions of mechanical systems with distributed parameters (infinitely many degrees of freedom) [36]. In

[37, 38], a special formulation of Hamilton's principle for systems with changing mass is proposed. According to this principle, the relation

$$0 = \int_{t_0}^{t_1} (\delta U + \delta G - \delta K + \delta W + \delta M) \mathrm{d}t \tag{2.6}$$

holds for two arbitrary points in time t_0 and t_1. In (2.6), U is the strain energy, G describes the potential energy due to gravity, K denotes the kinetic energy, W describes the work done by conservative (external) forces, and M denotes the momentum transport through the boundary Γ. The membrane strains ϵ^0_{xx}, ϵ^0_{yy}, and γ^0_{xy} and the curvatures ϵ^1_{xx}, ϵ^1_{yy}, and γ^1_{xy} read as

$$\boldsymbol{\varepsilon}^0 = \begin{bmatrix} \epsilon^0_{xx} \\ \epsilon^0_{yy} \\ \gamma^0_{xy} \end{bmatrix} = \begin{bmatrix} \partial_x u + \frac{1}{2}(\partial_x w)^2 \\ \partial_y v + \frac{1}{2}(\partial_y w)^2 \\ \partial_y u + \partial_x v + \partial_x w \partial_y w \end{bmatrix} \tag{2.7a}$$

and

$$\boldsymbol{\varepsilon}^1 = \begin{bmatrix} \epsilon^1_{xx} \\ \epsilon^1_{yy} \\ \gamma^1_{xy} \end{bmatrix} = \begin{bmatrix} -\partial_x^2 w \\ -\partial_y^2 w \\ -2\partial_x \partial_y w \end{bmatrix}, \tag{2.7b}$$

respectively. The variation of the strain energy can be written in the form

$$\delta U = \int_\Omega \Big(N_{xx}\delta\epsilon^0_{xx} + M_{xx}\delta\epsilon^1_{xx} + N_{yy}\delta\epsilon^0_{yy} + M_{yy}\delta\epsilon^1_{yy} + N_{xy}\delta\gamma^0_{xy} + M_{xy}\delta\gamma^1_{xy} \Big) \mathrm{d}x\mathrm{d}y \tag{2.8}$$

with the thickness-integrated forces N_{xx}, N_{yy}, and N_{xy} and the thickness-integrated moments M_{xx}, M_{yy}, and M_{xy} per unit width. These quantities are the so-called stress resultants. The variation of the potential energy due to gravity yields

$$\delta G = \rho g h \int_\Omega \delta u \mathrm{d}x\mathrm{d}y. \tag{2.9}$$

The variation of the position vector $\mathbf{r}^\mathrm{T} = [x+u, y+v, w]$, which corresponds to a point in the mid-plane of the strip, reads as

$$\delta \mathbf{r}^\mathrm{T} = \begin{bmatrix} \delta u, & \delta v, & \delta w \end{bmatrix} \tag{2.10}$$

and the total material velocity vector can be expressed as

$$\mathbf{v}^\mathrm{T} = \begin{bmatrix} V + \partial_t u + V\partial_x u, & \partial_t v + V\partial_x v, & \partial_t w + V\partial_x w \end{bmatrix}. \tag{2.11}$$

Using (2.11), the variation of the kinetic energy can be written in the form

$$\delta K = \rho h \int_\Omega \mathbf{v}^\mathrm{T} \delta \mathbf{v} \mathrm{d}x\mathrm{d}y. \tag{2.12}$$

The variation of the work done by the transverse load $q(x,y,t)$, the viscous damping force $c\partial_t w$, and the tensile load $N_{xx,\mathrm{L}}$ at the upper boundary (cf. Fig. 2.1) reads as

$$\delta W = -\int_\Omega (q - c\partial_t w)\delta w \mathrm{d}x\mathrm{d}y - \int_{-\frac{b}{2}}^{\frac{b}{2}} N_{xx,\mathrm{L}} \delta u|_{x=L} \mathrm{d}y. \tag{2.13}$$

Using (2.10) and (2.11), the variation of the momentum transport follows as [37, 38]

$$\delta M = \rho h V \int_{-\frac{b}{2}}^{\frac{b}{2}} \left[\mathbf{v}^{\mathrm{T}} \delta \mathbf{r}\right]_{x=0}^{x=L} \mathrm{d}y. \tag{2.14}$$

Insertion of (2.8), (2.9), (2.12), (2.13), and (2.14) into (2.6), integration by parts, and applying the fundamental lemma of calculus of variations yields the equations of motion

$$\mathcal{D}_u := \rho h\left(V^2\partial_x^2 u + 2V\partial_x\partial_t u + \partial_t^2 u + g\right) - \partial_x N_{xx} - \partial_y N_{xy} = 0 \tag{2.15a}$$

$$\mathcal{D}_v := \rho h\left(V^2\partial_x^2 v + 2V\partial_x\partial_t v + \partial_t^2 v\right) - \partial_y N_{yy} - \partial_x N_{xy} = 0 \tag{2.15b}$$

$$\begin{aligned}\mathcal{D}_w := {} & \rho h\left(V^2\partial_x^2 w + 2V\partial_x\partial_t w + \partial_t^2 w\right) \\ & - \partial_x^2 M_{xx} - 2\partial_x\partial_y M_{xy} - \partial_y^2 M_{yy} - q + c\partial_t w \\ & - \partial_x(N_{xx}\partial_x w + N_{xy}\partial_y w) - \partial_y(N_{xy}\partial_x w + N_{yy}\partial_y w) = 0,\end{aligned} \tag{2.15c}$$

which are valid in the domain Ω. The dynamics described by (2.15a), (2.15b) corresponds to the in-plane displacements $(u,\ v)$. Equation (2.15c) is related to the transverse (out-of-plane) displacement w. The terms with a second time-derivative, i.e., ∂_t^2, represent the inertia forces. The expressions containing V^2 or $2V$ constitute the centrifugal or Coriolis forces, respectively. The terms involving a moment M represent stiffness forces due to the bending of the strip. By analogy, the terms containing a force N constitute stiffness forces due to the in-plane deformation of the strip. The expression involving g represents the gravity force. The viscous damping force and transverse loads are considered by the terms involving $c\partial_t w$ and q, respectively. The inertia of the zinc pot can be captured via the transverse load q in the form $q_{\mathrm{pot}} = -\bar{m}_{\mathrm{pot}}\partial_t^2 w$ for $x \leq x_{\mathrm{pot}}$ with an accumulated mass density $\bar{m}_{\mathrm{pot}}$ of the liquid zinc and the pot level x_{pot}. Clearly, $q_{\mathrm{pot}} = 0$ for $x > x_{\mathrm{pot}}$. By analogy, the transverse loads due to the electromagnetic actuators and the cooling elements can be considered. The corresponding initial and boundary conditions will be discussed in Section 2.1.5.

2.1.4 Material model

Based on Hooke's law extended by a term for (internal) Kelvin-Voigt damping in transverse direction, the Kirchhoff-Love plate theory, and by taking into account residual membrane and flexual strains (curvatures) from prior deformation, the constitutive equations between the membrane strains and the forces per unit width as well as the curvatures and the moments per unit width are derived. The stress resultants can be written in the form

$$\underbrace{\begin{bmatrix} N_{xx} \\ N_{yy} \\ N_{xy} \end{bmatrix}}_{\mathbf{N}} = \underbrace{A \begin{bmatrix} 1 & \nu & 0 \\ \nu & 1 & 0 \\ 0 & 0 & \frac{1-\nu}{2} \end{bmatrix}}_{\mathbf{A}} \left(\underbrace{\begin{bmatrix} \epsilon_{xx}^{0} \\ \epsilon_{yy}^{0} \\ \gamma_{xy}^{0} \end{bmatrix}}_{\boldsymbol{\varepsilon}^{0}} + \underbrace{\begin{bmatrix} -\epsilon_{xx}^{\mathrm{r},0} \\ -\epsilon_{yy}^{\mathrm{r},0} \\ 0 \end{bmatrix}}_{\boldsymbol{\varepsilon}^{\mathrm{r},0}} \right) \tag{2.16a}$$

and

$$\underbrace{\begin{bmatrix} M_{xx} \\ M_{yy} \\ M_{xy} \end{bmatrix}}_{\mathbf{M}} = \underbrace{D \begin{bmatrix} 1 & \nu & 0 \\ \nu & 1 & 0 \\ 0 & 0 & \frac{1-\nu}{2} \end{bmatrix}}_{\mathbf{D}} \left(\underbrace{\begin{bmatrix} \epsilon_{xx}^{1} \\ \epsilon_{yy}^{1} \\ \gamma_{xy}^{1} \end{bmatrix}}_{\boldsymbol{\varepsilon}^{1}} + \underbrace{\begin{bmatrix} -\epsilon_{xx}^{\mathrm{r},1} \\ -\epsilon_{yy}^{\mathrm{r},1}(y) \\ 0 \end{bmatrix}}_{\boldsymbol{\varepsilon}^{\mathrm{r},1}(y)} + \beta \underbrace{\begin{bmatrix} \partial_t \epsilon_{xx}^{1} \\ \partial_t \epsilon_{yy}^{1} \\ \partial_t \gamma_{xy}^{1} \end{bmatrix}}_{\dot{\boldsymbol{\varepsilon}}^{1}} \right) \tag{2.16b}$$

with the abbreviations $A = \frac{Eh}{1-\nu^2}$ and $D = \frac{Eh^3}{12(1-\nu^2)}$. Here, E denotes the temperature-dependent Young's modulus and ν is the known Poisson's ratio. In (2.16), βE denotes the Kelvin-Voigt damping factor. A mathematical model is used in this work to compute E as a function of the temperature measured in the vicinity of the zinc pot. According to (2.16), the expressions $\mathbf{N} = \bar{\mathbf{N}} + \mathbf{N}^{\mathrm{r}}$ and $\mathbf{M} = \bar{\mathbf{M}} + \mathbf{M}^{\mathrm{r}} + \bar{\mathbf{M}}^{\mathrm{d}}$ can be defined using the abbreviations $\bar{\mathbf{N}} = \mathbf{A}\boldsymbol{\varepsilon}^0$, $\bar{\mathbf{M}} = \mathbf{D}\boldsymbol{\varepsilon}^1$, $\mathbf{N}^{\mathrm{r}} = \mathbf{A}\boldsymbol{\varepsilon}^{\mathrm{r},0}$, $\mathbf{M}^{\mathrm{r}} = \mathbf{D}\boldsymbol{\varepsilon}^{\mathrm{r},1}$, and $\bar{\mathbf{M}}^{\mathrm{d}} = \beta\mathbf{D}\dot{\boldsymbol{\varepsilon}}^1$. Residual strain in the strip is considered with the parameters $\epsilon_{xx}^{\mathrm{r},0}$, $\epsilon_{yy}^{\mathrm{r},0}$, $\epsilon_{xx}^{\mathrm{r},1}$, and the function $\epsilon_{yy}^{\mathrm{r},1}(y)$. The latter is assumed to depend on the lateral coordinate y. In fact, it is approximated in the polynomial form

$$\epsilon_{yy}^{\mathrm{r},1}(y) = \mathbf{y}_p^{\mathrm{T}}(y)\boldsymbol{\varepsilon}_{yy}^{\mathrm{r},1}, \tag{2.17}$$

where the vector $\mathbf{y}_p^{\mathrm{T}}(y) = \begin{bmatrix} 1 & y & \dots & y^p \end{bmatrix} \in \mathbb{R}^{p+1}$ is a function of y and the vector $\left(\boldsymbol{\varepsilon}_{yy}^{\mathrm{r},1}\right)^{\mathrm{T}} = \begin{bmatrix} \epsilon_{yy}^{\mathrm{c},0} & \epsilon_{yy}^{\mathrm{c},1} & \dots & \epsilon_{yy}^{\mathrm{c},p} \end{bmatrix}$ contains polynomial coefficients. Clearly, the dependence on y vanishes for the choice $p = 0$. The parametrization of the four residual strain quantities for different models is given in Tab. 2.1. In Section 2.2, four constant residual strain parameters are used, which are calculated by means of the elasto-plastic beam model of the bending line in the zinc pot. For the estimator of the residual curvature in Section 4.2, a lateral residual curvature profile $\epsilon_{yy}^{\mathrm{r},1}(y)$ is determined, where $p \in \mathbb{N}_0$.

Parametrization	Section	$\epsilon_{xx}^{\mathrm{r},0}$	$\epsilon_{yy}^{\mathrm{r},0}$	$\epsilon_{xx}^{\mathrm{r},1}$	$\epsilon_{yy}^{\mathrm{r},1}(y)$
Constant parameters determined by the elasto-plastic beam model	2.2	$\in \mathbb{R}$	$\in \mathbb{R}$	$\in \mathbb{R}$	$\epsilon_{yy}^{\mathrm{c},0} \in \mathbb{R}$ $(p = 0)$
Estimation of a lateral residual curvature profile	4.2	0	0	0	$\epsilon_{yy}^{\mathrm{c},i} \in \mathbb{R}$ for $i = 0, \dots, p$ $(p \in \mathbb{N}_0)$

Table 2.1: Parametrization of the residual strain quantities.

Insertion of (2.7) into (2.16) yields stress resultants N_{xx}, N_{yy}, and N_{xy} as functions of the displacements u, v, and w. This shows how the in-plane dynamics (2.15a), (2.15b) is coupled with the out-of-plane dynamics (2.15c).

2.1.5 Initial and boundary conditions

In order to solve (2.15) and (2.16), it is necessary to define suitable initial and boundary conditions. The initial conditions are given by

$$
\begin{aligned}
u(x,y)|_{t=0} &= \breve{u}_0(x,y) & \partial_t u(x,y)|_{t=0} &= \breve{u}_1(x,y) && \text{(2.18a)}\\
v(x,y)|_{t=0} &= \breve{v}_0(x,y) & \partial_t v(x,y)|_{t=0} &= \breve{v}_1(x,y) && \text{(2.18b)}\\
w(x,y)|_{t=0} &= \tilde{w}_0(x,y) & \partial_t w(x,y)|_{t=0} &= \tilde{w}_1(x,y) && \text{(2.18c)}
\end{aligned}
$$

and describe the initial deflection and velocity of the strip in the domain $(x, y) \in [0, L] \times [-b/2, b/2]$.

In this work, four strip models are used with different boundary conditions at $x = 0$ and $x = L$. They are abbreviated as I–IV and specified in Tab. 2.2. However, only the model with the boundary condition I is documented here in detail. The implementation of the boundary conditions II–IV is possible with minor modifications.

Boundary condition	Abbreviation	$x = 0$	$x = L$
Uniform tensile load with fixed slope at the stabilization roll	I	$w\|_{x=0} = w_0$ $\partial_x w\|_{x=0} = w_{\mathrm{x},0}$ $u\|_{x=0} = 0$	$w\|_{x=L} = 0$ $M_{xx}\|_{x=L} = 0$ $N_{xx}\|_{x=L} = N_{xx,\mathrm{L}}$
Prestrained strip with fixed slope at the stabilization roll	II	$w\|_{x=0} = w_0$ $\partial_x w\|_{x=0} = w_{\mathrm{x},0}$ $u\|_{x=0} = 0$	$w\|_{x=L} = 0$ $M_{xx}\|_{x=L} = 0$ $u\|_{x=L} = u_{\mathrm{L}}$
Constant tensile load with simply supported strip	III	$w\|_{x=0} = 0$ $M_{xx}\|_{x=0} = 0$ $u\|_{x=0} = 0$	$w\|_{x=L} = 0$ $M_{xx}\|_{x=L} = 0$ $N_{xx}\|_{x=L} = N_{xx,\mathrm{L}}$
Prestrained and simply supported strip	IV	$w\|_{x=0} = 0$ $M_{xx}\|_{x=0} = 0$ $u\|_{x=0} = 0$	$w\|_{x=L} = 0$ $M_{xx}\|_{x=L} = 0$ $u\|_{x=L} = u_{\mathrm{L}}$

Table 2.2: Boundary conditions at the supporting rolls.

Purely geometric boundary conditions are assumed at $x = 0$ for the models I and II, e.g., calculated via the elasto-plastic beam model described in Section 2.2. Hence, the displacement $w|_{x=0} = w_0$ and the slope $\partial_x w|_{x=0} = w_{\mathrm{x},0}$ are prescribed. A simply supported strip, i.e., $M_{xx}|_{x=0} = 0$ and $w|_{x=0} = 0$, is assumed at $x = 0$ for the boundary conditions III and IV.

In longitudinal direction, the boundary conditions I and III define a uniform tensile load[1] $N_{xx}|_{x=L} = N_{xx,\mathrm{L}}$ at $x = L$, see also Fig. 2.1. In contrast, the geometrical boundary conditions II and IV define a uniform displacement u_{L} at $x = L$.

For all models, the strip is assumed to be simply supported at $x = L$ $(M_{xx}|_{x=L} = 0, w|_{x=L} = 0)$ and the deflection $u|_{x=0} = 0$ is prescribed at $x = 0$. Free lateral contraction is assumed at $x = 0$ and $x = L$ $(N_{xy}|_{x=0,y\neq0} = N_{xy}|_{x=L,y\neq0} = 0)$ apart from the displacements $v|_{x=0,y=0} = v|_{x=L,y=0} = 0$, which are prescribed to obtain a unique solution. The lateral strip edges at $y = -b/2$ and $y = b/2$ constitute free boundaries for all degrees of freedom, i.e., $N_{xy}|_{y=-b/2} = N_{xy}|_{y=b/2} = 0$, $N_{yy}|_{y=-b/2} = N_{yy}|_{y=b/2} = 0$, $M_{yy}|_{y=-b/2} = M_{yy}|_{y=b/2} = 0$, and $Q|_{y=-b/2} = Q|_{y=b/2} = 0$ with $Q = \partial_y M_{yy} + 2\partial_x M_{xy} + N_{xy}\partial_x w + N_{yy}\partial_y w$, cf. [36]. Clearly, the initial conditions (2.18) have to be compatible with these boundary conditions.

2.1.6 Spatial discretization

The spatial discretization of (2.15) and the boundary conditions I according to Section 2.1.5 is carried out by means of the Galerkin weighted residual method.

[1] For the experiment in Section 3.3, it was assumed that the tensile load varies linearly over the width of the strip $(N_{xx}(y)|_{x=L} = N_{xx,L}(y))$.

For this purpose, the weak form

$$\int_\Omega \bar{u}\mathcal{D}_u + \bar{v}\mathcal{D}_v + \bar{w}\mathcal{D}_w \mathrm{d}x\mathrm{d}y + \int_{-b/2}^{b/2} [\bar{u}(N_{xx} - N_{xx,\mathrm{L}})]_{x=L} \mathrm{d}y = 0 \tag{2.19}$$

of the equations of motion is used, where $\bar{u}$, $\bar{v}$, and $\bar{w}$ are the weighting functions. Homogeneous boundary conditions, i.e., $\bar{u}|_{x=0} = 0$, $\bar{v}|_{x=0,y=0} = \bar{v}|_{x=L,y=0} = 0$, and $\bar{w}|_{x=L} = 0$, according to Section 2.1.5 are taken into account by a suitable choice of the basis functions. Partial integration of (2.19) yields

$$\begin{aligned}
&\int_\Omega -\partial_x\bar{u}\rho h V^2 \partial_x u + \bar{u}\rho h\Big(2V\partial_x\partial_t u + \partial_t^2 u + g\Big) - \partial_x\bar{v}\rho h V^2\partial_x v \\
&+ \bar{v}\rho h\Big(2V\partial_x\partial_t v + \partial_t^2 v\Big) - \partial_x\bar{w}\rho h V^2 \partial_x w + \bar{w}\rho h\Big(2V\partial_x\partial_t w + \partial_t^2 w\Big) \\
&+ \partial_x\bar{u}N_{xx} + \partial_y\bar{u}N_{xy} + \partial_y\bar{v}N_{yy} + \partial_x\bar{v}N_{xy} - \partial_x^2\bar{w}M_{xx} - 2\partial_x\partial_y\bar{w}M_{xy} - \partial_y^2\bar{w}M_{yy} \\
&+ \partial_x\bar{w}(N_{xx}\partial_x w + N_{xy}\partial_y w) + \partial_y\bar{w}(N_{xy}\partial_x w + N_{yy}\partial_y w) \\
&- \bar{w}(q - c\partial_t w)\mathrm{d}x\mathrm{d}y + \int_{-\frac{b}{2}}^{\frac{b}{2}} \Big(\Big[\bar{u}\rho h V^2 \partial_x u\Big]_{x=L} + \Big[\bar{v}\rho h V^2\partial_x v\Big]_{x=L} \\
&- \Big[\bar{v}\rho h V^2 \partial_x v\Big]_{x=0} - \Big[\bar{w}\rho h V^2\partial_x w\Big]_{x=0}\Big)\mathrm{d}y = \int_{-b/2}^{b/2} \bar{u}|_{x=L} N_{xx,\mathrm{L}}\mathrm{d}y.
\end{aligned} \tag{2.20}$$

2.1.6.1 Finite elements

In the spatial discretization of (2.20), a distinction is made between the in-plane dynamics (terms weighted with $\bar{u}$ or $\bar{v}$) and the out-of-plane dynamics (terms weighted with $\bar{w}$). As indicated in Fig. 2.8, the finite elements of the in-plane and the out-of-plane problem are marked with the diacritics ˘ and ˜, respectively. For the in-plane discretization, the domain Ω is divided into n rectangular finite elements in the longitudinal direction x, see Fig. 2.8a. Let the index $e \in \{1, 2, \ldots, n\}$ denote a finite element with the length a_e, the domain $\breve{\Omega}_e = [0, a_e] \times [0, b]$, and the local coordinates $\breve{x}$, $\breve{y}$. The free choice of the element lengths allows a tailored discretization in terms of accuracy requirements in different areas of the strip. For instance, a finite element near a supporting roll, the gas wiping dies, or the electromagnets can be chosen with a smaller length a_e compared to a finite element in the tower, e.g., near a cooling element. An additional discretization into m finite elements with equal widths ($\tilde{b} = b/m$) along the direction y is used for the out-of-plane problem, see Fig. 2.8b. The chosen equidistant discretization in lateral direction is not a limitation because the accuracy of the model can also be adapted by the number of lateral basis functions. Generally, the additional discretization for the out-of-plane problem in lateral direction facilitates to calculate transverse strip profiles with higher accuracy. Furthermore, let $f \in \{1, 2, \ldots, m\}$ be the associated index of a finite element with the domain $\tilde{\Omega}_{e,f} = [0, a_e] \times [0, \tilde{b}]$ and the local coordinates $\tilde{x}$, $\tilde{y}$. A comparison of Figs. 2.8a and 2.8b shows that the relations

$$\breve{y} = \tilde{y} + (f-1)\tilde{b}, \qquad \breve{x} = \tilde{x} \tag{2.21a}$$

and

$$x = \tilde{x} + \sum_{j=1}^{e-1} a_j, \qquad\qquad y = \tilde{y} - \frac{b}{2} + (f-1)\tilde{b} = \breve{y} - \frac{b}{2} \tag{2.21b}$$

define the transformations between local coordinates in the domains $\breve{\Omega}_e$, $\tilde{\Omega}_{e,f}$, and Ω for elements with the same index e.

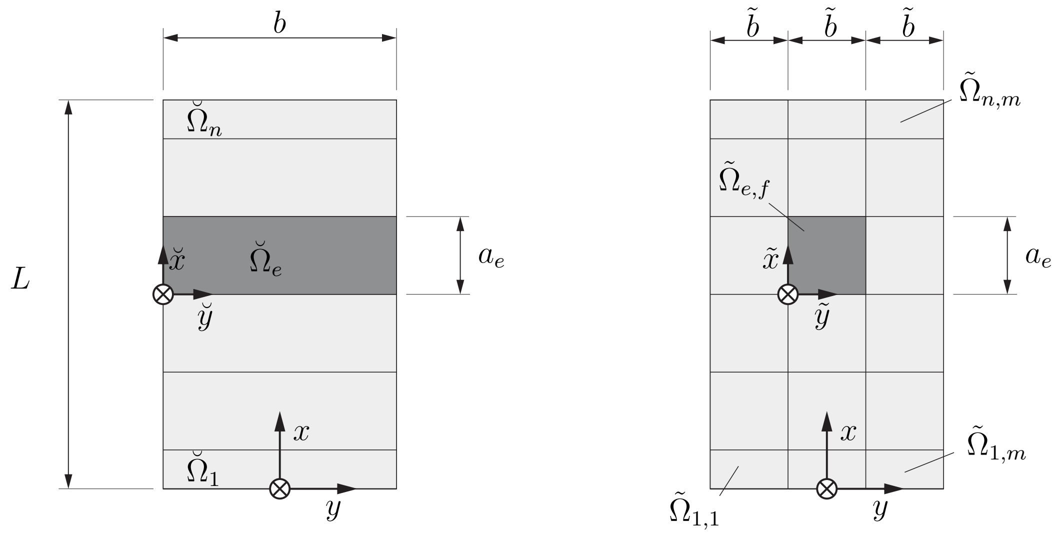

(a) In-plane discretization. (b) Out-of-plane discretization.

Figure 2.8: Discretization with $n = 6$ finite elements in x-direction and $m = 3$ finite elements in y-direction.

For a finite element, the transverse strip displacements are approximated by local basis functions in the form

$$u = \left(\mathbf{\Psi}_e^u(\breve{x}, \breve{y})\right)^{\mathrm{T}} \breve{\mathbf{t}}_e^u(t) \qquad \forall(\breve{x}, \breve{y}) \in \breve{\Omega}_e \tag{2.22a}$$

$$v = \left(\mathbf{\Psi}_e^v(\breve{x}, \breve{y})\right)^{\mathrm{T}} \breve{\mathbf{t}}_e^v(t) \qquad \forall(\breve{x}, \breve{y}) \in \breve{\Omega}_e \tag{2.22b}$$

$$w = \left(\mathbf{\Psi}_{e,f}^w(\tilde{x}, \tilde{y})\right)^{\mathrm{T}} \tilde{\mathbf{t}}_{e,f}^w(t) \qquad \forall(\tilde{x}, \tilde{y}) \in \tilde{\Omega}_{e,f}, \tag{2.22c}$$

where the time-dependent vectors $\breve{\mathbf{t}}_e^u(t)$, $\breve{\mathbf{t}}_e^v(t)$, and $\tilde{\mathbf{t}}_{e,f}^w(t)$ contain the Galerkin coefficients. The basis functions are assembled in the form

$$(\mathbf{\Psi}_e^u)^{\mathrm{T}} = \Big[\underbrace{\breve{\Psi}_{0,0}, \breve{\Psi}_{0,1}, \dots, \breve{\Psi}_{0,n_{\mathrm{yu}}}}_{\left(\boldsymbol{\psi}_e^{u|\breve{x}=0}\right)^{\mathrm{T}}}, \underbrace{\breve{\Psi}_{1,0}, \dots, \breve{\Psi}_{1,n_{\mathrm{yu}}}}_{\left(\boldsymbol{\psi}_e^{\partial u|\breve{x}=0}\right)^{\mathrm{T}}},$$

$$\underbrace{\breve{\Psi}_{2,0},\dots,\breve{\Psi}_{2,n_{\mathrm{yu}}}}_{\left(\varphi_e^{u|\breve{x}=a_e}\right)^{\mathrm{T}}},\underbrace{\breve{\Psi}_{n_{\mathrm{x}},0},\dots,\breve{\Psi}_{n_{\mathrm{x}},n_{\mathrm{yu}}}}_{\left(\varphi_e^{\partial u|\breve{x}=a_e}\right)^{\mathrm{T}}}\Big]\in\mathbb{R}^{(n_{\mathrm{x}}+1)(n_{\mathrm{yu}}+1)} \tag{2.23a}$$

$$\left(\mathbf{\Psi}_e^v\right)^{\mathrm{T}}=\Big[\underbrace{\breve{\Psi}_{0,0},\breve{\Psi}_{0,1},\dots,\breve{\Psi}_{0,n_{\mathrm{yv}}}}_{\left(\varphi_e^{v|\breve{x}=0}\right)^{\mathrm{T}}},\underbrace{\breve{\Psi}_{1,0},\dots,\breve{\Psi}_{1,n_{\mathrm{yv}}}}_{\left(\varphi_e^{\partial v|\breve{x}=0}\right)^{\mathrm{T}}},$$
$$\underbrace{\breve{\Psi}_{2,0},\dots,\breve{\Psi}_{2,n_{\mathrm{yv}}}}_{\left(\varphi_e^{v|\breve{x}=a_e}\right)^{\mathrm{T}}},\underbrace{\breve{\Psi}_{n_{\mathrm{x}},0},\dots,\breve{\Psi}_{n_{\mathrm{x}},n_{\mathrm{yv}}}}_{\left(\varphi_e^{\partial v|\breve{x}=a_e}\right)^{\mathrm{T}}}\Big]\in\mathbb{R}^{(n_{\mathrm{x}}+1)(n_{\mathrm{yv}}+1)} \tag{2.23b}$$

$$\left(\mathbf{\Psi}_{e,f}^w\right)^{\mathrm{T}}=\Big[\underbrace{\tilde{\Psi}_{0,0},\tilde{\Psi}_{0,1},\dots,\tilde{\Psi}_{0,n_{\mathrm{yw}}}}_{\left(\varphi_{e,f}^{w|\tilde{x}=0}\right)^{\mathrm{T}}},\underbrace{\tilde{\Psi}_{1,0},\dots,\tilde{\Psi}_{1,n_{\mathrm{yw}}}}_{\left(\varphi_{e,f}^{\partial w|\tilde{x}=0}\right)^{\mathrm{T}}},$$
$$\underbrace{\tilde{\Psi}_{2,0},\dots,\tilde{\Psi}_{2,n_{\mathrm{yw}}}}_{\left(\varphi_{e,f}^{w|\tilde{x}=a_e}\right)^{\mathrm{T}}},\underbrace{\tilde{\Psi}_{n_{\mathrm{x}},0},\dots,\tilde{\Psi}_{n_{\mathrm{x}},n_{\mathrm{yw}}}}_{\left(\varphi_{e,f}^{\partial w|\tilde{x}=a_e}\right)^{\mathrm{T}}}\Big]\in\mathbb{R}^{(n_{\mathrm{x}}+1)(n_{\mathrm{yw}}+1)} \tag{2.23c}$$

with $n_{\mathrm{x}}=3$ and the abbreviations $\breve{\Psi}_{i,j}=X_i(\breve{x})Y_j(b,\breve{y})$ and $\tilde{\Psi}_{i,j}=X_i(\tilde{x})Y_j(\tilde{b},\tilde{y})$. Four basis functions are used along the direction x ($n_{\mathrm{x}}=3$). The parameters n_{yu}, n_{yv}, and n_{yw} determine the number of basis functions along the direction y for the deflections u, v, and w, respectively. Hermite polynomials

$$X_0(x)=2x^3/a_e^3-3x^2/a_e^2+1 \tag{2.24a}$$
$$X_1(x)=-x^3/a_e^2+2x^2/a_e-x \tag{2.24b}$$
$$X_2(x)=-2x^3/a_e^3+3x^2/a_e^2 \tag{2.24c}$$
$$X_3(x)=-x^3/a_e^2+x^2/a_e \tag{2.24d}$$

and Legendre polynomials

$$Y_j(v,y)=\sum_{s=0}^{Z_j}\frac{(-1)^s(2j-2s)!\left(\frac{2y}{v}-1\right)^{j-2s}}{2^j s!(j-s)!(j-2s)!}, \tag{2.25}$$

with

$$Z_j=\frac{j}{2}-\frac{1}{4}\left(1-(-1)^j\right), \tag{2.26}$$

are used as local basis functions [75, 76]. As shown in (2.23a), (2.23b) for the in-plane displacements, the basis functions can be partitioned into four subvectors. The corresponding vectors of Galerkin coefficients, cf. (2.22a) or (2.22b), read as

$$\left(\breve{\mathbf{t}}_e^{\xi}\right)^{\mathrm{T}}=\left[\left(\boldsymbol{\tau}_e^{\xi|\breve{x}=0}\right)^{\mathrm{T}},\left(\boldsymbol{\tau}_e^{\partial\xi|\breve{x}=0}\right)^{\mathrm{T}},\left(\boldsymbol{\tau}_e^{\xi|\breve{x}=a_e}\right)^{\mathrm{T}},\left(\boldsymbol{\tau}_e^{\partial\xi|\breve{x}=a_e}\right)^{\mathrm{T}}\right] \tag{2.27}$$

with $\xi\in\{u,v\}$. Here, $\boldsymbol{\tau}_e^{\xi|\breve{x}=0}$ and $\boldsymbol{\tau}_e^{\xi|\breve{x}=a_e}$ are related to the displacements at $\breve{x}=0$ and $\breve{x}=a_e$, respectively. Similarly, $\boldsymbol{\tau}_e^{\partial\xi|\breve{x}=0}$ and $\boldsymbol{\tau}_e^{\partial\xi|\breve{x}=a_e}$ are connected to the slopes along the direction x at these element boundaries. In the same way, the basis functions of the out-of-plane displacements (2.23c) can be structured into four subvectors.

The weighting functions $\bar{u}$, $\bar{v}$, and $\bar{w}$ are defined by analogy to (2.23). In the context of the Galerkin approximation, the single entries of the $\bar{\mathbf{\Psi}}$ vectors are used to weight the residuals. The individual discretization of the in-plane and the out-of-plane dynamics in (2.20) yields a system of coupled ordinary differential equations.

Remark: Assume steady-state conditions for the in-plane problem, i.e., all time derivatives in (2.15a) and (2.15b) are neglected. Moreover, in the sense of a geometrically linear analysis all higher order terms in (2.7a) are neglected. Using this simplification, the in-plane system (2.15a), (2.15b) becomes independent of the out-of-plane system (2.15c). For the geometrically linear case and in-plane boundary conditions that are symmetric with respect to $y = 0$, e.g., a homogeneous tensile load, the finite-element solutions $u(x, y)$ and $v(x, y)$ must also be symmetric and asymmetric with respect to $y = 0$, respectively. Note that, in general, the solution $w(x, y)$ remains arbitrary since it depends on the forces in transverse direction. This simplification can be used to reduce the degrees of freedom of the in-plane system, i.e., (2.23a) and (2.23b) can be replaced by $(\mathbf{\Psi}_e^u)^{\mathrm{T}} = \left[\breve{\Psi}_{0,0}, \breve{\Psi}_{0,2}, \breve{\Psi}_{0,4}, \ldots, \breve{\Psi}_{0,\phi^u(n_{\mathrm{yu}})}, \breve{\Psi}_{1,0}, \ldots, \breve{\Psi}_{n_{\mathrm{x}},\phi^u(n_{\mathrm{yu}})}\right]$ and $(\mathbf{\Psi}_e^v)^{\mathrm{T}} = \left[\breve{\Psi}_{0,1}, \breve{\Psi}_{0,3}, \breve{\Psi}_{0,5}, \ldots, \breve{\Psi}_{0,\phi^v(n_{\mathrm{yv}})}, \breve{\Psi}_{1,1}, \ldots, \breve{\Psi}_{n_{\mathrm{x}},\phi^v(n_{\mathrm{yv}})}\right]$, respectively, with the functions $\phi^u(n_{\mathrm{yu}}) = n_{\mathrm{yu}}+1/2(1-(-1)^{n_{\mathrm{yu}}+1})-1$ and $\phi^v(n_{\mathrm{yv}}) = n_{\mathrm{yv}}+1/2(1-(-1)^{n_{\mathrm{yv}}})-1$.

In a first step, the equations of motion of the individual finite elements in Fig. 2.8 have to be derived. The matrix-vector-representation of the equations of motion is obtained by inserting the weighting and basis functions (2.23) into (2.20), where the transformations (2.21) have to be taken into account. As a second step, the individual systems are assembled to the full equations of motion. Generally, a time derivative is marked with a diacritic dot.

In-plane system The dynamics of an in-plane finite element e shown in Fig. 2.8a is described by the matrix-vector-representation

$$\begin{aligned}\breve{\mathbf{M}}_e\ddot{\breve{\mathbf{t}}}_e^{uv} + 2V\breve{\mathbf{G}}_e\dot{\breve{\mathbf{t}}}_e^{uv} + \left(\breve{\mathbf{K}}_e - V^2\breve{\mathbf{H}}_e\right)\breve{\mathbf{t}}_e^{uv} &= \breve{\mathbf{f}}_e^{\mathrm{g}} + \breve{\mathbf{f}}_e^{\mathrm{N}} \\ &- \breve{\mathbf{f}}_e^{\mathrm{w}}\left(\tilde{\mathbf{t}}_{e,f=1}^w, \ldots, \tilde{\mathbf{t}}_{e,f=m}^w\right) + \breve{\mathbf{b}}_e^{\mathrm{x}}\epsilon_{xx}^{\mathrm{r},0} + \breve{\mathbf{b}}_e^{\mathrm{y}}\epsilon_{yy}^{\mathrm{r},0},\end{aligned} \tag{2.28}$$

where the abbreviations $\left(\breve{\mathbf{t}}_e^{uv}\right)^{\mathrm{T}} = \left[\left(\breve{\mathbf{t}}_e^u\right)^{\mathrm{T}}\left(\breve{\mathbf{t}}_e^v\right)^{\mathrm{T}}\right]$,

$$\breve{\mathbf{M}}_e = \rho h\int_{\breve{\Omega}_e}\begin{bmatrix}\bar{\mathbf{\Psi}}_e^u(\mathbf{\Psi}_e^u)^{\mathrm{T}} & \mathbf{0}\\ \mathbf{0} & \bar{\mathbf{\Psi}}_e^v(\mathbf{\Psi}_e^v)^{\mathrm{T}}\end{bmatrix}\mathrm{d}\breve{x}\mathrm{d}\breve{y} \tag{2.29a}$$

$$\breve{\mathbf{G}}_e = \rho h\int_{\breve{\Omega}_e}\begin{bmatrix}\bar{\mathbf{\Psi}}_e^u(\partial_x\mathbf{\Psi}_e^u)^{\mathrm{T}} & \mathbf{0}\\ \mathbf{0} & \bar{\mathbf{\Psi}}_e^v(\partial_x\mathbf{\Psi}_e^v)^{\mathrm{T}}\end{bmatrix}\mathrm{d}\breve{x}\mathrm{d}\breve{y} \tag{2.29b}$$

$$\breve{\mathbf{H}}_e = \rho h \breve{\mathbf{H}}_e^{\Omega} + \rho h \breve{\mathbf{H}}_e^{\Gamma} \tag{2.29c}$$

$$\breve{\mathbf{H}}_e^{\Omega} = \int_{\breve{\Omega}_e} \begin{bmatrix} \partial_x \bar{\mathbf{\Psi}}_e^u (\partial_x \mathbf{\Psi}_e^u)^{\mathrm{T}} & \mathbf{0} \\ \mathbf{0} & \partial_x \bar{\mathbf{\Psi}}_e^v (\partial_x \mathbf{\Psi}_e^v)^{\mathrm{T}} \end{bmatrix} \mathrm{d}\breve{x}\mathrm{d}\breve{y} \tag{2.29d}$$

$$\breve{\mathbf{H}}_e^{\Gamma} = \begin{cases} \int_0^b \begin{bmatrix} \mathbf{0} & \mathbf{0} \\ \mathbf{0} & \bar{\mathbf{\Psi}}_1^v (\partial_x \mathbf{\Psi}_1^v)^{\mathrm{T}} \end{bmatrix}_{\breve{x}=0} \mathrm{d}\breve{y} & \text{for } e = 1 \\ -\int_0^b \begin{bmatrix} \bar{\mathbf{\Psi}}_n^u (\partial_x \mathbf{\Psi}_n^u)^{\mathrm{T}} & \mathbf{0} \\ \mathbf{0} & \bar{\mathbf{\Psi}}_n^v (\partial_x \mathbf{\Psi}_n^v)^{\mathrm{T}} \end{bmatrix}_{\breve{x}=a_e} \mathrm{d}\breve{y} & \text{for } e = n \\ \mathbf{0} & \text{else} \end{cases} \tag{2.29e}$$

$$\breve{\mathbf{K}}_e = A \int_{\breve{\Omega}_e} \begin{bmatrix} \breve{\mathbf{K}}_e^{11} & \breve{\mathbf{K}}_e^{12} \\ \left(\breve{\mathbf{K}}_e^{12}\right)^{\mathrm{T}} & \breve{\mathbf{K}}_e^{22} \end{bmatrix} \mathrm{d}\breve{x}\mathrm{d}\breve{y} \tag{2.29f}$$

$$\breve{\mathbf{K}}_e^{11} = \left(\partial_x \bar{\mathbf{\Psi}}_e^u\right)(\partial_x \mathbf{\Psi}_e^u)^{\mathrm{T}} + \left(\partial_y \bar{\mathbf{\Psi}}_e^u\right) \frac{1-\nu}{2} (\partial_y \mathbf{\Psi}_e^u)^{\mathrm{T}} \tag{2.29g}$$

$$\breve{\mathbf{K}}_e^{12} = \left(\partial_x \bar{\mathbf{\Psi}}_e^u\right)\nu(\partial_y \mathbf{\Psi}_e^v)^{\mathrm{T}} + \left(\partial_y \bar{\mathbf{\Psi}}_e^u\right) \frac{1-\nu}{2} (\partial_x \mathbf{\Psi}_e^v)^{\mathrm{T}} \tag{2.29h}$$

$$\breve{\mathbf{K}}_e^{22} = \left(\partial_y \bar{\mathbf{\Psi}}_e^v\right)(\partial_y \mathbf{\Psi}_e^v)^{\mathrm{T}} + \left(\partial_x \bar{\mathbf{\Psi}}_e^v\right) \frac{1-\nu}{2} (\partial_x \mathbf{\Psi}_e^v)^{\mathrm{T}} \tag{2.29i}$$

$$\breve{\mathbf{f}}_e^{\mathrm{w}} = \left[\left(\breve{\mathbf{f}}_e^{\mathrm{w}1}\right)^{\mathrm{T}} \quad \left(\breve{\mathbf{f}}_e^{\mathrm{w}2}\right)^{\mathrm{T}} \right]^{\mathrm{T}} \tag{2.29j}$$

$$\breve{\mathbf{f}}_e^{\mathrm{w}1} = \frac{A}{2} \int_{\breve{\Omega}_e} \left(\partial_x \bar{\mathbf{\Psi}}_e^u\right)\left[(\partial_x w)^2 + \nu(\partial_y w)^2\right] + \left(\partial_y \bar{\mathbf{\Psi}}_e^u\right)(1-\nu)\partial_x w \partial_y w \mathrm{d}\breve{x}\mathrm{d}\breve{y} \tag{2.29k}$$

$$\breve{\mathbf{f}}_e^{\mathrm{w}2} = \frac{A}{2} \int_{\breve{\Omega}_e} \left(\partial_y \bar{\mathbf{\Psi}}_e^v\right)\left[\nu(\partial_x w)^2 + (\partial_y w)^2\right] + \left(\partial_x \bar{\mathbf{\Psi}}_e^v\right)(1-\nu)\partial_x w \partial_y w \mathrm{d}\breve{x}\mathrm{d}\breve{y} \tag{2.29l}$$

$$\breve{\mathbf{b}}_e^{\mathrm{x}} = A \int_{\breve{\Omega}_e} \left[\left(\partial_x \bar{\mathbf{\Psi}}_e^u\right)^{\mathrm{T}} \quad \left(\partial_y \bar{\mathbf{\Psi}}_e^v\right)^{\mathrm{T}} \nu \right]^{\mathrm{T}} \mathrm{d}\breve{x}\mathrm{d}\breve{y} \tag{2.29m}$$

$$\breve{\mathbf{b}}_e^{\mathrm{y}} = A \int_{\breve{\Omega}_e} \left[\left(\partial_x \bar{\mathbf{\Psi}}_e^u\right)^{\mathrm{T}} \nu \quad \left(\partial_y \bar{\mathbf{\Psi}}_e^v\right)^{\mathrm{T}} \right]^{\mathrm{T}} \mathrm{d}\breve{x}\mathrm{d}\breve{y} \tag{2.29n}$$

$$\breve{\mathbf{f}}_e^{\mathrm{g}} = \left[-\rho h g \int_{\breve{\Omega}_e} \left(\bar{\mathbf{\Psi}}_e^u\right)^{\mathrm{T}} \mathrm{d}\breve{x}\mathrm{d}\breve{y} \quad \mathbf{0}^{\mathrm{T}} \right]^{\mathrm{T}} \tag{2.29o}$$

$$\breve{\mathbf{f}}_e^{\mathrm{N}} = \begin{cases} \begin{bmatrix} \int_0^b N_{xx,\mathrm{L}} \bar{\mathbf{\Psi}}_n^u|_{\breve{x}=a_n} \mathrm{d}\breve{y} \\ \mathbf{0} \end{bmatrix} & \text{for } e = n \\ \mathbf{0} & \text{else} \end{cases} \tag{2.29p}$$

are used. Here, $\breve{\mathbf{M}}_e$ is the mass matrix, the matrices $\breve{\mathbf{G}}_e$ and $\breve{\mathbf{H}}_e$ are associated with the gyroscopic (Coriolis) and centrifugal forces, respectively. The structural stiffness of the in-plane problem consists of two parts: The in-plane stiffness matrix $\breve{\mathbf{K}}_e$ represents a linear part. Because of the geometrical nonlinearity, an additional in-plane force $\breve{\mathbf{f}}_e^{\mathrm{w}}\left(\tilde{\mathbf{t}}_{e,f=1}^w, \ldots, \tilde{\mathbf{t}}_{e,f=m}^w\right)$ appears, which depends on the transverse displacement w. Before the integrals in (2.29k) and (2.29l) can be evaluated, the partial derivatives of w according to (2.22c) have to be expressed depending on the locally defined vectors of Galerkin coefficients $\tilde{\mathbf{t}}^w_{e,f=1}$ to $\tilde{\mathbf{t}}^w_{e,f=m}$. The vectors $\breve{\mathbf{b}}^{\mathrm{x}}_e$ and $\breve{\mathbf{b}}^{\mathrm{y}}_e$ account for the residual membrane strains $\epsilon^{\mathrm{r},0}_{xx}$ and $\epsilon^{\mathrm{r},0}_{yy}$, respectively. The dead load of the strip is incorporated by the vector $\breve{\mathbf{f}}^{\mathrm{g}}_e$. The vector $\breve{\mathbf{f}}^{\mathrm{N}}_e$ accounts for the tensile load $N_{xx,\mathrm{L}}$ at the boundary $x = L$. To fulfill the Dirichlet boundary condition $u|_{x=0} = 0$, the vector $\left(\psi_1^{u|_{\breve{x}=0}}\right)$ is omitted in the basis function (2.23a) of the finite element $e = 1$, i.e.,

$$\left(\mathbf{\Psi}^u_1\right)^{\mathrm{T}} = \left[\left(\psi_1^{\partial u|_{\breve{x}=0}}\right)^{\mathrm{T}} \quad \left(\psi_1^{u|_{\breve{x}=a_1}}\right)^{\mathrm{T}} \quad \left(\psi_1^{\partial u|_{\breve{x}=a_1}}\right)^{\mathrm{T}}\right]. \tag{2.30}$$

The corresponding $n_{\mathrm{yu}} + 1$ Galerkin coefficients in (2.22a) are eliminated because they are no longer degrees of freedom of the model. The implementation of the boundary conditions $v|_{x=0,y=0} = v|_{x=L,y=0} = 0$ requires an elimination of the symmetric Legendre polynomials in the basis functions of the finite elements $e = 1, n$ in (2.23b). To this end, the vectors

$$\left(\psi_1^{v|_{\breve{x}=0}}\right)^{\mathrm{T}} = \left[\breve{\Psi}_{0,1}, \breve{\Psi}_{0,3}, \ldots, \breve{\Psi}_{0,\phi^v(n_{\mathrm{yv}})}\right] \tag{2.31a}$$

and

$$\left(\psi_n^{v|_{\breve{x}=a_n}}\right)^{\mathrm{T}} = \left[\breve{\Psi}_{0,1}, \breve{\Psi}_{0,3}, \ldots, \breve{\Psi}_{0,\phi^v(n_{\mathrm{yv}})}\right] \tag{2.31b}$$

with the function $\phi^v(n_{\mathrm{yv}}) = n_{\mathrm{yv}} + 1/2(1 - (-1)^{n_{\mathrm{yv}}}) - 1$ are used instead of the corresponding vectors in (2.23b). In (2.22b), the number of Galerkin coefficients for the finite elements $e = 1, n$ reduces by $(\phi^v(n_{\mathrm{yv}}) + 1)/2$.

Out-of-plane system By analogy to the in-plane dynamics, the matrix-vector-representation of an out-of-plane finite element (e, f) according to Fig. 2.8b reads as

$$\begin{aligned}&\tilde{\mathbf{M}}_{e,f}\ddot{\tilde{\mathbf{t}}}^w_{e,f} + \left(2V\tilde{\mathbf{G}}_{e,f} + \tilde{\mathbf{D}}_{e,f}\right)\dot{\tilde{\mathbf{t}}}^w_{e,f} + \left[\tilde{\mathbf{K}}^{\bar{\mathrm{M}}}_{e,f} + \tilde{\mathbf{K}}^{\mathrm{N}}_{e,f}\left(\tilde{\mathbf{t}}^w_{e,f}, \breve{\mathbf{t}}^{uv}_e\right) - V^2\tilde{\mathbf{H}}_{e,f}\right]\tilde{\mathbf{t}}^w_{e,f} = \\ &\tilde{\mathbf{b}}^{\mathrm{x}}_{e,f}\epsilon^{\mathrm{r},1}_{xx} + \tilde{\mathbf{B}}^{\mathrm{y}}_{e,f}\boldsymbol{\epsilon}^{\mathrm{r},1}_{yy} + \tilde{\mathbf{B}}_{e,f}\mathbf{f}_{\mathrm{mag}} + \tilde{\mathbf{f}}^{\mathrm{clr}}_{e,f}\left(\tilde{\mathbf{t}}^w_{e,f}\right) + \tilde{\mathbf{h}}^{\mathrm{q_p}}_{e,f}q_{\mathrm{p}} - \tilde{\mathbf{b}}^{\mathrm{w_0}}_{e,f}w_0 - \tilde{\mathbf{b}}^{\partial\mathrm{w_0}}_{e,f}w_{\mathrm{x},0},\end{aligned} \tag{2.32}$$

with the abbreviations

$$\tilde{\mathbf{M}}_{e,f} = \begin{cases}(\rho h + \bar{m}_{\mathrm{pot}}) \int_{\tilde{\Omega}_{e,f}} \bar{\mathbf{\Psi}}^w_{e,f}\left(\mathbf{\Psi}^w_{e,f}\right)^{\mathrm{T}} \mathrm{d}\tilde{x}\mathrm{d}\tilde{y} & \text{for } e \in \{1, \ldots, n_{\mathrm{pot}}\} \\ \rho h \int_{\tilde{\Omega}_{e,f}} \bar{\mathbf{\Psi}}^w_{e,f}\left(\mathbf{\Psi}^w_{e,f}\right)^{\mathrm{T}} \mathrm{d}\tilde{x}\mathrm{d}\tilde{y} & \text{else}\end{cases} \tag{2.33a}$$

$$\tilde{\mathbf{G}}_{e,f} = \rho h \int_{\tilde{\Omega}_{e,f}} \bar{\mathbf{\Psi}}^w_{e,f}\left(\partial_x \mathbf{\Psi}^w_{e,f}\right)^{\mathrm{T}} \mathrm{d}\tilde{x}\mathrm{d}\tilde{y} \tag{2.33b}$$

$$\tilde{\mathbf{H}}_{e,f} = \rho h\tilde{\mathbf{H}}^{\Omega}_{e,f} + \rho h\tilde{\mathbf{H}}^{\Gamma}_{e,f} \tag{2.33c}$$

$$\tilde{\mathbf{H}}^{\Omega}_{e,f} = \int_{\tilde{\Omega}_{e,f}} \partial_x \bar{\mathbf{\Psi}}^w_{e,f} \left(\partial_x \mathbf{\Psi}^w_{e,f}\right)^{\mathrm{T}} \mathrm{d}\tilde{x}\mathrm{d}\tilde{y} \tag{2.33d}$$

$$\tilde{\mathbf{H}}^{\Gamma}_{e,f} = \begin{cases} \int_0^{\tilde{b}} \left[\bar{\mathbf{\Psi}}^w_{1,f}\left(\partial_x \mathbf{\Psi}^w_{1,f}\right)^{\mathrm{T}}\right]_{\tilde{x}=0} \mathrm{d}\tilde{y} & \text{for } e=1 \\ \mathbf{0} & \text{else} \end{cases} \tag{2.33e}$$

$$\begin{aligned} \tilde{\mathbf{K}}^{\bar{\mathrm{M}}}_{e,f} = D \int_{\tilde{\Omega}_{e,f}} &\partial_x^2 \bar{\mathbf{\Psi}}^w_{e,f}\left[\left(\partial_x^2 \mathbf{\Psi}^w_{e,f}\right)^{\mathrm{T}} + \nu\left(\partial_y^2 \mathbf{\Psi}^w_{e,f}\right)^{\mathrm{T}}\right] \\ &+ 2(1-\nu)\left(\partial_x\partial_y \bar{\mathbf{\Psi}}^w_{e,f}\right)\left(\partial_x\partial_y \mathbf{\Psi}^w_{e,f}\right)^{\mathrm{T}} \\ &+ \partial_y^2 \bar{\mathbf{\Psi}}^w_{e,f}\left[\nu\left(\partial_x^2 \mathbf{\Psi}^w_{e,f}\right)^{\mathrm{T}} + \left(\partial_y^2 \mathbf{\Psi}^w_{e,f}\right)^{\mathrm{T}}\right]\mathrm{d}\tilde{x}\mathrm{d}\tilde{y} \end{aligned} \tag{2.33f}$$

$$\begin{aligned} \tilde{\mathbf{K}}^{\mathrm{N}}_{e,f} = \int_{\tilde{\Omega}_{e,f}} &N_{xx}\left(\partial_x \bar{\mathbf{\Psi}}^w_{e,f}\right)\left(\partial_x \mathbf{\Psi}^w_{e,f}\right)^{\mathrm{T}} + N_{yy}\left(\partial_y \bar{\mathbf{\Psi}}^w_{e,f}\right)\left(\partial_y \mathbf{\Psi}^w_{e,f}\right)^{\mathrm{T}} \\ &+ N_{xy}\left[\left(\partial_x \bar{\mathbf{\Psi}}^w_{e,f}\right)\left(\partial_y \mathbf{\Psi}^w_{e,f}\right)^{\mathrm{T}} + \left(\partial_y \bar{\mathbf{\Psi}}^w_{e,f}\right)\left(\partial_x \mathbf{\Psi}^w_{e,f}\right)^{\mathrm{T}}\right]\mathrm{d}\tilde{x}\mathrm{d}\tilde{y} \end{aligned} \tag{2.33g}$$

$$\tilde{\mathbf{b}}^{\mathrm{x}}_{e,f} = -D \int_{\tilde{\Omega}_{e,f}} \left(\partial_x^2 \bar{\mathbf{\Psi}}^w_{e,f} + \nu \partial_y^2 \bar{\mathbf{\Psi}}^w_{e,f}\right)\mathrm{d}\tilde{x}\mathrm{d}\tilde{y} \tag{2.33h}$$

$$\tilde{\mathbf{B}}^{\mathrm{y}}_{e,f} = -D \int_{\tilde{\Omega}_{e,f}} \left(\nu\partial_x^2 \bar{\mathbf{\Psi}}^w_{e,f} + \partial_y^2 \bar{\mathbf{\Psi}}^w_{e,f}\right)\mathbf{y}_p^{\mathrm{T}}\mathrm{d}\tilde{x}\mathrm{d}\tilde{y} \tag{2.33i}$$

$$\tilde{\mathbf{B}}_{e,f} = \left[\tilde{\mathbf{b}}^1_{e,f}, \ldots, \tilde{\mathbf{b}}^{\kappa}_{e,f}\right] \tag{2.33j}$$

$$\tilde{\mathbf{b}}^{l}_{e,f} = \frac{1}{2x_{\mathrm{p}}y_{\mathrm{p}}} \int_{\tilde{\Omega}_{e,f}\cap\Omega^l_{\mathrm{p}}} \bar{\mathbf{\Psi}}^w_{e,f}\mathrm{d}\tilde{x}\mathrm{d}\tilde{y} \tag{2.33k}$$

$$\tilde{\mathbf{f}}^{\mathrm{clr}}_{e,f} = \sum_{l=1}^{\iota} \int_{\tilde{\Omega}_{e,f}\cap\Omega^l_{\mathrm{clr}}} \bar{\mathbf{\Psi}}^w_{e,f} q^l_{\mathrm{clr}}\mathrm{d}\tilde{x}\mathrm{d}\tilde{y} \tag{2.33l}$$

$$\tilde{\mathbf{h}}^{q_{\mathrm{p}}}_{e,f} = \int_{\tilde{\Omega}_{e,f}} \bar{\mathbf{\Psi}}^w_{e,f}\mathrm{d}\tilde{x}\mathrm{d}\tilde{y}. \tag{2.33m}$$

Prior to the integration of (2.33g), the stress resultants (2.16a) have to be evaluated using (2.7) and (2.23). The expressions (2.33i) and (2.33k) can be calculated using (2.17) and (2.2), respectively, and the transformation (2.21). Similarly, the vector (2.33l) is calculated using (2.5). The mass matrix $\tilde{\mathbf{M}}_{e,f}$ captures both the inertia of the strip as well as the inertia caused by the liquid zinc in the pot, where it is assumed that the first n_{pot} finite elements are below the pot level. By analogy to the in-plane problem, the matrices $\tilde{\mathbf{G}}_{e,f}$ and $\tilde{\mathbf{H}}_{e,f}$ contribute the gyroscopic (Coriolis) and the centrifugal forces, respectively. The matrices $\tilde{\mathbf{K}}^{\bar{\mathrm{M}}}_{e,f}$ and $\tilde{\mathbf{K}}^{\mathrm{N}}_{e,f}$ are the out-of-plane stiffnesses due to bending and in-plane tension, respectively. In (2.32), the abbreviation

$$\tilde{\mathbf{D}}_{e,f} = \alpha\tilde{\mathbf{M}}_{e,f} + \beta\tilde{\mathbf{K}}^{\bar{\mathrm{M}}}_{e,f} \tag{2.34}$$

is used, which constitutes a Rayleigh-type damping formulation for external viscous and internal material damping, see, e.g., [77]. Here, $\alpha\tilde{\mathbf{M}}_{e,f}$ with $\alpha = \frac{c}{\rho h}$ is the damping matrix associated with viscous air friction, and $\beta\tilde{\mathbf{K}}^{\bar{\mathrm{M}}}_{e,f}$ is the damping matrix associated with material damping. The vector $\tilde{\mathbf{b}}^{\mathrm{x}}_{e,f}$ is used to consider the residual curvature in longitudinal direction. The matrix $\tilde{\mathbf{B}}^{\mathrm{y}}_{e,f}$ incorporates the impact of the residual curvature in lateral direction. The vector $\tilde{\mathbf{f}}^{\mathrm{clr}}_{e,f}$ considers the transverse load due to the ι cooling elements. The vector $\tilde{\mathbf{h}}^{\mathrm{q_p}}_{e,f}$ incorporates the influence of the transverse load q_{p}. The geometric boundary conditions $w|_{x=0} = w_0$, $\partial_x w|_{x=0} = w_{\mathrm{x},0}$, and $w|_{x=L} = 0$ at the finite elements $e = 1, n$ are realized by means of the basis functions

$$\left(\boldsymbol{\Psi}^{w}_{1,f}\right)^{\mathrm{T}} = \left(\bar{\boldsymbol{\Psi}}^{w}_{1,f}\right)^{\mathrm{T}} = \left[\left(\boldsymbol{\psi}^{w|_{\tilde{x}=a_1}}_{1,f}\right)^{\mathrm{T}}, \left(\boldsymbol{\psi}^{\partial w|_{\tilde{x}=a_1}}_{1,f}\right)^{\mathrm{T}}\right] \tag{2.35a}$$

$$\left(\boldsymbol{\Psi}^{w}_{n,f}\right)^{\mathrm{T}} = \left(\bar{\boldsymbol{\Psi}}^{w}_{n,f}\right)^{\mathrm{T}} = \left[\left(\boldsymbol{\psi}^{w|_{\tilde{x}=0}}_{n,f}\right)^{\mathrm{T}}, \left(\boldsymbol{\psi}^{\partial w|_{\tilde{x}=0}}_{n,f}\right)^{\mathrm{T}}, \left(\boldsymbol{\psi}^{\partial w|_{\tilde{x}=a_n}}_{n,f}\right)^{\mathrm{T}}\right] \tag{2.35b}$$

in (2.33). In addition, the vectors

$$\tilde{\mathbf{b}}^{\mathrm{w_0}}_{e,f} = \begin{cases} \left[\tilde{\mathbf{K}}^{\bar{\mathrm{M}}}_{1,f} + \tilde{\mathbf{K}}^{\mathrm{N}}_{1,f}\left(\tilde{\mathbf{t}}^{w}_{1,f}, \check{\mathbf{t}}^{uv}_{1}\right) - V^2\tilde{\mathbf{H}}_{1,f}\right]_{\boldsymbol{\Psi}^{w}_{1,f}=\tilde{\Psi}_{0,0}} & \text{for } e = 1 \\ \mathbf{0} & \text{else} \end{cases} \tag{2.36a}$$

$$\tilde{\mathbf{b}}^{\partial\mathrm{w_0}}_{e,f} = \begin{cases} \left[\tilde{\mathbf{K}}^{\bar{\mathrm{M}}}_{1,f} + \tilde{\mathbf{K}}^{\mathrm{N}}_{1,f}\left(\tilde{\mathbf{t}}^{w}_{1,f}, \check{\mathbf{t}}^{uv}_{1}\right) - V^2\tilde{\mathbf{H}}_{1,f}\right]_{\boldsymbol{\Psi}^{w}_{1,f}=\tilde{\Psi}_{1,0}} & \text{for } e = 1 \\ \mathbf{0} & \text{else} \end{cases} \tag{2.36b}$$

have to be considered on the right-hand side of (2.32) to account for non-zero values of w_0 and $w_{\mathrm{x},0}$. Several expressions in (2.33), e.g., $\tilde{\mathbf{M}}_{e,f}$, $\tilde{\mathbf{K}}^{\bar{\mathrm{M}}}_{e,f}$, or $\tilde{\mathbf{b}}^{\mathrm{x}}_{e,f}$ are independent of the index f. That is, they are independent of the lateral position of the finite element. In contrast, $\tilde{\mathbf{K}}^{\mathrm{N}}_{e,f}$, $\tilde{\mathbf{B}}^{\mathrm{y}}_{e,f}$, $\tilde{\mathbf{B}}_{e,f}$, $\tilde{\mathbf{b}}^{\mathrm{w_0}}_{e,f}$, $\tilde{\mathbf{b}}^{\partial\mathrm{w_0}}_{e,f}$, and $\tilde{\mathbf{f}}^{\mathrm{clr}}_{e,f}$ usually depend on the index f. The Eqs. (2.28), (2.29), (2.32), and (2.33) will be assembled to the full dynamic model of the strip in Section 2.1.6.2.

The integration of the single expressions in (2.29) and (2.33) can be performed in analytical form. To this end, the vectors of Galerkin coefficients $\check{\mathbf{t}}^{uv}_{e}$ and $\tilde{\mathbf{t}}^{w}_{e,f}$ are defined in symbolic form using a computer algebra system. These vectors are inserted into the integrals. The integrals are evaluated with the computer algebra system in advance. From this system, a numerically optimized algebraic formulation is exported to Matlab. The expressions (2.29k), (2.29l), (2.33g), and (2.33l) depend on the Galerkin coefficients $\tilde{\mathbf{t}}^{w}_{e,f}$ and $\check{\mathbf{t}}^{uv}_{e}$. The remaining matrices and vectors are independent of the Galerkin coefficients.

For a finite element (e, f), the vector

$$\tilde{\mathbf{w}}_{e,f} = \tilde{\mathbf{C}}_{e,f}\tilde{\mathbf{t}}^{w}_{e,f} \in \mathbb{R}^{\chi} \tag{2.37a}$$

with the local output matrix

$$\left(\tilde{\mathbf{C}}_{e,f}\right)^{\mathrm{T}} = \left[\boldsymbol{\Psi}^{w}_{e,f}(\tilde{x}_1, \tilde{y}_1), \ldots, \boldsymbol{\Psi}^{w}_{e,f}(\tilde{x}_{\chi}, \tilde{y}_{\chi})\right] \tag{2.37b}$$

defines the transverse displacement outputs at the local points $(\tilde{x}_l, \tilde{y}_l)$, where $l \in \{1, \ldots, \chi\}$. Note that the structure of (2.37a) implies that $e \neq 1$ holds since otherwise the transverse displacement outputs would also depend on w_0 and $w_{\mathrm{x},0}$.

2.1.6.2 Assembly

An assembly of the in-plane and the out-of-plane systems according to (2.28) and (2.32), respectively, yields the full system equations.

In-plane system The in-plane system with the displacements u and v is considered. Continuity conditions between neighboring elements require that the constraints $\boldsymbol{\tau}_e^{\xi|_{\breve{x}=a_e}} = \boldsymbol{\tau}_{e+1}^{\xi|_{\breve{x}=0}}$ and $\boldsymbol{\tau}_e^{\partial\xi|_{\breve{x}=a_e}} = \boldsymbol{\tau}_{e+1}^{\partial\xi|_{\breve{x}=0}}$ hold for $\xi \in \{u, v\}$. Hence, the components of (2.27) can be renamed to get

$$\left(\breve{\mathbf{t}}_e^{\xi}\right)^{\mathrm{T}} = \left[\left(\boldsymbol{\tau}_{e-1,e}^{\xi}\right)^{\mathrm{T}}, \left(\boldsymbol{\tau}_{e-1,e}^{\partial\xi}\right)^{\mathrm{T}}, \left(\boldsymbol{\tau}_{e,e+1}^{\xi}\right)^{\mathrm{T}}, \left(\boldsymbol{\tau}_{e,e+1}^{\partial\xi}\right)^{\mathrm{T}}\right]. \tag{2.38}$$

An assembly of these components yields the vector of Galerkin coefficients of the full system $\breve{\mathbf{t}}^{\mathrm{T}} = \left[\left(\breve{\mathbf{t}}^{u}\right)^{\mathrm{T}}, \left(\breve{\mathbf{t}}^{v}\right)^{\mathrm{T}}\right]$ with

$$\left(\breve{\mathbf{t}}^{u}\right)^{\mathrm{T}} = \left[\left(\boldsymbol{\tau}_{-,1}^{\partial u}\right)^{\mathrm{T}}, \left(\boldsymbol{\tau}_{1,2}^{u}\right)^{\mathrm{T}}, \dots, \left(\boldsymbol{\tau}_{n,-}^{u}\right)^{\mathrm{T}}, \left(\boldsymbol{\tau}_{n,-}^{\partial u}\right)^{\mathrm{T}}\right] \tag{2.39a}$$

$$\left(\breve{\mathbf{t}}^{v}\right)^{\mathrm{T}} = \left[\left(\boldsymbol{\tau}_{-,1}^{v}\right)^{\mathrm{T}}, \left(\boldsymbol{\tau}_{-,1}^{\partial v}\right)^{\mathrm{T}}, \dots, \left(\boldsymbol{\tau}_{n,-}^{v}\right)^{\mathrm{T}}, \left(\boldsymbol{\tau}_{n,-}^{\partial v}\right)^{\mathrm{T}}\right]. \tag{2.39b}$$

This parametrization guarantees an in-plane solution that is continuous and continuously differentiable with respect to x and y. The absence of $\boldsymbol{\tau}_{-,1}^{u}$ in (2.39a) is a consequence of the boundary condition $u|_{x=0} = 0$, cf. (2.30).

Finally, the full system is obtained using standard assembly methods, cf. [78, 79]. The computational load of the model can be significantly reduced by means of an optimized code. Here, the MATLAB-Coder can be used to automatically generate parallelized MATLAB executables from scripting language, i.e., MEX-functions in the form of automatically generated and compiled C/C++-code.

Out-of-plane system The assembly of the out-of-plane system in longitudinal direction is done by analogy to the in-plane system. Therefore, the vector $\tilde{\mathbf{t}}_{e,f}^{w}$ of an element (e, f) can be partitioned into subvectors of the form

$$\left(\tilde{\mathbf{t}}_{e,f}^{w}\right)^{\mathrm{T}} = \left[\left(\boldsymbol{\tau}_{e-1,e,f}^{w}\right)^{\mathrm{T}}, \left(\boldsymbol{\tau}_{e-1,e,f}^{\partial w}\right)^{\mathrm{T}}, \left(\boldsymbol{\tau}_{e,e+1,f}^{w}\right)^{\mathrm{T}}, \left(\boldsymbol{\tau}_{e,e+1,f}^{\partial w}\right)^{\mathrm{T}}\right]. \tag{2.40}$$

Hence, the Galerkin coefficients of an array of elements along the direction x can be assembled in the form

$$\left(\breve{\mathbf{t}}_{f}^{w}\right)^{\mathrm{T}} = \left[\left(\boldsymbol{\tau}_{1,2,f}^{w}\right)^{\mathrm{T}}, \left(\boldsymbol{\tau}_{1,2,f}^{\partial w}\right)^{\mathrm{T}}, \dots, \left(\boldsymbol{\tau}_{n-1,n,f}^{w}\right)^{\mathrm{T}}, \left(\boldsymbol{\tau}_{n-1,n,f}^{\partial w}\right)^{\mathrm{T}}, \left(\boldsymbol{\tau}_{n,-,f}^{\partial w}\right)^{\mathrm{T}}\right], \tag{2.41}$$

which already incorporates the corresponding boundary conditions I from Tab. 2.2. The vector

$$\left(\breve{\mathbf{t}}^{w}\right)^{\mathrm{T}} = \left[\left(\breve{\mathbf{t}}_{1}^{w}\right)^{\mathrm{T}}, \dots, \left(\breve{\mathbf{t}}_{m}^{w}\right)^{\mathrm{T}}\right] \tag{2.42}$$

contains the Galerkin coefficients of m stripes of the strip. To enforce continuity conditions along the direction y, a transformation $\check{\mathbf{t}}^w = \mathbf{Z}\tilde{\mathbf{t}}$ is used so that $\tilde{\mathbf{t}}$ contains only independent Galerkin coefficients of the assembled system. Clearly, $\mathbf{Z} = \mathbf{I}$ holds for $m = 1$. To couple neighboring stripes with the indices f, $f+1$ and $f \in \{1, \dots, m-1\}$, the algebraic equations

$$\boldsymbol{\Upsilon}_{\tilde{b}}^{\mathrm{T}} \boldsymbol{\tau}_{e-1,e,f}^{w} - \boldsymbol{\Upsilon}_{0}^{\mathrm{T}} \boldsymbol{\tau}_{e-1,e,f+1}^{w} = 0 \tag{2.43a}$$

$$(\partial_y \boldsymbol{\Upsilon}_{\tilde{b}})^{\mathrm{T}} \boldsymbol{\tau}_{e-1,e,f}^{\partial w} - (\partial_y \boldsymbol{\Upsilon}_{0})^{\mathrm{T}} \boldsymbol{\tau}_{e-1,e,f+1}^{\partial w} = 0, \tag{2.43b}$$

with the vectors

$$\boldsymbol{\Upsilon}_{\tilde{b}}^{\mathrm{T}} = \left[Y_0\left(\tilde{b}, \tilde{b}\right), \dots, Y_{n_{\mathrm{yw}}}\left(\tilde{b}, \tilde{b}\right) \right] \tag{2.44a}$$

$$\boldsymbol{\Upsilon}_{0}^{\mathrm{T}} = \left[[Y_0\left(\tilde{b}, 0\right), \dots, Y_{n_{\mathrm{yw}}}\left(\tilde{b}, 0\right) \right] \tag{2.44b}$$

$$(\partial_y \boldsymbol{\Upsilon}_{\tilde{b}})^{\mathrm{T}} = \left[\partial_y Y_0\left(\tilde{b}, y\right), \dots, \partial_y Y_{n_{\mathrm{yw}}}\left(\tilde{b}, y\right) \right]_{y=\tilde{b}} \tag{2.44c}$$

$$(\partial_y \boldsymbol{\Upsilon}_{0})^{\mathrm{T}} = \left[\partial_y Y_0\left(\tilde{b}, y\right), \dots, \partial_y Y_{n_{\mathrm{yw}}}\left(\tilde{b}, y\right) \right]_{y=0} \tag{2.44d}$$

depending on the Legendre polynomials according to (2.25), have to be fulfilled for all subvectors in (2.41). This guarantees that $w(x, y)$ is continuous and continuously differentiable with respect to y.

Remark: The discretization $m > 1$ and a subvector of (2.41) is considered in the following. The choice $n_{\mathrm{yw}} > 1$ is necessary to achieve a model with additional degrees of freedom compared to a model with a single finite element in lateral direction ($m = 1$). This is because $n_{\mathrm{yw}} + 1$ basis functions are used in (2.23c) for the discretization in lateral direction and the two conditions according to (2.43) have to be fulfilled. For $n_{\mathrm{yw}} = 1$, all Galerkin coefficients of the stripe $f + 1$ would depend on the Galerkin coefficients of the stripe f.

For the assumption $m \geq 3$ with an odd number m, the vector of Galerkin coefficients of the full system is introduced as

$$\tilde{\mathbf{t}}^{\mathrm{T}} = \left[\left(\check{\mathbf{t}}_1^{w,\mathrm{c}}\right)^{\mathrm{T}}, \dots, \left(\check{\mathbf{t}}_{\check{m}-1}^{w,\mathrm{c}}\right)^{\mathrm{T}}, \left(\check{\mathbf{t}}_{\check{m}}^{w}\right)^{\mathrm{T}}, \left(\check{\mathbf{t}}_{\check{m}+1}^{w,\mathrm{c}}\right)^{\mathrm{T}}, \dots, \left(\check{\mathbf{t}}_{m}^{w,\mathrm{c}}\right)^{\mathrm{T}} \right], \tag{2.45}$$

with the abbreviation $\check{m} = (m+1)/2$. The Galerkin coefficients of the middle stripe, i.e., $\check{\mathbf{t}}_{\check{m}}^{w}$, remain unreduced. All other subvectors with the superscripts c in (2.45) correspond to stripes, where dependent Galerkin coefficients have been eliminated. Accordingly, the transformations $\tilde{\boldsymbol{\Theta}} = \mathbf{Z}^{\mathrm{T}} \check{\boldsymbol{\Theta}} \mathbf{Z}$ with $\boldsymbol{\Theta} \in \{\mathbf{M}, \mathbf{G}, \mathbf{D}, \mathbf{K}^{\bar{\mathrm{M}}}, \mathbf{K}^{\mathrm{N}}, \mathbf{H}\}$, $\tilde{\boldsymbol{\Xi}} = \mathbf{Z}^{\mathrm{T}} \check{\boldsymbol{\Xi}}$ with $\boldsymbol{\Xi} \in \{\mathbf{b}^{\mathrm{x}}, \mathbf{B}^{\mathrm{y}}, \mathbf{B}, \mathbf{f}^{\mathrm{clr}}, \mathbf{h}^{\mathrm{q_P}}, \mathbf{b}^{\mathrm{w_0}}, \mathbf{b}^{\partial \mathrm{w_0}}\}$, and $\tilde{\mathbf{C}} = \check{\mathbf{C}} \mathbf{Z}$, are used to compute the transformed system matrices and vectors. In the original system with the vector of Galerkin coefficients (2.42), the single quantities can be interpreted by analogy to the matrices and vectors in (2.32) for a single finite element. For instance, $\breve{\mathbf{M}}$ and $\breve{\mathbf{B}}$ denote the mass matrix and input matrix for the electromagnetic forces, respectively, of the partially assembled system with the vector of Galerkin coefficients (2.42). The output matrix $\breve{\mathbf{C}}$ is obtained by an individual assembly of the local matrices given in (2.37).

Assembled full system The full system for the boundary conditions I in Tab. 2.2 is given by

$$\breve{\mathbf{M}}\ddot{\breve{\mathbf{t}}} + 2V\breve{\mathbf{G}}\dot{\breve{\mathbf{t}}} + \left(\breve{\mathbf{K}} - V^2\breve{\mathbf{H}}\right)\breve{\mathbf{t}} = \breve{\mathbf{f}}^{\mathrm{g}} + \breve{\mathbf{f}}^{\mathrm{N}} - \breve{\mathbf{f}}^{\mathrm{w}}\left(\tilde{\mathbf{t}}\right) + \breve{\mathbf{b}}^{\mathrm{x}}\epsilon_{xx}^{\mathrm{r},0} + \breve{\mathbf{b}}^{\mathrm{y}}\epsilon_{yy}^{\mathrm{r},0} \tag{2.46a}$$

$$\begin{aligned}&\tilde{\mathbf{M}}\ddot{\tilde{\mathbf{t}}} + \left(2V\tilde{\mathbf{G}} + \tilde{\mathbf{D}}\right)\dot{\tilde{\mathbf{t}}} + \left[\tilde{\mathbf{K}}^{\bar{\mathrm{M}}} + \tilde{\mathbf{K}}^{\mathrm{N}}\left(\tilde{\mathbf{t}}, \breve{\mathbf{t}}\right) - V^2\tilde{\mathbf{H}}\right]\tilde{\mathbf{t}} = \\ &\tilde{\mathbf{b}}^{\mathrm{x}}\epsilon_{xx}^{\mathrm{r},1} + \tilde{\mathbf{B}}^{\mathrm{y}}\boldsymbol{\varepsilon}_{yy}^{\mathrm{r},1} + \tilde{\mathbf{B}}\mathbf{f}_{\mathrm{mag}} + \tilde{\mathbf{f}}^{\mathrm{clr}}\left(\tilde{\mathbf{t}}\right) + \tilde{\mathbf{h}}^{q_{\mathrm{p}}}q_{\mathrm{p}} - \tilde{\mathbf{b}}^{\mathrm{w}_0}w_0 - \tilde{\mathbf{b}}^{\partial\mathrm{w}_0}w_{\mathrm{x},0}\end{aligned} \tag{2.46b}$$

$$\tilde{\mathbf{w}}_{\mathrm{mag}} = \tilde{\mathbf{C}}_{\mathrm{mag}}\tilde{\mathbf{t}} \tag{2.46c}$$

$$\tilde{\mathbf{w}}_{\mathrm{gwd}} = \tilde{\mathbf{C}}_{\mathrm{gwd}}\tilde{\mathbf{t}}, \tag{2.46d}$$

where (2.46a) and (2.46b) describe the in- and out-of-plane dynamics, respectively. The terms $\breve{\mathbf{M}}$ and $\tilde{\mathbf{M}}$ denote the mass matrices, $\breve{\mathbf{G}}$ and $\tilde{\mathbf{G}}$ are the gyroscopic matrices, and $\tilde{\mathbf{D}}$ is the Rayleigh-type damping matrix. The expressions $\breve{\mathbf{H}}$ and $\tilde{\mathbf{H}}$ are associated with centrifugal forces, $\breve{\mathbf{K}}$, $\tilde{\mathbf{K}}^{\bar{\mathrm{M}}}$, and $\tilde{\mathbf{K}}^{\mathrm{N}}$ represent the in-plane stiffness, the out-of-plane stiffness due to bending, and the out-of-plane stiffness due to in-plane tension, respectively. The vectors $\breve{\mathbf{f}}^{\mathrm{g}}$ and $\breve{\mathbf{f}}^{\mathrm{N}}$ take into account the gravity and the tensile load, respectively. The quantity $\breve{\mathbf{f}}^{\mathrm{w}}\left(\tilde{\mathbf{t}}\right)$ accounts for the influence of the geometric nonlinearity on the in-plane dynamics. The expressions $\breve{\mathbf{b}}^{\mathrm{x}}$, $\breve{\mathbf{b}}^{\mathrm{y}}$ and $\tilde{\mathbf{b}}^{\mathrm{x}}$, $\tilde{\mathbf{B}}^{\mathrm{y}}$ incorporate the effects of the residual membrane strains and curvatures, respectively. The matrix $\tilde{\mathbf{B}}$ describes the coupling to the electromagnetic forces $\mathbf{f}_{\mathrm{mag}}$. The vector $\tilde{\mathbf{f}}^{\mathrm{clr}}\left(\tilde{\mathbf{t}}\right)$ takes into account the transverse loads due to the cooling elements. The expression $\tilde{\mathbf{h}}^{q_{\mathrm{p}}}$ incorporates the transverse load q_{p}. The input vectors $\tilde{\mathbf{b}}^{\mathrm{w}_0}$ and $\tilde{\mathbf{b}}^{\partial\mathrm{w}_0}$ capture the influences of the non-zero boundary conditions. In (2.46c), the output matrix $\tilde{\mathbf{C}}_{\mathrm{mag}}$ calculates the transverse strip displacements $\tilde{\mathbf{w}}_{\mathrm{mag}}$ at the height of the electromagnets, cf. (1.2). Similarly, the output matrix $\tilde{\mathbf{C}}_{\mathrm{gwd}}$ in (2.46d) is used to evaluate the transverse strip profile at the height of the gas wiping dies, cf. (1.3). In a similar way, the transverse strip displacement can be computed at any other position of the strip, see Fig. 2.1. Henceforth, $\tilde{\mathbf{w}}_{\mathrm{tow}} \in \mathbb{R}^{\mu}$ denotes the transverse strip displacement at the position $x = x_{\mathrm{tow}}$ of the temporary displacement sensors in the tower, where μ is the number of sensors in lateral direction.

2.1.7 Transient solution

In order to solve the coupled nonlinear dynamic system (2.46a) and (2.46b), quasi-static relations with $\partial_t u \approx 0$ and $\partial_t v \approx 0$ are assumed for the in-plane problem. This simplification can be justified based on the findings published in [80].

Remark: The large membrane stiffness of the strip leads to high frequencies of the in-plane strip vibrations. These in-plane strip vibrations typically decay very fast due to the structural damping of the strip (which is not considered in the model). In contrast, the out-of-plane strip vibrations are known to decay significantly slower, cf. [80]. For such systems, the singular perturbation theory can be utilized [81]. To this end, the system dynamics is divided into a fast and a slow subsystem, where the fast subsystem can be approximated by its quasi-static solution.

Using (2.46a) and assuming quasi-static relations, the Galerkin coefficients of the in-plane system can be expressed by the algebraic equation

$$\breve{\mathbf{t}}\left(\tilde{\mathbf{t}}\right) = \left(\breve{\mathbf{K}} - V^2\breve{\mathbf{H}}\right)^{-1}\left(\breve{\mathbf{f}}^{\mathrm{g}} + \breve{\mathbf{f}}^{\mathrm{N}} - \breve{\mathbf{f}}^{\mathrm{w}}\left(\tilde{\mathbf{t}}\right) + \breve{\mathbf{b}}^{\mathrm{x}}\epsilon_{xx}^{\mathrm{r},0} + \breve{\mathbf{b}}^{\mathrm{y}}\epsilon_{yy}^{\mathrm{r},0}\right). \tag{2.47}$$

A substitution of (2.47) into (2.46b) allows to define a residuum in the form

$$\mathbf{r} = \tilde{\mathbf{M}}\ddot{\tilde{\mathbf{t}}} + \grave{\mathbf{D}}\dot{\tilde{\mathbf{t}}} + \left[\grave{\mathbf{K}} + \grave{\mathbf{K}}^{\mathrm{N}}\left(\tilde{\mathbf{t}}\right)\right]\tilde{\mathbf{t}} - \grave{\mathbf{f}}\left(\tilde{\mathbf{t}}\right), \tag{2.48}$$

with the abbreviations

$$\grave{\mathbf{D}} = 2V\tilde{\mathbf{G}} + \tilde{\mathbf{D}} \tag{2.49a}$$
$$\grave{\mathbf{K}} = \tilde{\mathbf{K}}^{\bar{\mathrm{M}}} - V^2\tilde{\mathbf{H}} \tag{2.49b}$$
$$\grave{\mathbf{K}}^{\mathrm{N}}\left(\tilde{\mathbf{t}}\right) = \tilde{\mathbf{K}}^{\mathrm{N}}\left(\tilde{\mathbf{t}}, \breve{\mathbf{t}}\left(\tilde{\mathbf{t}}\right)\right) \tag{2.49c}$$
$$\grave{\mathbf{f}}\left(\tilde{\mathbf{t}}\right) = \tilde{\mathbf{b}}^{\mathrm{x}}\epsilon_{xx}^{\mathrm{r},1} + \tilde{\mathbf{B}}^{\mathrm{y}}\boldsymbol{\varepsilon}_{yy}^{\mathrm{r},1} + \tilde{\mathbf{B}}\mathbf{f}_{\mathrm{mag}} + \tilde{\mathbf{f}}^{\mathrm{clr}}\left(\tilde{\mathbf{t}}\right) + \tilde{\mathbf{h}}^{q_{\mathrm{p}}}q_{\mathrm{p}} - \tilde{\mathbf{b}}^{w_0}w_0 - \tilde{\mathbf{b}}^{\partial w_0}w_{\mathrm{x},0}. \tag{2.49d}$$

The solution of the nonlinear ordinary differential equation $\mathbf{r} = \mathbf{0}$ with $\mathbf{r}$ according to (2.48) and the related initial conditions $\tilde{\mathbf{t}}_0$ and $\dot{\tilde{\mathbf{t}}}_0$ (cf. (2.18c)) is calculated based on an implicit time-integration method reported in [34]. The solution in the time interval $[0, t_{\bar{E}}]$ is computed at the discrete-time instants t_k with $k \in \{0, \ldots, \bar{E}\}$. A prediction step is used to estimate the states and their time derivatives at the next sampling point. The subsequent correction of these estimates is based on the Newton-Raphson method, which is augmented by a line search algorithm as proposed in [35]. The correction step is repeated until $||\mathbf{r}||$ is smaller than a desired tolerance, cf. [35]. Figure 2.9 shows the principle of the time-integration scheme, which is based on the one proposed in [34].

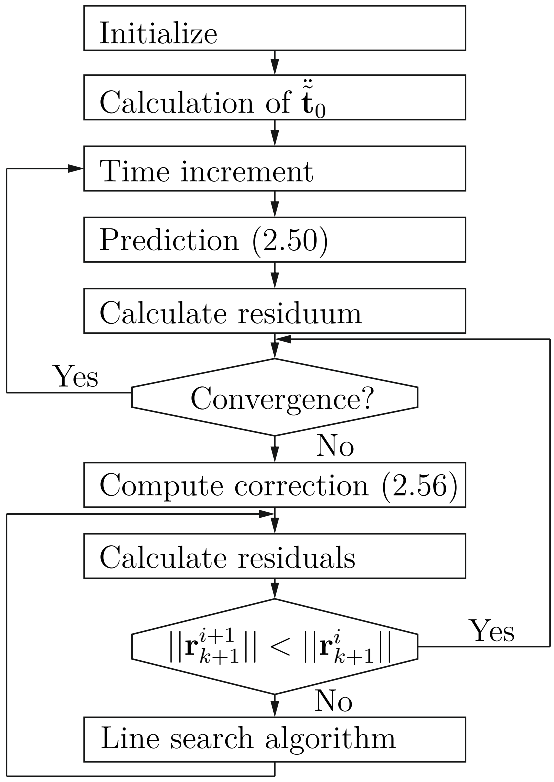

Figure 2.9: Implicit time integration method.

The first step is to initialize the procedure. For instance, the mass matrix $\tilde{\mathbf{M}}$ and parts of (2.49) are calculated. The initial conditions $\tilde{\mathbf{t}}_0$ and $\dot{\tilde{\mathbf{t}}}_0$ are determined. Using (2.48) and $\mathbf{r} = \mathbf{0}$ in a second step, the initial acceleration $\ddot{\tilde{\mathbf{t}}}_0$ can be computed. All required quantities at the time index $k = 0$ are specified. Now, the main procedure can be carried out using the time increment (step size) $T_\mathrm{s} = t_{k+1} - t_k$.

2.1.7.1 Prediction

The values $\tilde{\mathbf{t}}_k$, $\dot{\tilde{\mathbf{t}}}_k$, and $\ddot{\tilde{\mathbf{t}}}_k$ at the present time step k are known. In [34], the relations

$$\tilde{\mathbf{t}}_{k+1}^* = \tilde{\mathbf{t}}_k + T_\mathrm{s}\dot{\tilde{\mathbf{t}}}_k + \left(\frac{1}{2} - \bar{\beta}\right) T_\mathrm{s}^2 \ddot{\tilde{\mathbf{t}}}_k \tag{2.50a}$$

$$\dot{\tilde{\mathbf{t}}}_{k+1}^* = \dot{\tilde{\mathbf{t}}}_k + (1 - \bar{\gamma}) T_\mathrm{s} \ddot{\tilde{\mathbf{t}}}_k \tag{2.50b}$$

$$\ddot{\tilde{\mathbf{t}}}_{k+1}^* = \mathbf{0} \tag{2.50c}$$

are proposed to predict the values at the time step $k + 1$. Here, the superscript * refers to a predicted value. The parameters $\bar{\gamma}$ and $\bar{\beta}$ control the behavior of the numerical quadrature. For example, the choice $\bar{\gamma} = 1/2$ and $\bar{\beta} = 1/4$ yields a time-integration scheme with an acceleration average value $\ddot{\tilde{\mathbf{t}}}(t) = \frac{\ddot{\tilde{\mathbf{t}}}_k + \ddot{\tilde{\mathbf{t}}}_{k+1}}{2}$ over each time step T_s, cf. [34].

If the convergence criterion $||\mathbf{r}_{k+1}|| \leq r_\mathrm{min}$ holds for the residuum $\mathbf{r}$ according to (2.48), the time-integration procedure can proceed with the prediction for the next time index. Otherwise, the estimated values have to be corrected.

2.1.7.2 Correction

Expansion of the residuum (2.48) into a linear Taylor series (higher-order terms are neglected) yields

$$\mathbf{r}^{i+1}_{k+1} = \mathbf{r}^{i}_{k+1} + \mathbf{S}\Big(\tilde{\mathbf{t}}^{i}_{k+1}\Big)\Delta\tilde{\mathbf{t}}^{i}_{k+1}, \tag{2.51}$$

where i refers to the iteration index. The Jacobian matrix reads as

$$\mathbf{S}\Big(\tilde{\mathbf{t}}^{i}_{k+1}\Big) = \left[\frac{\partial \mathbf{r}_{k+1}}{\partial \tilde{\mathbf{t}}}\right]_{\tilde{\mathbf{t}}^{i}_{k+1}}. \tag{2.52}$$

Relations in the form

$$\frac{\partial \ddot{\tilde{\mathbf{t}}}}{\partial \tilde{\mathbf{t}}} = \frac{1}{\bar{\beta} T_\mathrm{s}^2}\mathbf{I} \quad \text{and} \quad \frac{\partial \dot{\tilde{\mathbf{t}}}}{\partial \tilde{\mathbf{t}}} = \frac{\bar{\gamma}}{\bar{\beta} T_\mathrm{s}}\mathbf{I}, \tag{2.53}$$

with the identity matrix $\mathbf{I}$, are suggested in [34]. This yields the Jacobian matrix of (2.48) in the form

$$\mathbf{S}\big(\tilde{\mathbf{t}}\big) = \tilde{\mathbf{M}}\frac{1}{\bar{\beta} T_\mathrm{s}^2} + \grave{\mathbf{D}}\frac{\bar{\gamma}}{\bar{\beta} T_\mathrm{s}} + \grave{\mathbf{K}} + \frac{\partial}{\partial \tilde{\mathbf{t}}}\Big(\grave{\mathbf{K}}^\mathrm{N}\big(\tilde{\mathbf{t}}\big)\tilde{\mathbf{t}}\Big) - \frac{\partial}{\partial \tilde{\mathbf{t}}}\Big(\grave{\mathbf{f}}\big(\tilde{\mathbf{t}}\big)\Big). \tag{2.54}$$

The derivation of the last two terms in (2.54) is explained in Appendix A. By analogy to Section 2.1.6.2, a parallel implementation can be used for the computation of the Jacobian matrix. The displacement correction is obtained from (2.51) by setting $\mathbf{r}^{i+1}_{k+1} = \mathbf{0}$

$$\Delta\tilde{\mathbf{t}}^{i}_{k+1} = -\Big[\mathbf{S}\Big(\tilde{\mathbf{t}}^{i}_{k+1}\Big)\Big]^{-1}\mathbf{r}^{i}_{k+1}. \tag{2.55}$$

The states and their time derivatives are thus corrected in the form

$$\tilde{\mathbf{t}}^{i+1}_{k+1} = \tilde{\mathbf{t}}^{i}_{k+1} + \Delta\tilde{\mathbf{t}}^{i}_{k+1} \tag{2.56a}$$

$$\dot{\tilde{\mathbf{t}}}^{i+1}_{k+1} = \dot{\tilde{\mathbf{t}}}^{i}_{k+1} + \frac{\bar{\gamma}}{\bar{\beta} T_\mathrm{s}}\Delta\tilde{\mathbf{t}}^{i}_{k+1} \tag{2.56b}$$

$$\ddot{\tilde{\mathbf{t}}}^{i+1}_{k+1} = \ddot{\tilde{\mathbf{t}}}^{i}_{k+1} + \frac{1}{\bar{\beta} T_\mathrm{s}^2}\Delta\tilde{\mathbf{t}}^{i}_{k+1}. \tag{2.56c}$$

An additional correction step is executed for $||\mathbf{r}^{i+1}_{k+1}|| < ||\mathbf{r}^{i}_{k+1}||$ and $||\mathbf{r}^{i+1}_{k+1}|| > r_\mathrm{min}$. The iteration is repeated until a desired residuum $||\mathbf{r}^{i+1}_{k+1}|| \leq r_\mathrm{min}$ is achieved.

For systems with a large number of degrees of freedom, however, a situation $||\mathbf{r}_{k+1}^{i+1}|| \geq ||\mathbf{r}_{k+1}^{i}||$ may occur. In such cases, a line search algorithm is used instead of the standard Newton-Raphson method correction, cf. [35, 82, 83]. The corrector step is then modified using a scaling factor $\bar{\alpha}$ (damped Newton step) in the form

$$\Delta\tilde{\mathbf{t}}_{k+1}^{i} = \bar{\alpha}\Big(-\Big[\mathbf{S}\big(\tilde{\mathbf{t}}_{k+1}^{i}\big)\Big]^{-1}\mathbf{r}_{k+1}^{i}\Big), \tag{2.57}$$

where $\bar{\alpha}$ results from a minimization of a quadratic polynomial. In order to determine this polynomial, an upper bound ($\bar{\alpha}_{\mathrm{u}}$) and a lower bound ($\bar{\alpha}_{\mathrm{l}}$) are chosen in the form

$$0 < \bar{\alpha}_{\mathrm{l}} < \bar{\alpha} < \bar{\alpha}_{\mathrm{u}} < 1. \tag{2.58}$$

The residuums for different values of $\bar{\alpha}$ and the associated norms are evaluated. Finally, suitable values for $\bar{\alpha}_{\mathrm{u}}$ and $\bar{\alpha}_{\mathrm{l}}$ have to be determined. The optimal choice $\bar{\alpha}$ is obtained by a quadratic interpolation of the form

$$\bar{\alpha} = \frac{1}{2}\frac{\bar{\xi}}{\bar{\chi}} \tag{2.59a}$$

$$\bar{\xi} = \big(\bar{\alpha}_{\mathrm{m}}^2 - \bar{\alpha}_{\mathrm{u}}^2\big)||\mathbf{r}_{\mathrm{l}}|| + \big(\bar{\alpha}_{\mathrm{u}}^2 - \bar{\alpha}_{\mathrm{l}}^2\big)||\mathbf{r}_{\mathrm{m}}|| + \big(\bar{\alpha}_{\mathrm{l}}^2 - \bar{\alpha}_{\mathrm{m}}^2\big)||\mathbf{r}_{\mathrm{u}}|| \tag{2.59b}$$

$$\bar{\chi} = (\bar{\alpha}_{\mathrm{m}} - \bar{\alpha}_{\mathrm{u}})||\mathbf{r}_{\mathrm{l}}|| + (\bar{\alpha}_{\mathrm{u}} - \bar{\alpha}_{\mathrm{l}})||\mathbf{r}_{\mathrm{m}}|| + (\bar{\alpha}_{\mathrm{l}} - \bar{\alpha}_{\mathrm{m}})||\mathbf{r}_{\mathrm{u}}||, \tag{2.59c}$$

where $||\mathbf{r}_{\mathrm{m}}||$ is computed at the position $\bar{\alpha}_{\mathrm{m}} = \frac{\bar{\alpha}_{\mathrm{u}}+\bar{\alpha}_{\mathrm{l}}}{2}$. Usually, this method yields an excellent solution for the value of $\Delta\tilde{\mathbf{t}}_{k+1}^{i}$.

2.1.8 Steady-state solution

Because the conditions in industrial hot-dip galvanizing lines vary only slowly, the equations of motion (2.46a) and (2.46b) are often simplified, i.e., steady-state conditions are assumed. Neglecting all time derivatives in (2.48), an algebraic equation is obtained in the form

$$\mathbf{r} = \Big[\grave{\mathbf{K}} + \grave{\mathbf{K}}^{\mathrm{N}}\big(\tilde{\mathbf{t}}\big)\Big]\tilde{\mathbf{t}} - \grave{\mathbf{f}}\big(\tilde{\mathbf{t}}\big). \tag{2.60}$$

Moreover, the Jacobian matrix (2.54) simplifies to

$$\mathbf{S}\big(\tilde{\mathbf{t}}\big) = \grave{\mathbf{K}} + \frac{\partial}{\partial\tilde{\mathbf{t}}}\Big(\grave{\mathbf{K}}^{\mathrm{N}}\big(\tilde{\mathbf{t}}\big)\tilde{\mathbf{t}}\Big) - \frac{\partial}{\partial\tilde{\mathbf{t}}}\Big(\grave{\mathbf{f}}\big(\tilde{\mathbf{t}}\big)\Big). \tag{2.61}$$

Finally, $\mathbf{r} = \mathbf{0}$ is solved with the Newton-Raphson method, which is augmented by the line search method, see Section 2.1.7.2. For the Newton-Raphson method, the relations $\Delta\tilde{\mathbf{t}}^{i} = -\Big[\mathbf{S}\big(\tilde{\mathbf{t}}^{i}\big)\Big]^{-1}\mathbf{r}^{i}$ and $\tilde{\mathbf{t}}^{i+1} = \tilde{\mathbf{t}}^{i} + \Delta\tilde{\mathbf{t}}^{i}$ are evaluated.

2.1.9 Normalization of parameters

To ensure a benign numerical behavior, it is useful to normalize all parameters and Galerkin coefficients of the system before solving. The following dimensionless parameters are used throughout the numerical simulations, cf. [31, 84]:

$$
\begin{aligned}
&\acute{u} = \frac{u}{L},\ \acute{v} = \frac{v}{L},\ \acute{w} = \frac{w}{L},\ \acute{x} = \frac{x}{L},\ \acute{y} = \frac{y}{L},\ \acute{b} = \frac{b}{L},\ \acute{h} = \frac{h}{L}\\
&\acute{t} = \frac{t}{L}\sqrt{\frac{N_{xx,\mathrm{L}}/h}{\rho}},\ \acute{V} = V\sqrt{\frac{\rho}{N_{xx,\mathrm{L}}/h}},\ \acute{E} = \frac{E}{N_{xx,\mathrm{L}}/h},\ \acute{q} = \frac{q}{N_{xx,\mathrm{L}}/h}\\
&\acute{N}_{xx} = \frac{N_{xx}}{N_{xx,\mathrm{L}}},\ \acute{N}_{yy} = \frac{N_{yy}}{N_{xx,\mathrm{L}}},\ \acute{N}_{xy} = \frac{N_{xy}}{N_{xx,\mathrm{L}}}
\end{aligned}
\tag{2.62}
$$

2.1.10 Conclusions

A dynamic mathematical model of an axially moving steel strip in an industrial hot-dip galvanizing lines was derived. The model captures the forces of different electromagnetic actuators as well as the transverse loads due to the impinging air jets of the cooling elements in the tower. The main findings are as follows:

- The model is based on the Kirchhoff-Love plate theory and a linear elastic material model. The Galerkin weighted residual method was used for spatial discretization.

- A FEM analysis was used to study the force of an electromagnetic actuator depending on the coil current and the pole-shoe-to-strip distance.

- An experimental flow simulator was designed to analyze the transverse loads due to the impinging air jets of a cooling element.

- External viscous damping and internal Kelvin-Voigt damping can be considered.

- The model can take into account different boundary conditions at the pot and tower rolls, geometrical nonlinearities, residual membrane strains in the strip, and residual curvatures of the strip.

- The accuracy of the model is influenced by the numbers n and m of finite elements in longitudinal and lateral direction of the strip, respectively. Similarly, the numbers of basis functions n_{yu}, n_{yv} for the in-plane problem and n_{yw} for the out-of-plane problem can be used to adjust the precision of the model.

- A tailored time-integration method was presented for dynamic simulations.

2.2 Beam model of the strip in the zinc pot

The elasto-plastic deformation of the strip in the tension leveler submerged in the zinc pot has to be taken into account in the plate model from Section 2.1. In the constitutive law (2.16), this deformation is captured via four parameters: $\epsilon_{xx}^{\mathrm{r},0}$ and $\epsilon_{yy}^{\mathrm{r},0}$ describe the residual membrane strains and $\epsilon_{xx}^{\mathrm{r},1}$ and $\epsilon_{yy}^{\mathrm{r},1}$ are the residual curvatures in longitudinal and lateral direction of the strip, respectively. These parameters can be calculated with the elasto-plastic beam model of the bending line $w(x)$ in the domain $x_{\mathrm{BR}}^{\mathrm{c}} < x \leq x_{\mathrm{SR}}^{\mathrm{c}}$, cf. Fig. 1.4. Here, the superscript c refers to the contact points between the strip and the respective roll. The influence of gravity and acceleration forces on the strip are neglected. Hence, the strip is assumed to be subject to a uniform tensile force. The geometry of the tension leveler virtually prevents a crossbow in the zinc pot. In principle, the beam model could be directly coupled with the plate model from Section 2.1 at the stabilization roll. However, it is simpler to extend the domain of the beam model up to the tower roll. In this way, the beam model can be utilized as a stand-alone preprocessing tool, which generates the parameters for the plate model, i.e., the residual membrane strains and curvatures in Tab. 2.1 and also the geometrical boundary conditions at the stabilization roll in Tab. 2.2. The steady-state equation of the beam model is obtained from (2.15c) in the form (cf. [19])

$$\partial_x^2 M_{xx} + N_{xx}\partial_x^2 w + q = 0 \tag{2.63}$$

with the bending moment M_{xx} depending nonlinearly on the strip curvature $\epsilon_{xx}^1 = -\partial_x^2 w$. Boundary conditions at a-priori unknown strip-roll contact points x_ξ^{c}, $\xi \in \{\mathrm{BR}, \mathrm{CR}, \mathrm{SR}, \mathrm{TR}\}$, cf. Fig. 1.4, complement (2.63). The resultant boundary value problem is discretized by means of finite elements with Hermite polynomials of order five. The resulting algebraic problem can be solved by means of the Newton-Raphson method. A contact algorithm iteratively calculates the unknown strip-roll contact points, cf. [19]. It computes the contact points such that the strip touches the rolls tangentially.

A standard method for calculating the load-deformation relation $M_{xx}(\epsilon_{xx}^1)$ is the numerical integration of the constitutive law, i.e., the Prandtl-Reuß equations, for every material point within the considered cross section of the strip [9]. This is usually straightforward for strictly monotonous changes of ϵ_{xx}^1. In the hot-dip galvanizing line, ϵ_{xx}^1 is typically piecewise monotonous, which leads to a hysteresis in the curve $M_{xx}(\epsilon_{xx}^1)$. Based on the assumption of steady-state operating conditions, all cross sections of the strip undergo the same deformation history. Hence, the same curve $M_{xx}(\epsilon_{xx}^1)$ is applicable for all cross sections.

The plastic deformations in different upstream process steps, e.g., in the annealing furnace and at the bottom roll, influence the initial values $\epsilon_{xx}^{\mathrm{BR},1}$ and M_{xx}^{BR} at the position $x_{\mathrm{BR}}^{\mathrm{c}}$ of the bottom roll. Downstream of the zinc pot, i.e., after the stabilization roll, the deformation is usually purely elastic (the strip is simply

Parameter	Symbol	Value
Strip length	L	$56.5\,\mathrm{m}$
Strip width	b	$1.46\,\mathrm{mm}$
Strip thickness	h	$2.01\,\mathrm{mm}$
Young's modulus	E	$1.22 \cdot 10^{11}\,\mathrm{N/m^2}$
Yield stress	σ_{yld}	$1.6 \cdot 10^{8}\,\mathrm{N/m^2}$
Tensile load	$N_{xx,\mathrm{L}}$	$22.65 \cdot 10^{3}\,\mathrm{N}$
Position CR	z_{CR}	$34\,\mathrm{mm}$

Table 2.3: Parameters used for the calculation of the history of deformation.

straightened in this domain). As reported in [19], a numerical integration of the Prandtl-Reuß equations results in the curve shown in Fig. 2.10. The extremal values of this curve are simultaneously computed with the solution of (2.63). The lateral bending moment $M_{yy}(\epsilon^1_{xx})$ between the bottom and the stabilization roll depends only on the evolution of the strip curvature ϵ^1_{xx} because ϵ^1_{yy} is assumed to be zero in this domain.

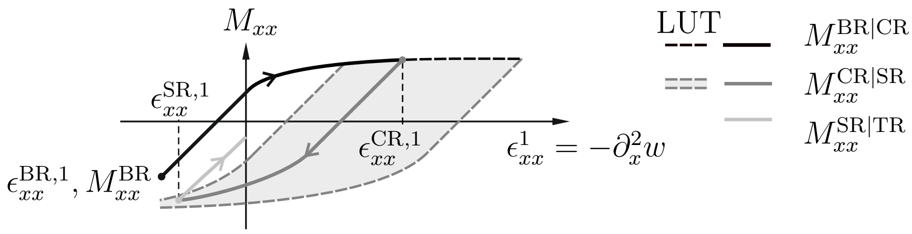

Figure 2.10: Load-deformation relation $M_{xx}(\epsilon^1_{xx})$. The relations $M_{xx}(\epsilon^1_{xx})$ and $M_{xx}(\epsilon^1_{xx}, \epsilon^{\mathrm{CR},1}_{xx})$ are numerically calculated and stored in a one- and a two-dimensional look-up table (LUT), respectively, to reduce the computational load [19].

2.2.1 Evaluation of the deformation history

The execution of the beam model yields parameters for the constitutive law (2.16) and the boundary conditions w_0 and $w_{\mathrm{x},0}$ at the stabilization roll, cf. [19]. Note that the deflection in longitudinal direction of the strip at the position $x = 0$ can be neglected ($u|_{x=0} \ll L$). The out-of-plane deformation state at the stabilization roll is defined by the longitudinal curvature $\epsilon^{\mathrm{SR},1}_{xx}$ and the bending moments M^{SR}_{xx} and M^{SR}_{yy}. The lateral curvature of the strip is zero at this point ($\epsilon^{\mathrm{SR},1}_{yy} = 0$). The in-plane (membrane) deformation state is given by the strain $\epsilon^{\mathrm{SR},0}_{xx}$ and the forces N^{SR}_{xx} and N^{SR}_{yy}.

The beam model (2.63) is executed with the parameters given in Tab. 2.3. This yields the constitutive relation $M_{xx}(\epsilon^1_{xx})$ shown in Fig. 2.11, cf. [19].

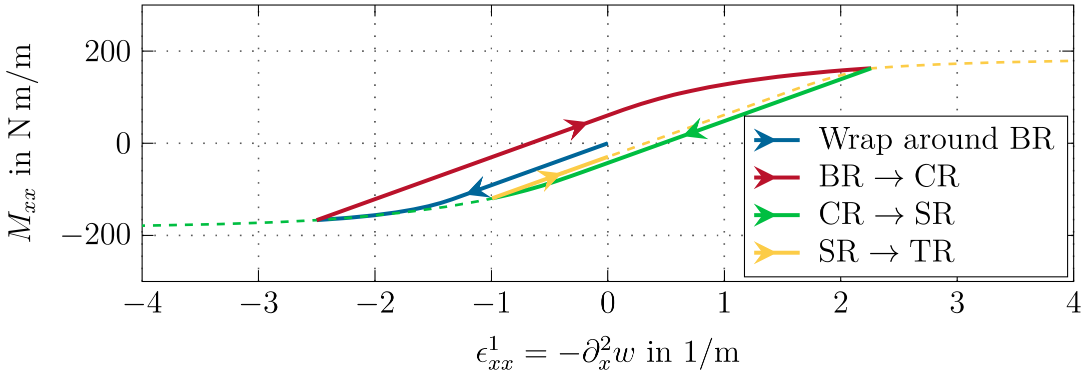

Figure 2.11: Constitutive relation describing the longitudinal bending moment M_{xx} as a function of the strip curvature ϵ^1_{xx} and its history.

Actually, the assumption of zero curvature in lateral direction does not strictly hold in the domain above the stabilization roll (SR $\rightarrow$ TR). Here, the curvature ϵ^1_{yy} in lateral direction is not forced to zero and the crossbow can freely develop. However, the bending moment M_{xx} along the curve SR $\rightarrow$ TR in Fig. 2.11 is obtained based on the assumption $\epsilon^1_{yy} = 0$. In practice, the influence of this model-plant mismatch on the deformation history at the stabilization roll is negligible [19]. Moreover, based on the elasto-plastic beam model of the bending line, the tendency of the transverse strip profile in lateral direction can be captured with sufficient accuracy, cf. [9, 11]. Because usually only elastic deformations occur above the stabilization roll, the affine material law

$$\begin{bmatrix} M_{xx} \\ M_{yy} \end{bmatrix} = D \begin{bmatrix} 1 & \nu \\ \nu & 1 \end{bmatrix} \begin{bmatrix} \epsilon^1_{xx} - \epsilon^{\mathrm{SR},1}_{xx} \\ \epsilon^1_{yy} \end{bmatrix} + \begin{bmatrix} M^{\mathrm{SR}}_{xx} \\ M^{\mathrm{SR}}_{yy} \end{bmatrix} \tag{2.64}$$

is valid. Equation (2.64) has to be equal to the steady-state material law

$$\begin{bmatrix} M_{xx} \\ M_{yy} \end{bmatrix} = D \begin{bmatrix} 1 & \nu \\ \nu & 1 \end{bmatrix} \begin{bmatrix} \epsilon^1_{xx} - \epsilon^{\mathrm{r},1}_{xx} \\ \epsilon^1_{yy} - \epsilon^{\mathrm{r},1}_{yy} \end{bmatrix}, \tag{2.65}$$

which results from (2.16b) for $\beta = 0$ and the choice $p = 0$, see Tab. 2.1. Hence, the residual strain parameters for the plate model in Tab. 2.1 can be calculated as follows: The relation

$$\begin{bmatrix} \epsilon^{\mathrm{r},1}_{xx} \\ \epsilon^{\mathrm{r},1}_{yy} \end{bmatrix} = \begin{bmatrix} \epsilon^{\mathrm{SR},1}_{xx} \\ 0 \end{bmatrix} - \frac{1}{D} \begin{bmatrix} \frac{-1}{\nu^2-1} & \frac{\nu}{\nu^2-1} \\ \frac{\nu}{\nu^2-1} & \frac{-1}{\nu^2-1} \end{bmatrix} \begin{bmatrix} M^{\mathrm{SR}}_{xx} \\ M^{\mathrm{SR}}_{yy} \end{bmatrix} \tag{2.66}$$

is used to evaluate the residual curvatures of the strip for the out-of-plane problem. By analogy, the relation

$$\begin{bmatrix} \epsilon^{\mathrm{r},0}_{xx} \\ \epsilon^{\mathrm{r},0}_{yy} \end{bmatrix} = \begin{bmatrix} \epsilon^{\mathrm{SR},0}_{xx} \\ 0 \end{bmatrix} - \frac{1}{A} \begin{bmatrix} \frac{-1}{\nu^2-1} & \frac{\nu}{\nu^2-1} \\ \frac{\nu}{\nu^2-1} & \frac{-1}{\nu^2-1} \end{bmatrix} \begin{bmatrix} N^{\mathrm{SR}}_{xx} \\ N^{\mathrm{SR}}_{yy} \end{bmatrix} \tag{2.67}$$

is employed to compute the residual membrane strains in the strip for the in-plane problem, cf. [19].

Fig. 2.12 shows the simulation results from both models for the parameters given in Tab. 2.3. Using the beam model to calculate the bending line $w(x)$, the strip experiences elasto-plastic deformation before it touches the correction and stabilization roll (sections shown in red). Crosses highlight the contact points. Purely elastic deformations occur in the sections shown in blue. In the domain downstream of the stabilization roll, the bending line of the beam model is in line with the lateral mean displacement of the plate model from Section 2.1. Due to the deformation history, a crossbow is predicted by the plate model, which yields a minimum (boundary) and maximum (centerline) deflection of the strip.

The incoming strip wraps around the bottom roll so that the curvature of the strip equals the curvature of the bottom roll. Afterwards, the strip curvature ϵ^1_{xx} undergoes rapid changes in the vicinity of the correction and the stabilization roll. The corresponding bending moment M_{xx} is influenced by the saturation characteristic shown in Fig. 2.11. For both models, the resulting curvatures and the bending moments agree well above the stabilization roll.

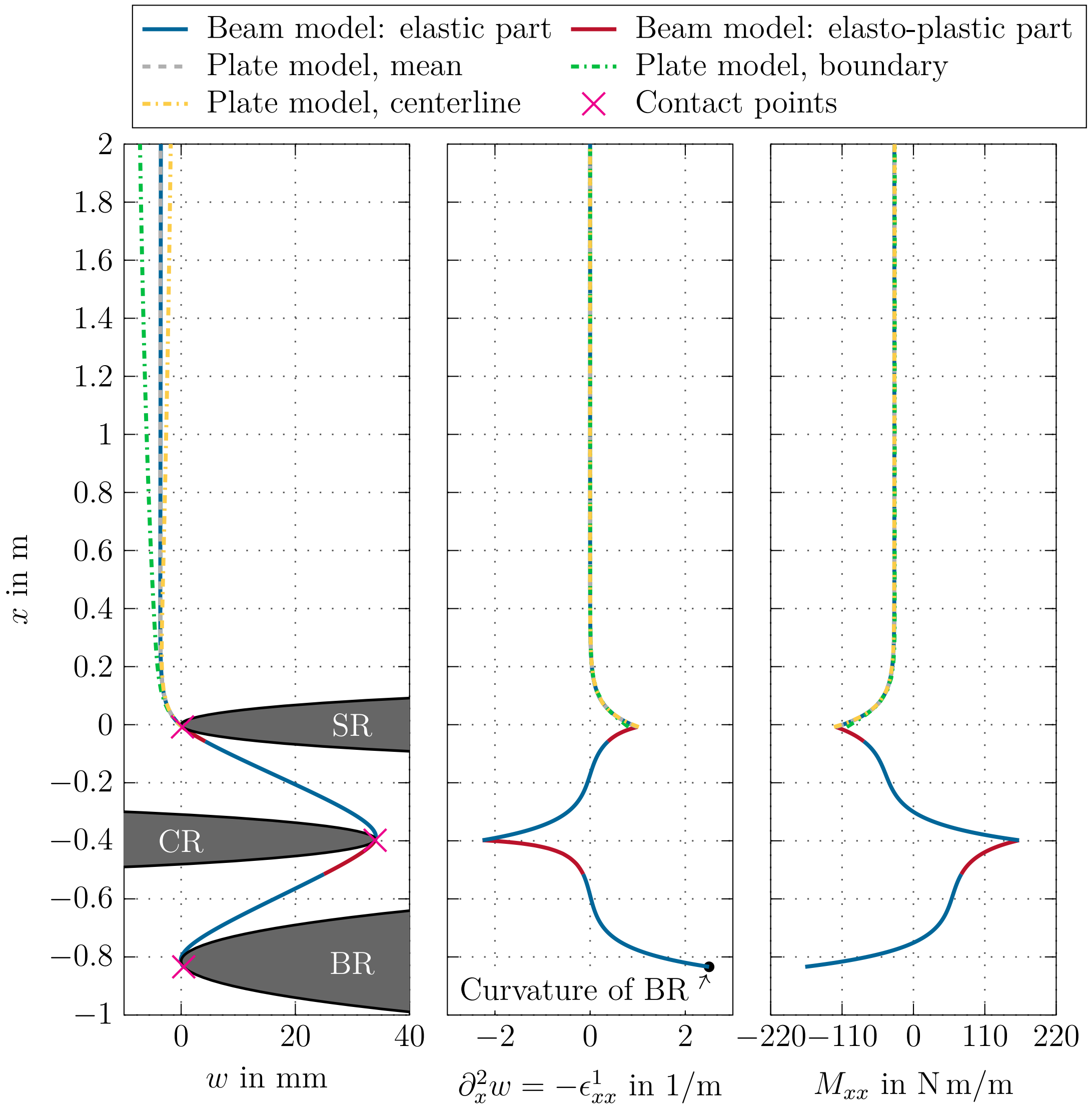

Figure 2.12: Simulation results from the beam model compared to the plate model. The plate model utilizes the residual strains, residual curvatures, and the boundary conditions which are obtained from the beam model.

2.2.2 Maximum crossbow downstream of the zinc pot

The elasto-plastic beam model can also be used to calculate the maximum crossbow that appears between the stabilization roll and the tower roll. Because of the straightening effect as a consequence of the tensile load $N_{xx,\mathrm{L}}$, it is assumed that $\epsilon_{xx}^1 = 0$ holds. In an adequate distance downstream of the stabilization roll ($x_{\mathrm{SR}}^{\mathrm{c}} \ll x \ll x_{\mathrm{TR}}^{\mathrm{c}}$), the bending moment M_{yy} vanishes, i.e., $M_{yy} = 0$ because the strip boundaries are free and there are no supporting rolls. Applying these assumptions to (2.64) yields

$$\epsilon^1_{yy,\max} = \nu\epsilon^{\mathrm{SR},1}_{xx} - \frac{M^{\mathrm{SR}}_{yy}}{D}, \tag{2.68}$$

which is integrated twice from $y = 0$ to $y = b/2$ to obtain the maximum crossbow deflection

$$w_{\max} = -\epsilon^1_{yy,\max}\frac{b^2}{8}. \tag{2.69}$$

Using (2.68) and (2.69) for the considered scenario results in the residual curvature $\epsilon^1_{yy,\max} = -0.028/\mathrm{m}$ and the maximum crossbow deflection $w_{\max} = -7.51\,\mathrm{mm}$, respectively.

Figure 2.13 shows the steady-state strip shape $w(x, y)$ calculated with the plate model from Section 2.1. For $x \ll L$, the crossbow rises for an increasing distance from the stabilization roll, see Fig. 2.13. A comparison of the beam model with the plate model reveals a good agreement between the calculated quantities ($\epsilon^{\mathrm{plate},1}_{yy,\max} = -0.029/\mathrm{m}$, $w^{\mathrm{plate}}_{\max} = -7.68\,\mathrm{mm}$). For this example scenario, the observed relative deviation between the plate ($w^{\mathrm{plate}}_{\max}$) and the beam model ($w_{\max}$) is less than 2.5 %.

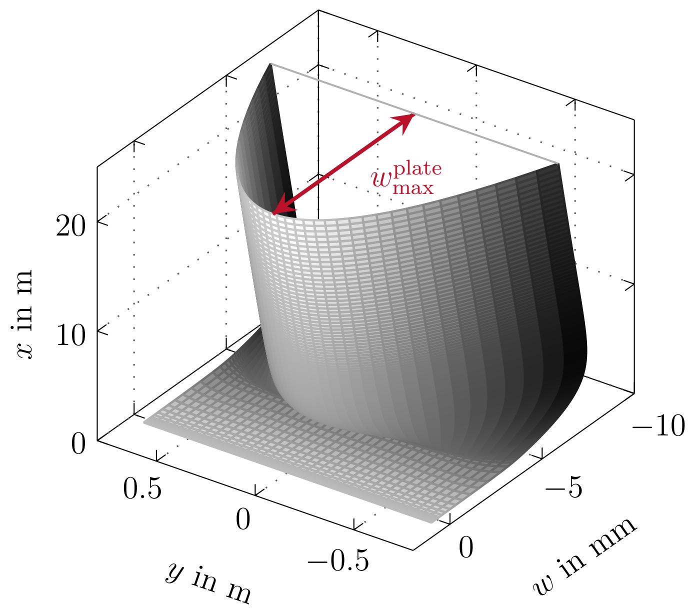

Figure 2.13: The strip exhibits a significant crossbow downstream of the stabilization roll. The results are calculated with the plate model.

2.2.3 Conclusions

The elasto-plastic beam model of the bending line in the zinc pot was developed to study the influence of the position z_{CR} of the correction roll on the deformation history of the strip above the stabilization roll. The main findings of this development are as follows:

- Depending on the position z_{CR} of the correction roll, plastic deformations of the strip may occur near the pot rolls. This influences the crossbow of the strip above the stabilization roll.
- The beam model can be used as a stand-alone preprocessing tool to calculate the elasto-plastic deformation history of the strip at the stabilization roll. The calculated deformation history is then inserted into the constitutive relation used by the plate model.
- In practice, the computationally more sophisticated plate model in Section 2.1 can be used to evaluate the transverse strip profile $w(x, y)$ at an arbitrary position x, e.g., at the gas wiping dies.
- In contrast to the beam model, the plate model can also consider the influence of transverse loads on the strip profile $w(x, y)$.

CHAPTER 3

System analysis

This chapter is significantly based on the author's publications [23, 24].

The plate model from Section 2.1 and the beam model from Section 2.2 can be used to study different aspects of the industrial hot-dip galvanizing line. In Section 3.1, the influence of the geometric nonlinearity on the transverse strip displacement is analyzed for different boundary conditions. Section 3.2 is concerned with the impact of the cooling elements on the stability of the strip motion between the stabilization and the tower roll. This industrial plant is equipped with $\iota = 4$ cooling elements shown in Fig. 2.7. The dynamic plate model is validated in Section 3.3 by experiments conducted at an industrial hot-dip galvanizing plant equipped with an electromagnetic strip stabilizer. For the analysis, a steel strip with the mass density $\rho = 7850\,\mathrm{kg/m^3}$ and the Poisson's ratio $\nu = 0.3$ is assumed. The gravitational acceleration is $g = 9.81\,\mathrm{m/s^2}$. The transverse load q_p in (2.46) is not used in the following and is therefore set to zero.

3.1 Geometrically nonlinear and linear models

Different dynamic and steady-state simulations with the plate model from Section 2.1 are carried out to study the influence of geometric nonlinearities on the transverse strip displacements. To this end, the models use the residual membrane strains and curvatures given in Tab. 2.1 and the boundary conditions I and II according to Tab. 2.2. The boundary conditions I and II involve the constant tensile load $N_{xx,\mathrm{L}}$ and the constant deflection u_L, respectively, at the tower roll. For a better comparability of the simulation results, the deflection u_L (boundary condition II) is chosen to depend on the tensile load $N_{xx,\mathrm{L}}$. In fact, the quantity u_L

Parameter	Symbol	Value
Strip length	L	$56.5\,\mathrm{m}$
Strip width	b	$1.48\,\mathrm{m}$
Strip thickness	h	$0.95\,\mathrm{mm}$
Tensile load	$N_{xx,\mathrm{L}}$	$31.1\,\mathrm{kN/m}$
Young's modulus	E	$1.58 \cdot 10^{11}\,\mathrm{N/m^2}$

Table 3.1: Nominal parameters of the test strip used for the analysis of the natural frequencies.

is assumed to be the mean value of the steady-state strip deflection in longitudinal direction, which occurs for the case of the constant tensile load $N_{xx,\mathrm{L}}$ with zero transverse loads ($q = 0$). The parameters $n = 89$, $m = 1$, $n_{\mathrm{yu}} = n_{\mathrm{yv}} = 7$, and $n_{\mathrm{yw}} = 4$ are used for the following investigations.

3.1.1 Natural oscillation frequencies of the strip

First, the influence of the initial transverse strip displacement and the boundary conditions I ($N_{xx,\mathrm{L}}$) and II (u_{L}) on the natural oscillation frequency f of the strip are analyzed in simulations. For this analysis, the displacement w_0 and the slope $w_{\mathrm{x},0}$ at the stabilization roll as well as the bulk velocity V, the damping factors α and β, and all transverse loads q are set to zero. Moreover, a test strip without any residual membrane strains and curvatures is assumed. The parameters of the test strip are given in Tab. 3.1.

Figure 3.1 shows the simulation results for different initial shapes $\tilde{w}_0$ and $\tilde{w}_1 = 0$ according to (2.18). The quantities $\tilde{w}_0$ and $\tilde{w}_1$ are found from an eigenvalue analysis of the linearized system at $w = 0$. For each node in Fig. 3.1, $\bar{w}_0$ denotes the maximum deflection of the considered initial transverse strip profile mode in longitudinal direction ($\bar{w}_0 = \max |\tilde{w}_0|$). The simulations of the nonlinear systems were executed with a time-integration procedure based on the method described in Section 2.1.7. For the prescribed tensile load $N_{xx,\mathrm{L}}$ (boundary condition I), the natural frequencies of the strip vibrations are virtually identical to the frequencies determined via the eigenvalue analysis. A specific initial shape of the strip is associated with a certain natural frequency. Moreover, for a specific initial shape, the natural frequency is independent of $\bar{w}_0$. Different characteristics are obtained for the prescribed displacement u_{L} (boundary condition II). In this case, the natural frequencies of the strip vibrations strongly depend on the initial shape of the strip, and they increase for larger initial displacements $\bar{w}_0$.

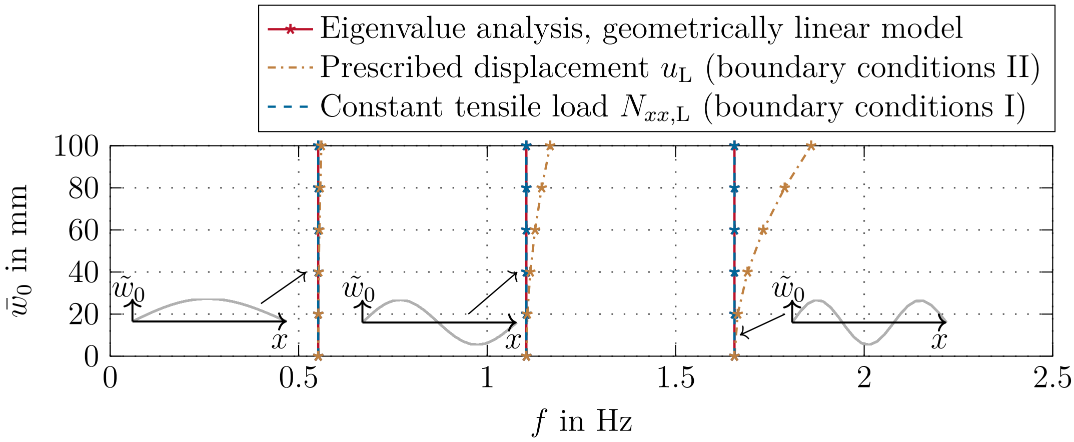

Figure 3.1: Frequency of strip vibrations for different boundary conditions and initial displacements $\bar{w}_0$.

3.1.2 Steady-state shape of the strip

In the next simulation, the influence of geometric nonlinearities on the steady-state strip shape is analyzed. The boundary conditions I and II are used, where the displacement w_0 and the slope $w_{\mathrm{x},0}$ of the strip are prescribed at the stabilization roll. The dimensions of the three test strips are given in Tab. 3.2. Moreover, the beam model from Section 2.2 is used to calculate the corresponding boundary conditions at $x = 0$, the residual membrane strains, and the residual curvatures. By means of the steady-state models, the influence of a faulty cooler on the shape of the strip is investigated. The considered scenario is depicted in Fig. 2.7, where one half of the cooling element 3 does not supply cooling air (zero pressure load). All other cooling elements operate at the same supply pressure p_{clr}. The pressure level is varied in the simulations below. The maximum transverse displacement w_{max} of the geometrically nonlinear strip model and the maximum error $e_{\mathrm{max}} = \max |w_{\mathrm{N}} - w_{\mathrm{L}}|$ between the geometrically nonlinear (subscript N) and linear (subscript L) strip models are shown in Fig. 3.2a for a prescribed tensile load $N_{xx,\mathrm{L}}$ (boundary condition I). Corresponding results for a prescribed displacement u_{L} (boundary condition II) can be seen in Fig. 3.2b. As a consequence of the elasto-plastic deformation history of the strip, a small error exists even for $p_{\mathrm{clr}} = 0$. A higher pressure level p_{clr} leads to a higher transverse strip displacement w and a larger error for both simulations. However, the error is about 10 times larger in case of the prescribed displacement u_{L} boundary condition. The steady-state shape of test strip A calculated with the geometrically nonlinear model for $p_{\mathrm{clr}} = 25\,\mathrm{mbar}$ and $N_{xx,\mathrm{L}} = 24.2\,\mathrm{kN/m}$ is shown in Fig. 3.3.

Parameter	Symbol	Value		
Strip length	L		56.5 m	
Strip velocity	V		1.75 m/s	
		Strip A	Strip B	Strip C
Strip width	b	1.34 m	1.66 m	1.48 m
Strip thickness	h	0.5 mm	1.5 mm	0.95 mm
Strip displ.	w_0	0.074 mm	0.063 mm	0.22 mm
Slope of strip	$w_{\mathrm{x},0}$	-0.034 m/m	-0.032 m/m	-0.06 m/m
Tensile load	$N_{xx,\mathrm{L}}$	24.2 kN/m	27.7 kN/m	31.1 kN/m
Young's mod.	E	$1.6 \cdot 10^{11}\,\mathrm{N/m^2}$	$1.56 \cdot 10^{11}\,\mathrm{N/m^2}$	$1.58 \cdot 10^{11}\,\mathrm{N/m^2}$
Residual strain	$\epsilon_{xx}^{\mathrm{r},0}$	$0.5402 \cdot 10^{-3}$	$0.0611 \cdot 10^{-3}$	$0.3592 \cdot 10^{-3}$
Residual strain	$\epsilon_{yy}^{\mathrm{r},0}$	$-0.0629 \cdot 10^{-3}$	$-0.0081 \cdot 10^{-3}$	$-0.0274 \cdot 10^{-3}$
Residual curv.	$\epsilon_{xx}^{\mathrm{r},1}$	-0.3856 1/m	-0.1752 1/m	-0.4110 1/m
Residual curv.	$\epsilon_{yy}^{\mathrm{r},1}$	0.2415 1/m	-0.0118 1/m	0.2629 1/m

Table 3.2: Nominal and calculated parameters for three test strips used to conduct a steady-state analysis.

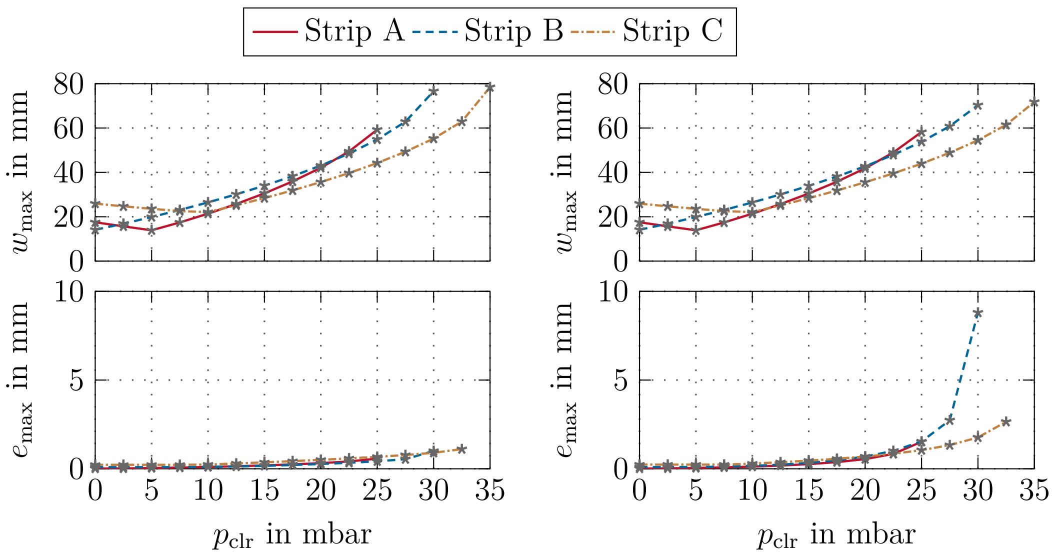

(a) Scenario with a prescribed tensile load $N_{xx,\mathrm{L}}$ boundary condition.

(b) Scenario with a prescribed displacement u_{L} boundary condition.

Figure 3.2: Simulation study for different boundary conditions used to calculate the maximum displacement $w_{\max}$ based on the geometrically nonlinear model and the corresponding deviation $e_{\max}$ from the linear model.

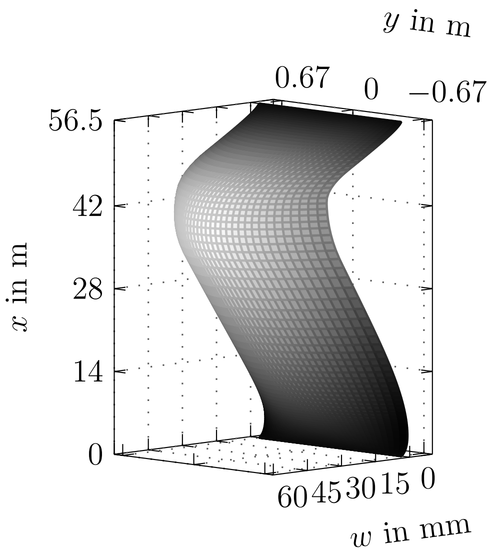

Figure 3.3: Steady-state shape of test strip A for $p_{\mathrm{clr}} = 25\,\mathrm{mbar}$ and $N_{xx,\mathrm{L}} = 24.2\,\mathrm{kN/m}$ computed with the geometrically nonlinear model.

3.1.3 Conclusions

Dynamic and steady-state simulations were conducted for different boundary conditions of the strip to analyze the impact of the geometric nonlinearity on the traverse strip displacements. The main findings from these simulations are as follows:

- Depending on the boundary condition at the tower roll, e.g., the prescribed tensile load $N_{xx,\mathrm{L}}$ or the prescribed displacement u_{L}, different deflection errors between geometrically nonlinear and linear models occur.
- A geometrically linear model with the constant tensile load $N_{xx,\mathrm{L}}$ boundary condition is sufficiently accurate for many control engineering applications.
- If larger displacements occur for a strip with the prescribed displacement u_{L} boundary condition, the geometrically nonlinear model should be used.
- There is only a minor difference in the oscillation frequencies between the geometrically nonlinear and linear model for the prescribed tensile load $N_{xx,\mathrm{L}}$ boundary condition.
- For the geometrically nonlinear model, larger values of the maximum deflection $\bar{w}_0$ result in higher vibrational frequencies for the prescribed displacement u_{L} boundary condition. The frequencies are strongly influenced by the initial transverse strip profile in longitudinal direction.

3.2 Impact of air cooling jets on strip stability

The influence of the impinging air cooling jets on the stability of the strip transport is analyzed with the dynamic model from Section 2.1 and the boundary conditions III and IV according to Tab. 2.2. Since larger transverse displacements may occur and the boundary conditions IV entail a prescribed displacement u_{L}, the geometrically nonlinear model is used, cf. Section 3.1.

The asymptotic stability of the equilibrium points is analyzed by an early-lumping approach and Lyapunov's indirect method. Using (2.46) and assuming steady-state conditions for the in-plane displacement field (the time derivatives in (2.46a) are neglected), an ordinary differential equation and an algebraic equation can be obtained in the form

$$\dot{\boldsymbol{\xi}} = \mathbf{f}_{\mathrm{s}}\left(\boldsymbol{\xi}, \breve{\mathbf{t}}\right) \quad \text{and} \quad \mathbf{0} = \mathbf{g}_{\mathrm{s}}\left(\tilde{\mathbf{t}}, \breve{\mathbf{t}}\right), \tag{3.1}$$

with the state vector $\boldsymbol{\xi}^{\mathrm{T}} = \begin{bmatrix} \tilde{\mathbf{t}} & \dot{\tilde{\mathbf{t}}} \end{bmatrix}$ and vector-valued functions $\mathbf{f}_{\mathrm{s}}$ and $\mathbf{g}_{\mathrm{s}}$. The vectors $\breve{\mathbf{t}}$ and $\tilde{\mathbf{t}}$ contain the Galerkin coefficients of the in-plane and out-of-plane system, respectively. A linearization of the nonlinear system (3.1) at the equilibrium is carried out and the eigenvalues of the linear system are calculated to analyze the local stability. The eigenvalue with the largest real part is referred to as e_{s}. If the real part of e_{s} is positive, the system (2.15) with the related boundary conditions, i.e., III or IV, is unstable.

3.2.1 Numerical results

The parameter values given in Tab. 3.3 are used for the stability analysis. Other parameters, e.g., the strip thickness h, the tensile load $N_{xx,\mathrm{L}}$, the supply pressure p_{clr} of the cooling elements, and the offset w_{off}, vary from simulation to simulation. The influence of gravity is small and therefore neglected. As a simplification, all cooling elements are kept at the same supply pressure for every simulation. Scenarios without an offset lead to solutions that are symmetric with respect to the plane $z = 0$. Hence, only the solution for one side (one sign of w) is presented in the following.

3.2.1.1 Types of equilibria

Three different scenarios occur depending on the existence of one or two equilibria in the non-negative displacement range $0 \leq w \leq L_{\mathrm{w}}/2$. For simplicity, the offset w_{off} is set to zero, cf. Fig. 2.7.

- One unstable equilibrium $w = 0$ (case I): The entire domain of the physically possible transverse strip displacements is unstable. This case can occur for low and moderate tensile loads $N_{xx,\mathrm{L}}$ (boundary conditions III and

Parameter	Symbol	Value
Strip length	L	56.5 m
Strip width	b	1.65 m
Strip velocity	V	1.75 m/s
Young's modulus	E	$1.8 \cdot 10^{11}$ N/m^2
No. of longitudinal finite elements	n	60
No. of lateral finite elements	m	1

Table 3.3: Nominal parameters of the test strips and discretization parameters used for the stability analysis.

IV). A minor deviation from $w = 0$ causes w to grow until the strip collides with the pipes of the coolers.

- One stable equilibrium $w = 0$ (case II): The entire domain of the physically possible transverse strip displacements belongs to the region of attraction of this equilibrium. A high value of $N_{xx,\mathrm{L}}$ ensures this type of equilibrium.

- Two equilibria $w = 0$ and $w \neq 0$ (case III): The inner equilibrium $w = 0$ is always stable, whereas the outer one $w \neq 0$ is always unstable. The region of attraction of the inner (stable) equilibrium contains the range from $w = 0$ to the outer (unstable) equilibrium.

Example 1: For the case III, the influence of the thickness h and the tensile load $N_{xx,\mathrm{L}}$ on the unstable equilibrium $w \neq 0$ is illustrated in Fig. 3.4a. The offset shift is set to zero ($w_{\mathrm{off}} = 0$) and the supply pressure of the cooling elements is $p_{\mathrm{clr}} = 40$ mbar. Based on (2.3), the associated fan speed of the blower is approximately $n_{\mathrm{clr}} = 1830$ 1/min.

For $N_{xx,\mathrm{L}} = 30$ kN/m, two equilibria can be calculated: The inner one $w = 0$ is stable and the outer one $w \neq 0$ is unstable. The same situation occurs for 40 kN/m. Both unstable equilibria are illustrated in Fig. 3.4a. For 30 kN/m, an estimation of the region of attraction is highlighted as green-shaded area. The cooling elements are shown as blue-shaded boxes.

For 55 kN/m, only one stable equilibrium exists at the point $w = 0$ (case II). The strip cannot become unstable for physically possible values of w.

A low tensile load of 15 kN/m results in one unstable equilibrium $w = 0$ (case I). This operating condition has to be avoided.

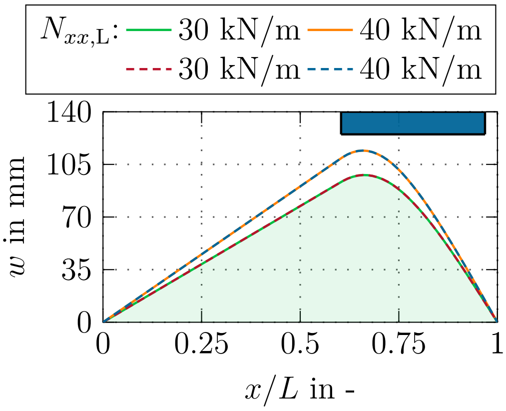

(a) Unstable equilibria for boundary condition III and different values of $N_{xx,\mathrm{L}}$ (solid line: $h = 1.5\,\mathrm{mm}$, dashed line: $h = 1\,\mathrm{mm}$).

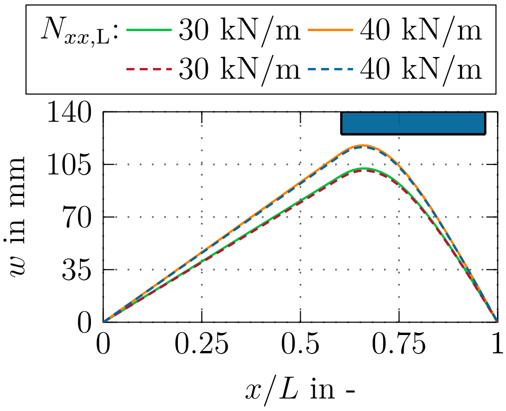

(b) Unstable equilibria for boundary condition IV and different values of $N_{xx,\mathrm{L}}$ (solid line: $h = 1.5\,\mathrm{mm}$, dashed line: $h = 1\,\mathrm{mm}$).

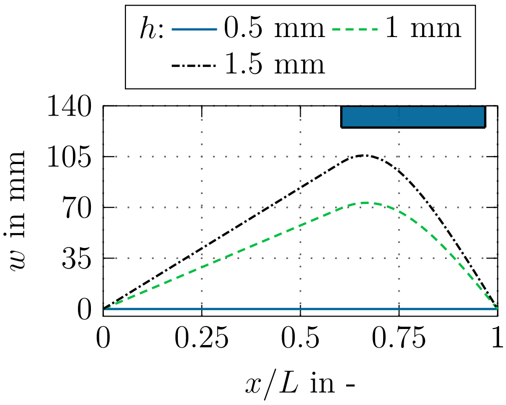

(c) Unstable equilibria for various strips preloaded by the same displacement u_{L}.

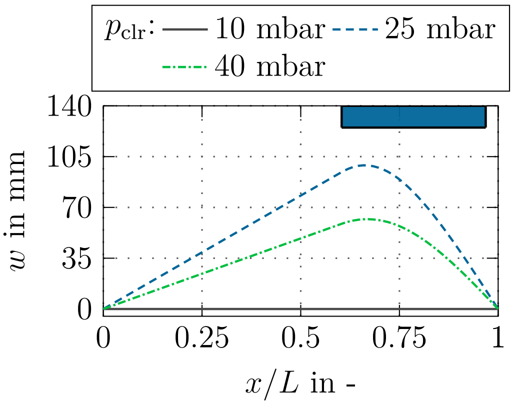

(d) Stable ($p_{\mathrm{clr}} = 10\,\mathrm{mbar}$) and unstable ($p_{\mathrm{clr}} = 25\,\mathrm{mbar}, p_{\mathrm{clr}} = 40\,\mathrm{mbar}$) equilibria for boundary condition III (constant tensile load) and various cooler loads p_{clr}.

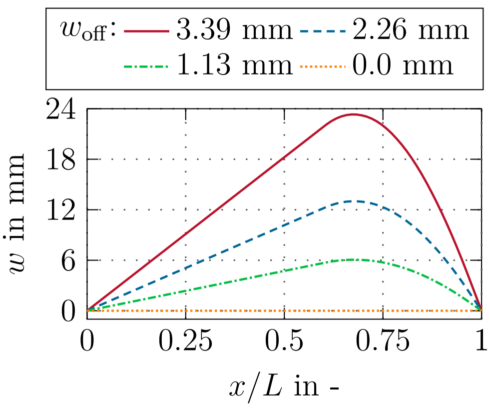

(e) Stable equilibria for boundary condition III and different offset shifts w_{off}.

Figure 3.4: Simulation study to analyze the stability of the strip motion for different configurations.

3.2.1.2 Influence of the boundary conditions

Henceforth only the equilibrium $w \neq 0$ is considered. It is investigated how the shape of the unstable equilibrium (case III) changes depending on the thickness h, the tensile load $N_{xx,\mathrm{L}}$, and the boundary conditions III or IV. Moreover, the case of using an equal boundary displacement u_L for all strips with different thicknesses is analyzed.

Example 2: For the boundary conditions III with the constant tensile load, the strip thickness h has no noticeable effect on the equilibrium. In contrast, however, the tensile load $N_{xx,\mathrm{L}}$ has a significant influence on the equilibrium as shown in Fig. 3.4a. This is because the bending moments are almost negligible as a consequence of small curvatures of the strip in longitudinal direction.

The situation turned out to be different for the boundary conditions IV. After prestressing the strip with a tensile load $N_{xx,\mathrm{L}}$, the emerging mean boundary displacement u_L depends on the strip thickness. This unique deflection value is fixed at the upper boundary, i.e., $u(L) = u_\mathrm{L}$. For an additional strip extension due to a transverse strip displacement w, a thicker strip will exhibit a higher stiffness against the transverse strip displacement w. Thus, the equilibrium of the thicker strip will appear slightly further away from the x-axis compared to the thinner strip since the destabilizing effect of the cooling elements must also be greater. Figure 3.4b shows this behavior. In Fig. 3.4c, the same reference displacement $u_\mathrm{L} = 6.7\,\mathrm{mm}$ is applied to different test strips. According to Hooke's law, this deflection ($u_\mathrm{L} = (LN_{xx,\mathrm{L}})/(Eh)$) would appear for a strip with the dimensions $h = 1\,\mathrm{mm}$ and $b = 1.65\,\mathrm{m}$ and a tensile force $N_{xx,\mathrm{L}}b = 35\,\mathrm{kN}$. The thinnest strip would collide with the cooling elements in case of a small disturbance (case I). The remaining two test strips are stable inside the region of attraction of the stable equilibrium $w = 0$ (case III). Note that the remarkable difference between Figs. 3.4b and 3.4c is only caused by the difference of the boundary condition u_L.

3.2.1.3 Influence of pressure and cooler fan speed

Example 3: The impact of the cooler pressure on the equilibrium $w \neq 0$ is analyzed using the pressure levels 10, 25, and 40 mbar. They correspond to the fan speeds 912, 1446, and 1830/min of the blower, see (2.3). Figure 3.4d shows the simulation results for a thin test strip with the thickness $h = 0.5\,\mathrm{mm}$ and the tensile load of $20\,\mathrm{kN/m}$ (boundary conditions III). For $p_\mathrm{clr} = 10\,\mathrm{mbar}$, only the equilibrium $w = 0$ occurs within the physically possible displacement range. The system (3.1) is linearized with respect to this equilibrium. This yields stability case II, where the entire physically possible displacement range belongs to the region of attraction of the equilibrium. For $p_\mathrm{clr} = 25\,\mathrm{mbar}$ and $p_\mathrm{clr} = 40\,\mathrm{mbar}$, the case III applies. The outer unstable equilibria are shown in Fig. 3.4d.

3.2.1.4 Influence of an offset of the strip pass line

Example 4: An offset w_{off} of the strip pass line can be caused by a misalignment between the ideal pass line of the strip and the cooling elements, see Fig. 2.7. Figure 3.4e shows the influence on the stable equilibrium shape (case III) for a test strip with the thickness $h = 1\,\text{mm}$ and the constant tensile load $35\,\text{kN/m}$ (boundary conditions III). The supply pressure of the cooler is set to $25\,\text{mbar}$.

A misalignment between the strip and all cooling elements causes a noticeable shift of the stable equilibrium in transverse direction. A positive offset yields a drift in positive direction and vice versa. This follows directly from the destabilising effect of the cooling elements. The outer equilibria are also affected by an offset of the strip pass line. For $w \geq 0$, a positive offset w_{off} moves the unstable equilibrium more inwards. Hence, the region of attraction shrinks. In contrast, the unstable equilibrium for $w \leq 0$ is moved outward. The unstable equilibria for the different values of w_{off} are not shown in Fig. 3.4e.

3.2.2 Conclusions

The main findings of the stability analysis are summarized in the following:

- Depending on the single plant parameters, e.g., the supply pressure level p_{clr} and the tensile load $N_{xx,\text{L}}$, three different types of equilibria may occur.

- The inner equilibrium has to be stable to ensure a proper strip processing. Otherwise, the strip will collide with the cooling elements. Increasing the tensile load $N_{xx,\text{L}}$ is the easiest way to keep the equilibrium stable.

- For a constant tensile load (boundary conditions III), the strip thickness h has virtually no influence on the equilibrium. This is not the case for a preloaded and fixed strip (boundary conditions IV).

- A misalignment between the ideal pass line of the strip and the cooling elements, i.e., a non-zero offset w_{off} of the strip pass line, can have a noticeable influence on the stability.

Most of the presented scenarios constitute extreme test cases, see, e.g., Fig. 3.4, where a relatively high cooling power was supplied by all coolers. Clearly, this also yields high transverse loads on the strip. The measurement results from the industrial plant in Fig. 1.9 are obtained in a similar way. Note that only moderate cooling power is required for normal operation and the corresponding transverse loads are significantly smaller.

3.3 Identification of damping parameters

To model the dynamic behavior of the strip, the Rayleigh-type damping parameters α and β according to (2.34) have to be determined. Moreover, the influence of the zinc pot on the transient vibration of the strip is analyzed in detail.

Remark: In the industrial plant, the tensile load $N_{xx,\mathrm{L}}$ is kept high enough to avoid stability problems of the strip transport, cf. Section 3.2. Moreover, due to the straightening effect of a high tensile load $N_{xx,\mathrm{L}}$, the stable equilibrium is located near $w = 0$. For such high tensile loads $N_{xx,\mathrm{L}}$, the out-of-plane boundary conditions, i.e., w_0 and $w_{\mathrm{x},0}$, have just a small local influence on the transverse strip shape. Actually, the effect of a non-zero slope $w_{\mathrm{x},0}$ can be practically neglected due to this straightening effect (the slope is eliminated directly above the stabilization roll). In contrast, it turned out that the in-plane boundary conditions $N_{xx,\mathrm{L}}$ and u_L can have a significant influence on the transverse strip shape. Because the controller of the tensile load $N_{xx,\mathrm{L}}$ keeps the strip tension almost constant during normal operation, the utilization of geometrically linear relations in (2.7) is justified, see Section 3.1. Also, the simpler boundary conditions III according to Tab. 2.2 can be used in the following.

To simulate the strip vibrations, the time-integration method from Section 2.1.7 is used. The damping parameters α and β and the influence of the zinc pot on the vibration of the strip are estimated using measurement data from free oscillation experiments. For this, the measured strip displacements at the electromagnets serve as the basis for the identification of the unknown parameters. The measurements of the extra displacement sensors in the cooling tower are used to validate the model. Table 3.4 contains the nominal parameters of the test strips A and B, the associated positions of the electromagnets and the tower sensors, and the parameters used for spatial discretization. Figure 3.5 shows the two setups used for the analysis. For both test strips, the residual curvatures $\boldsymbol{\varepsilon}_{yy}^{\mathrm{r},1}$ in (2.17) and the offset $\mathbf{p}$ in (1.4) are estimated based on the method proposed and validated in Section 4.2. However, in contrast to the estimator in Section 4.2 and to minimize the initial deviation between the measurement and the simulation, all displacement measurements (at the electromagnets and in the tower) were used for this estimation. The estimates $\boldsymbol{\varepsilon}_{yy}^{\mathrm{r},1}$ and $\mathbf{p}$ are then fixed for all simulations.

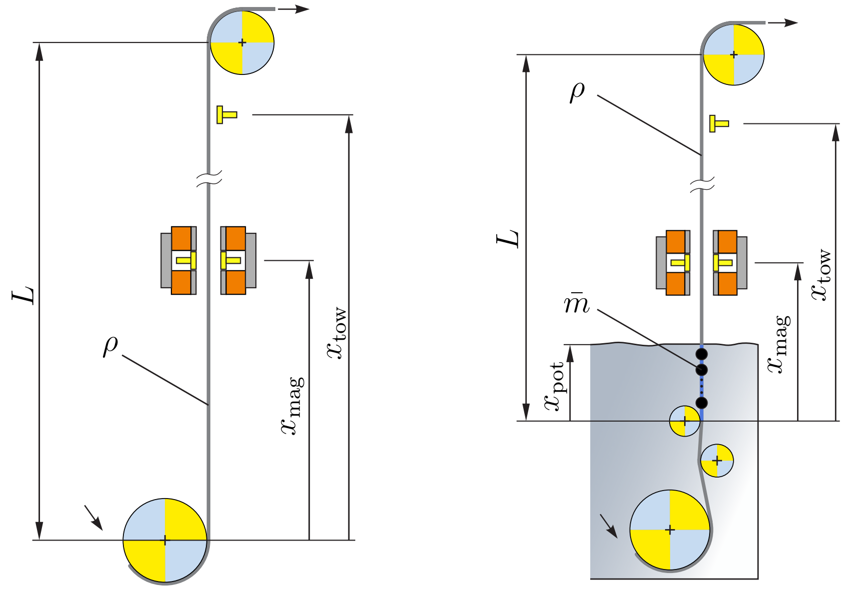

(a) Test strip A: experiment without zinc pot.

(b) Test strip B: experiment with zinc pot. The accumulated mass density for the strip in the zinc pot is indicated by the black points.

Figure 3.5: Different experimental setups to identify the damping of the strip and to evaluate the influence of the zinc pot on the strip dynamics.

3.3.1 Strip vibration without the zinc pot

The test strip A in Tab. 3.4 is used for the free oscillation experiment without the zinc pot, see Fig. 3.5a. It turned out that the free oscillation experiment is unsuitable to identify the internal Kelvin-Voigt damping, i.e., the parameter β. However, the internal Kelvin-Voigt damping is important for the considered steel strips because it is mainly responsible for the damping of the higher frequency strip vibrations. Thus, the experiment is only used to assess the viscous damping behavior of the strip, which is governed by the parameter α. Figure 3.6 shows the measured and simulated strip displacements w^l_{mag}, $l = 1, \dots, 5$ and w^l_{tow}, $l = 2, \dots, 4$ at the positions x_{mag} and x_{tow}, respectively, for a laterally uniform initial displacement $\mathbf{w}^{\text{s}}_{\text{mag}}|_{t=0} = [7, 7, 7, 7, 7]^{\text{T}}$ mm at the electromagnets. Because of the estimated non-zero offsets $\hat{w}^{\text{s}}_{\text{mean}} = 0.99\,\text{mm}$ and $\hat{\varphi}^{\text{s}} = -0.15°$ in (1.1), the initial values $\mathbf{w}_{\text{mag}}|_{t=0}$ slightly deviate from 7 mm. However, the estimated value $\hat{\varphi}^{\text{s}}$ is small and does not explain a dynamic asymmetry observed in the measurements at the electromagnets ($\mathbf{w}_{\text{mag}}$) and at the tower ($\mathbf{w}_{\text{tow}}$). To simulate a similar behavior, the tensile load $N_{xx,\text{L}}(y)$ applied to the model was assumed to depend linearly on y with the mean value $N_{xx,\text{L}}(0)$ given in Tab. 3.4. The true

	Parameter	Symbol	Value
General parameters	Young's modulus	E	$1.58 \cdot 10^{11}\,\mathrm{N/m^2}$
	Distance between the outer tower sensors (see Fig. 1.2)	L_o	$1.14\,\mathrm{m}$
	Distance between the inner tower sensors (see Fig. 1.2)	L_i	$0.57\,\mathrm{m}$
	No. of longitudinal finite elements	n	30
	No. of lateral finite elements	m	5
	No. of basis functions	n_yu	5
	No. of basis functions	n_yv	5
	No. of basis functions	n_yw	2
	Degree of polynomial (residual curv.)	p	4
Test strip A: absence of the zinc pot	Strip width	b	$1.103\,\mathrm{m}$
	Strip thickness	h	$0.81\,\mathrm{mm}$
	Tensile load	$N_{xx,\mathrm{L}}$	$25.07\,\mathrm{kN/m}$
	Strip velocity	V	$0.54\,\mathrm{m/s}$
	Pos. of tower sensors	x_tow	$0.663L$
	No. of tower sensors	μ	3
	Pos. of magnets	x_mag	$0.053L$
	No. of actuators	κ	5
Test strip B: presence of the zinc pot	Strip width	b	$1.340\,\mathrm{m}$
	Strip thickness	h	$0.56\,\mathrm{mm}$
	Tensile load	$N_{xx,\mathrm{L}}$	$17.23\,\mathrm{kN/m}$
	Strip velocity	V	$1.65\,\mathrm{m/s}$
	Pos. of tower sensors	x_tow	$0.657L$
	No. of tower sensors	μ	5
	Pos. of magnets	x_mag	$0.033L$
	No. of actuators	κ	6
	Pot level	x_pot	$0.0071L$

Table 3.4: Nominal strip parameters of the free oscillation experiments with a uniform initial displacement $w^{\mathrm{s},l}_{\mathrm{mag}} = 7\,\mathrm{mm}$, $l = 1, \ldots, \kappa$ and parameters used for spatial discretization.

lateral profile of the tensile load $N_{xx,\mathrm{L}}$ cannot be measured in the considered plant. However, an asymmetry of $N_{xx,\mathrm{L}}$ is often observed in other plants, where the reaction forces can be measured in both bearings of the tower roll. The considered asymmetric tensile load $N_{xx,\mathrm{L}}(y)$ improves but does not completely explain the asymmetric measurements.

After releasing the strip at $t = 0$, see Fig. 3.6a, a first wave front starts at $x = x_{\mathrm{mag}}$ and travels upwards to the tower roll. Note that a second wave front travels downwards to the roll at $x = 0$. However, since the electromagnets are positioned in the vicinity of this roll, only one wave front can develop. The wave passes the tower sensors at x_{tow} at about $t = 0.55\,\mathrm{s}$, see Fig. 3.6b. At approximately $t = 1\,\mathrm{s}$, the wave that was reflected at the tower roll returns to the sensors at x_{tow}. This wave passes the sensors at the position x_{mag} at about $t = 1.64\,\mathrm{s}$, before it is reflected at $x = 0$. The observed velocity of the wave is $61\,\mathrm{m/s}$. Because the steel strip has a very low structural damping, a superimposed vibration with small amplitude appears in the measurements shown in Fig. 3.6. Such vibrations arise from different unknown sources in the plant and cannot be captured by the model. For the conducted experiment, the simulations and measurements are in good agreement in the domain $y < 0$ of the strip. In the domain $y > 0$, the measurement reveals a slightly reduced wave velocity compared to the simulation. The magnitude of the wave decays over time. The overall damping behavior at the electromagnets and at the tower sensors can be sufficiently captured with the dynamic model (2.46) using the damping parameters $\alpha = 0.25\,1/\mathrm{s}$ and $\beta = 0.01\,\mathrm{s}$.

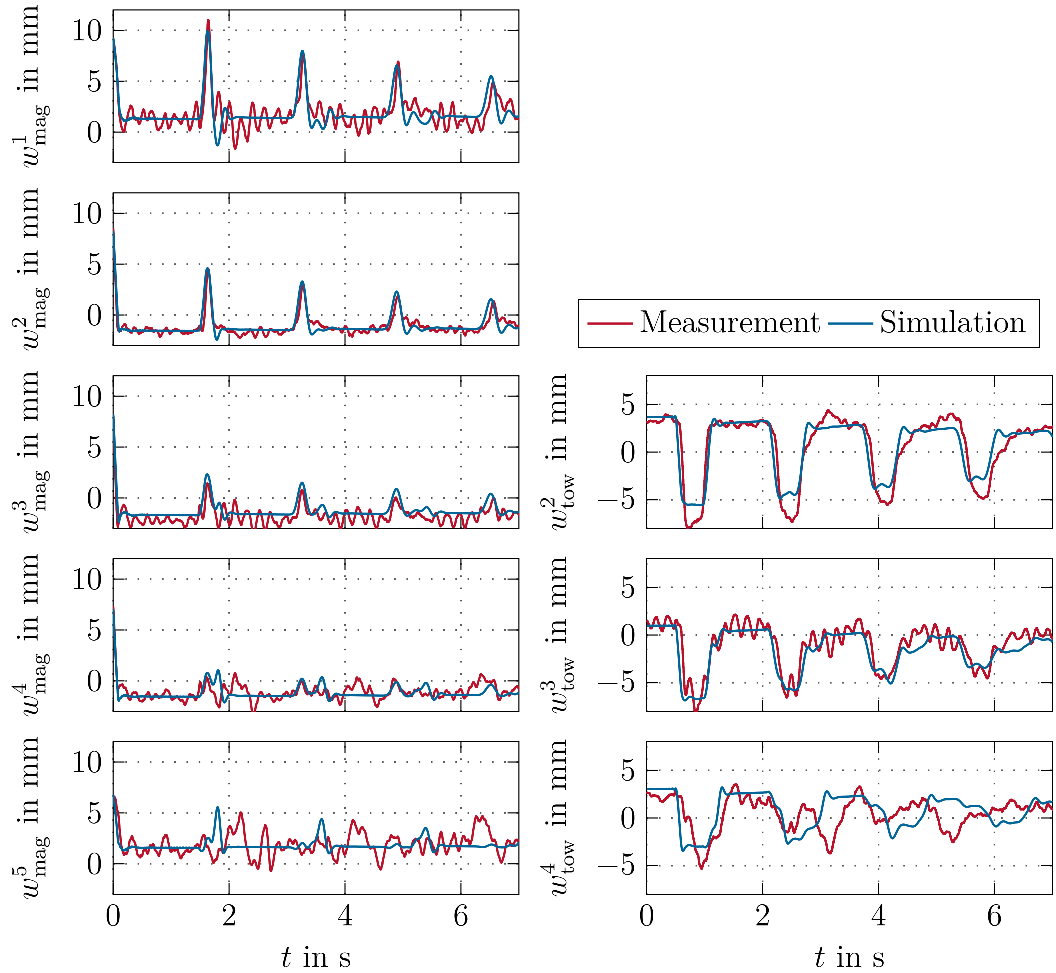

(a) Strip displacements w^l_{mag}, $l = 1, \ldots, 5$ at the electromagnets.

(b) Strip displacements w^l_{tow}, $l = 2, \ldots, 4$ at the tower sensors.

Figure 3.6: Strip displacements for a laterally uniform initial displacement $\mathbf{w}^{\mathrm{s}}_{\mathrm{mag}}|_{t=0} = [7, 7, 7, 7, 7]^{\mathrm{T}}$ mm in the setup without the zinc pot.

Figure 3.7 shows the measured and simulated strip displacements $\mathbf{w}_{\mathrm{mag}}$ and $\mathbf{w}_{\mathrm{tow}}$ for the case of a laterally non-uniform initial displacement $\mathbf{w}^{\mathrm{s}}_{\mathrm{mag}}|_{t=0} = [7, 3.5, 0, -3.5, -7]^{\mathrm{T}}$ mm at the electromagnets. Again, applying the dynamic model (2.46) with the asymmetric tensile load $N_{xx,\mathrm{L}}(y)$ yields fairly good results. Simulations and measurements are in good accordance in the domain $y < 0$ of the strip. Again, the wave velocity observed in the measurement is lower in the domain $y > 0$.

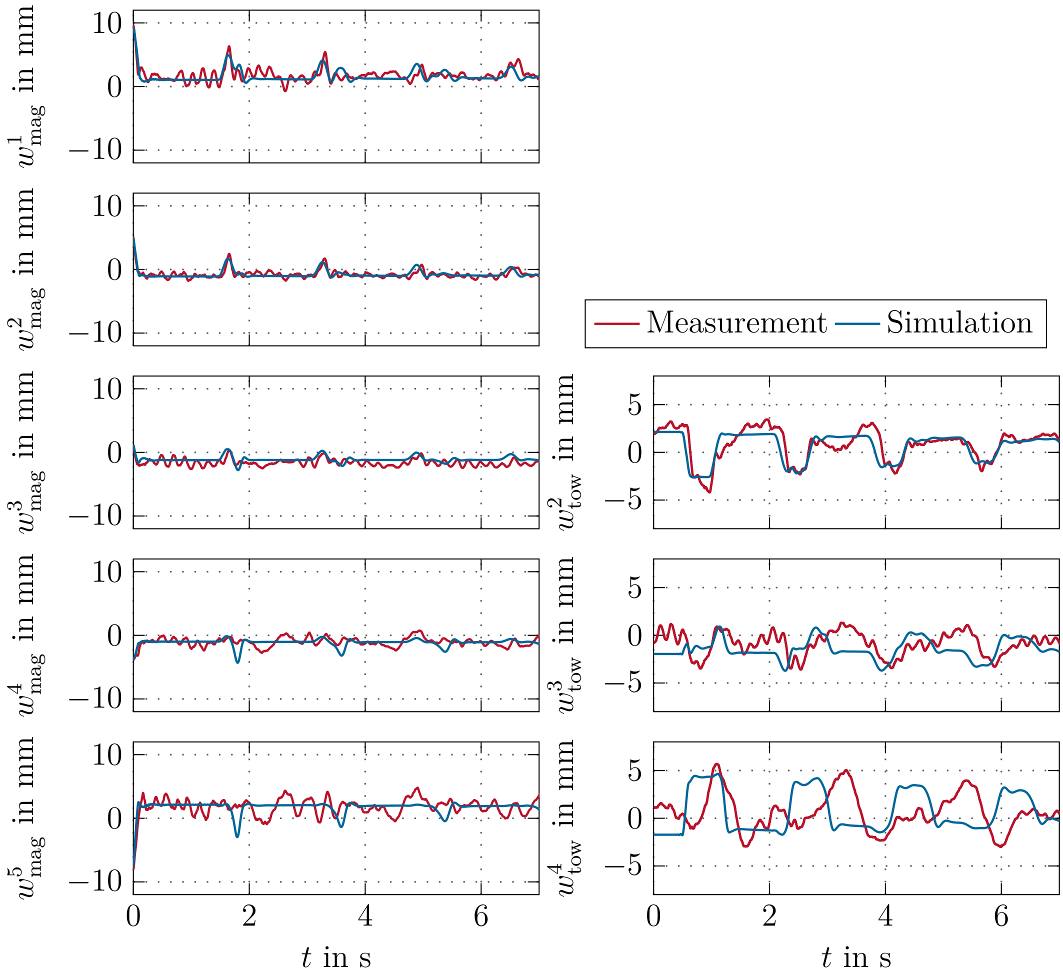

(a) Strip displacements w^l_{mag}, $l = 1, \dots, 5$ at the electromagnets.

(b) Strip displacements w^l_{tow}, $l = 2, \dots, 4$ at the tower sensors.

Figure 3.7: Strip displacements for a laterally non-uniform initial displacement $\mathbf{w}^{\mathrm{s}}_{\mathrm{mag}}|_{t=0} = [7, 3.5, 0, -3.5, -7]^{\mathrm{T}}$ mm in the setup without the zinc pot.

3.3.2 Strip vibration with the zinc pot

Figure 3.5b outlines the plant with the zinc pot as it is used in normal production. The test strip B specified in Tab. 3.4 is used for this free oscillation experiment. In addition to the identification of the viscous damping factor α, this scenario is used to assess the influence of the zinc pot on the strip dynamics. Clearly, the zinc pot increases the effective inertia in the pot ($0 \leq x \leq x_{\mathrm{pot}}$), see Fig. 3.5b. This can be considered by the accumulated mass density $\bar{m}_{\mathrm{pot}}$ according to (2.33a). The viscous damping factor α depends, e.g., on the geometry of the strip and the amplitude of the strip vibration, and hence varies from strip to strip. To avoid the necessity to estimate separate viscous damping factors for the strip domain in and above the zinc pot, only one common damping factor is used. Therefore, a significantly increased viscous damping factor $\alpha = 1.02\,1/\mathrm{s}$ for the test strip B has to be used compared to the test strip A in order to capture a higher damping behavior of the system, e.g., due to damping effects of the liquid zinc in the pot. The accumulated mass density for the strip in the zinc pot was found to be $\bar{m}_{\mathrm{pot}} = 415\,\mathrm{kg/m^2}$. The measurements and the simulations are in good agreement in Fig. 3.8 for the laterally uniform initial displacement $\mathbf{w}^{\mathrm{s}}_{\mathrm{mag}}|_{t=0} = [7, 7, 7, 7, 7, 7]^{\mathrm{T}}$ mm and in Fig. 3.9 for the laterally non-uniform initial displacement $\mathbf{w}^{\mathrm{s}}_{\mathrm{mag}}|_{t=0} = [6, 4, 2, -2, -4, -6]^{\mathrm{T}}$ mm. In the Figs. 3.8 and 3.9, the superimposed vibration with the higher frequency is caused by the increased inertia within the zinc pot. The free vibration of the strip causes the liquid zinc to slosh back and forth, where considerable dynamic pressure loads are exerted on the strip.

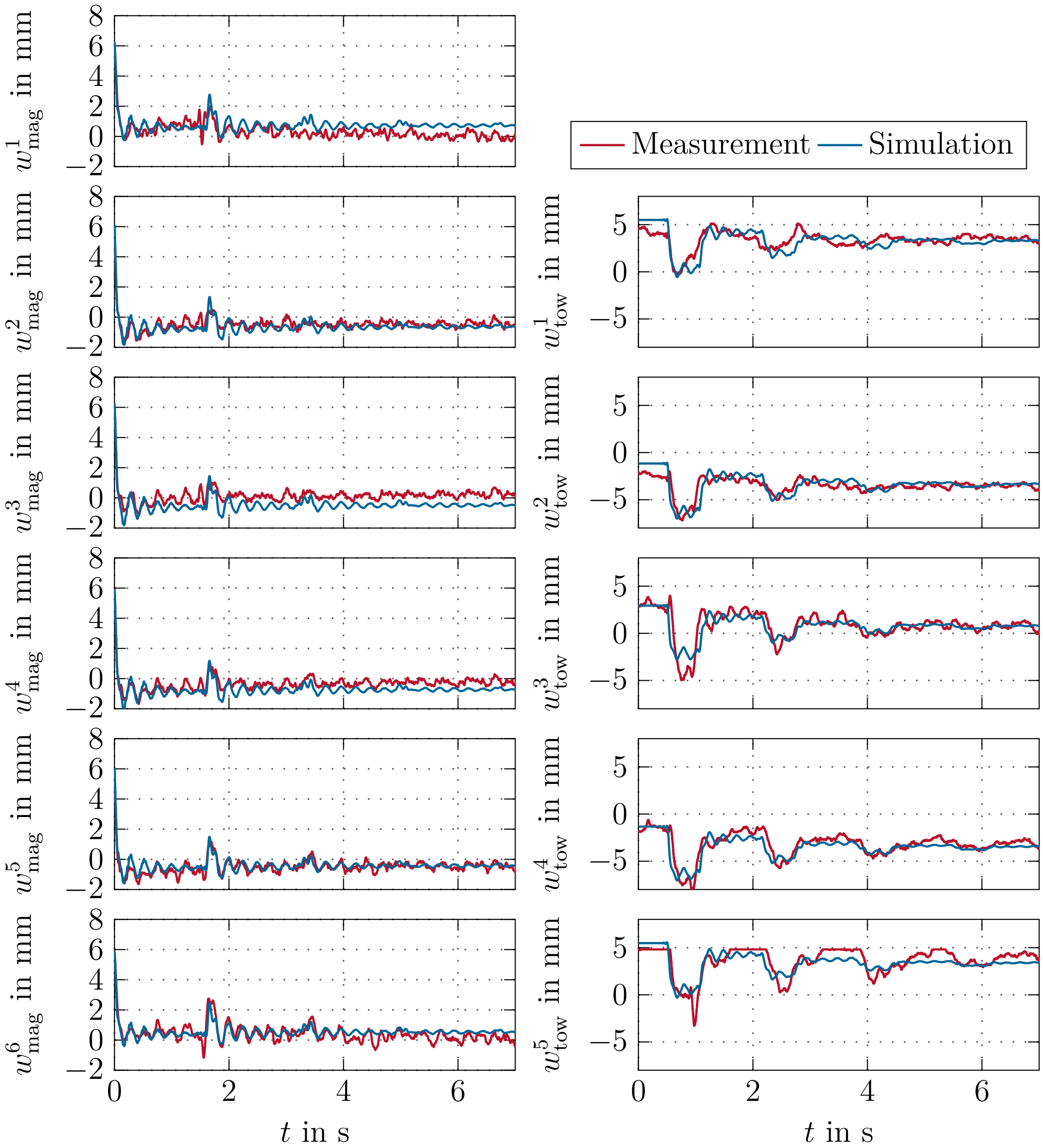

(a) Strip displacements w^l_{mag}, $l = 1, \ldots, 6$ at the electromagnets.

(b) Strip displacements w^l_{tow}, $l = 1, \ldots, 5$ at the tower sensors.

Figure 3.8: Strip displacements for a laterally uniform initial displacement $\mathbf{w}^{\mathrm{s}}_{\mathrm{mag}}|_{t=0} = [7, 7, 7, 7, 7, 7]^{\mathrm{T}}$ mm in the setup with the zinc pot.

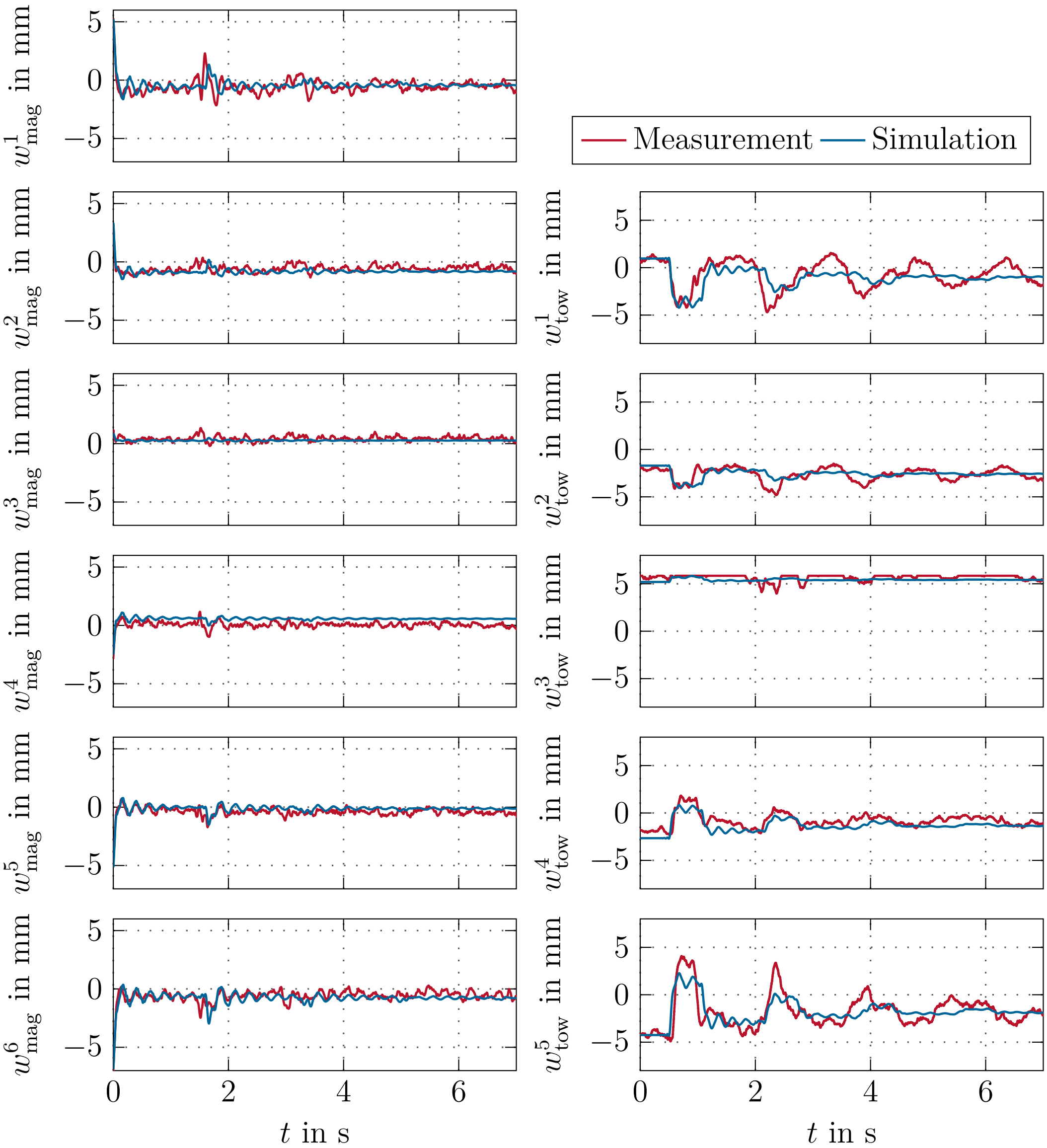

(a) Strip displacements w^l_{mag}, $l = 1, \dots, 6$ at the electromagnets.

(b) Strip displacements w^l_{tow}, $l = 1, \dots, 5$ at the tower sensors.

Figure 3.9: Strip displacements for a laterally non-uniform initial displacement $\mathbf{w}^{\mathrm{s}}_{\mathrm{mag}}|_{t=0} = [6, 4, 2, -2, -4, -6]^{\mathrm{T}}$ mm in the setup with the zinc pot.

3.3.3 Conclusions

The main findings in terms of the dynamic behavior of the strip are as follows:

- The model qualitatively captures the dynamic behavior of the steel strip in the setups with and without the zinc pot. The displacement sensors of the electromagnetic stabilizer and in the cooling tower were used to compare the simulation results with the measurements.

- In the considered scenario, the damping of strip vibrations is significantly influenced by external viscous damping. The internal Kelvin-Voigt damping cannot be identified by such an experiment.
- A small area of the strip is submerged in the zinc pot. Due to the high density of zinc, the effective inertia of the strip significantly increases in this domain. Moreover, dissipation effects of the liquid zinc lead to a higher damping of strip vibrations.

CHAPTER 4

Controller and estimator design

This chapter is significantly based on the author's publications [17, 20, 30].

4.1 Application of new model-based control concepts in the industrial plant

Figure 4.1 shows the block diagram of the proposed control concept for industrial hot-dip galvanizing lines. The plant is shown in the top of Fig. 4.1. Devices that influence the shape of the strip are described in the previous chapters. Besides the process quantities, e.g., the nominal parameters of the current production, the strip shape is mainly influenced by the residual curvature $\epsilon_{yy}^{\mathrm{r},1}(y)$, the boundary conditions w_0 and $w_{\mathrm{x},0}$, and the transverse loads $q = q_{\mathrm{pot}} + q_{\mathrm{mag}} + q_{\mathrm{clr}}$ exerted on the strip. The load q_{pot} is caused by the inertia of the zinc pot, q_{mag} is exerted by the electromagnets, and q_{clr} results from the cooling elements as a function of the fan speeds $\mathbf{n}_{\mathrm{clr}}^{\mathrm{T}} = [n_{\mathrm{clr}}^{1}, \ldots, n_{\mathrm{clr}}^{\iota}]$ of the respective blowers. Because of a sufficiently large tensile load $N_{xx,\mathrm{L}}$ in normal operating situations, the influence of the cooling elements on the strip shape as well as the influence of the boundary conditions w_0 and $w_{\mathrm{x},0}$ are assumed to be negligible. The tension leveler in the zinc pot is used to adjust the residual curvature $\epsilon_{yy}^{\mathrm{r},1}(y)$ of the strip via the position z_{CR} of the correction roll. Typically, the position z_{CR} is manually tuned by an operator. The horizontal position $\mathbf{z}_{\mathrm{mag}}$ of the electromagnetic strip stabilizer is usually automatically adapted, e.g., to minimize the coil currents. The lateral positions $\mathbf{y}_{\mathrm{mag}}$ of the single actuators are also automatically adapted, i.e., the electromagnets are equidistantly aligned in lateral direction of the strip.

In the bottom of Fig. 4.1, the block diagram of the developed control concept is shown. The sampling time of the individual blocks is indicated by their color, i.e., orange blocks are executed slowly, blue blocks fast, and red blocks very fast. Usually, a zinc coating controller is used to directly optimize the coating thickness (orange block). The pressure p_{gwd} in the supply duct of the gas wiping dies, the nozzle-to-nozzle distance Δz_{gwd}, and the horizontal position $\mathbf{z}_{\mathrm{gwd}}$ of the gas wiping dies are controlled by the zinc coating controller. This controller is tuned to respond slowly because of the significant transport delay between the gas wiping dies and the radiometric gauges that measure the zinc coating thickness. The quantities $\mathbf{h}_{\mathrm{Zn}}^{\mathrm{T}} = \left[h_{\mathrm{Zn}}^{\mathrm{t}}, h_{\mathrm{Zn}}^{\mathrm{b}}\right]$ denote the zinc coating thicknesses and $\left(\mathbf{h}_{\mathrm{Zn}}^{\mathrm{td}}\right)^{\mathrm{T}} = \left[h_{\mathrm{Zn}}^{\mathrm{t,td}}, h_{\mathrm{Zn}}^{\mathrm{b,td}}\right]$ represent the corresponding time-delayed measurements.

The state-of-the-art control approach to indirectly optimize the zinc coating thickness (without using the measured zinc coating thicknesses) is to realize an approximately flat transverse strip profile at the electromagnets. This also improves the transverse strip profile at the gas wiping dies. The set-point values for the position controllers are zero ($\tilde{\mathbf{w}}_{\mathrm{mag}}^{\mathrm{s,des}} = \mathbf{0}$). In contrast, the objective of this work is to control the transverse strip profile directly at the gas wiping dies. Based on a validated mathematical model of the strip shape, a model-based control concept will be developed, which includes multiple cascaded control loops. The electromagnetic forces $\hat{\mathbf{f}}_{\mathrm{mag}}$ are estimated based on measurements (air gaps $\boldsymbol{\delta} = \left[\boldsymbol{\delta}^{\mathrm{t}}, \boldsymbol{\delta}^{\mathrm{b}}\right]$ and coil currents $\mathbf{i}_{\mathrm{c}} = \left[\mathbf{i}_{\mathrm{c}}^{\mathrm{t}}, \mathbf{i}_{\mathrm{c}}^{\mathrm{b}}\right]$) for a given BH-curve of the strip material, see Section 2.1.1. Consequently, the estimated forces are also related to the estimated transverse loads according to (2.2).

An optimal compensation method is developed that consists of the estimator of the residual curvature presented in Section 4.2 and the optimal feedforward controller described in Section 4.3 (blocks shown in blue). The former estimates the initial curvature $\hat{\boldsymbol{\varepsilon}}_{yy}^{\mathrm{r},1}$ of the strip and the offset $\hat{\mathbf{p}}$ according to (1.1). The feedforward controller uses these estimates and calculates the set-point values $\tilde{\mathbf{w}}_{\mathrm{mag}}^{\mathrm{s,des}}$ for a subordinate position controller in order to attain the desired strip profile $\mathbf{w}_{\mathrm{gwd}}^{\mathrm{g,des}}$ at the gas wiping dies. The position controller calculates the desired currents for the individual subordinate and very fast current controllers. In practice, standard control laws are used for this purpose. In this way, the optimal compensation method can quickly respond to process variations and disturbances because it does not depend on the time-delayed measurements $\mathbf{h}_{\mathrm{Zn}}^{\mathrm{td}}$ of the zinc coating thickness. As an alternative to the original subordinate position controller of the electromagnetic stabilizer, the desired set-point values can also be used as reference signals for a position controller, which calculates a (discrete-time) reference electromagnetic force $\mathbf{f}_{\mathrm{mag},k}^{\mathrm{des}}$.

Moreover, in the case of a persistently exciting disturbance, e.g., due to an eccentric zinc-pot roll, an additional model-based disturbance rejection controller can be employed. Its objective is to eliminate the influence of the disturbance on the transverse strip position at the gas wiping dies. The force, which is required for the compensation of such a narrow-band vibration, can be added to the control force of the position controller because of the linear character of the system.

The resulting forces $\mathbf{f}_{\mathrm{mag}}^{\mathrm{des}}$ is realized by the subordinate current controllers. The desired coil currents are calculated by means of the inverse electromagnetic force characteristics.

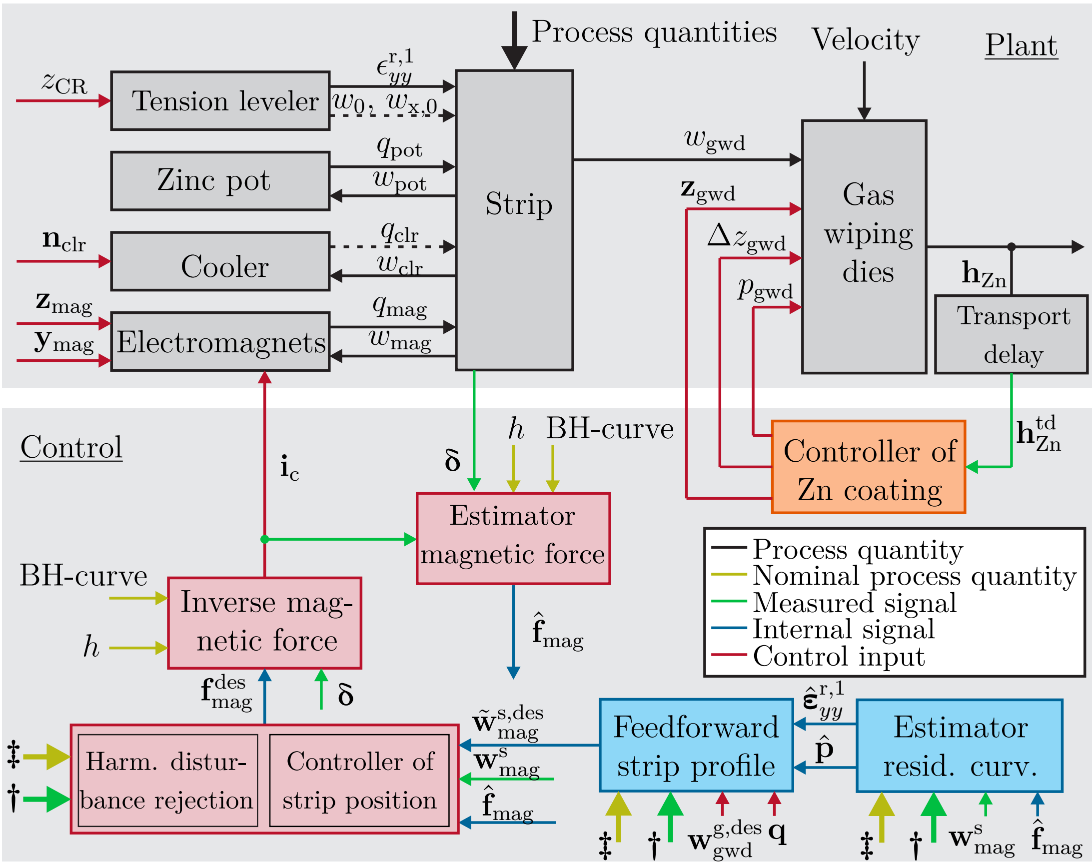

Figure 4.1: Block diagram of the proposed control concept. The block color indicates the sampling time: orange - slow; blue - fast; red - very fast. Abbreviations: ‡ - nominal process quantities, e.g., L, h, b, E,...; † - measured signals, e.g., $N_{xx,\mathrm{L}}$, V,...;

4.2 Estimator of the residual curvature

As an alternative to the calculation of the residual strain parameters, i.e., the residual membrane strains and residual curvatures, by means of the beam model from Section 2.2, a different estimation approach is developed. According to Tab. 2.1, only a profile of the residual curvature $\epsilon_{yy}^{\mathrm{r},1}(y)$ from upstream plastic bending deformations is considered in the material model (2.16) for the model-based estimator. The steady-state plate model using this estimated residual curvature profile is validated in Section 4.2.1 based on the measurements of tower sensors. Assuming steady-state conditions, the stress resultants thus simplify to

$$\begin{bmatrix} N_{xx} \\ N_{yy} \\ N_{xy} \end{bmatrix} = A \begin{bmatrix} 1 & \nu & 0 \\ \nu & 1 & 0 \\ 0 & 0 & \frac{1-\nu}{2} \end{bmatrix} \begin{bmatrix} \epsilon_{xx}^0 \\ \epsilon_{yy}^0 \\ \gamma_{xy}^0 \end{bmatrix} \tag{4.1a}$$

$$\begin{bmatrix} M_{xx} \\ M_{yy} \\ M_{xy} \end{bmatrix} = D \begin{bmatrix} 1 & \nu & 0 \\ \nu & 1 & 0 \\ 0 & 0 & \frac{1-\nu}{2} \end{bmatrix} \left(\begin{bmatrix} \epsilon_{xx}^1 \\ \epsilon_{yy}^1 \\ \gamma_{xy}^1 \end{bmatrix} + \underbrace{\begin{bmatrix} 0 \\ -\epsilon_{yy}^{\mathrm{r},1}(y) \\ 0 \end{bmatrix}}_{\boldsymbol{\varepsilon}^{\mathrm{r},1}(y)} \right), \tag{4.1b}$$

with the function $\epsilon_{yy}^{\mathrm{r},1}(y)$ according to (2.17). By the same line of reasoning as in Section 3.3, a geometrically linear model with the boundary conditions III according to Tab. 2.2 can be used for this purpose. To obtain a steady-state model based on geometrically linear relations and the boundary conditions III according to Tab. 2.2, (2.46) is simplified to

$$\left(\breve{\mathbf{K}} - V^2 \breve{\mathbf{H}}\right) \breve{\mathbf{t}} = \breve{\mathbf{f}}^{\mathrm{g}} + \breve{\mathbf{f}}^{\mathrm{N}} \tag{4.2a}$$

$$\left[\tilde{\mathbf{K}}^{\bar{\mathrm{M}}} + \tilde{\mathbf{K}}^{\mathrm{N}}\left(\breve{\mathbf{t}}\right) - V^2 \tilde{\mathbf{H}}\right] \tilde{\mathbf{t}} = \tilde{\mathbf{B}}^{\mathrm{y}} \boldsymbol{\varepsilon}_{yy}^{\mathrm{r},1} + \tilde{\mathbf{B}} \mathbf{f}_{\mathrm{mag}}, \tag{4.2b}$$

where (4.2a) describes the in-plane and (4.2b) the out-of-plane displacements. The model is used to calculate the transverse strip displacements at the electromagnets according to (2.46c) and at the tower sensors.

Remark: A different possibility to consider the incoming flatness defects in (4.1b) is given by the choice $\left(\boldsymbol{\varepsilon}^{\mathrm{r},1}\right)^{\mathrm{T}} = \begin{bmatrix} -\epsilon_{xx}^{\mathrm{r},1}(y) & -\epsilon_{yy}^{\mathrm{r},1}(y) & 0 \end{bmatrix}$ with two residual curvatures $\epsilon_{xx}^{\mathrm{r},1}$ and $\epsilon_{yy}^{\mathrm{r},1}$. However, both residual curvatures $\epsilon_{xx}^{\mathrm{r},1}$ and $\epsilon_{yy}^{\mathrm{r},1}$ have a quite similar effect on the transverse profile of the strip under tensile load. Therefore, it is difficult to independently estimate the unknowns $\epsilon_{xx}^{\mathrm{r},1}$ and $\epsilon_{yy}^{\mathrm{r},1}$ from measurements of the transverse strip profile. Thus, $\epsilon_{xx}^{\mathrm{r},1}$ is neglected and only the incoming residual curvature $\epsilon_{yy}^{\mathrm{r},1}$ is used.

The design of the model-based feedforward controller requires an accurate mechanical model of the plant. For this purpose, the residual curvature $\epsilon_{yy}^{\mathrm{r},1}$ of the incoming strip and the unknown position offset $\mathbf{p}$ of the electromagnetic strip stabilizer, cf. (1.1), have to be estimated. Utilizing (4.2) and (2.46c) leads to the steady-state input/output relation

$$\tilde{\mathbf{w}}_{\mathrm{mag}} = \boldsymbol{\Gamma}_{\mathrm{mag}} \boldsymbol{\varepsilon}_{yy}^{\mathrm{r},1} + \boldsymbol{\Delta}_{\mathrm{mag}} \mathbf{f}_{\mathrm{mag}}, \tag{4.3}$$

with $\boldsymbol{\Gamma}_{\mathrm{mag}} = \tilde{\mathbf{C}}_{\mathrm{mag}} \mathbf{R} \tilde{\mathbf{B}}^{\mathrm{y}}$, $\boldsymbol{\Delta}_{\mathrm{mag}} = \tilde{\mathbf{C}}_{\mathrm{mag}} \mathbf{R} \tilde{\mathbf{B}}$, and the abbreviation

$$\mathbf{R} = \left[\tilde{\mathbf{K}}^{\bar{\mathrm{M}}} + \tilde{\mathbf{K}}^{\mathrm{N}}\left(\left(\breve{\mathbf{K}} - V^2 \breve{\mathbf{H}}\right)^{-1} \left(\breve{\mathbf{f}}^{\mathrm{g}} + \breve{\mathbf{f}}^{\mathrm{N}}\right)\right) - V^2 \tilde{\mathbf{H}}\right]^{-1}. \tag{4.4}$$

$\mathbf{R}$ is well defined for normal operating conditions as long as the tensile load $N_{xx,\mathrm{L}}$ at the tower roll is high enough to keep the strip prestressed, see Fig. 2.1. These matrices $\mathbf{\Gamma}_{\mathrm{mag}}$ and $\mathbf{\Delta}_{\mathrm{mag}}$ are computed using the nominal parameters of the production. The unknowns $\boldsymbol{\varepsilon}_{yy}^{\mathrm{r},1}$ and $\mathbf{p}$ are estimated by solving the least-squares problem

$$\min_{\hat{\boldsymbol{\varepsilon}}_{yy}^{\mathrm{r},1},\hat{\mathbf{p}}} \left\| \underbrace{\mathbf{\Gamma}_{\mathrm{mag}}\hat{\boldsymbol{\varepsilon}}_{yy}^{\mathrm{r},1} + \mathbf{\Delta}_{\mathrm{mag}}\hat{\mathbf{f}}_{\mathrm{mag}}}_{\tilde{\mathbf{w}}_{\mathrm{mag}}} - \underbrace{\left(\mathbf{w}_{\mathrm{mag}}^{\mathrm{s}} + \mathbf{\Phi}\hat{\mathbf{p}}\right)}_{\mathbf{w}_{\mathrm{mag}}} \right\|_2^2, \tag{4.5}$$

with the computed steady-state transverse strip displacement $\tilde{\mathbf{w}}_{\mathrm{mag}}$ at the electromagnets according to (4.3) and the associated measurement $\mathbf{w}_{\mathrm{mag}}$ according to (1.1). Note that the electromagnetic forces $\mathbf{f}_{\mathrm{mag}}$ in (4.3) are replaced by their estimates $\hat{\mathbf{f}}_{\mathrm{mag}}$ following the procedure described in Section 2.1.1. The solution of (4.5) can be written in the form

$$\begin{bmatrix} \hat{\boldsymbol{\varepsilon}}_{yy}^{\mathrm{r},1} \\ \hat{\mathbf{p}} \end{bmatrix} = \left(\mathbf{S}^{\mathrm{T}}\mathbf{S}\right)^{-1}\mathbf{S}^{\mathrm{T}}\left(\mathbf{\Delta}_{\mathrm{mag}}\hat{\mathbf{f}}_{\mathrm{mag}} - \mathbf{w}_{\mathrm{mag}}^{\mathrm{s}}\right), \tag{4.6}$$

with the abbreviation $\mathbf{S} = [-\mathbf{\Gamma}_{\mathrm{mag}}, \mathbf{\Phi}]$.

Remark: The constant (even) and linear (skew) components of the measured strip profile $\mathbf{w}_{\mathrm{mag}}$ in (4.5) can be influenced by $\hat{\mathbf{p}}^{\mathrm{T}} = [\hat{w}_{\mathrm{mean}}^{\mathrm{s}}, \hat{\varphi}^{\mathrm{s}}]$. In contrast, the mathematical model of the strip profile $\tilde{\mathbf{w}}_{\mathrm{mag}}$ in (4.5), see also (4.3), depends on the estimates $\left(\hat{\boldsymbol{\varepsilon}}_{yy}^{\mathrm{r},1}\right)^{\mathrm{T}} = \left[\hat{\epsilon}_{yy}^{\mathrm{c},0} \quad \hat{\epsilon}_{yy}^{\mathrm{c},1} \quad \ldots \quad \hat{\epsilon}_{yy}^{\mathrm{c},p}\right]$ of the residual curvatures, which influence the higher-order components of the calculated strip profile. For example, the first coefficient $\hat{\epsilon}_{yy}^{\mathrm{c},0}$ generates the typical crossbow component of the strip profile. Thus, the solution (4.6) is well defined and the individual estimation variables can be uniquely determined.

Here, (4.6) is employed to identify the unknown parameters $\boldsymbol{\varepsilon}_{yy}^{\mathrm{r},1}$ and $\mathbf{p}$. In the form (4.6), it is suitable for offline simulations. For an online implementation in the industrial plant, the proposed least-squares estimator has to be formulated in a recursive form, see, e.g., [85]. Because of slowly varying conditions in the industrial plant, only minor variations of the parameters occur within a coil. Hence, an iterative execution of the estimator with a suitable time step can easily track these parameters.

4.2.1 Validation of the estimator

The estimator of the residual curvature is validated using measurement data from the industrial hot-dip galvanizing line. To this end, the additional strip displacement sensors in the cooling tower are used, see Fig. 1.2. Table 4.1 contains the nominal parameters of the considered test strips A and B, the associated positions of the electromagnetic actuators and the tower sensors, and

	Parameter	Symbol	Value
General parameters	Young's modulus	E	$1.58 \cdot 10^{11}\,\mathrm{N/m^2}$
	Pos. of tower sensors	x_{tow}	$0.657L$
	No. of tower sensors	μ	5
	No. of lateral grid points	λ	100
	No. of longitudinal finite elements	n	30
	No. of lateral finite elements	m	3
	No. of basis functions	n_{yu}	2
	No. of basis functions	n_{yv}	3
	No. of basis functions	n_{yw}	4
Test strip A: control off	Strip width	b	$1.466\,\mathrm{m}$
	Strip thickness	h	$1.2\,\mathrm{mm}$
	Tensile load	$N_{xx,\mathrm{L}}$	$30.03\,\mathrm{kN/m}$
	Strip velocity	V	$1.34\,\mathrm{m/s}$
	Pos. of magnets	x_{mag}	$0.031L$
	No. of actuators	κ	6
Test strip B: control on	Strip width	b	$1.509\,\mathrm{m}$
	Strip thickness	h	$1.5\,\mathrm{mm}$
	Tensile load	$N_{xx,\mathrm{L}}$	$39.02\,\mathrm{kN/m}$
	Strip velocity	V	$1.12\,\mathrm{m/s}$
	Pos. of magnets	x_{mag}	$0.032L$
	No. of actuators	κ	7

Table 4.1: Nominal parameters of the test strips and discretization parameters used for the validation of the estimator.

the parameters used for spatial discretization. The functions $w_{\mathrm{gwd}}(y)$, $w_{\mathrm{mag}}(y)$, and $w_{\mathrm{tow}}(y)$ shown in the following graphs represent the transverse strip profiles at the gas wiping dies, the electromagnets, and the tower sensors, respectively. The functions $w_{\mathrm{mag}}(y)$ and $w_{\mathrm{tow}}(y)$ are computed analogous to the strip profile $w_{\mathrm{gwd}}(y)$, which is calculated in the discretized form at the lateral grid points (1.3).

Utilizing the estimator (4.6) for the test strips A (inactive position controller of the electromagnets) and B (active position controller of the electromagnets using zero set-points) and assuming a constant residual curvature in the lateral direction, i.e. $p = 0$ in (2.17), leads to the results shown in Fig. 4.2. The strip profiles shown as solid lines are computed by the model (4.5) with the estimated parameters $\hat{\epsilon}_{yy}^{\mathrm{c},0}$ and $\hat{\mathbf{p}}^{\mathrm{T}} = [\hat{w}_{\mathrm{mean}}^{\mathrm{s}}, \hat{\varphi}^{\mathrm{s}}]$. The points in Fig. 4.2 represent measured strip displacements. In case of the activated position controller, an almost flat strip profile is realized at the electromagnets, see Fig. 4.2b (top). To validate the model with displacement measurements that are not used for the estimation, the bottom graphs of Fig. 4.2 show the strip profiles and the measurements at the tower sensors.

The measurements were recorded for several positions z_{CR} of the correction roll, see Fig. 1.2. The normalized positions $\bar{z}_{\mathrm{CR}} = z_{\mathrm{CR}}/z_{\mathrm{CR,max}}$ of the correction roll are indicated by the different colors in Fig. 4.2. This demonstrates the significant influence of $\bar{z}_{\mathrm{CR}}$ on the size and direction of the crossbow.

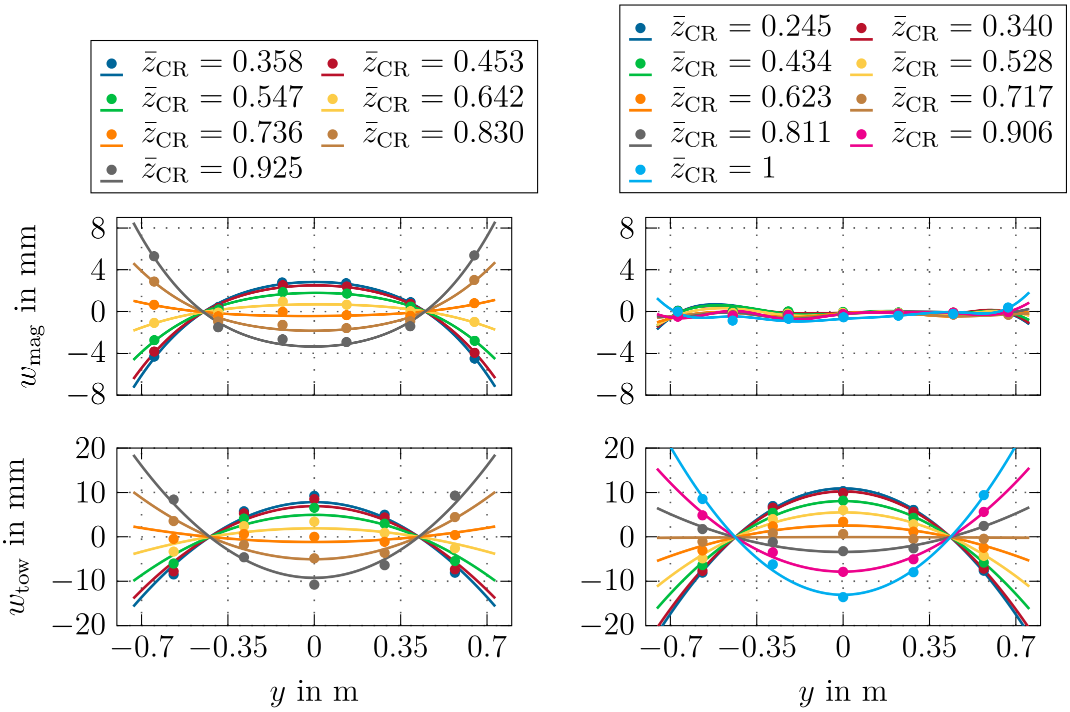

(a) Test strip A: without control. (b) Test strip B: with active control.

Figure 4.2: Estimation results for both test strips with a constant initial curvature ($p = 0$ in (2.17)) in lateral direction for various positions $\bar{z}_{\mathrm{CR}} = z_{\mathrm{CR}}/z_{\mathrm{CR,max}}$ of the correction roll (solid lines: model output, points: measurement data).

As can be inferred from Fig. 4.2, even a model with a constant residual curvature accurately captures the crossbow profiles at the electromagnets and in the cooling tower. The crossbow at the tower sensors is much more pronounced than the one at the electromagnets. Clearly, the size of the crossbow increases with the distance to the support rolls.

Figure 4.3 shows the results for the assumption of a quadratic residual curvature in lateral direction, i.e. $p = 2$ in (2.17). The results are very similar to those with $p = 0$. Because with $p = 2$ the five parameters $\epsilon_{yy}^{\mathrm{c},0}$, $\epsilon_{yy}^{\mathrm{c},1}$, $\epsilon_{yy}^{\mathrm{c},2}$, and $\mathbf{p}^{\mathrm{T}} = [w_{\mathrm{mean}}^{\mathrm{s}}, \varphi^{\mathrm{s}}]$ are used to fit the model output to the measured strip displacements at the electromagnets, the estimation error can be further reduced compared to the case with $p = 0$.

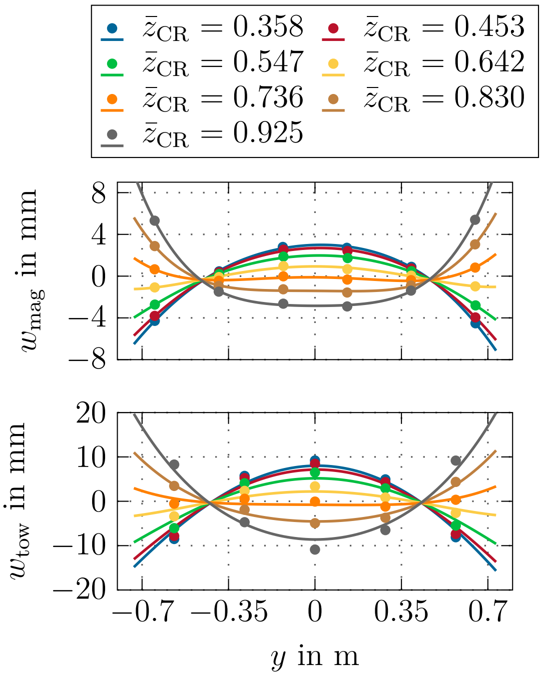

(a) Test strip A: without control.

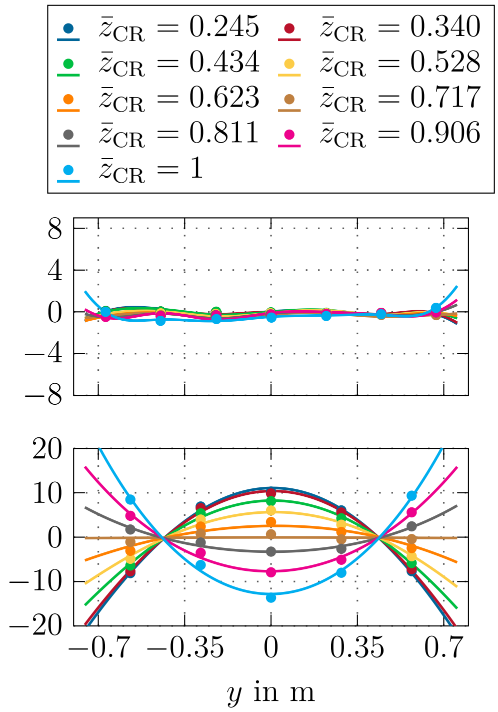

(b) Test strip B: with active control.

Figure 4.3: Estimation results for both test strips with a quadratic initial curvature ($p = 2$ in (2.17)) in lateral direction for various positions $\bar{z}_{CR} = z_{CR}/z_{CR,max}$ of the correction roll (solid lines: model output, points: measurement data).

Figure 4.4 shows the estimated parameters of the residual curvature for the test strips A and B and several positions $\bar{z}_{CR}$ of the correction roll. Circles indicate the estimation results for $p = 0$, triangles for $p = 2$. The solid ($p = 0$) and dashed ($p = 2$) black lines are determined by polynomial curve fitting. For the considered test strips, the results show that the influence of $\bar{z}_{CR}$ on $\hat{\epsilon}^{c,0}_{yy}$ is almost the same for $p = 0$ and $p = 2$. The fitted polynomials for $\hat{\epsilon}^{r,0}_{yy}(\bar{z}_{CR})$ can be used for control to select the optimal position of the correction roll, e.g., to eliminate the crossbow. The estimation results for the parameters $\hat{\epsilon}^{c,1}_{yy}$ and $\hat{\epsilon}^{c,2}_{yy}$ in case of $p = 2$ are also shown in Fig. 4.4.

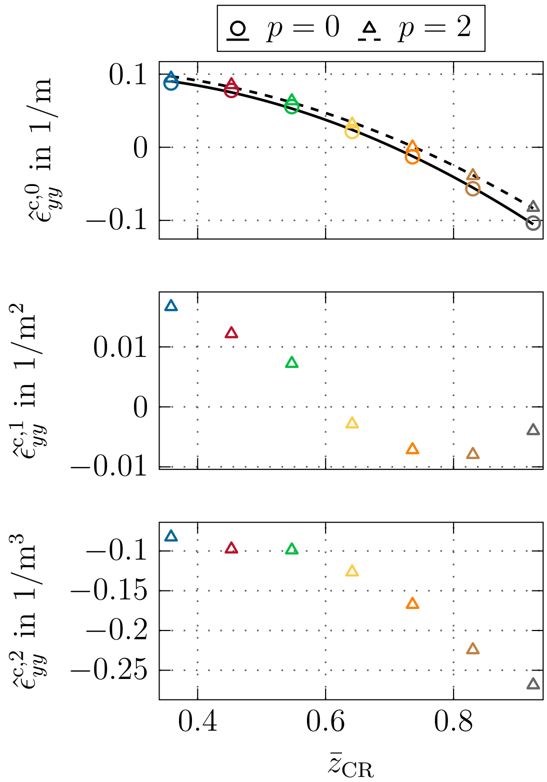

(a) Test strip A: without control.

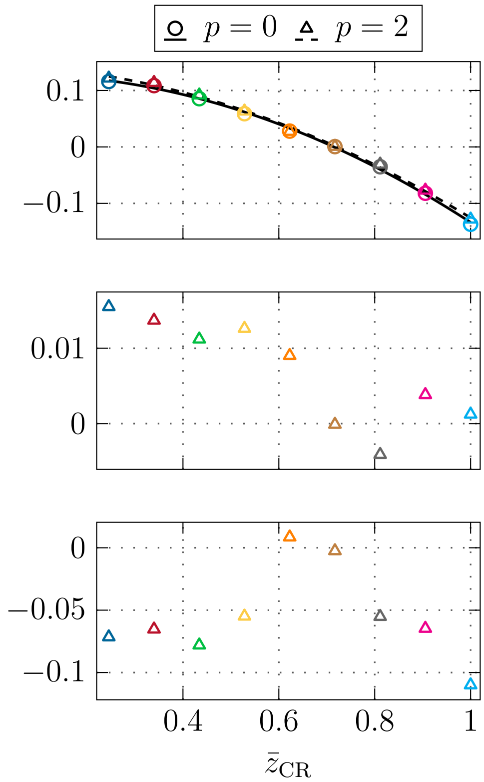

(b) Test strip B: with active control.

Figure 4.4: Estimation results for the initial curvatures of both test strips depending on the position $\bar{z}_{\mathrm{CR}} = z_{\mathrm{CR}}/z_{\mathrm{CR,max}}$ of the correction roll. The black lines illustrate fitted polynomials.

Although the tower sensors are positioned more than 30 m downstream of the electromagnetic stabilizer, the transverse strip profiles in the cooling tower can be accurately predicted by the developed model. Figure 4.5 shows the model-plant mismatch in terms of the deviation between the measured and the computed strip displacement $e^l_{\mathrm{tow}} = w^l_{\mathrm{tow}} - \tilde{w}^l_{\mathrm{tow}}$ for $l \in \{1, \ldots, \mu\}$, at the $\mu = 5$ lateral positions of the tower sensors, see also Fig. 1.2. Actually, the same small displacement error is observed for $p = 0$ and $p = 2$.

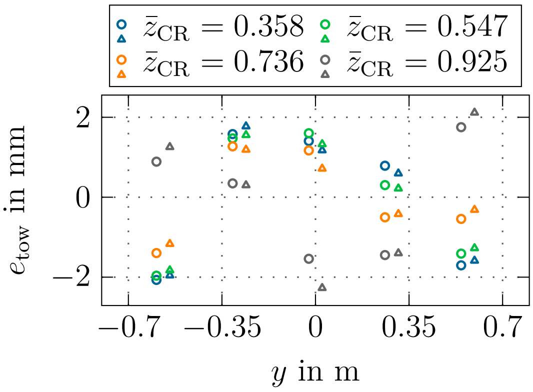

(a) Test strip A: without control.

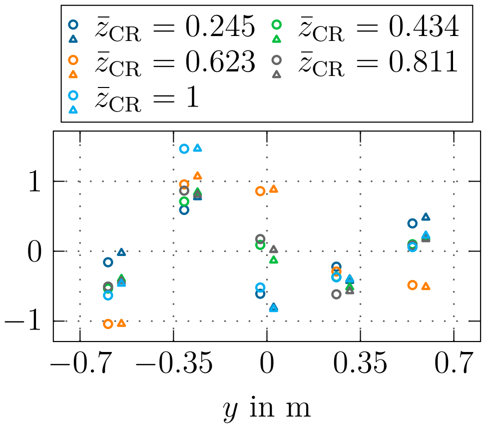

(b) Test strip B: with active control.

Figure 4.5: Displacement error e_{tow} in the cooling tower between the measurement and the model output for both test strips and various positions $\bar{z}_{CR} = z_{CR}/z_{CR,max}$ of the correction roll (circles: constant curvature with $p = 0$, triangles: polynomial curvature profile with $p = 2$).

Throughout the considered scenarios (two test strips, various positions $\bar{z}_{CR}$, $p = 0$, and $p = 2$), the estimates of $\hat{w}^s_{mean}$ range from -0.55 mm to 0.46 mm, and those of $\hat{\varphi}^s$ from $-0.034°$ to $0.041°$. These estimates cannot be validated but they are in a realistic range.

Figure 4.6 shows the estimated shape of the strips A and B for two selected scenarios. The top parts contain the domain between the stabilization roll and the tower roll, the bottom parts show the strip region near the stabilization roll in detail. On the left-hand side, test strip A with $\bar{z}_{CR} = 0.925$ and an inactive position controller of the strip stabilizer is shown. The right-hand side shows test strip B with $\bar{z}_{CR} = 0.245$ and an active electromagnetic stabilizer. Note that these two scenarios represent extreme test cases since such large crossbows are usually avoided during normal production. Figure 4.6 clearly demonstrates that an active position controller of the strip stabilizer significantly reduces the crossbow at the gas wiping dies.

Two calculated strip profiles at the gas wiping dies for test strip B with active position controller of the strip stabilizer are analyzed in more detail. Figure 4.7 shows that the realization of a flat strip profile at the electromagnets does not guarantee a flat profile at the gas wiping dies. The measured inhomogeneous zinc coating profiles Δh_{Zn} are clearly correlated with the estimated transverse strip profile at the gas wiping dies. Actually, more zinc is wiped off if the strip-to-nozzle distance is smaller and vice versa. Figure 4.3b shows the corresponding strip profiles at the electromagnets and at the tower sensors.

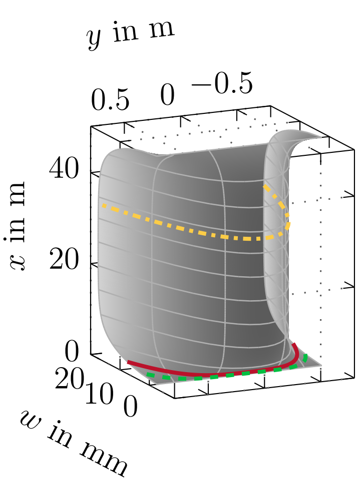

(a) Without control.

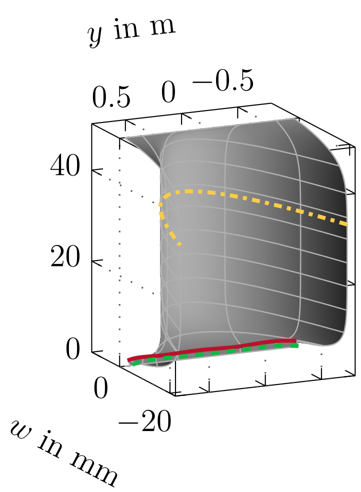

(b) With active control.

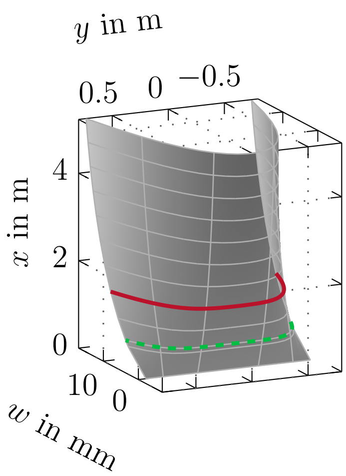

(c) Detail view of (a).

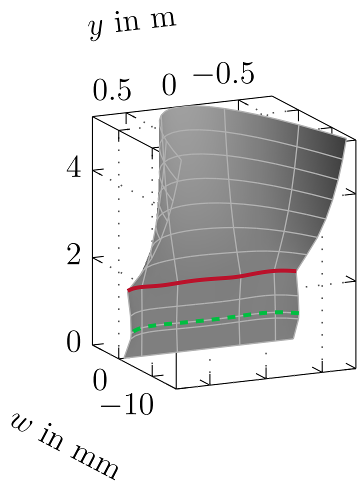

(d) Detail view of (b).

Figure 4.6: Estimation results showing steady-state shapes of the strip ($p = 2$): left column - inactive position control of the electromagnetic stabilizer (test strip A, $\bar{z}_{\mathrm{CR}} = 0.925$), right column - active position control (test strip B, $\bar{z}_{\mathrm{CR}} = 0.245$).

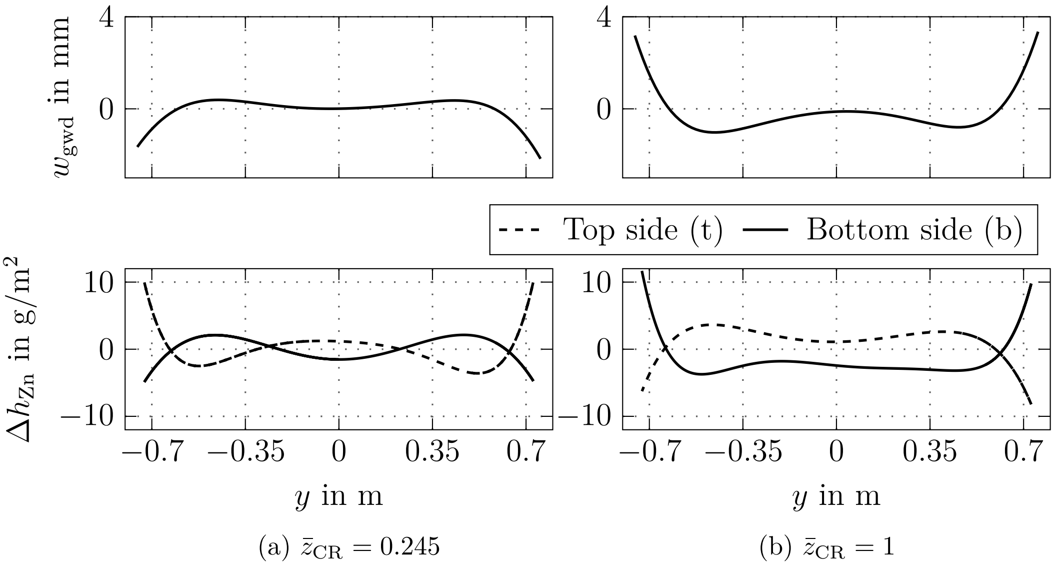

Figure 4.7: Estimated transverse strip profiles w_{gwd} at the gas wiping dies for test strip B ($p = 2$) with active position controller and deviations Δh_{Zn} of the measured zinc coating thickness from the mean value.

4.2.2 Conclusions

This section can be summarized as follows:

- The mathematical plate model of the transverse strip shape was used with the nominal production parameters of the industrial hot-dip galvanizing line.
- Two test strips were used to estimate the unknowns, i.e., the residual curvature of the strip and the offset of the electromagnetic strip stabilizer.
- Besides the model of the strip shape, the estimator uses measurements from the electromagnetic strip stabilizer, i.e., the coil currents of the electromagnets and the pole-shoe-to-strip distances.
- The model-based estimator was successfully validated based on additional displacement measurements in the cooling tower.

4.3 Feedforward control of the transverse strip profile

Based on the results of Section 4.2, it is clear that in general the thickness profile of the zinc coating is not completely homogeneous if the position controllers of the electromagnetic stabilizer make the lateral strip profile ideally flat at the position x_{mag} of the electromagnets. In such a scenario, the non-uniformity of the lateral strip profile increases if the distance Δx between the gas wiping dies and the electromagnets becomes larger. In several hot-dip galvanizing lines, the distance Δx cannot be as short as desired due to design reasons. Therefore, another way is pursued in this work, i.e., the design of a feedforward controller.

4.3.1 Feedforward control

Assume that the parameters of the residual curvature $\hat{\boldsymbol{\varepsilon}}_{yy}^{\mathrm{r},1}$ according to (2.17) and the offset $\hat{\mathbf{p}}^{\mathrm{T}} = [\hat{w}^{\mathrm{s}}_{\mathrm{mean}}, \hat{\varphi}^{\mathrm{s}}]$ according to (1.1) are correctly estimated using the procedure from Section 4.2. In the following, the model outputs according to (2.46d) and (2.46c) are used to calculate the transverse strip profiles at the gas wiping dies and at the electromagnets, respectively. Based on this model, the transverse strip displacement $\tilde{\mathbf{w}}_{\mathrm{gwd}}$ at the gas wiping dies follows from the steady-state model (4.2) in the form

$$\tilde{\mathbf{w}}_{\mathrm{gwd}} = \boldsymbol{\Gamma}_{\mathrm{gwd}} \hat{\boldsymbol{\varepsilon}}_{yy}^{\mathrm{r},1} + \boldsymbol{\Delta}_{\mathrm{gwd}} \mathbf{f}_{\mathrm{mag}}, \tag{4.7}$$

where $\boldsymbol{\Gamma}_{\mathrm{gwd}} = \tilde{\mathbf{C}}_{\mathrm{gwd}} \mathbf{R} \tilde{\mathbf{B}}^{\mathrm{y}}$ and $\boldsymbol{\Delta}_{\mathrm{gwd}} = \tilde{\mathbf{C}}_{\mathrm{gwd}} \mathbf{R} \tilde{\mathbf{B}}$ with $\mathbf{R}$ from (4.4). Now the electromagnets have to be controlled (in particular the electromagnetic force $\mathbf{f}_{\mathrm{mag}}$) in such a way that a desired transverse strip profile $\mathbf{w}^{\mathrm{g,des}}_{\mathrm{gwd}}$ at the gas wiping dies is achieved in a least-squares sense. Note that typically $\mathbf{w}^{\mathrm{g,des}}_{\mathrm{gwd}} = \mathbf{0}$ is chosen for a homogeneous zinc coating thickness. Hence, the least-squares problem

$$\min_{\mathbf{f}_{\mathrm{mag}} \in \mathbb{R}^{\kappa}} \left\| \underbrace{\boldsymbol{\Gamma}_{\mathrm{gwd}} \hat{\boldsymbol{\varepsilon}}_{yy}^{\mathrm{r},1} + \boldsymbol{\Delta}_{\mathrm{gwd}} \mathbf{f}_{\mathrm{mag}}}_{\tilde{\mathbf{w}}_{\mathrm{gwd}}} - \underbrace{\left(\mathbf{w}^{\mathrm{g,des}}_{\mathrm{gwd}} + \boldsymbol{\Omega}(\hat{\mathbf{p}} - \mathbf{q}) \right)}_{\mathbf{w}^{\mathrm{des}}_{\mathrm{gwd}}} \right\|_2^2, \tag{4.8}$$

which is similar to (4.5), has to be solved. The vector $\mathbf{w}^{\mathrm{des}}_{\mathrm{gwd}}$ follows from (1.4) depending on the estimated offset $\hat{\mathbf{p}}$. The solution of (4.8) can be straightforwardly computed using the pseudoinverse of $\boldsymbol{\Delta}_{\mathrm{gwd}}$. This approach works in principle but it tends to yield large deformations of the strip profile at the electromagnets and is thus practically unfeasible.

To analyze the reasons for this behavior, $\boldsymbol{\Delta}_{\mathrm{gwd}}$ is decomposed by the singular value decomposition (SVD). This yields

$$\boldsymbol{\Delta}_{\mathrm{gwd}} = \mathbf{U}_{\mathrm{gwd}} \boldsymbol{\Sigma}_{\mathrm{gwd}} \mathbf{V}^{\mathrm{T}}_{\mathrm{gwd}} = \sum_{l=1}^{\kappa} \mathbf{u}_l \sigma_l \mathbf{v}_l^{\mathrm{T}}, \tag{4.9}$$

with $\boldsymbol{\Sigma}_{\mathrm{gwd}} = \mathrm{diag}\{\sigma_1, \ldots, \sigma_\kappa\}$, $\mathbf{U}_{\mathrm{gwd}} = [\mathbf{u}_1, \ldots, \mathbf{u}_\kappa] \in \mathbb{R}^{\lambda \times \kappa}$, $\mathbf{V}_{\mathrm{gwd}} = [\mathbf{v}_1, \ldots, \mathbf{v}_\kappa] \in \mathbb{R}^{\kappa \times \kappa}$ and $\lambda \gg \kappa$. The transverse strip profile at the gas wiping dies is then decomposed into the modes $u_l(y)$, $l = 1, \ldots, \kappa$, which are represented by the vectors $\mathbf{u}_l \in \mathbb{R}^\lambda$ at the grid points defined by the vector $\mathbf{y}_{\mathrm{gwd}} \in \mathbb{R}^\lambda$ according to (1.3).

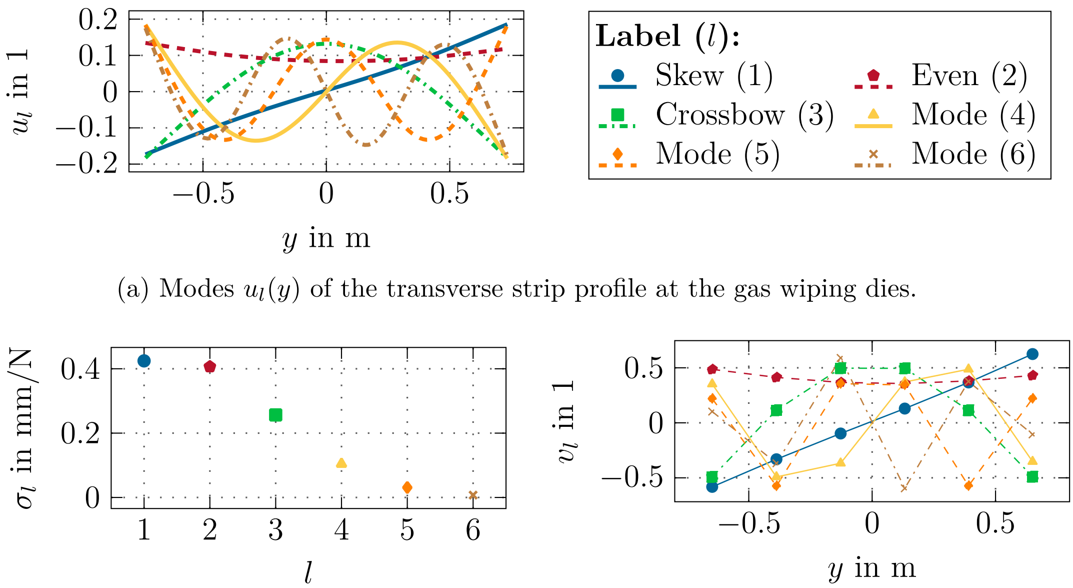

(a) Modes $u_l(y)$ of the transverse strip profile at the gas wiping dies.

(b) Singular values σ_l.

(c) Modes $v_l(y)$ of the electromagnetic forces.

Figure 4.8: Singular value decomposition of $\mathbf{\Delta}_{\mathrm{gwd}}$ for test strip A of Table 4.1, $x_{\mathrm{gwd}} = 0.0126L$, $\lambda = 100$, $\kappa = 6$, $p = 2$ in (2.17), $\bar{z}_{\mathrm{CR}} = 0.547$, and $\mathbf{p}^{\mathrm{T}} = [0\,\mathrm{mm}, 0°]$ in (1.1).

By analogy, the entries of $\mathbf{v}_l$, $l = 1, \ldots, \kappa$ are associated with the lateral positions of the electromagnets $\mathbf{y}^l_{\mathrm{mag}}$, $l = 1, \ldots, \kappa$, see also Fig. 1.6, and may be interpreted as the modes $v_l(y)$, $l = 1, \ldots, \kappa$, of the electromagnetic forces exerted on the strip. The singular values σ_l, $l = 1, \ldots, \kappa$, correspond to the sensitivities between the input force profile $v_l(y)$ and the output displacement profile $u_l(y)$. A transverse strip profile mode with a high sensitivity value σ_l can be realized with a small electromagnetic force and vice versa. Figure 4.8 shows the modes $u_l(y)$ and $v_l(y)$ with the corresponding singular values σ_l for test strip A from Tab. 4.1, with $x_{\mathrm{gwd}} = 0.0126L$, $\lambda = 100$, $\kappa = 6$, $p = 2$ in (2.17), $\bar{z}_{\mathrm{CR}} = 0.547$, and $\mathbf{p}^{\mathrm{T}} = [0\,\mathrm{mm}, 0°]$ in (1.1). Figure 4.8 reveals that a suppression of the skew ($l = 1$) and even ($l = 2$) modes only requires small forces and the crossbow mode ($l = 3$) demands moderate forces. For the compensation of the higher modes ($l \geq 4$), large forces have to be applied by the electromagnets. This can be traced back to the fact that the suppression of higher profile modes requires alternate bending by neighboring electromagnets.

Based on this analysis, it seems reasonable to suppress only the profile modes that exhibit a higher sensitivity, i.e., the corresponding singular value σ_l is above a user-defined threshold. The indices of the profile modes to be compensated are summarized in the index set I and the least-squares problem (4.8) is rewritten as

$$\min_{\mathbf{f}_{\mathrm{mag}}} \left\| \mathbf{\Gamma}_{\mathrm{gwd}} \hat{\boldsymbol{\varepsilon}}_{yy}^{\mathrm{r},1} + \sum_{l \in I} \sigma_l \mathbf{u}_l \mathbf{v}_l^{\mathrm{T}} \mathbf{f}_{\mathrm{mag}} - \mathbf{w}_{\mathrm{gwd}}^{\mathrm{des}} \right\|_2^2 \tag{4.10}$$

with $\mathbf{w}_{\mathrm{gwd}}^{\mathrm{des}} = \mathbf{w}_{\mathrm{gwd}}^{\mathrm{g,des}} + \mathbf{\Omega}(\hat{\mathbf{p}} - \mathbf{q})$. The optimal solution of (4.10) yields the feedforward control input

$$\mathbf{f}_{\mathrm{mag}}^{\star} = \sum_{l \in I} \frac{1}{\sigma_l} \mathbf{v}_l \mathbf{u}_l^{\mathrm{T}} \left(\mathbf{w}_{\mathrm{gwd}}^{\mathrm{des}} - \mathbf{\Gamma}_{\mathrm{gwd}} \hat{\boldsymbol{\varepsilon}}_{yy}^{\mathrm{r},1} \right), \tag{4.11}$$

where $\sum_{l \in I} \frac{1}{\sigma_l} \mathbf{v}_l \mathbf{u}_l^{\mathrm{T}}$ is the pseudoinverse of $\sum_{l \in I} \sigma_l \mathbf{u}_l \mathbf{v}_l^{\mathrm{T}}$. With $\mathbf{f}_{\mathrm{mag}}^{\star}$ from (4.11), the desired set-point values for the position controllers of the electromagnetic strip stabilizer can be computed in the form, see (4.5),

$$\tilde{\mathbf{w}}_{\mathrm{mag}}^{\mathrm{s,des}} = \mathbf{\Gamma}_{\mathrm{mag}} \hat{\boldsymbol{\varepsilon}}_{yy}^{\mathrm{r},1} + \mathbf{\Delta}_{\mathrm{mag}} \mathbf{f}_{\mathrm{mag}}^{\star} - \mathbf{\Phi} \hat{\mathbf{p}}. \tag{4.12}$$

Remark: The feedforward controller (4.11) calculates the optimal electromagnetic forces. The κ electromagnetic actuators are located at distinct positions in the lateral direction of the strip. Assume that υ profile modes should be compensated. The desired strip profile $\mathbf{w}_{\mathrm{gwd}}^{\mathrm{des}}$ at the gas wiping dies is specified at λ equidistant grid points, where $\lambda \gg \kappa \geq \upsilon$ holds. Thus, the optimal solution (4.11) is uniquely defined.

4.3.2 Performance evaluation based on the validated model

For the following simulation study, the performance indicators

$$J_{\mathrm{gwd}} = \sqrt{\frac{1}{\lambda} \left\| \tilde{\mathbf{w}}_{\mathrm{gwd}}^{\mathrm{g}} \right\|_2^2} \quad \text{and} \quad J_{\mathrm{mag}} = \sqrt{\frac{1}{\kappa} \left\| \tilde{\mathbf{w}}_{\mathrm{mag}}^{\mathrm{s,des}} \right\|_2^2} \tag{4.13}$$

are introduced, where $\tilde{\mathbf{w}}_{\mathrm{gwd}}^{\mathrm{g}} = \mathbf{\Gamma}_{\mathrm{gwd}} \hat{\boldsymbol{\varepsilon}}_{yy}^{\mathrm{r},1} + \mathbf{\Delta}_{\mathrm{gwd}} \mathbf{f}_{\mathrm{mag}}^{\star} - \mathbf{\Omega}(\hat{\mathbf{p}} - \mathbf{q})$ is calculated with $\mathbf{f}_{\mathrm{mag}}^{\star}$ from (4.11), and $\tilde{\mathbf{w}}_{\mathrm{mag}}^{\mathrm{s,des}}$ is defined according to (4.12). The value J_{gwd} measures how much the steady-state transverse strip profile at the gas wiping dies deviates from the ideal flat strip profile $\mathbf{w}_{\mathrm{gwd}}^{\mathrm{g,des}} = \mathbf{0}$. Hence, J_{gwd} is also an indicator for the homogeneity of the zinc coating thickness. At the same time, J_{mag} indicates the required non-uniformity of the transverse strip profile at the electromagnets to achieve a flat gap at the gas wiping dies.

Figure 4.9 shows two strip shapes obtained by the optimal feedforward (FF) controller $\mathbf{f}_{\mathrm{mag}}^{\star}$ from (4.11) with the index sets $I = \{1, 2, \ldots, 6\}$ and $I = \{1, 2, 3\}$.

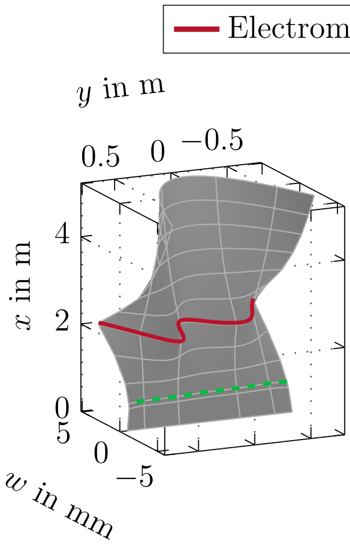

(a) FF modes 1-6: strip profile modes $u_l(y)$, $l = 1, \ldots, 6$ are compensated.

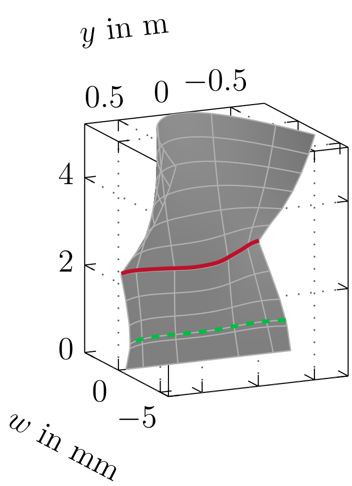

(b) FF modes 1-3: strip profile modes $u_l(y)$, $l = 1, 2, 3$ are compensated.

Figure 4.9: Strip shapes obtained by the feedforward (FF) controller $\mathbf{f}^{\star}_{\mathrm{mag}}$ from (4.11).

Parameter	Symbol	Value
Estimated displacement	$\hat{w}^{\mathrm{s}}_{\mathrm{mean}}$	$0.37\,\mathrm{mm}$
Estimated angle	$\hat{\varphi}^{\mathrm{s}}$	$-0.034°$
Position of gas wiping dies	x_{gwd}	$0.0126L$
Distance	Δx	$0.03L$
No. of lateral grid points	λ	100

Table 4.2: Parameters used for the simulation study to test the feedforward controller of the transverse strip profile at the gas wiping dies.

In these scenarios, $\bar{z}_{\mathrm{CR}} = 0.547$ is used for the position of the correction roll, which constitutes a suboptimal value and hence results in a distinct crossbow. Certainly, these are worst-case scenarios, which could be avoided by a suitable position of the correction roll in the zinc pot. Figure 4.9a shows the results if the strip profile modes $u_l(y)$, $l = 1, \ldots, 6$, are suppressed. The solid line illustrates the transverse strip profile at the electromagnets, and the dashed line highlights the profile at the gas wiping dies. The results for the case where just the first three profile modes $u_l(y)$, $l = 1, 2, 3$, are suppressed are shown in Fig. 4.9b. The simulations were executed for the parameters given in Tab. 4.2. Furthermore, $\mathbf{q}^{\mathrm{T}} = [w^{\mathrm{g,s}}_{\mathrm{mean}}, \varphi^{\mathrm{g,s}}]$ was set to zero.

The influence of the distance Δx between the gas wiping dies and the electromagnets on the results of the optimal feedforward controller is analyzed in detail in Fig. 4.10.

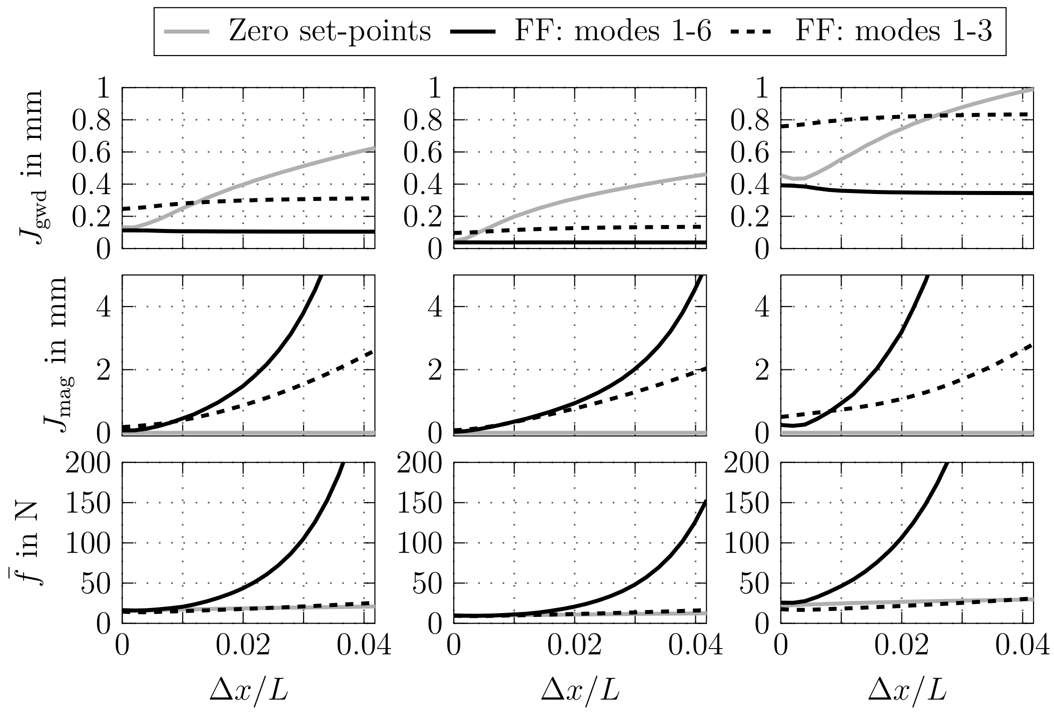

(a) $\bar{z}_{CR} = 0.358$ (b) $\bar{z}_{CR} = 0.547$ (c) $\bar{z}_{CR} = 0.925$

Figure 4.10: Simulation results with and without the optimal feedforward (FF) controller for test strip A and different positions $\bar{z}_{CR}$ of the correction roll: J_{gwd} - performance indicator of the transverse strip profile at the gas wiping dies; J_{mag} - performance indicator of the transverse strip profile at the electromagnets; $\bar{f}$ - mean absolute electromagnetic force;

In the considered scenario, the position x_{gwd} of the gas wiping dies is constant, while the position x_{mag} of the electromagnets is varied in a practically reasonable range. The performance indicators J_{gwd} and J_{mag} according to (4.13) are plotted as functions of $\Delta x/L$ for three positions $\bar{z}_{CR}$ of the correction roll and for the cases with feedforward controller compensation of three (FF: modes 1-3) and six (FF: modes 1-6) transverse strip profile modes and without (zero set-points) feedforward controller. In the latter case, zero-set points are used for the κ position controllers of the electromagnetic stabilizer. The quantity $\bar{f} = \frac{1}{\kappa}||\mathbf{f}_{mag}||_1$ defines the mean absolute electromagnetic force and is shown at the bottom of Fig. 4.10.

In the considered scenarios, the feedforward controller suppressing six modes yields always the best results, i.e., the smallest values J_{gwd}, irrespective of the value $\Delta x/L$. Figure 4.10 reveals that small values Δx result in small deformations of the transverse strip profile at the electromagnetic stabilizer, i.e., J_{mag} is small. Typically, the corresponding forces $\bar{f}$ are also small. As Δx increases, J_{gwd} remains almost constant if the feedforward controller is used. However, both the required forces $\bar{f}$ and the deformation of the strip profile at the electromagnets, i.e., J_{mag}, grow disproportionally with Δx when all six profile modes are compensated by the feedforward controller. Figure 4.10 also shows that the feedforward controller suppressing three profile modes can only improve the transverse strip profile at the gas wiping dies compared to the standard control approach (controller with zero set-points) if Δx exceeds a certain value. The advantage of not suppressing higher profile modes is that reduced electromagnetic forces are required.

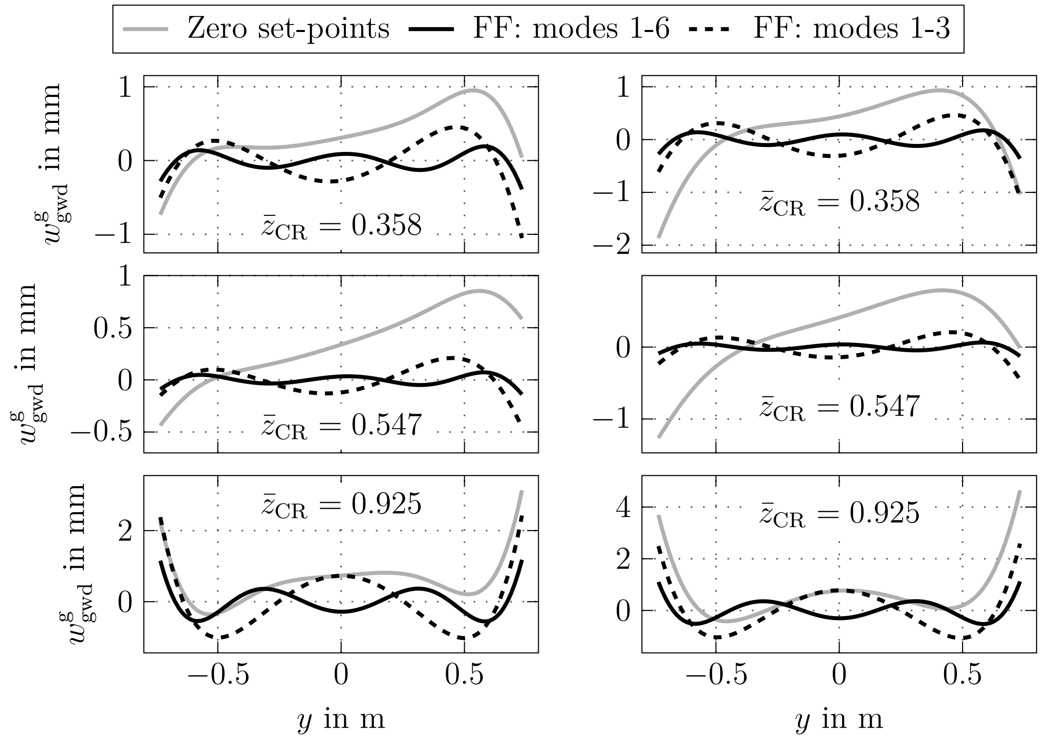

(a) $\Delta x = 0.01L$ (b) $\Delta x = 0.04L$

Figure 4.11: Transverse strip profiles in the local coordinate system of the gas wiping dies achieved by different feedforward (FF) control methods for different positions $\bar{z}_{\mathrm{CR}}$ of the correction roll, $w^{\mathrm{g,s}}_{\mathrm{mean}} = 0.5\,\mathrm{mm}$, and $\varphi^{\mathrm{g,s}} = 0.03°$.

As a last point, a scenario with an additional offset between the gas wiping dies and the electromagnetic stabilizer defined by $w^{\mathrm{g,s}}_{\mathrm{mean}} = 0.5\,\mathrm{mm}$ and $\varphi^{\mathrm{g,s}} = 0.03°$ is assumed, see also (1.4). Figure 4.11a shows the corresponding transverse strip profiles in the local coordinate system of the gas wiping dies for three positions $\bar{z}_{\mathrm{CR}}$ of the correction roll and the distance $\Delta x = 0.01L$. Commanding zero set-points to the κ position controllers of the electromagnetic stabilizer results in a shifted and skewed strip profile at the gas wiping dies (solid gray line). The feedforward controller that accounts for all six strip profile modes (solid black line), and the one that only considers the first three profile modes (dashed black line) can effectively improve the flatness of the strip profile and its transverse deviation from the centerline of the gas wiping dies. Analogous results for a setup with $\Delta x = 0.04L$ are given in Fig. 4.11b. Again, the best results are obtained if the feedforward controller suppresses all profile modes. However, according to Fig. 4.10, it may be better in this case to suppress just the first three strip profile modes with the feedforward controller to keep the electromagnetic forces low.

4.3.3 Conclusions

In the simulations, the proposed feedforward controller succeeds in improving the homogeneity of the strip profile at the gas wiping dies. The main contributions concerning the feedforward controller of the transverse strip profile at the gas wiping dies can be summarized as follows:

- An optimization-based feedforward controller was developed that improves the flatness of the transverse strip profile at the gas wiping dies.
- The feedforward controller was tested with the validated model of the transverse strip shape.
- A singular value decomposition of the sensitivity matrix between the electromagnetic forces and the transverse strip profile at the gas wiping dies was conducted to analyze the influence of individual transverse profile modes on the electromagnetic forces.
- The compensation of higher profile modes at the gas wiping dies generally leads to a larger deformation of the strip profile at the electromagnets. In addition, the force inputs required at the electromagnets strongly depend on the distance between the gas wiping dies and the electromagnets.
- In favor of lower required electromagnetic forces, it can be better to compensate only certain modes of the transverse strip profile at the gas wiping dies by the feedforward controller.
- The results of the optimal feedforward controller were compared to those of the standard control approach, where zero position set-points are commanded to all position controllers of the electromagnetic stabilizer.

CHAPTER 5

Suppression of harmonic disturbances

This chapter is significantly based on the author's publications [28, 29].

5.1 Motivation and design

The following investigations are carried out on the experimental test rig shown in Fig. 5.1. This experimental test rig takes into account the main effects necessary for the design of a robust and feasible vibration control strategy. The test rig mimics the scenario of the industrial hot-dip galvanizing line presented in Section 1, see also [21]. The positions ❶ to ❹ highlighted in Fig. 5.1 correspond to those in Fig. 1.11a. In Fig. 5.1, ❶ is the position of a disturbance actuator, the transverse strip displacement at the position ❷ is the system output y, the electromagnetic actuator at the position ❸ serves as the control input, and ❹ is the position of the (single) displacement sensor output $\bar{y}$ used for the observer. All remaining laser displacement sensors in the experimental test rig (including the one that measures y) are only used for validation purposes during the experiments. The moderate axial bulk velocities of the strips in hot-dip galvanizing lines only have a small effect on the transverse strip dynamics. Therefore, it is justified to work without an axial bulk velocity in the experimental test rig. The tensile load N_{xx} on the strip of the experimental test rig can be precisely adjusted.

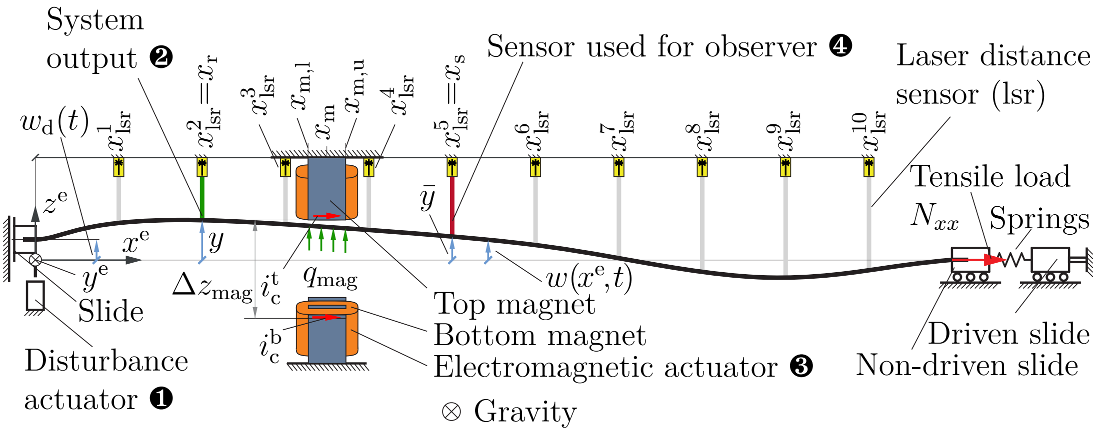

Figure 5.1: Experimental test rig with a clamped steel strip.

The steel strip has the length L, the width b, and the thickness h. Because the width b of the strip is small compared to its length L, the strip may be considered as a beam with the transverse displacement $w = w(x^\mathrm{e}, t)$. For the boundary conditions, a cantilever-mounted strip is considered at the position $x^\mathrm{e} = L$ and a zero-slope-mounted strip with an external disturbance $w(0,t) = w_\mathrm{d}(t)$ at $x^\mathrm{e} = 0$. At the boundary $x^\mathrm{e} = L$, the constant tensile load N_{xx} on the strip is realized by an actively controlled slide. Gravity acts along the lateral direction y^e of the strip and thus does not influence the transverse strip displacement. Air resistance at the surface of the strip is assumed to cause viscous damping. Also, the viscoelastic material behavior of the strip is taken into account. The residual curvatures of the strip are assumed to be zero. The distributed transverse load caused by the electromagnetic actuator is denoted by $q_\mathrm{mag} = q_\mathrm{mag}(x^\mathrm{e}, t)$ and assumed to be uniform. It thus reads as

$$q_\mathrm{mag}(x^\mathrm{e}, t) = \begin{cases} \frac{f_\mathrm{mag}(t)}{\Delta x_\mathrm{m} b} & \text{for } x_\mathrm{m,l} \leq x^\mathrm{e} \leq x_\mathrm{m,u} \\ 0 & \text{else,} \end{cases} \tag{5.1}$$

where the total electromagnetic force f_mag serves as control input. Figure 5.1 indicates the positions $x_\mathrm{m,l} = x_\mathrm{m} - \frac{\Delta x_\mathrm{m}}{2}$ and $x_\mathrm{m,u} = x_\mathrm{m} + \frac{\Delta x_\mathrm{m}}{2}$.

5.2 State-space model of the strip shape

Assume a periodic disturbance $w_\mathrm{d}(t) = w_\mathrm{d}^1 + \cdots + w_\mathrm{d}^v$ with v harmonics and an unknown but constant fundamental angular frequency ω_d. Thus, the continuous-time linear exogenous disturbance model can be written in the form

$$\dot{\mathbf{w}}_\mathrm{d} = \mathbf{A}_\mathrm{d}(\omega_\mathrm{d})\mathbf{w}_\mathrm{d}, \qquad \mathbf{w}_{\mathrm{d},0} = \mathbf{w}_\mathrm{d}(0) \tag{5.2a}$$

$$\mathbf{w}_\mathrm{d} = \begin{bmatrix} w_\mathrm{d}^1 & \dot{w}_\mathrm{d}^1 & w_\mathrm{d}^2 & \dot{w}_\mathrm{d}^2 & \dots & w_\mathrm{d}^v & \dot{w}_\mathrm{d}^v \end{bmatrix}^\mathrm{T} \tag{5.2b}$$

$$\mathbf{A}_\mathrm{d}^l(\omega_\mathrm{d}) = \begin{bmatrix} 0 & 1 \\ -(l\omega_\mathrm{d})^2 & 0 \end{bmatrix} \tag{5.2c}$$

$$\mathbf{A}_{\mathrm{d}}(\omega_{\mathrm{d}}) = \mathrm{diag}\Big(\mathbf{A}_{\mathrm{d}}^{1}(\omega_{\mathrm{d}}),\ \dots\ ,\mathbf{A}_{\mathrm{d}}^{\upsilon}(\omega_{\mathrm{d}})\Big) \tag{5.2d}$$

$$w_{\mathrm{d}} = \begin{bmatrix}1 & 0 & 1 & 0 & \dots & 1 & 0\end{bmatrix}\mathbf{w}_{\mathrm{d}}, \tag{5.2e}$$

with υ decoupled, independent systems. The states w_{d}^{l} and $\dot{w}_{\mathrm{d}}^{l}$ denote the displacement and the velocity of the harmonics $l = 1, \dots, \upsilon$, respectively.

A geometrically linear beam model of the strip in the experimental test rig can be deduced from (2.46). In this case, the solution of the in-plane system (2.46a) is trivial. It yields a constant tensile load N_{xx} on the strip. For the out-of-plane system (2.46b), the choice $n_{\mathrm{yw}} = 0$ is used to eliminate the dependence on y^{e}. Note that $D = \frac{Eh^3}{12}$ is used in (2.16b) instead of $D = \frac{Eh^3}{12(1-\nu^2)}$. Applying the assumptions from Section 5.1, the out-of-plane system changes to

$$\tilde{\mathbf{M}}\ddot{\tilde{\mathbf{t}}} + \tilde{\mathbf{D}}\dot{\tilde{\mathbf{t}}} + \tilde{\mathbf{K}}\tilde{\mathbf{t}} = \tilde{\mathbf{b}}u + \tilde{\mathbf{h}}^{q_{\mathrm{p}}}q_{\mathrm{p}} - \sum_{l=1}^{\upsilon}\Big(\tilde{\mathbf{b}}^{w_0}w_{\mathrm{d}}^{l} + \tilde{\mathbf{b}}^{\dot{w}_0}\dot{w}_{\mathrm{d}}^{l} + \tilde{\mathbf{b}}^{\ddot{w}_0}\ddot{w}_{\mathrm{d}}^{l}\Big) \tag{5.3a}$$

$$\bar{y} = w_{\mathrm{s}} = \tilde{\mathbf{c}}_{\mathrm{s}}^{\mathrm{T}}\tilde{\mathbf{t}}, \qquad y = w_{\mathrm{r}} = \tilde{\mathbf{c}}_{\mathrm{r}}^{\mathrm{T}}\tilde{\mathbf{t}}, \quad \text{and} \qquad w_{\mathrm{m}} = \tilde{\mathbf{c}}_{\mathrm{m}}^{\mathrm{T}}\tilde{\mathbf{t}}, \tag{5.3b}$$

with the abbreviation $\tilde{\mathbf{K}} = \tilde{\mathbf{K}}^{\bar{\mathrm{M}}} + \tilde{\mathbf{K}}^{\mathrm{N}}$. Using n finite elements in longitudinal direction, the model (5.3a) has $\bar{n} = 2(n-1)$ mechanical degrees of freedom. Note that in contrast to the model (2.46b), where a simply supported strip is assumed at $x = L$, the Dirichlet boundary condition $\partial_x w|_{x=L} = 0$ is considered in (5.3a). On the left-hand side, $\tilde{\mathbf{M}}$, $\tilde{\mathbf{D}}$, and $\tilde{\mathbf{K}}$ denote the mass, damping, and stiffness matrices, respectively. On the right-hand side, $\tilde{\mathbf{b}}$ amplifies the control input $u = f_{\mathrm{mag}}$ and $\tilde{\mathbf{h}}^{q_{\mathrm{p}}}$ accounts for the distributed load q_{p}. The quantity w_0 in (2.46) was renamed to w_{d}^{l}. Moreover, since w_{d}^{l} is a function of time, the influence of its time derivatives $\dot{w}_{\mathrm{d}}^{l}$ and $\ddot{w}_{\mathrm{d}}^{l}$ is considered by the additional input vectors $\tilde{\mathbf{b}}^{\dot{w}_0}$ and $\tilde{\mathbf{b}}^{\ddot{w}_0}$, respectively. They are obtained by analogy to $\tilde{\mathbf{b}}^{w_0}$. In (5.3b), $\bar{y}$ is the sensor output at the position $x^{\mathrm{e}} = x_{\mathrm{s}}$, y denotes the system output at the position $x^{\mathrm{e}} = x_{\mathrm{r}}$, and w_{m} is the displacement output at the electromagnets, i.e., at the position $x^{\mathrm{e}} = x_{\mathrm{m}}$.

If (5.2) is combined with (5.3a), this yields the state-space representation of the strip model

$$\dot{\mathbf{x}} = \mathbf{A}\mathbf{x} + \mathbf{b}u + \mathbf{G}_{\mathrm{d}}(\omega_{\mathrm{d}})\mathbf{w}_{\mathrm{d}} + \mathbf{h}_{\mathrm{p}}q_{\mathrm{p}} \tag{5.4a}$$

$$\bar{y} = w_{\mathrm{s}} = \mathbf{c}_{\mathrm{s}}^{\mathrm{T}}\mathbf{x}, \qquad y = w_{\mathrm{r}} = \mathbf{c}_{\mathrm{r}}^{\mathrm{T}}\mathbf{x}, \quad \text{and} \qquad w_{\mathrm{m}} = \mathbf{c}_{\mathrm{m}}^{\mathrm{T}}\mathbf{x}, \tag{5.4b}$$

with the state vector $\mathbf{x}^{\mathrm{T}} = \begin{bmatrix}\tilde{\mathbf{t}}^{\mathrm{T}} & \dot{\tilde{\mathbf{t}}}^{\mathrm{T}}\end{bmatrix} \in \mathbb{R}^{2\bar{n}}$, the states $\mathbf{w}_{\mathrm{d}}$ of the disturbance model, the abbreviations

$$\mathbf{A} = \begin{bmatrix}\mathbf{0}^{\bar{n}\times\bar{n}} & \mathbf{I}^{\bar{n}\times\bar{n}} \\ -\tilde{\mathbf{M}}^{-1}\tilde{\mathbf{K}} & -\tilde{\mathbf{M}}^{-1}\tilde{\mathbf{D}}\end{bmatrix}, \qquad \mathbf{b} = \begin{bmatrix}\mathbf{0}^{\bar{n}\times 1} \\ \tilde{\mathbf{M}}^{-1}\tilde{\mathbf{b}}\end{bmatrix} \tag{5.5a}$$

$$\mathbf{h}_{\mathrm{p}} = \begin{bmatrix}\mathbf{0}^{\bar{n}\times 1} \\ \tilde{\mathbf{M}}^{-1}\tilde{\mathbf{h}}^{q_{\mathrm{p}}}\end{bmatrix} \tag{5.5b}$$

$$\mathbf{G}_{\mathrm{d}}(\omega_{\mathrm{d}}) = \begin{bmatrix} \mathbf{G}_{\mathrm{d},1}(\omega_{\mathrm{d}}) & \dots & \mathbf{G}_{\mathrm{d},v}(\omega_{\mathrm{d}}) \end{bmatrix} \tag{5.5c}$$

$$\mathbf{G}_{\mathrm{d},l}(\omega_{\mathrm{d}}) = \begin{bmatrix} \mathbf{0}^{\bar{n}\times 1} & \mathbf{0}^{\bar{n}\times 1} \\ -\tilde{\mathbf{M}}^{-1}\left(\tilde{\mathbf{b}}^{\mathrm{w}_0} - (l\omega_{\mathrm{d}})^2\tilde{\mathbf{b}}^{\ddot{\mathrm{w}}_0}\right) & -\tilde{\mathbf{M}}^{-1}\tilde{\mathbf{b}}^{\dot{\mathrm{w}}_0} \end{bmatrix} \tag{5.5d}$$

$$\mathbf{c}_{\mathrm{s}} = \begin{bmatrix} \tilde{\mathbf{c}}_{\mathrm{s}}^{\mathrm{T}} & \mathbf{0}^{1\times\bar{n}} \end{bmatrix}^{\mathrm{T}}, \quad \mathbf{c}_{\mathrm{r}} = \begin{bmatrix} \tilde{\mathbf{c}}_{\mathrm{r}}^{\mathrm{T}} & \mathbf{0}^{1\times\bar{n}} \end{bmatrix}^{\mathrm{T}}, \quad \mathbf{c}_{\mathrm{m}} = \begin{bmatrix} \tilde{\mathbf{c}}_{\mathrm{m}}^{\mathrm{T}} & \mathbf{0}^{1\times\bar{n}} \end{bmatrix}^{\mathrm{T}}, \tag{5.5e}$$

and the identity matrix $\mathbf{I}$. The model (5.2) and (5.4) is used as a basis for designing the vibration control strategy. The zero-order-hold discretization of (5.2) and (5.4) for the sampling time T_{s} has the form

$$\mathbf{x}_{k+1} = \mathbf{\Phi}_{\mathrm{s}}\mathbf{x}_k + \boldsymbol{\gamma}u_k + \mathbf{\Delta}(\omega_{\mathrm{d},k})\mathbf{w}_{\mathrm{d},k} + \boldsymbol{\sigma}q_{\mathrm{p},k}, \ \mathbf{x}_0 = \mathbf{x}(0) \tag{5.6a}$$

$$\mathbf{w}_{\mathrm{d},k+1} = \mathbf{\Phi}_{\mathrm{d}}(\omega_{\mathrm{d},k})\mathbf{w}_{\mathrm{d},k}, \qquad \mathbf{w}_{\mathrm{d},0} = \mathbf{w}_{\mathrm{d}}(0) \tag{5.6b}$$

$$\omega_{\mathrm{d},k+1} = \omega_{\mathrm{d},k}, \qquad \omega_{\mathrm{d},0} = \omega_{\mathrm{d}}(0) \tag{5.6c}$$

$$\bar{y}_k = w_{\mathrm{s},k} = \mathbf{c}_{\mathrm{s}}^{\mathrm{T}}\mathbf{x}_k, \quad y_k = w_{\mathrm{r},k} = \mathbf{c}_{\mathrm{r}}^{\mathrm{T}}\mathbf{x}_k, \quad w_{\mathrm{m},k} = \mathbf{c}_{\mathrm{m}}^{\mathrm{T}}\mathbf{x}_k \tag{5.6d}$$

$$\mathbf{\Phi}_{\mathrm{s}} = \exp(\mathbf{A}T_{\mathrm{s}}), \qquad \mathbf{\Phi}_{\mathrm{d}}(\omega_{\mathrm{d},k}) = \exp(\mathbf{A}_{\mathrm{d}}(\omega_{\mathrm{d},k})T_{\mathrm{s}}) \tag{5.6e}$$

$$\boldsymbol{\gamma} = \int_0^{T_{\mathrm{s}}} \exp(\mathbf{A}\tau)\mathrm{d}\tau\mathbf{b} \tag{5.6f}$$

$$\mathbf{\Delta}(\omega_{\mathrm{d},k}) = \int_0^{T_{\mathrm{s}}} \exp(\mathbf{A}\tau)\mathbf{G}_{\mathrm{d}}(\omega_{\mathrm{d},k})\exp(\mathbf{A}_{\mathrm{d}}(\omega_{\mathrm{d},k})(T_{\mathrm{s}}-\tau))\mathrm{d}\tau \tag{5.6g}$$

$$\boldsymbol{\sigma} = \int_0^{T_{\mathrm{s}}} \exp(\mathbf{A}\tau)\mathrm{d}\tau\mathbf{h}_{\mathrm{p}}, \tag{5.6h}$$

where the index k refers to the time instant $t = kT_{\mathrm{s}}$. In this model, the frequency ω_{d} of the disturbance is assumed to be constant. Nevertheless, as will be shown in the observer design, the estimated frequency can vary over time.

5.3 Vibration control strategy

Non-collocated control systems typically exhibit a non-minimum phase behavior. This may cause difficulties in the design of a compensator in the frequency domain if any of the right-half-plane zeros of the system is within the bandwidth of the closed-loop system, see, e.g., [48]. However, the non-minimum phase behavior is of minor importance when using a state-space description for the design of a vibration control strategy. Using the state-space description (5.6), the non-minimum phase behavior just renders the tuning of the controller and observer parameters slightly more difficult.

In a first step, a control strategy will be designed under the assumption that all states of the system (5.6a), of the exogenous disturbance model (5.6b), and of the disturbance frequency model (5.6c) are known. The controller design is based on a combination of a linear quadratic regulator (LQR), which ensures broadband suppression of disturbances, and a disturbance feedforward concept that exploits the theory of invariant manifolds. The design is tailored to the rejection of multi-harmonic disturbances (narrowband disturbances), see, e.g., [72–74, 86]. Since the transverse displacement can be measured at only one position of the strip, see sensor output at the position x_s in Fig. 5.1, an observer has to be developed in a second step.

5.3.1 Controller design

The input $q_{\mathrm{p},k}$ in (5.6) is set to zero for the controller design. The frequency ω_d is constant or only slowly varying and is estimated by the state observer. Hence, it is reasonable to consider $\omega_{\mathrm{d},k} = \omega_\mathrm{d}(kT_\mathrm{s})$ to be known and constant within the sampling interval $kT_\mathrm{s} \leq t < (k+1)T_\mathrm{s}$. Moreover, the exogenous disturbance model (5.2) is marginally stable because all eigenvalues of $\mathbf{A}_\mathrm{d}(\omega_{\mathrm{d},k})$ are on the imaginary axis and distinct, see, e.g., [62, 87].

The state feedback control law

$$u_k = u_{\mathrm{x},k} + u_{\mathrm{w},k} = \mathbf{k}_\mathrm{x}^\mathrm{T}\mathbf{x}_k + \mathbf{k}_\mathrm{w}^\mathrm{T}\mathbf{w}_{\mathrm{d},k} \tag{5.7}$$

is proposed, where the feedback gains $\mathbf{k}_\mathrm{x} \in \mathbb{R}^{2\bar{n}}$ and $\mathbf{k}_\mathrm{w} \in \mathbb{R}^{2\upsilon}$ have to be properly designed. The LQR with the static feedback gain $\mathbf{k}_\mathrm{x}$ ensures broadband suppression of disturbances. However, narrowband disturbances cannot be rejected by the LQR, cf. [60]. To eliminate such narrowband disturbances, the LQR feedback signal is augmented by a feedforward signal of the disturbance state $\mathbf{w}_{\mathrm{d},k}$ with the gain $\mathbf{k}_\mathrm{w}$. The feedback gain $\mathbf{k}_\mathrm{x}$ follows from the solution of the LQR problem for the cost function

$$\bar{J}(\mathbf{x}_0) = \sum_{k=0}^{\infty}\Big(\mathbf{x}_k^\mathrm{T}\mathbf{Q}\mathbf{x}_k + u_{\mathrm{x},k}Ru_{\mathrm{x},k}\Big), \tag{5.8}$$

with the positive semi-definite weighting matrix $\mathbf{Q}$ and the positive weighting factor R, subject to the constraint $\mathbf{x}_{k+1} = \mathbf{\Phi}_\mathrm{s}\mathbf{x}_k + \boldsymbol{\gamma}u_{\mathrm{x},k}$ according to (5.6a). For this design step, $\mathbf{w}_{\mathrm{d},k}$ and $q_{\mathrm{p},k}$ are set to zero. In (5.8), the matrix $\mathbf{Q}$ is chosen to weight the transverse strip displacements $w(x_l,t)$ and the corresponding velocities $\dot{w}(x_l,t)$ at equidistant positions $x_l, l = 1,\ldots,\hat{m}$ along the direction x^e of the strip in the form

$$\mathbf{Q} = \begin{bmatrix} f_\mathrm{p}\hat{\mathbf{c}}^\mathrm{T}\hat{\mathbf{c}} & \mathbf{0} \\ \mathbf{0} & f_\mathrm{v}\hat{\mathbf{c}}^\mathrm{T}\hat{\mathbf{c}} \end{bmatrix}, \tag{5.9}$$

where positive weights f_p, f_v and $\hat{\mathbf{c}} = [\tilde{\mathbf{c}}_1,\ldots,\tilde{\mathbf{c}}_l,\ldots,\tilde{\mathbf{c}}_{\hat{m}}]^\mathrm{T}$ are used. The entries $\tilde{\mathbf{c}}_l$ are defined analogous to (5.3b). The optimal feedback gain $\mathbf{k}_\mathrm{x}$ can be calculated in the form, see, e.g., [88]

$$\mathbf{k}_\mathrm{x}^\mathrm{T} = -\Big(R + \boldsymbol{\gamma}^\mathrm{T}\mathbf{P}\boldsymbol{\gamma}\Big)^{-1}\Big(\boldsymbol{\gamma}^\mathrm{T}\mathbf{P}\mathbf{\Phi}_\mathrm{s}\Big), \tag{5.10}$$

where $\mathbf{P}$ denotes the solution of the discrete algebraic Riccati equation given by

$$\mathbf{P} = \mathbf{Q} + \mathbf{\Phi}_\mathrm{s}^\mathrm{T}\mathbf{P}\mathbf{\Phi}_\mathrm{s} - \Big(\boldsymbol{\gamma}^\mathrm{T}\mathbf{P}\mathbf{\Phi}_\mathrm{s}\Big)^\mathrm{T}\Big(R + \boldsymbol{\gamma}^\mathrm{T}\mathbf{P}\boldsymbol{\gamma}\Big)^{-1}\Big(\boldsymbol{\gamma}^\mathrm{T}\mathbf{P}\mathbf{\Phi}_\mathrm{s}\Big). \tag{5.11}$$

In case that the pair $(\mathbf{\Phi}_\mathrm{s}, \boldsymbol{\gamma})$ is stabilizable and the pair $\left(\sqrt{\mathbf{Q}}, \mathbf{\Phi}_\mathrm{s}\right)$ is detectable, the system

$$\mathbf{x}_{k+1} = \left(\mathbf{\Phi}_\mathrm{s} + \boldsymbol{\gamma}\mathbf{k}_\mathrm{x}^\mathrm{T}\right)\mathbf{x}_k, \quad \mathbf{x}_0 = \mathbf{x}(0) \tag{5.12}$$

is asymptotically stable.

In the next design step, non-zero values $\mathbf{w}_{\mathrm{d},k}$ are considered. Inserting (5.7) into (5.6) for $q_{\mathrm{p},k} = 0$ gives the closed-loop system

$$\mathbf{x}_{k+1} = \left(\mathbf{\Phi}_\mathrm{s} + \boldsymbol{\gamma}\mathbf{k}_\mathrm{x}^\mathrm{T}\right)\mathbf{x}_k + \left(\boldsymbol{\gamma}\mathbf{k}_\mathrm{w}^\mathrm{T} + \mathbf{\Delta}(\omega_{\mathrm{d},k})\right)\mathbf{w}_{\mathrm{d},k} \tag{5.13a}$$

$$y_k = \mathbf{c}_\mathrm{r}^\mathrm{T}\mathbf{x}_k. \tag{5.13b}$$

Applying the transformation

$$\mathbf{z}_k = \mathbf{x}_k - \mathbf{\Pi}\mathbf{w}_{\mathrm{d},k}, \tag{5.14}$$

see [86], with a yet unknown matrix $\mathbf{\Pi}$ to (5.13) yields the transformed closed-loop system

$$\mathbf{z}_{k+1} = \left(\mathbf{\Phi}_\mathrm{s} + \boldsymbol{\gamma}\mathbf{k}_\mathrm{x}^\mathrm{T}\right)\mathbf{z}_k + \left(\mathbf{\Delta}(\omega_{\mathrm{d},k}) + \boldsymbol{\gamma}\mathbf{k}_\mathrm{w}^\mathrm{T} - \mathbf{\Pi}\mathbf{\Phi}_\mathrm{d}(\omega_{\mathrm{d},k}) + \left(\mathbf{\Phi}_\mathrm{s} + \boldsymbol{\gamma}\mathbf{k}_\mathrm{x}^\mathrm{T}\right)\mathbf{\Pi}\right)\mathbf{w}_{\mathrm{d},k} \tag{5.15a}$$

$$y_k = \mathbf{c}_\mathrm{r}^\mathrm{T}\mathbf{z}_k + \mathbf{c}_\mathrm{r}^\mathrm{T}\mathbf{\Pi}\mathbf{w}_{\mathrm{d},k} \tag{5.15b}$$

with the new state $\mathbf{z}_k$. If

$$\mathbf{\Delta}(\omega_{\mathrm{d},k}) + \boldsymbol{\gamma}\mathbf{k}_\mathrm{w}^\mathrm{T} - \mathbf{\Pi}\mathbf{\Phi}_\mathrm{d}(\omega_{\mathrm{d},k}) + \left(\mathbf{\Phi}_\mathrm{s} + \boldsymbol{\gamma}\mathbf{k}_\mathrm{x}^\mathrm{T}\right)\mathbf{\Pi} = \mathbf{0} \tag{5.16a}$$

$$\mathbf{c}_\mathrm{r}^\mathrm{T}\mathbf{\Pi} = \mathbf{0} \tag{5.16b}$$

can be solved for the unknown quantities $\mathbf{\Pi}$ and $\mathbf{k}_\mathrm{w}$, (5.15) simplifies to the exponentially stable autonomous system

$$\mathbf{z}_{k+1} = \left(\mathbf{\Phi}_\mathrm{s} + \boldsymbol{\gamma}\mathbf{k}_\mathrm{x}^\mathrm{T}\right)\mathbf{z}_k \tag{5.17a}$$

$$y_k = \mathbf{c}_\mathrm{r}^\mathrm{T}\mathbf{z}_k. \tag{5.17b}$$

Hence, the hyperplane (attractive manifold) $\mathbf{z}_k = \mathbf{0}$ is invariant and asymptotically stable and the system output y_k asymptotically converges to zero. Thus, the closed-loop system (5.6a) and (5.7) with $q_{\mathrm{p},k} = 0$ is asymptotically stable in the new state $\mathbf{z}_k$ and the multi-harmonic disturbance w_d is asymptotically rejected in the output y. The condition (5.16a) can be rewritten as a Sylvester equation [86]

$$\hat{\mathbf{A}}\mathbf{\Pi} + \mathbf{\Pi}\hat{\mathbf{B}} = \hat{\mathbf{C}}, \tag{5.18}$$

with

$$\hat{\mathbf{A}} = \left(\mathbf{\Phi}_\mathrm{s} + \boldsymbol{\gamma}\mathbf{k}_\mathrm{x}^\mathrm{T}\right) \tag{5.19a}$$

$$\hat{\mathbf{B}} = -\mathbf{\Phi}_{\mathrm{d}}(\omega_{\mathrm{d},k}) \tag{5.19b}$$

$$\hat{\mathbf{C}}(\mathbf{k}_{\mathrm{w}}) = -\mathbf{\Delta}(\omega_{\mathrm{d},k}) - \boldsymbol{\gamma}\mathbf{k}_{\mathrm{w}}^{\mathrm{T}}. \tag{5.19c}$$

All eigenvalues of $-\hat{\mathbf{B}}$ are on the unit circle, whereas all eigenvalues of the closed-loop dynamic matrix $\hat{\mathbf{A}}$ are within the unit circle. A unique solution $\mathbf{\Pi}$ of (5.18) exists because all eigenvalues of $\hat{\mathbf{A}}$ and $-\hat{\mathbf{B}}$ are distinct, see, e.g., [89]. A unique solution $\mathbf{\Pi}$ and $\mathbf{k}_{\mathrm{w}}$ of the constrained Sylvester equation (5.16) can be calculated, if the eigenvalues of $-\hat{\mathbf{B}}$ and $\hat{\mathbf{A}}$ are distinct and if the discrete-time transfer function of the closed-loop system from the control input $u_{\mathrm{w},k}$ to the system output y_k does not exhibit transmission zeros at $\exp(\pm jl\omega_{\mathrm{d}}T_{\mathrm{s}})$ with $l \in \{1, \ldots, \upsilon\}$. In [73], necessary and sufficient conditions concerning the solvability of the so-called regulator equations (5.18) and (5.16b) are described for continuous-time systems.

Finally, the feedback gain $\mathbf{k}_{\mathrm{w}}$ can be calculated by solving (5.16) for a given frequency ω_{d}. Because $\omega_{\mathrm{d},k}$ can vary and is not known in advance, the feedback gains $\mathbf{k}_{\mathrm{w}}$ are computed up front and stored in a look-up table for various values of ω_{d} in the relevant range $[\omega_{\mathrm{l}}, \omega_{\mathrm{u}}]$. A linear interpolation between the stored values is performed upon execution of the control law to calculate the feedback gains for the respective frequency. In this way, the control algorithm can be executed with modest computational effort and thus in realtime.

5.3.2 Observer design

Because the states $\mathbf{x}$, $\mathbf{w}_{\mathrm{d}}$, and ω_{d} cannot be directly measured, a state observer is designed in the form of an extended Kalman filter (EKF) [90] for online estimation of these quantities. The state observer is based on the measured transverse strip displacement $\bar{y}_k$ at the sensor position $x = x_{\mathrm{s}}$. Two slightly different versions of the extended Kalman filter are proposed. An EKF using the explicit discrete-time solution of the observer model is described in Section 5.3.2.1. A drawback of this method is the necessity of costly interpolations of precalculated higher-dimensional look-up tables. In Section 5.3.2.2, a more advanced and efficient implementation of the extended Kalman filter is proposed, where this costly interpolation is avoided.

5.3.2.1 EKF based on the explicit discrete-time model

For the observer design, the quantity $q_{\mathrm{p},k}$ in (5.6a) is considered as process noise acting on the strip dynamics. Moreover, the quantities $p^l_{\mathrm{w_d},k}$, $p^l_{\dot{\mathrm{w}}_\mathrm{d},k}$ with $l = 1, \ldots, \upsilon$, and $p_{\omega,k}$ are added as process noise to (5.6b) and (5.6c), respectively, and $v_{\mathrm{n},k}$ is considered as measurement noise in the output equation (5.6d). This finally leads to a system in the form

$$\bar{\mathbf{x}}_{k+1} = \bar{\mathbf{\Phi}}(\omega_{\mathrm{d},k})\bar{\mathbf{x}}_k + \bar{\boldsymbol{\gamma}}u_k + \bar{\mathbf{\Sigma}}\bar{\mathbf{p}}_k \tag{5.20a}$$

$$\bar{y}_k = \bar{\mathbf{c}}_s^{\mathrm{T}}\bar{\mathbf{x}}_k + v_{\mathrm{n},k}, \tag{5.20b}$$

with the state vector $\bar{\mathbf{x}}_k = [\mathbf{x}_k^{\mathrm{T}}, \mathbf{w}_{\mathrm{d},k}^{\mathrm{T}}, \omega_{\mathrm{d},k}]^{\mathrm{T}} \in \mathbb{R}^{\bar{m}}$ with $\bar{m} = 2\bar{n} + 2\upsilon + 1$ and

$$\bar{\mathbf{\Phi}}(\omega_{\mathrm{d},k}) = \begin{bmatrix} \mathbf{\Phi}_{\mathrm{s}} & \mathbf{\Delta}(\omega_{\mathrm{d},k}) & \mathbf{0} \\ \mathbf{0} & \mathbf{\Phi}_{\mathrm{d}}(\omega_{\mathrm{d},k}) & \mathbf{0} \\ \mathbf{0} & \mathbf{0} & 1 \end{bmatrix} \tag{5.21a}$$

$$\bar{\boldsymbol{\gamma}} = \begin{bmatrix} \boldsymbol{\gamma}^{\mathrm{T}} & \mathbf{0} & 0 \end{bmatrix}^{\mathrm{T}} \tag{5.21b}$$

$$\bar{\mathbf{\Sigma}} = \begin{bmatrix} \boldsymbol{\sigma} & \mathbf{0} & \mathbf{0} \\ \mathbf{0} & \mathbf{I}^{2\upsilon\times 2\upsilon} & \mathbf{0} \\ 0 & \mathbf{0} & 1 \end{bmatrix} \tag{5.21c}$$

$$\bar{\mathbf{p}}_k = \begin{bmatrix} q_{\mathrm{p},k} & \mathbf{p}_{\mathrm{d},k}^{\mathrm{T}} & p_{\omega,k} \end{bmatrix}^{\mathrm{T}}, \quad \mathbf{p}_{\mathrm{d},k}^{\mathrm{T}} = \begin{bmatrix} p_{\mathrm{w_d},k}^{1} & p_{\dot{\mathrm{w}}_\mathrm{d},k}^{1} & \dots & p_{\mathrm{w_d},k}^{\upsilon} & p_{\dot{\mathrm{w}}_\mathrm{d},k}^{\upsilon} \end{bmatrix} \tag{5.21d}$$

$$\bar{\mathbf{c}}_{\mathrm{s}} = \begin{bmatrix} \mathbf{c}_{\mathrm{s}}^{\mathrm{T}} & \mathbf{0}^{\mathrm{T}} & 0 \end{bmatrix}^{\mathrm{T}}. \tag{5.21e}$$

The model (5.20) serves as a basis for the EKF design. It is assumed that the process noise $\bar{\mathbf{p}}_k$ and the measurement noise $\upsilon_{\mathrm{n},k}$ meet the following conditions

$$\bar{\mathrm{E}}(\upsilon_{\mathrm{n},k}) = 0 \qquad \bar{\mathrm{E}}(\upsilon_{\mathrm{n},k}\upsilon_{\mathrm{n},j}) = \bar{R}\delta_{kj} \tag{5.22a}$$

$$\bar{\mathrm{E}}(\bar{\mathbf{p}}_k) = \mathbf{0} \qquad \bar{\mathrm{E}}\left(\bar{\mathbf{p}}_k\bar{\mathbf{p}}_j^{\mathrm{T}}\right) = \bar{\mathbf{Q}}_k\delta_{kj} \tag{5.22b}$$

$$\bar{\mathrm{E}}(\bar{\mathbf{p}}_k\upsilon_{\mathrm{n},j}) = \mathbf{0}, \tag{5.22c}$$

with the expected value $\bar{\mathrm{E}}(\cdot)$, the Kronecker delta δ_{kj}, the positive definite covariance matrix $\bar{\mathbf{Q}}_k$, and the positive variance $\bar{R}$. According to [71], the EKF discrete-time (a priori) prediction equations of the state and error covariance are given by

$$\hat{\bar{\mathbf{x}}}_{k+1}^{-} = \bar{\mathbf{\Phi}}\left(\hat{\omega}_{\mathrm{d},k}^{+}\right)\hat{\bar{\mathbf{x}}}_k^{+} + \bar{\boldsymbol{\gamma}}u_k \tag{5.23a}$$

$$\mathbf{P}_{k+1}^{-} = \Delta\bar{\mathbf{\Phi}}\left(\hat{\omega}_{\mathrm{d},k}^{+}, \hat{\mathbf{w}}_{\mathrm{d},k}^{+}\right)\mathbf{P}_k^{+}\Delta\bar{\mathbf{\Phi}}^{\mathrm{T}}\left(\hat{\omega}_{\mathrm{d},k}^{+}, \hat{\mathbf{w}}_{\mathrm{d},k}^{+}\right) + \bar{\mathbf{\Sigma}}\bar{\mathbf{Q}}_k\bar{\mathbf{\Sigma}}^{\mathrm{T}}, \tag{5.23b}$$

where $\mathbf{P}_k$ denotes the state error covariance matrix. The estimated values are labeled by the diacritic $\hat{\ }$. The discrete-time (a posteriori) update equations are given by

$$\hat{\mathbf{l}}_k = \mathbf{P}_k^{-}\bar{\mathbf{c}}_{\mathrm{s}}\left(\bar{\mathbf{c}}_{\mathrm{s}}^{\mathrm{T}}\mathbf{P}_k^{-}\bar{\mathbf{c}}_{\mathrm{s}} + \bar{R}\right)^{-1} \tag{5.24a}$$

$$\hat{\bar{\mathbf{x}}}_k^{+} = \hat{\bar{\mathbf{x}}}_k^{-} + \hat{\mathbf{l}}_k\left(\bar{y}_k - \bar{\mathbf{c}}_{\mathrm{s}}^{\mathrm{T}}\hat{\bar{\mathbf{x}}}_k^{-}\right) \tag{5.24b}$$

$$\mathbf{P}_k^{+} = (\mathbf{I} - \hat{\mathbf{l}}_k\bar{\mathbf{c}}_{\mathrm{s}}^{\mathrm{T}})\mathbf{P}_k^{-}. \tag{5.24c}$$

Here, $\hat{\mathbf{l}}_k$ from (5.24a) denotes the near-optimal Kalman gain, (5.24b) gives the updated state estimate, and (5.24c) yields the updated covariance estimate. Moreover, $\Delta\bar{\mathbf{\Phi}}\left(\hat{\omega}_{\mathrm{d},k}^{+}, \hat{\mathbf{w}}_{\mathrm{d},k}^{+}\right)$ in (5.23b) results from the linearization of (5.20a) with respect to the state vector $\bar{\mathbf{x}}_k$ at the point $\hat{\bar{\mathbf{x}}}_k^+$. Using (5.6e), (5.6g), and (5.21a), this yields

$$\Delta\bar{\boldsymbol{\Phi}}\left(\hat{\omega}_{\mathrm{d},k}^+, \hat{\mathbf{w}}_{\mathrm{d},k}^+\right) = \frac{\partial\bar{\boldsymbol{\Phi}}\left(\hat{\omega}_{\mathrm{d},k}^+\right)\hat{\bar{\mathbf{x}}}_k^+}{\partial\hat{\bar{\mathbf{x}}}_k^+} = \begin{bmatrix} \boldsymbol{\Phi}_\mathrm{s} & \boldsymbol{\Delta}\left(\hat{\omega}_{\mathrm{d},k}^+\right) & \boldsymbol{\Xi}\left(\hat{\omega}_{\mathrm{d},k}^+\right)\hat{\mathbf{w}}_{\mathrm{d},k}^+ \\ \mathbf{0} & \boldsymbol{\Phi}_\mathrm{d}\left(\hat{\omega}_{\mathrm{d},k}^+\right) & \boldsymbol{\Xi}_\mathrm{d}\left(\hat{\omega}_{\mathrm{d},k}^+\right)\hat{\mathbf{w}}_{\mathrm{d},k}^+ \\ \mathbf{0} & \mathbf{0} & 1 \end{bmatrix} \tag{5.25}$$

with

$$\begin{aligned} \boldsymbol{\Xi}\left(\hat{\omega}_{\mathrm{d},k}^+\right) = \frac{\partial\boldsymbol{\Delta}\left(\hat{\omega}_{\mathrm{d},k}^+\right)}{\partial\hat{\omega}_{\mathrm{d},k}^+} &= \int_0^{T_\mathrm{s}} \exp(\mathbf{A}\tau)\left(\frac{\partial\mathbf{G}_\mathrm{d}}{\partial\omega_\mathrm{d}}\right)\left(\hat{\omega}_{\mathrm{d},k}^+\right)\exp\left(\mathbf{A}_\mathrm{d}\left(\hat{\omega}_{\mathrm{d},k}^+\right)(T_\mathrm{s}-\tau)\right)\mathrm{d}\tau \\ &+ \int_0^{T_\mathrm{s}} \exp(\mathbf{A}\tau)\mathbf{G}_\mathrm{d}\left(\hat{\omega}_{\mathrm{d},k}^+\right)\exp\left(\mathbf{A}_\mathrm{d}\left(\hat{\omega}_{\mathrm{d},k}^+\right)(T_\mathrm{s}-\tau)\right)\left(\frac{\partial\mathbf{A}_\mathrm{d}}{\partial\omega_\mathrm{d}}\right)\left(\hat{\omega}_{\mathrm{d},k}^+\right)(T_\mathrm{s}-\tau)\mathrm{d}\tau \end{aligned} \tag{5.26a}$$

$$\boldsymbol{\Xi}_\mathrm{d}\left(\hat{\omega}_{\mathrm{d},k}^+\right) = \frac{\partial\boldsymbol{\Phi}_\mathrm{d}\left(\hat{\omega}_{\mathrm{d},k}^+\right)}{\partial\hat{\omega}_{\mathrm{d},k}^+} = \exp\left(\mathbf{A}_\mathrm{d}\left(\hat{\omega}_{\mathrm{d},k}^+\right)T_\mathrm{s}\right)\left(\frac{\partial\mathbf{A}_\mathrm{d}}{\partial\omega_\mathrm{d}}\right)\left(\hat{\omega}_{\mathrm{d},k}^+\right)T_\mathrm{s}. \tag{5.26b}$$

An appropriate choice of the initial conditions $\hat{\bar{\mathbf{x}}}_0^-$ and $\mathbf{P}_0^-$ completes the observer design.

The estimated transverse strip displacement at the positions $x = x_\mathrm{s}$ of the displacement sensor, $x = x_\mathrm{r}$ of the system output (gas wiping dies), $x = x_\mathrm{m}$ of the electromagnets, and at the laser distance sensor positions $x = x_\mathrm{lsr}^l$, $l = 1, \ldots, 10$ (only used for validation purpose) read as

$$\hat{\bar{y}}_k = \hat{w}_{\mathrm{s},k} = \bar{\mathbf{c}}_\mathrm{s}^\mathrm{T}\hat{\bar{\mathbf{x}}}_k, \quad \hat{y}_k = \hat{w}_{\mathrm{r},k} = \bar{\mathbf{c}}_\mathrm{r}^\mathrm{T}\hat{\bar{\mathbf{x}}}_k, \quad \hat{w}_{\mathrm{m},k} = \bar{\mathbf{c}}_\mathrm{m}^\mathrm{T}\hat{\bar{\mathbf{x}}}_k, \tag{5.27}$$

and

$$\hat{w}_{\mathrm{lsr},k}^l = \left(\bar{\mathbf{c}}_\mathrm{lsr}^l\right)^\mathrm{T}\hat{\bar{\mathbf{x}}}_k, \qquad l \in [1, \ldots, 10]. \tag{5.28}$$

The structure of $\bar{\mathbf{c}}_\mathrm{lsr}^l$ is similar to (5.21e). Finally, the control law (5.7) is combined with the extended Kalman filter (5.23), (5.24). This yields

$$u_k = \begin{bmatrix} \mathbf{k}_\mathrm{x}^\mathrm{T} & \left(\mathbf{k}_\mathrm{w}|_{\omega_\mathrm{d}=\hat{\omega}_{\mathrm{d},k+1}^-}\right)^\mathrm{T} & 0 \end{bmatrix}\hat{\bar{\mathbf{x}}}_{k+1}^- \tag{5.29}$$

with $\mathbf{k}_\mathrm{x}$ from (5.10) and $\mathbf{k}_\mathrm{w}|_{\omega_\mathrm{d}=\hat{\omega}_{\mathrm{d},k+1}^-}$ from the solution of the regulator equations (5.18) and (5.16b) for the estimated frequency $\hat{\omega}_{\mathrm{d},k+1}^-$. Here, the predicted state $\hat{\bar{\mathbf{x}}}_{k+1}^-$ at the time step $k+1$ is used instead of $\hat{\bar{\mathbf{x}}}_k^+$ to compensate for the single-step time shift of the input signals.

Using this approach, the discrete-time solution of the system is explicitly calculated, provided that the disturbance frequency ω_d remains constant within every sampling period T_s. In the considered application, the real-time execution of an extended Kalman filter using the explicitly calculated discrete-time model requires an a priori computation and storage of the discrete-time model for the relevant frequency range $\omega_\mathrm{d} \in [\omega_\mathrm{l}, \omega_\mathrm{u}]$ since it depends on ω_d in a complicated way, cf. (5.6) and (5.26). In practice, the system matrices of the model are thus computed for discretized values of ω_d and then evaluated by linear interpolation at every time step, similarly to the interpolation of $\mathbf{k}_\mathrm{w}$ suggested in Section 5.3.1. However, in contrast to the controller, the workload associated with the extended Kalman filter is considerably higher due to the high dimension of the discrete-time model used by the observer, especially in the case of a disturbance with a high number of harmonics.

5.3.2.2 EKF based on an implicit Euler discretization

Combining the continuous-time models (5.2) and (5.4) with the model for a constant disturbance frequency yields the observer design model

$$\dot{\bar{\mathbf{x}}} = \bar{\mathbf{A}}(\omega_\mathrm{d})\bar{\mathbf{x}} + \bar{\mathbf{b}}u + \bar{\mathbf{h}}q_\mathrm{p} \tag{5.30a}$$

$$\bar{\mathbf{y}} = \bar{\mathbf{c}}_\mathrm{s}^\mathrm{T}\bar{\mathbf{x}}. \tag{5.30b}$$

It involves the state vector $\bar{\mathbf{x}} = [\mathbf{x}^\mathrm{T}, \mathbf{w}_\mathrm{d}^\mathrm{T}, \omega_\mathrm{d}]^\mathrm{T}$, the quantities

$$\bar{\mathbf{A}}(\omega_\mathrm{d}) = \begin{bmatrix} \mathbf{A} & \mathbf{G}_\mathrm{d}(\omega_\mathrm{d}) & \mathbf{0} \\ \mathbf{0} & \mathbf{A}_\mathrm{d}(\omega_\mathrm{d}) & \mathbf{0} \\ \mathbf{0} & \mathbf{0} & 0 \end{bmatrix} \tag{5.31a}$$

$$\bar{\mathbf{b}} = \begin{bmatrix} \mathbf{b}^\mathrm{T} & \mathbf{0} & 0 \end{bmatrix}^\mathrm{T} \tag{5.31b}$$

$$\bar{\mathbf{h}} = \begin{bmatrix} \mathbf{h}_\mathrm{p}^\mathrm{T} & \mathbf{0} & 0 \end{bmatrix}^\mathrm{T}, \tag{5.31c}$$

and $\bar{\mathbf{c}}_\mathrm{s}$ according to (5.21e). To avoid the costly interpolation of the look-up table when utilizing a zero-order-hold discretization, (5.30) is discretized using the implicit Euler discretization method together with a zero-order-hold assumption for the inputs u and q_p. The implicit Euler method guarantees a simple and even for large sampling times T_s numerically stable discrete-time model. However, the time integration error grows with larger values of T_s. The simpler explicit Euler method is not used as it would require too small sampling times to ensure numerical stability for the considered weakly damped mechanical system. Finally, the discrete-time model obtained by the implicit Euler method reads as

$$\bar{\mathbf{x}}_{k+1} = \bar{\mathbf{\Phi}}(\omega_{\mathrm{d},k})\bar{\mathbf{x}}_k + \bar{\boldsymbol{\gamma}}(\omega_{\mathrm{d},k})u_k + \bar{\mathbf{\Sigma}}(\omega_{\mathrm{d},k})\bar{\mathbf{p}}_k \tag{5.32a}$$

$$\bar{y}_k = \bar{\mathbf{c}}_s^\mathrm{T}\bar{\mathbf{x}}_k + v_{\mathrm{n},k}, \tag{5.32b}$$

with the abbreviations

$$\bar{\mathbf{\Phi}}(\omega_{\mathrm{d},k}) = \left(\mathbf{I}^{\bar{m}\times\bar{m}} - T_\mathrm{s}\bar{\mathbf{A}}(\omega_{\mathrm{d},k})\right)^{-1} \tag{5.33a}$$

$$\bar{\boldsymbol{\gamma}}(\omega_{\mathrm{d},k}) = \bar{\mathbf{\Phi}}(\omega_{\mathrm{d},k})T_\mathrm{s}\bar{\mathbf{b}} \tag{5.33b}$$

$$\bar{\boldsymbol{\Sigma}}(\omega_{\mathrm{d},k}) = \left[\bar{\boldsymbol{\Phi}}(\omega_{\mathrm{d},k})T_{\mathrm{s}}\bar{\mathbf{h}} \quad \begin{bmatrix} \mathbf{0}^{2\bar{n}\times 2\upsilon+1} \\ \mathbf{I}^{2\upsilon+1\times 2\upsilon+1} \end{bmatrix}\right], \tag{5.33c}$$

$\bar{m} = 2\bar{n} + 2\upsilon + 1$, and $\bar{\mathbf{p}}_{\mathrm{d},k}$ according to (5.21d). In contrast to the system (5.20), the matrices $\bar{\boldsymbol{\Upsilon}}(\omega_{\mathrm{d},k})$ and $\bar{\boldsymbol{\Sigma}}(\omega_{\mathrm{d},k})$ in (5.32) depend on $\omega_{\mathrm{d},k}$. In (5.33), $\omega_{\mathrm{d},k+1}$ was replaced by $\omega_{\mathrm{d},k}$, which is valid due to the assumption of a constant disturbance frequency ω_{d}. Because of the zero-order-hold assumption on the inputs u and q_{p} and contrary to the original implicit Euler method, u_k and $q_{\mathrm{p},k}$ are used in (5.32a) instead of u_{k+1} and $q_{\mathrm{p},k+1}$, respectively.

For an efficient calculation of (5.33a), the special structure of $\mathbf{I}^{\bar{m}\times\bar{m}} - T_{\mathrm{s}}\bar{\mathbf{A}}(\omega_{\mathrm{d},k})$ with many zero entries is utilized. For this, the matrices

$$\boldsymbol{\Lambda} = (\mathbf{I} - T_{\mathrm{s}}\mathbf{A})^{-1} \tag{5.34a}$$

$$\boldsymbol{\Theta}(\omega_{\mathrm{d},k}) = \left(\mathbf{I} - T_{\mathrm{s}}\begin{bmatrix} \mathbf{A}_{\mathrm{d}}(\omega_{\mathrm{d},k}) & \mathbf{0} \\ \mathbf{0} & 0 \end{bmatrix}\right)^{-1} \tag{5.34b}$$

are introduced. This yields

$$\bar{\boldsymbol{\Phi}}(\omega_{\mathrm{d},k}) = \begin{bmatrix} \boldsymbol{\Lambda} & \boldsymbol{\Lambda}T_{\mathrm{s}}\bar{\mathbf{G}}_{\mathrm{d}}(\omega_{\mathrm{d},k})\boldsymbol{\Theta}(\omega_{\mathrm{d},k}) \\ \mathbf{0}^{2\upsilon+1\times 2\bar{n}} & \boldsymbol{\Theta}(\omega_{\mathrm{d},k}) \end{bmatrix}, \tag{5.35}$$

with $\bar{\mathbf{G}}_{\mathrm{d}}(\omega_{\mathrm{d},k}) = \begin{bmatrix}\mathbf{G}_{\mathrm{d}}(\omega_{\mathrm{d},k}) & \mathbf{0}^{2\bar{n}\times 1}\end{bmatrix}$. $\boldsymbol{\Lambda}$ can be numerically calculated in advance and an analytical expression for $\boldsymbol{\Theta}(\omega_{\mathrm{d},k}) \in \mathbb{R}^{2\upsilon+1\times 2\upsilon+1}$ exists. The discrete-time EKF update equations are already defined in (5.24). However, the prediction equations of the state and error covariance in (5.23) have to be replaced by

$$\hat{\bar{\mathbf{x}}}_{k+1}^{-} = \bar{\boldsymbol{\Phi}}\left(\hat{\omega}_{\mathrm{d},k}^{+}\right)\hat{\bar{\mathbf{x}}}_{k}^{+} + \bar{\boldsymbol{\Upsilon}}\left(\hat{\omega}_{\mathrm{d},k}^{+}\right)u_k \tag{5.36a}$$

$$\mathbf{P}_{k+1}^{-} = \Delta\bar{\boldsymbol{\Phi}}\left(\hat{\bar{\mathbf{x}}}_{k}^{+}, u_k\right)\mathbf{P}_{k}^{+}\Delta\bar{\boldsymbol{\Phi}}^{\mathrm{T}}\left(\hat{\bar{\mathbf{x}}}_{k}^{+}, u_k\right) + \bar{\boldsymbol{\Sigma}}\left(\hat{\omega}_{\mathrm{d},k}^{+}\right)\bar{\mathbf{Q}}_k\bar{\boldsymbol{\Sigma}}^{\mathrm{T}}\left(\hat{\omega}_{\mathrm{d},k}^{+}\right), \tag{5.36b}$$

according to (5.32) where $\Delta\bar{\boldsymbol{\Phi}}(\cdot,\cdot)$ is derived below. An implicit equation equivalent to (5.32a) with the assumption $\bar{\mathbf{p}}_k = \mathbf{0}$ reads as

$$\bar{\mathbf{r}}(\bar{\mathbf{x}}_{k+1}, \bar{\mathbf{x}}_k) = \left(\bar{\boldsymbol{\Phi}}(\omega_{\mathrm{d},k})\right)^{-1}\bar{\mathbf{x}}_{k+1} - \bar{\mathbf{x}}_k - T_{\mathrm{s}}\bar{\mathbf{b}}u_k = \mathbf{0}. \tag{5.37}$$

The total differential of (5.37) takes the form

$$\frac{\partial\bar{\mathbf{r}}}{\partial\bar{\mathbf{x}}_{k+1}}\mathrm{d}\bar{\mathbf{x}}_{k+1} + \frac{\partial\bar{\mathbf{r}}}{\partial\bar{\mathbf{x}}_k}\mathrm{d}\bar{\mathbf{x}}_k = \mathbf{0}, \tag{5.38}$$

with

$$\frac{\partial\bar{\mathbf{r}}}{\partial\bar{\mathbf{x}}_{k+1}} = \left(\bar{\boldsymbol{\Phi}}(\omega_{\mathrm{d},k})\right)^{-1} \tag{5.39a}$$

$$\frac{\partial\bar{\mathbf{r}}}{\partial\bar{\mathbf{x}}_k} = -\begin{bmatrix}\mathbf{0}^{\bar{m}\times\bar{m}-1} & T_{\mathrm{s}}\frac{\partial\bar{\mathbf{A}}(\omega_{\mathrm{d},k})}{\partial\omega_{\mathrm{d},k}}\bar{\mathbf{x}}_{k+1}\end{bmatrix} - \mathbf{I}^{\bar{m}\times\bar{m}}. \tag{5.39b}$$

This results in the expression

$$\Delta\bar{\mathbf{\Phi}}(\bar{\mathbf{x}}_k, u_k) = \frac{\mathrm{d}\bar{\mathbf{x}}_{k+1}}{\mathrm{d}\bar{\mathbf{x}}_k} = \bar{\mathbf{\Phi}}(\omega_{\mathrm{d},k}) + \begin{bmatrix}\mathbf{0}^{\bar{m}\times\bar{m}-1} & \bar{\upsilon}(\bar{\mathbf{x}}_k, u_k)\end{bmatrix}, \tag{5.40}$$

with the vector-valued function

$$\bar{\upsilon}(\bar{\mathbf{x}}_k, u_k) = \bar{\mathbf{\Phi}}(\omega_{\mathrm{d},k})\left[T_{\mathrm{s}}\frac{\partial\bar{\mathbf{A}}(\omega_{\mathrm{d},k})}{\partial\omega_{\mathrm{d},k}}\Big(\bar{\mathbf{\Phi}}(\omega_{\mathrm{d},k})\bar{\mathbf{x}}_k + \bar{\mathbf{\gamma}}(\omega_{\mathrm{d},k})u_k\Big)\right]. \tag{5.41}$$

5.4 Overview of the components

In the following, the components of the experimental test rig shown in Fig. 5.1 are described in more detail. A photograph of the setup is shown in Fig. 5.2. Its components are listed in Tab. 5.1. The test strips to be used in the experiment can have lengths L between 1.9 m and 2.1 m, their thicknesses h can range from 0.5 mm to 1.5 mm, and their width b is 150 mm. A dSPACE control system platform is used as real-time hardware to record the measurement signals and to execute the observer and controller algorithms.

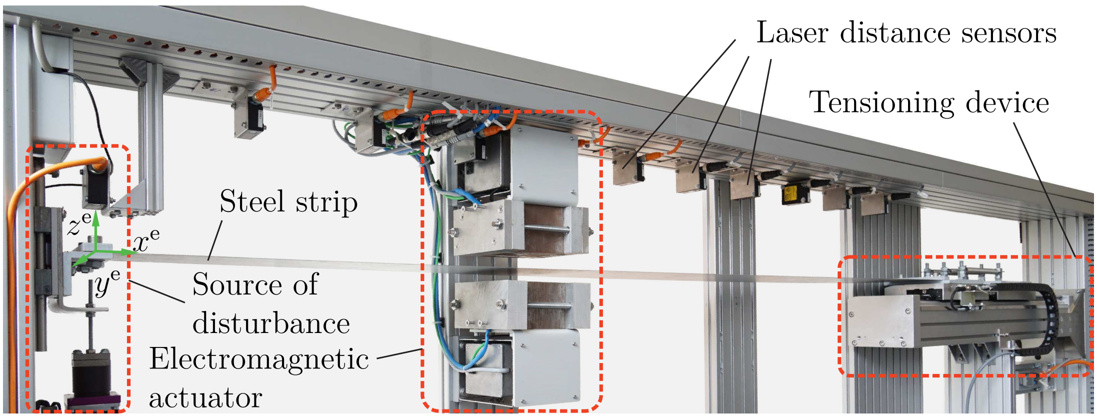

Figure 5.2: Experimental test rig with a clamped test strip.

5.4.1 Tensioning device

The tensioning device for adjusting the tensile load N_{xx} in the strip consists of a non-driven (passive) and a driven (active) horizontal slide. They are connected by three springs in parallel with a measured force-elongation characteristics. One end of the strip is clamped in the non-driven slide. At the other end, the strip is connected to a vertical slide, which is moved by an actuator along the direction z^{e} (transverse strip direction) for applying a disturbance. The tensile load N_{xx} in the strip is controlled based on the measured elongation of the springs. A force

Component	Product, Type (Specification)
Tensioning device	
Linear axis (slides)	Festo, *EGC-185-700-BS*
Parallel kit	Festo, *EAMM-U*
Gear unit	Festo, *EMGA-SAS*
Servo drive	Festo, *EMME-AS*
Force sensor	inelta, *KMM20-5kN*
Spring	Gutekunst, *RZ-162U-43I*
	(three springs in parallel)
Source of disturbance	
Electromechanical cylinder	GUNDA-GmbH, *Colibri-L KE 23K10*
Linear guide	igus, *DryLin W: WS-10-120*
	igus, *WW-10-120-10*
Laser distance sensors	WELOTEC, *OWLE 5060 S1*
Electromagnets	
Current controller	maxon, *ESCON 50/5*
Air gap Δz_{mag}	(50 mm)
Number of windings	(280)
Dimension of core in x^{e}-direction	(100 mm)
Real-time system	dSPACE, *MicroLabBox*

Table 5.1: Components used in the experimental test rig.

sensor was used to calibrate the springs. In contrast to the strip, the spring has a low tensile stiffness. This allows an accurate adjustment of the desired tensile load N_{xx} by controlling the position of the driven slide.

5.4.2 Displacement sensors

As shown in Fig. 5.1, the experimental test rig is equipped with ten laser triangulation sensors referred to as lsr 1, ..., lsr 10. The sensors are located at the equidistant positions $x_{\mathrm{lsr}}^{1}, \ldots, x_{\mathrm{lsr}}^{10}$. They are used for measuring the transverse strip shape during the experiments. Just a single sensor is used for control, i.e., the sensor at the position x_{s} (sensor output). The remaining sensors are only used for monitoring and validation during the experiments but not for control.

5.4.3 Source of disturbance

At the boundary $x^{\mathrm{e}} = 0$, the transverse strip displacement $w_{\mathrm{d}}(t) = w(0,t)$ is prescribed by a disturbance actuator, cf. [91]. This displacement is considered as an external disturbance in the form of a multi-harmonic signal with an arbitrary number of harmonics and various frequencies and amplitudes. The slope of the strip is zero at this point.

5.4.4 Electromagnetic actuator

Figure 5.3 shows the custom-made electromagnetic actuators. Detailed information about the electromagnets is reported in [22]. The electromagnetic force f_{mag} is always attractive, which is why a pair of magnets is required to realize forces in both directions (positive and negative z^{e}-direction).

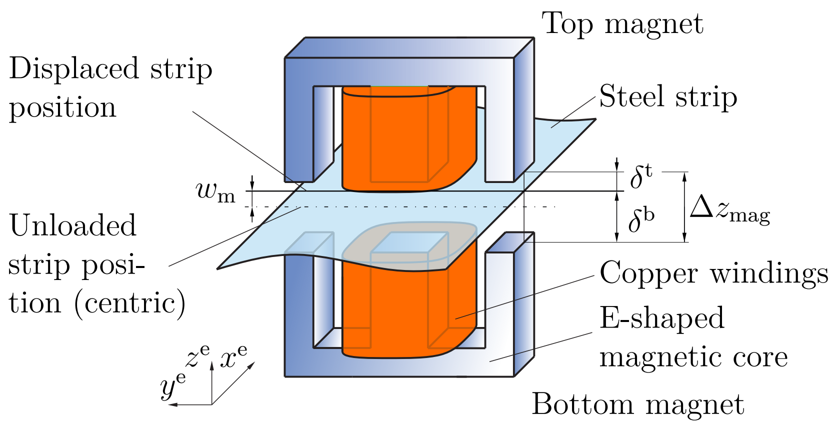

Figure 5.3: Electromagnetic actuator.

Based on the transverse strip displacement w_{m} and the assumption of a negligible strip thickness ($h \ll \Delta z_{\mathrm{mag}}$), the air gaps between the strip and the top

(t) and bottom (b) magnet read as

$$\delta^{\mathrm{t}} = \frac{\Delta z_{\mathrm{mag}}}{2} - w_{\mathrm{m}} \quad \text{and} \quad \delta^{\mathrm{b}} = \frac{\Delta z_{\mathrm{mag}}}{2} + w_{\mathrm{m}}, \tag{5.42}$$

respectively. Here, Δz_{mag} denotes the air gap between the top and bottom magnet. For the electromagnets, a compact design that allows high forces without saturation of the magnetic core was chosen. The magnetic core is laminated to minimize eddy currents, see also [17, 55, 92, 93]. However, saturation of the thin steel strip itself usually occurs, see [17]. Figure 5.4 shows the measured quasi-static electromagnetic force $f_{\mathrm{mag}} = f_{\mathrm{mag}}\left(i_{\mathrm{c}}^{\mathrm{t}}, i_{\mathrm{c}}^{\mathrm{b}}, w_{\mathrm{m}}\right)$ as a function of the transverse strip displacement w_{m} and the coil currents $i_{\mathrm{c}}^{\mathrm{t}}$ and $i_{\mathrm{c}}^{\mathrm{b}}$ at the top and the bottom coil, respectively. The measurement was performed in a special setup for characterizing the electromagnets, which is equipped with force sensors. In [17], a quasi-static electromagnetic FEM analysis was conducted to study the setup with two magnetic cores and the strip. The simulation results indicate a negligible interaction between opposing magnetic cores. Therefore, the quasi-static electromagnetic force characteristics of the actuators can be modeled as

$$f_{\mathrm{mag}} = \bar{f}_{\mathrm{mag}}\left(i_{\mathrm{c}}^{\mathrm{t}}, w_{\mathrm{m}}\right) - \bar{f}_{\mathrm{mag}}\left(i_{\mathrm{c}}^{\mathrm{b}}, -w_{\mathrm{m}}\right), \tag{5.43}$$

where $\bar{f}_{\mathrm{mag}}(\cdot,\cdot)$ denotes the identified nonlinear force-current-displacement characteristics of a single magnet.

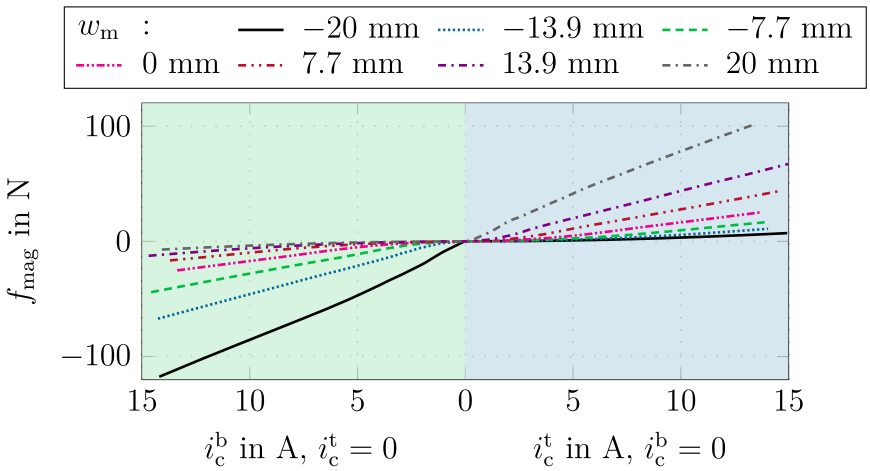

Figure 5.4: Measured electromagnetic force exerted on the strip depending on the transverse strip displacement w_{m} and the currents $i_{\mathrm{c}}^{\mathrm{t}}$ and $i_{\mathrm{c}}^{\mathrm{b}}$ supplied to the top and bottom magnet.

The coil currents of the electromagnetic actuator pairs are used as control inputs. In practice, the application of an additional offset current is useful to achieve a better compensation of the nonlinear force characteristics. Introducing a differential current Δi between i_c^t (top coil) and i_c^b (bottom coil) and substituting $i_\mathrm{c}^\mathrm{t} = \max\{0, i_\mathrm{off} + \Delta i/2\}$ and $i_\mathrm{c}^\mathrm{b} = \max\{0, i_\mathrm{off} - \Delta i/2\}$, with the offset current $i_\mathrm{off} > 0$, into (5.43) results in $u = f_\mathrm{mag} = \tilde{f}_\mathrm{mag}(\Delta i, w_\mathrm{m})$. A non-zero offset current i_off reduces the dynamics of the current since it prevents $\partial f_\mathrm{mag}/\partial\Delta i = 0$ at the point $\Delta i = 0$ [94]. This simplifies the current control task. A direct measurement of the air gaps δ^t and δ^b is avoided to make the scenario more realistic, cf. Fig. 1.11a. Instead, the air gaps are estimated based on the EKF output, where the estimate of the transverse strip displacement $\hat{w}_{\mathrm{m},k}$ can be calculated according to (5.27). The electromagnetic force f_mag exerted on the strip cannot be directly measured in the industrial plant according to Fig. 1.2. To obtain similar conditions in the experiment, a feedforward controller for the forces is used. This controller inverts the current-force characteristics shown in Fig. 5.4. In a discrete-time setting, the desired electromagnetic force $f_{\mathrm{mag},k}^\mathrm{des}$ at the sampling time t_k for the estimated transverse displacement $\hat{w}_{\mathrm{m},k}$ is realized by two subordinate PI current controllers with the desired coil currents

$$i_{\mathrm{c},k}^{\mathrm{t,des}} = \max\{0, i_\mathrm{off} + \tilde{f}_\mathrm{mag}^{-1}\Big(f_{\mathrm{mag},k}^\mathrm{des}, \hat{w}_{\mathrm{m},k}\Big)/2\} \tag{5.44a}$$

$$i_{\mathrm{c},k}^{\mathrm{b,des}} = \max\{0, i_\mathrm{off} - \tilde{f}_\mathrm{mag}^{-1}\Big(f_{\mathrm{mag},k}^\mathrm{des}, \hat{w}_{\mathrm{m},k}\Big)/2\}, \tag{5.44b}$$

where $\tilde{f}_\mathrm{mag}^{-1}(\cdot,\cdot)$ is calculated in advance and stored in a look-up table. The mapping (5.44) and the PI current controllers serve as the basis for the discrete-time feedforward controller of the electromagnetic force.

Remark: In the considered application, eddy currents are negligible, i.e., it is feasible to assume a quasi-static operation of the electromagnets. According to Faraday's law of induction, eddy currents in the steel strip and in the magnetic cores are caused by the rate of change in the magnetic field and therefore significantly increase with the frequency and the amplitude of the disturbance. Furthermore, the force dynamics of the electromagnetic actuator is negatively affected by eddy currents, see [17]. Because only low disturbance frequencies are observed in industrial hot dip galvanizing lines, see, e.g., Fig. 1.11b, the influence of eddy currents on the dynamics of the electromagnetic actuators can be neglected.

5.4.4.1 PI current controllers

Both PI current controllers have sampling times of $T_\mathrm{s}^\mathrm{PI} = 1/(53.6 \cdot 10^3)\,\mathrm{s}$. The parameters of the controllers were manually tuned and configured with the software MAXON ESCON STUDIO to achieve a good control performance. Figure 5.5 shows a comparison between the desired ($i_\mathrm{c}^\mathrm{t,des}$, $i_\mathrm{c}^\mathrm{b,des}$) and the measured currents (i_c^t, i_c^b)

of both PI current controllers for the top and bottom magnet. For this experiment, the desired force was almost sinusoidal with $\max |f_{\mathrm{mag}}^{\mathrm{des}}| \approx 2\,\mathrm{N}$. The signals shown in Fig. 5.5 constitute a worst case scenario with the high disturbance frequency $f_{\mathrm{d}} = \omega_{\mathrm{d}}/(2\pi) = 9\,\mathrm{Hz}$. However, the measurements show that the controlled currents accurately coincide with the desired trajectories $i_{\mathrm{c}}^{\mathrm{t,des}}$ and $i_{\mathrm{c}}^{\mathrm{b,des}}$.

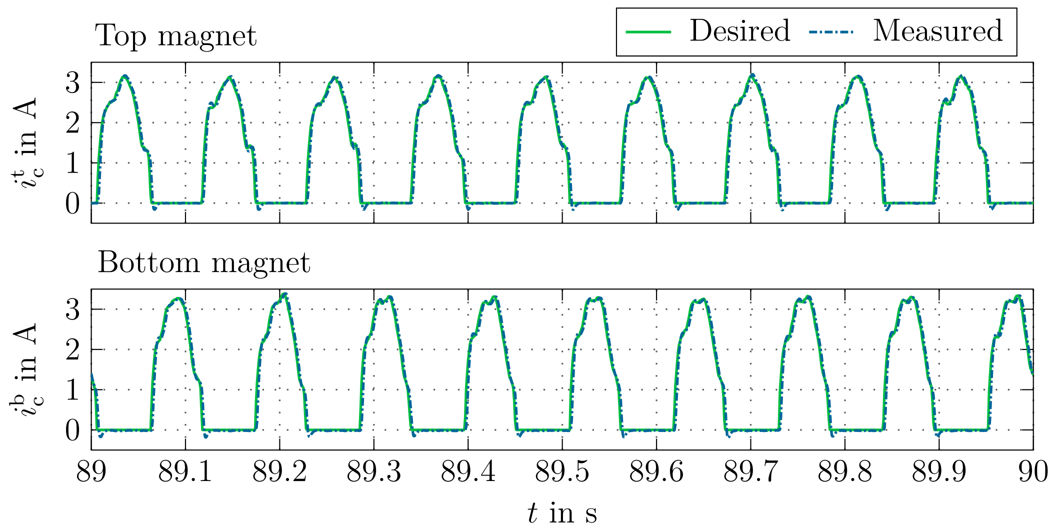

Figure 5.5: Measurements of the coil currents showing the performance of the PI controllers. Settings in the software MAXON ESCON STUDIO: proportional gain $K_{\mathrm{p}} = 11\,831$; integral time constant $T_{\mathrm{n}} = 2442\,\mu\mathrm{s}$. A supply voltage of 48 V was chosen.

5.5 Model parametrization

Table 5.2 contains the parameters used in the mathematical beam model according to (5.4). Except for the viscous damping parameter α and the material damping parameter β, which were identified in a separate measurement campaign, all other parameters are assigned their nominal values. For the case without control, Fig. 5.6 shows the measured and simulated transverse strip displacement w_{m} at the point x_{m}. Since w_{m} is not directly measurable, see Fig. 5.1, a linear interpolation of the measurements w_{lsr}^{3} and w_{lsr}^{4} is used. These results show that the mathematical model of the strip accurately captures the dynamic behavior of the real system.

Parameter	Symbol	Value
Strip length	L	$2.04\,\mathrm{m}$
Strip width	b	$150\,\mathrm{mm}$
Strip thickness	h	$0.76\,\mathrm{mm}$
Young's modulus	E	$2.1 \cdot 10^{11}\,\mathrm{N/m^2}$
Tensile load	N_{xx}	$4580\,\mathrm{N/m}$
Viscous damping factor	α	$0.232/\mathrm{s}$
Material damping factor	β	$4.67 \cdot 10^{-6}\,\mathrm{s}$
Position of magnet	x_m	$0.649\,\mathrm{m}$
Dimension of magnet	Δx_m	$0.1\,\mathrm{m}$
Position of sensor	x_s	$0.927\,\mathrm{m}$
Position of output	x_r	$0.371\,\mathrm{m}$
Offset current	i_off	$0\,\mathrm{A}$ (sinusoidal disturbance) $1\,\mathrm{A}$ (multi-harmonic disturbance)
No. of finite elements	n	9 (sinusoidal disturbance) 8 (multi-harmonic disturbance)

Table 5.2: Parameters of the mathematical beam model.

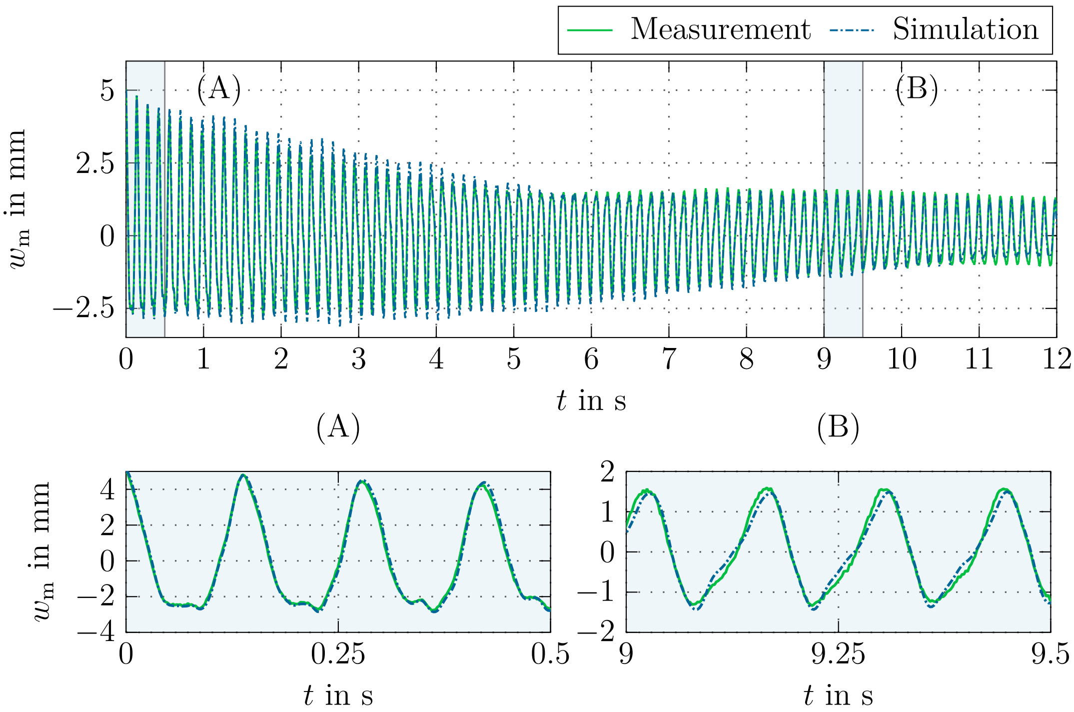

Figure 5.6: Transverse strip displacement w_m at the position x_m of the electromagnets for an initial displacement $w_\mathrm{m}(0) = 5\,\mathrm{mm}$ (without control).

Figure 5.7 shows Bode plots of the transfer functions from the system inputs (disturbance w_{d} and control input $u = f_{\mathrm{mag}}$) to the displacement outputs (w_{m} at the electromagnets and y at the system output), where s denotes the Laplace variable. Solid blue lines show the Bode plots calculated with the mathematical model using the parameters in Tab. 5.2. Dashed red lines represent measured Bode plots from an experiment. In a wide range, the measurements and the model coincide accurately. The deviations near the transmission zeros can be explained by a torsional mode, which cannot be completely avoided and which deteriorates the displacement measurements. However, the torsional mode was neither considered in the mathematical model (5.3b) nor in the vibration control strategy because it cannot be rejected in a setup with the electromagnets shown in Fig. 5.3. The resonance frequencies are accurately captured by the model. However, the air damping at these frequencies in the real system is higher than in the model. For this experiment, the amplitude of the input was held constant while the frequency of the input was gradually varied in the relevant frequency range. Therefore, high transverse strip displacements up to 20 mm occurred at the resonance frequencies. This causes the viscous damping to increase.

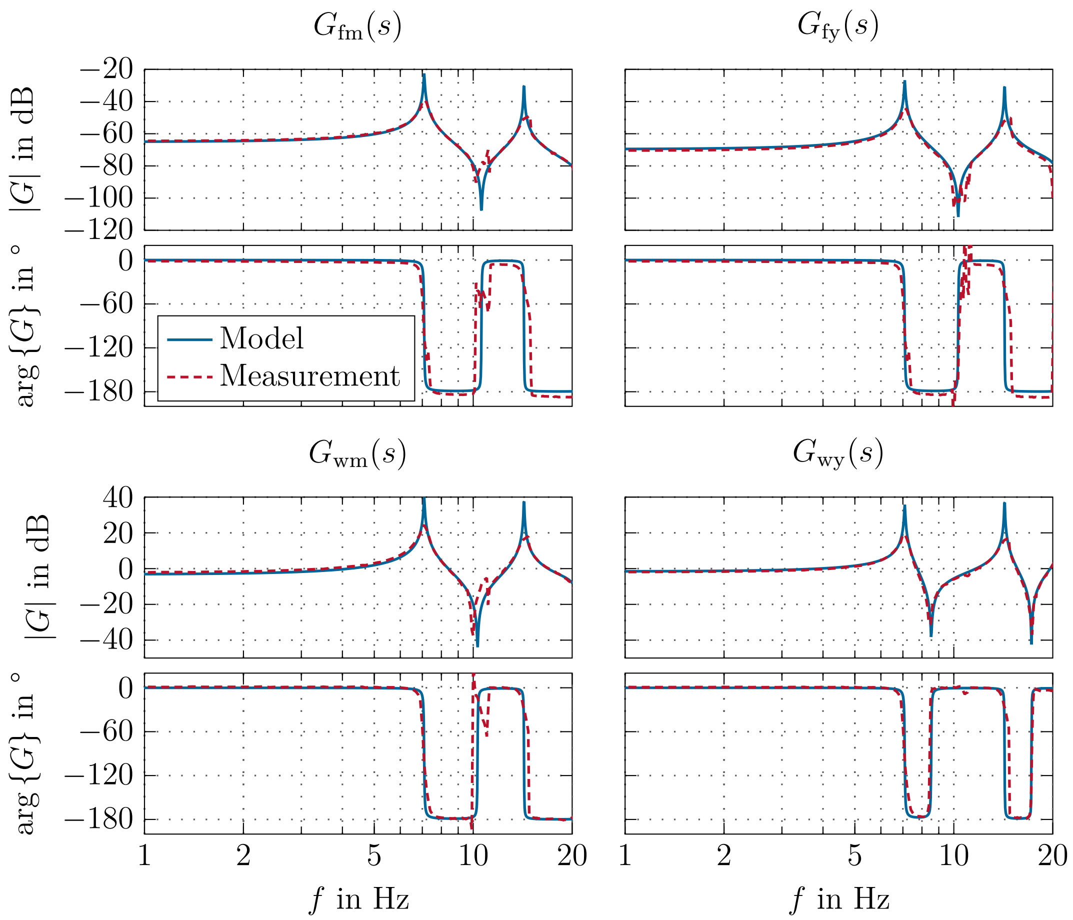

Figure 5.7: Bode plots of the transfer functions $G_{\mathrm{fm}}(s)$ (from f_{mag} to w_{m}, normalized with respect to $1\,\mathrm{m/N}$), $G_{\mathrm{fy}}(s)$ (from f_{mag} to y, normalized with respect to $1\,\mathrm{m/N}$), $G_{\mathrm{wm}}(s)$ (from w_{d} to w_{m}), and $G_{\mathrm{wy}}(s)$ (from w_{d} to y): solid blue line - computed with nominal parameters; dashed red line - pointwise measurement in the experimental test rig.

5.6 Proof of concept at the test rig

5.6.1 Overall disturbance rejection control system

A block diagram of the overall control system with the EKF from Section 5.3.2.1 is shown in Fig. 5.8. Here, the green block containing the two subordinate PI current controllers with the desired values according to (5.44) realizes the discrete-time feedforward controller for the electromagnetic force presented in Section 5.4.4. The blue block containing the LQR, the disturbance feedforward controller from Section 5.3.1, and the state observer from Section 5.3.2 represents the discrete-time vibration control strategy presented in Section 5.3. This block is implemented on the dSPACE real-time hardware with the sampling time $T_\mathrm{s} = 1 \cdot 10^{-3}\,\mathrm{s}$.

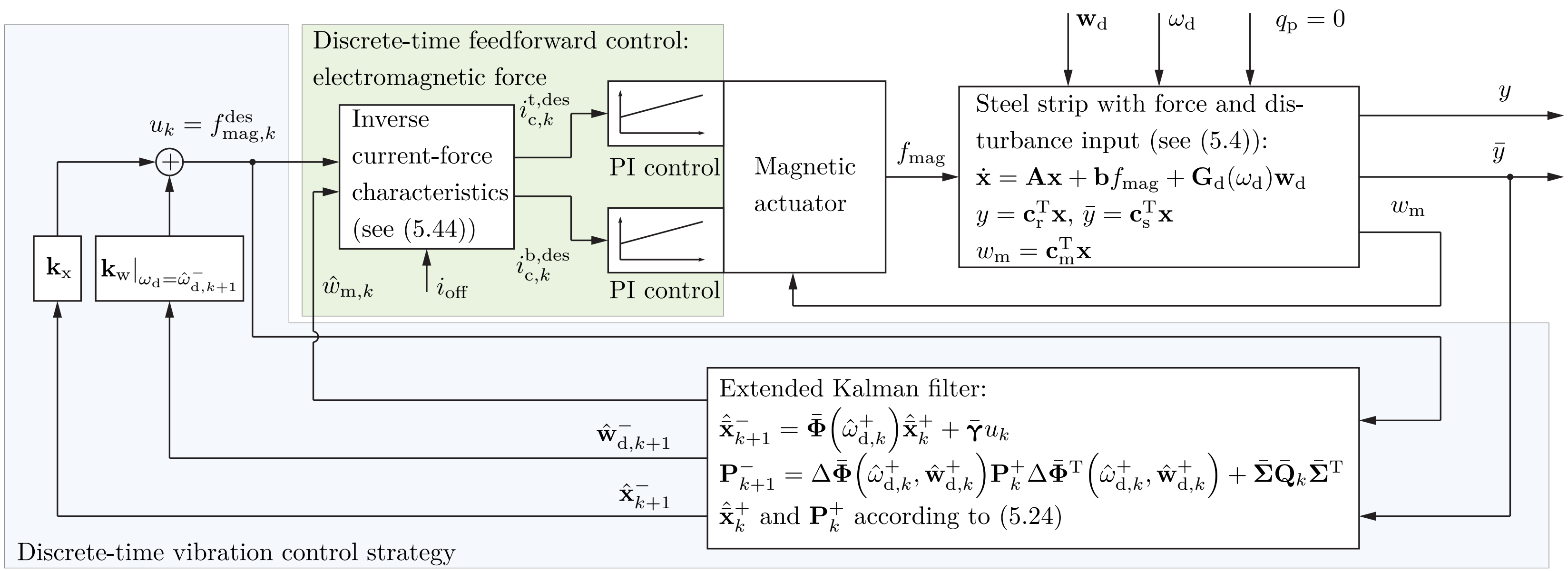

Figure 5.8: Block diagram of the overall disturbance rejection control concept with the EKF from Section 5.3.2.1.

Parameter	Symbol	Value
Weighting factor position	f_{p}	$5\,(1/\mathrm{m})^2$
Weighting factor velocities	f_{v}	$0.06\,(\mathrm{s}/\mathrm{m})^2$
Weighting factor input	R	$0.005\,(1/\mathrm{N})^2$
Weighting points	$\hat{m}$	23

Table 5.3: Parameters used for the LQR.

The variance $\bar{R}$ of the measurement noise of the laser distance sensor at the position $x^{\mathrm{e}} = x_{\mathrm{s}}$ was estimated based on measurement results. The covariance matrix $\bar{\mathbf{Q}}_k \geq 0$ of the process noise in (5.23b) is empirically chosen in the form

$$\bar{\mathbf{Q}}_k = \mathrm{diag}\Big(\bar{Q}_{\mathrm{p}},\ \bar{Q}^1_{\mathrm{w_d},k},\ \bar{Q}^1_{\dot{\mathrm{w}}_\mathrm{d},k},\ \ldots\ ,\bar{Q}^{\upsilon}_{\mathrm{w_d},k},\ \bar{Q}^{\upsilon}_{\dot{\mathrm{w}}_\mathrm{d},k},\ \bar{Q}_{\omega}\Big), \tag{5.45}$$

with positive scalar values $\bar{Q}_{\mathrm{p}}$, $\bar{Q}_{\omega}$ and $\bar{Q}^l_{\mathrm{w_d},k}$, $\bar{Q}^l_{\dot{\mathrm{w}}_\mathrm{d},k}$ with $l \in \{1, \ldots, \upsilon\}$. While $\bar{Q}_{\mathrm{p}}$ and $\bar{Q}_{\omega}$ are constant, it turned out to be advantageous for the performance of the estimator to choose $\bar{Q}^l_{\mathrm{w_d},k}$ and $\bar{Q}^l_{\dot{\mathrm{w}}_\mathrm{d},k}$ as functions of the (slowly varying) estimated disturbance frequency $\hat{\omega}^-_{\mathrm{d},k}$. Actually, the affine relation

$$\bar{Q}^l_{\mathrm{w_d},k} = \bar{Q}^{2\pi}_{\mathrm{w_d}} + \left(\bar{Q}^{18\pi}_{\mathrm{w_d}} - \bar{Q}^{2\pi}_{\mathrm{w_d}}\right)\frac{l\hat{\omega}^-_{\mathrm{d},k} - 2\pi}{16\pi} \tag{5.46a}$$

$$\bar{Q}^l_{\dot{\mathrm{w}}_\mathrm{d},k} = \bar{Q}^{2\pi}_{\dot{\mathrm{w}}_\mathrm{d}} + \left(\bar{Q}^{18\pi}_{\dot{\mathrm{w}}_\mathrm{d}} - \bar{Q}^{2\pi}_{\dot{\mathrm{w}}_\mathrm{d}}\right)\frac{l\hat{\omega}^-_{\mathrm{d},k} - 2\pi}{16\pi} \tag{5.46b}$$

is employed for the relevant frequency range $2\pi\,\mathrm{rad/s} \leq \omega \leq 18\pi\,\mathrm{rad/s}$. The idea of an online adaption of the covariances can be found at various places in the literature, see, e.g., [90].

5.6.2 Sinusoidal disturbance

A sinusoidal disturbance ($\upsilon = 1$) with the amplitude $\max|w_{\mathrm{d}}| = 1\,\mathrm{mm}$ is considered. The manually tuned parametrization of the LQR according to Section 5.3.1 is given in Tab. 5.3. All tuning parameters for the EKF based on the explicit discrete-time model according to Section 5.3.2.1 are given in Tab. 5.4.

A validation of the EKF was conducted at the experimental test rig by comparing the observed transverse strip displacements with the displacements measured by the laser distance sensors according to Fig. 5.9. For this experiment, the disturbance frequency f_{d} was varied. Figure 5.9 shows a good accordance of the frequency estimate $\hat{f}_{\mathrm{d}}$ with the time-varying frequency f_{d}. A slightly increased estimation error of the disturbance frequency occurs at approximately 110 s. Here, the undamped natural vibrations of the strip are dominant compared to vibrations caused by the disturbance actuator. Therefore, it is hard for the state observer to accurately track the disturbance frequency f_{d}. The results for two arbitrarily

Parameter	Symbol	Value
Sensor noise	$\bar{R}$	$2.25 \cdot 10^{-8}\,\mathrm{m}^2$
Process noise strip	$\bar{Q}_{\mathrm{p}}$	$67\,(\mathrm{N/m}^2)^2$
Process noise disturbance		
Position (lower limit)	$\bar{Q}_{\mathrm{w_d}}^{2\pi}$	$2.25 \cdot 10^{-12}\,\mathrm{m}^2$
Position (upper limit)	$\bar{Q}_{\mathrm{w_d}}^{18\pi}$	$2.25 \cdot 10^{-10}\,\mathrm{m}^2$
Velocity (lower limit)	$\bar{Q}_{\dot{\mathrm{w}}_\mathrm{d}}^{2\pi}$	$4.4 \cdot 10^{-9}\,(\mathrm{m/s})^2$
Velocity (upper limit)	$\bar{Q}_{\dot{\mathrm{w}}_\mathrm{d}}^{18\pi}$	$4.4 \cdot 10^{-7}\,(\mathrm{m/s})^2$
Frequency	$\bar{Q}_{\omega}$	$2 \cdot 10^{-4}\,(\mathrm{rad/s})^2$

Table 5.4: Parameters used for the EKF.

chosen distance sensors, i.e., lsr 2 and lsr 7, are shown in Fig. 5.9. All other distance sensors yield similar results. In particular, the bottom part of Fig. 5.9 shows an excellent performance of the EKF.

For a scenario without control, a typical strip vibration induced by a harmonic disturbance $w_{\mathrm{d}}(t)$ with the frequency $f_{\mathrm{d}} = 4\,\mathrm{Hz}$ is shown in Fig. 5.10. The disturbance is shown as blue line and the output as green line. All other measured strip displacements are depicted as gray lines. For a scenario with active disturbance rejection controller, Fig. 5.11 shows the measured transverse strip displacements. The blue line corresponds to the disturbance $w_{\mathrm{d}}(t)$, the red line is the only sensor signal used by the observer, and the green line corresponds to the generally unknown system output, where the vibrations have to be rejected. As can be inferred from Fig. 5.11, the controller does an excellent job in suppressing the vibrations in the system output y.

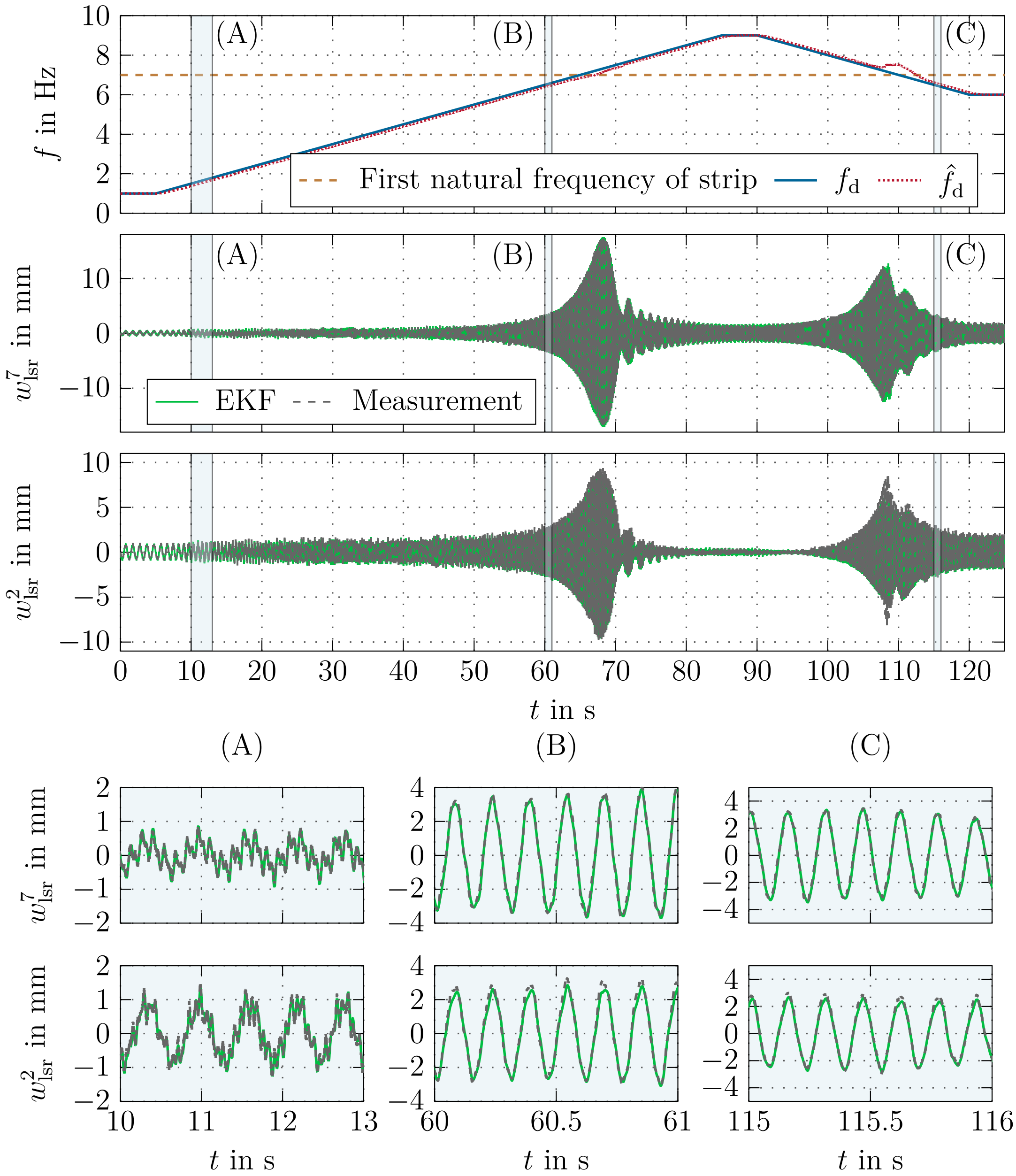

Figure 5.9: Validation of the EKF for two arbitrarily chosen distance sensors.

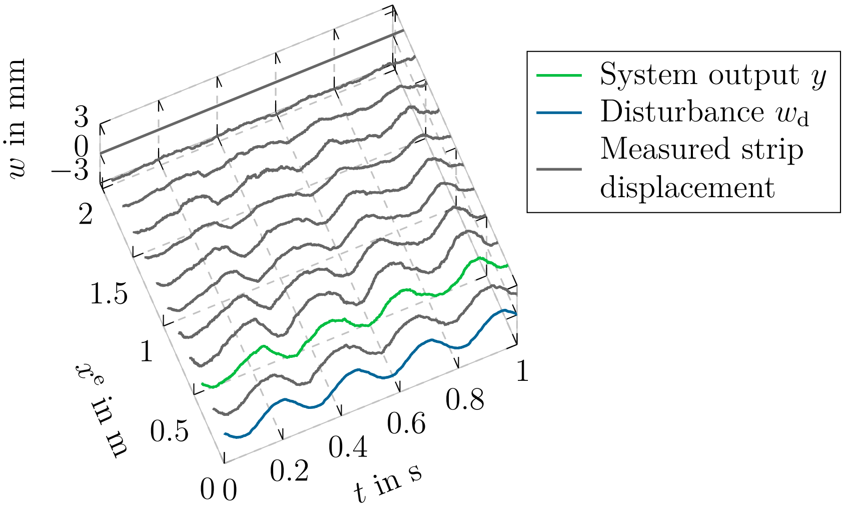

Figure 5.10: Measured transverse strip displacements caused by a disturbance w_d with the frequency $f_\mathrm{d} = 4\,\mathrm{Hz}$ and the amplitude of $1\,\mathrm{mm}$ without control.

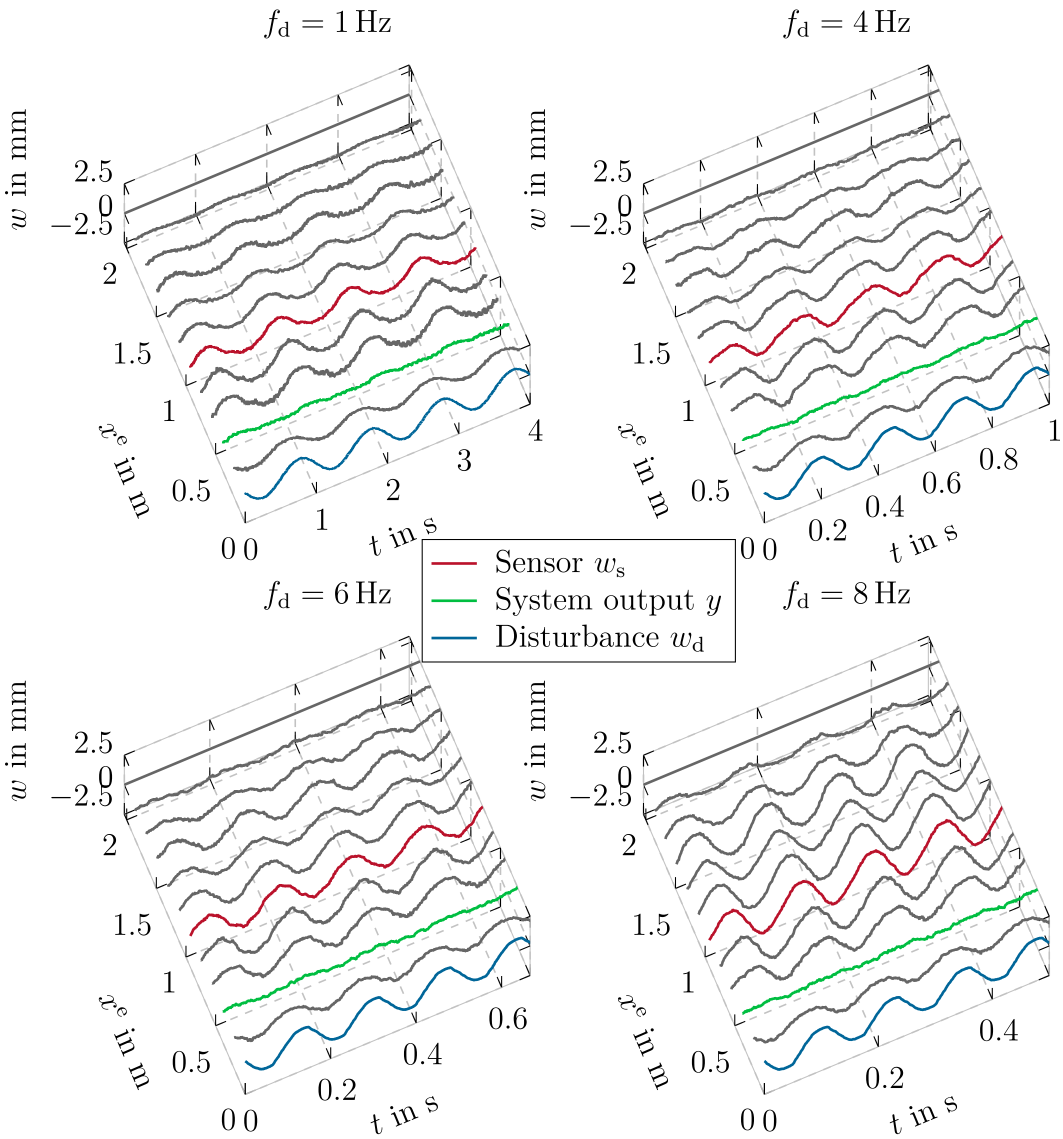

Figure 5.11: Measured transverse strip displacements with active control: blue line - disturbance w_d with the amplitude 1 mm and different frequencies f_d; red line - sensor signal w_s used for control; green line - system output y to be controlled; grey lines - measured displacements used for validation purpose.

The frequency spectra of the measured transverse strip displacements are shown in Fig. 5.12, without control on the left-hand side and with active control on the right-hand side. Furthermore, the peak values $\max|f_{mag}^{des}|$ of the desired electromagnetic force f_{mag}^{des} (control input) are given in these subplots. The natural frequencies of the strip are highlighted as dashed brown lines. The applied disturbance is not a strictly sinusoidal signal, see Figs. 5.10 and 5.11. However, higher harmonics are small and therefore neglected.

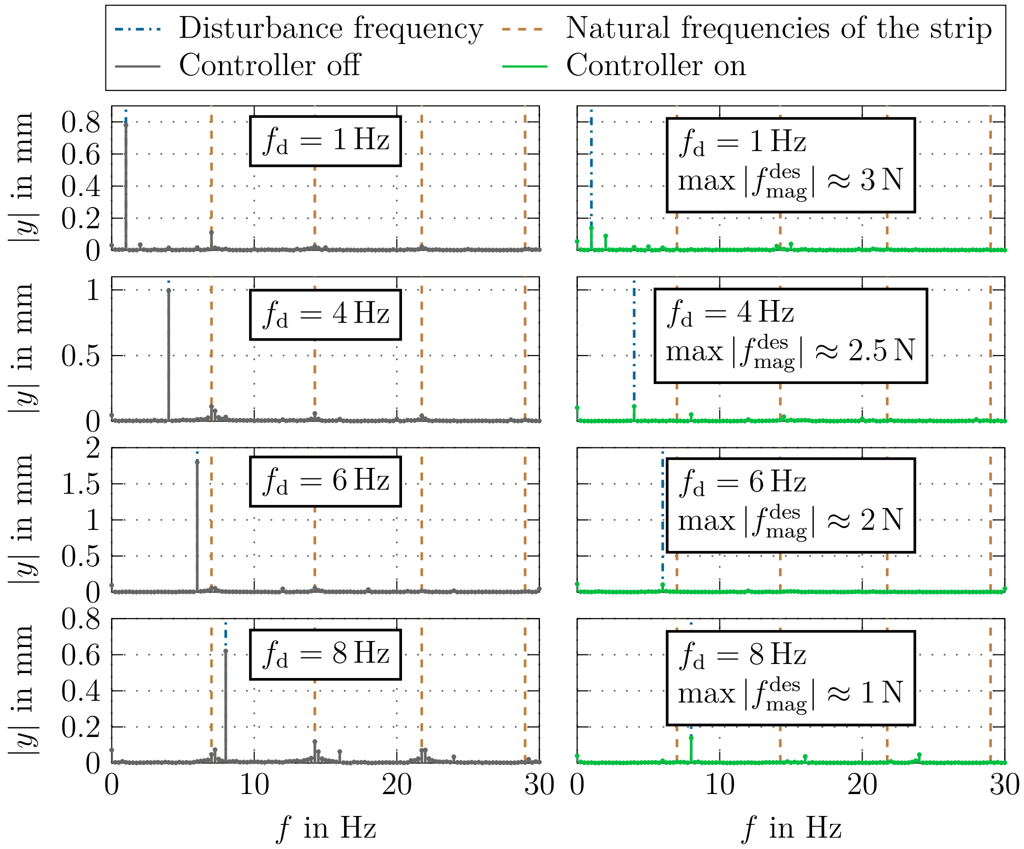

Figure 5.12: Amplitude spectra of measured transverse strip displacements without and with control for different disturbance frequencies f_d.

Despite the assumption of a constant disturbance frequency f_d used in the controller and observer design, the concept was also tested for a slowly varying disturbance frequency. Figure 5.13 shows the corresponding results. The range of the disturbance frequency f_d was chosen to include the first natural frequency of the strip. In Fig. 5.13, the disturbance frequency equals the first natural frequency in the vicinity of 65 s and 110 s. If the controller is turned off, high amplitudes of the system output y can be observed at these times (resonance). The vibrations are significantly reduced if the controller is active. In contrast to the estimated disturbance frequency $\hat{f}_d$ of the uncontrolled case in Fig. 5.9, where the estimation error is slightly increased in the vicinity of the natural frequency of the strip (110 s), the frequency estimate $\hat{f}_d$ tracks the time-varying disturbance frequency f_d quite well in the controlled case, see Fig. 5.13. Here, the oscillations due to the natural frequency of the strip are significantly reduced by the LQR. The disturbance frequency passes a transmission zero of the system at approximately 81 s and 95 s, see Fig. 5.13, which results in small amplitudes even in the uncontrolled case. Nevertheless, the amplitudes are further reduced in the controlled case. During the whole experiment, the desired electromagnetic force

$f_{\mathrm{mag}}^{\mathrm{des}}$ does not exceed $\pm 4\,\mathrm{N}$. The details (A)-(C) in Fig. 5.13 highlight the excellent performance of the proposed control concept. The transverse strip vibration at the system output y is clearly reduced, even if the frequency of the disturbance is changing.

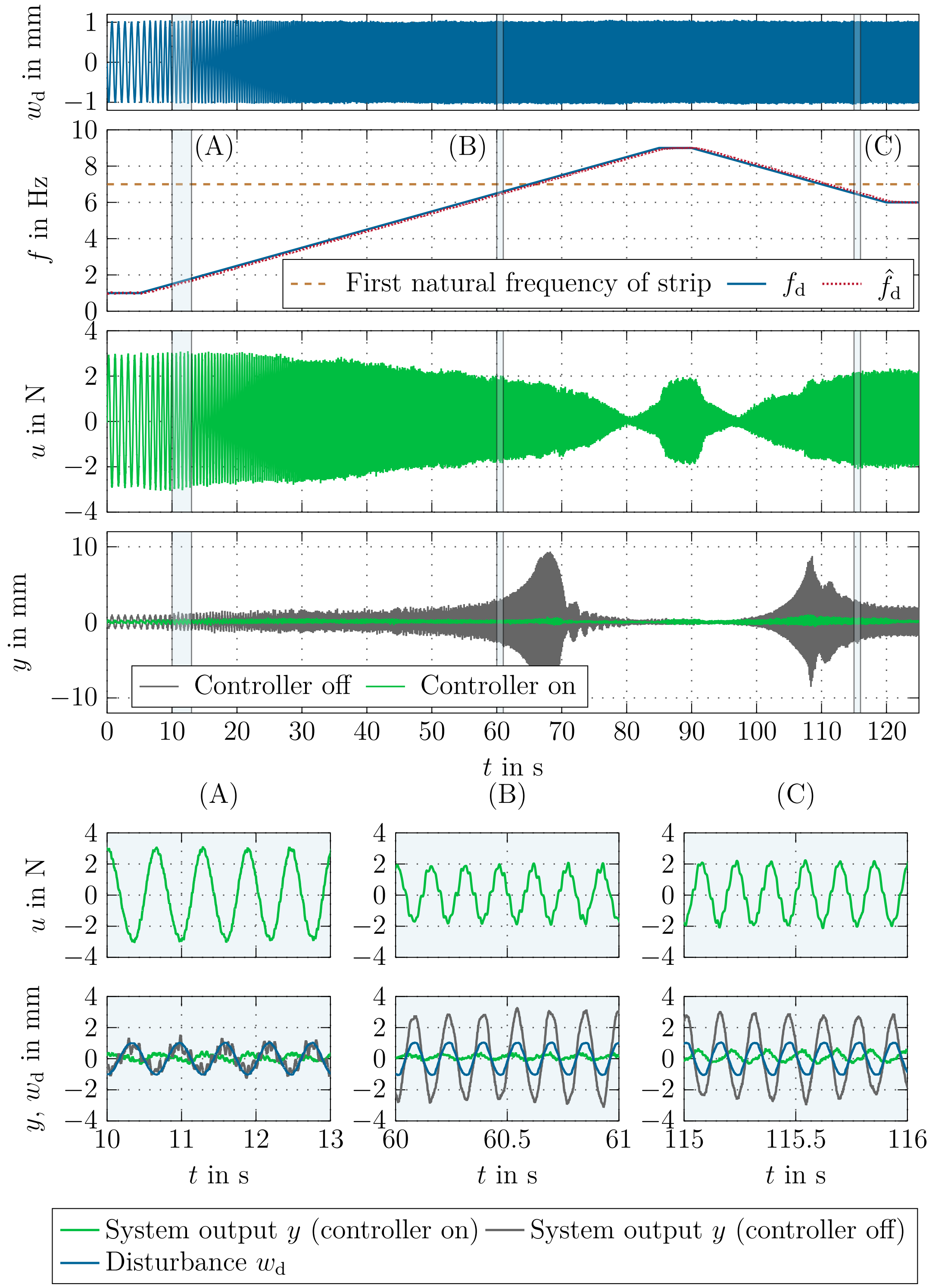

Figure 5.13: Measurement results for a sinusoidal disturbance with a slowly varying frequency. The second row shows the estimated frequency $\hat{f}_d$ in the case of active control.

5.6.3 Multi-harmonic disturbance

A multi-harmonic disturbance with up to three harmonics ($\upsilon = 3$) is considered in the following. To estimate the states of the system, the EKF described in Section 5.3.2.2 is used. All design parameters were manually tuned similar to Section 5.6.2.

Figure 5.14 shows the amplitude spectra of the system output y for the controlled and uncontrolled case and for different fundamental frequencies f_d of the disturbance. The three non-zero harmonic modes of the disturbance w_d have the nominal amplitudes $|w_\mathrm{d}^1| = 0.8\,\mathrm{mm}$, $|w_\mathrm{d}^2| = 0.25\,\mathrm{mm}$, and $|w_\mathrm{d}^3| = 0.1\,\mathrm{mm}$. The spectra shown on the left-hand side of Fig. 5.14 are obtained without control. The spectra on the right-hand side demonstrate that the proposed control concept can accurately reject such multi-harmonic disturbances.

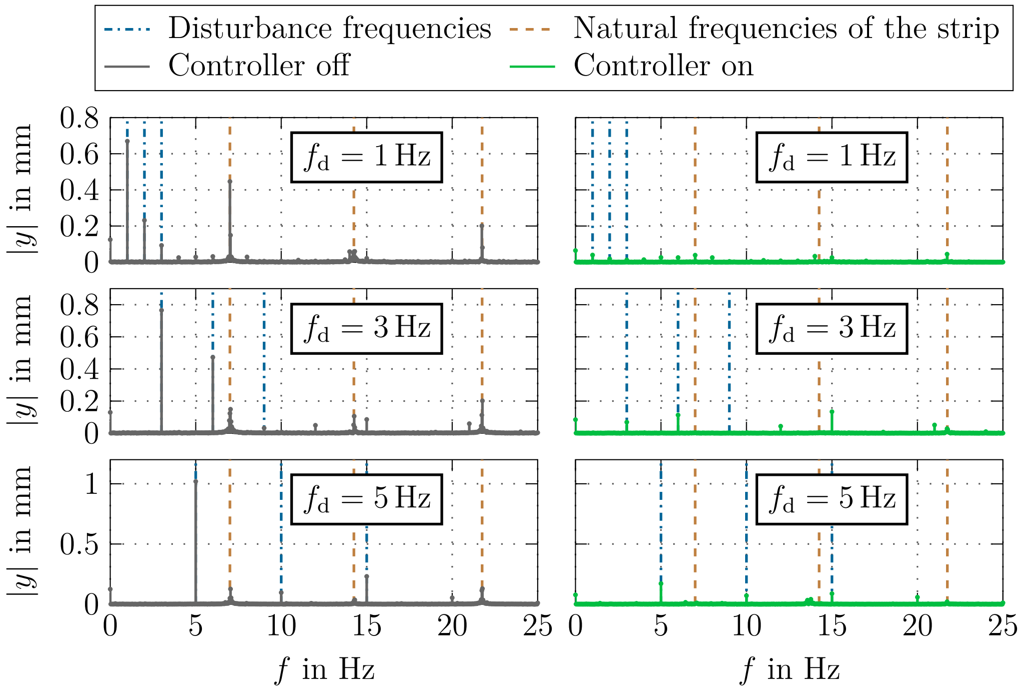

Figure 5.14: Amplitude spectra of measured transverse strip displacement signals for different disturbance frequencies f_d.

Figure 5.15 shows measured strip vibrations for the fundamental disturbance frequency $f_\mathrm{d} = 1\,\mathrm{Hz}$ if the control is inactive (A) and if the control is active (B). The results demonstrate that the developed controller accurately rejects the unknown disturbance in the unmeasured system output y.

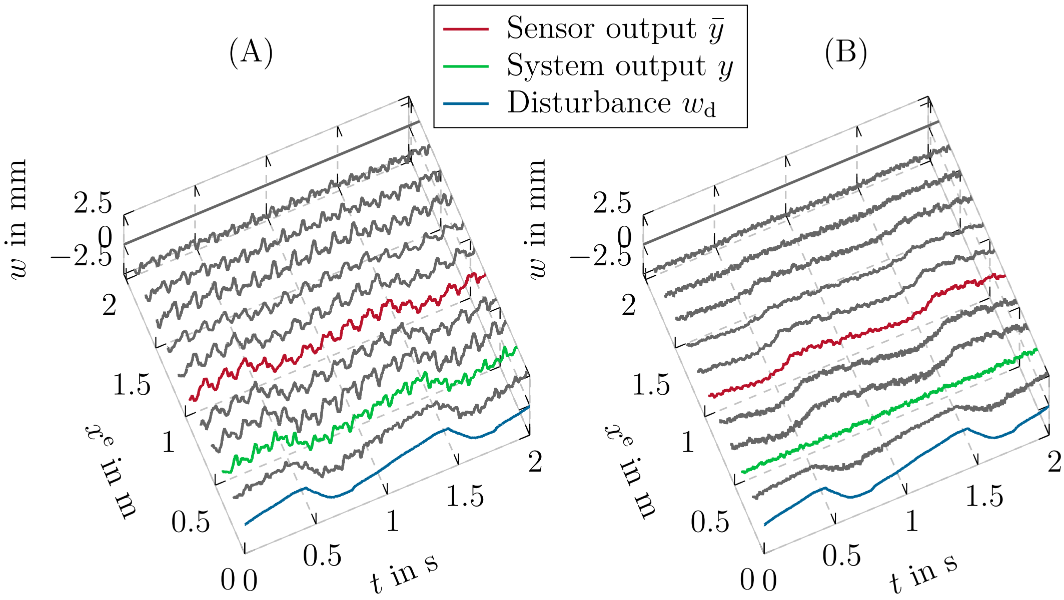

Figure 5.15: Measured strip displacement without (A) and with active control (B) for the fundamental disturbance frequency $f_\mathrm{d} = 1\,\mathrm{Hz}$.

Figure 5.16 shows the performance of the developed control method for a slowly varying disturbance frequency f_d. The estimated frequency $\hat{f}_\mathrm{d}$ accurately tracks the time-varying disturbance frequency f_d. The remarkable difference between the uncontrolled and the controlled case again demonstrates the effectiveness of the developed control method. Although the frequency of a harmonic mode exceeds the first natural frequency of the strip, the control performance is excellent. The details (A)-(C) in Fig. 5.16 clearly point out the perfect rejection behavior.

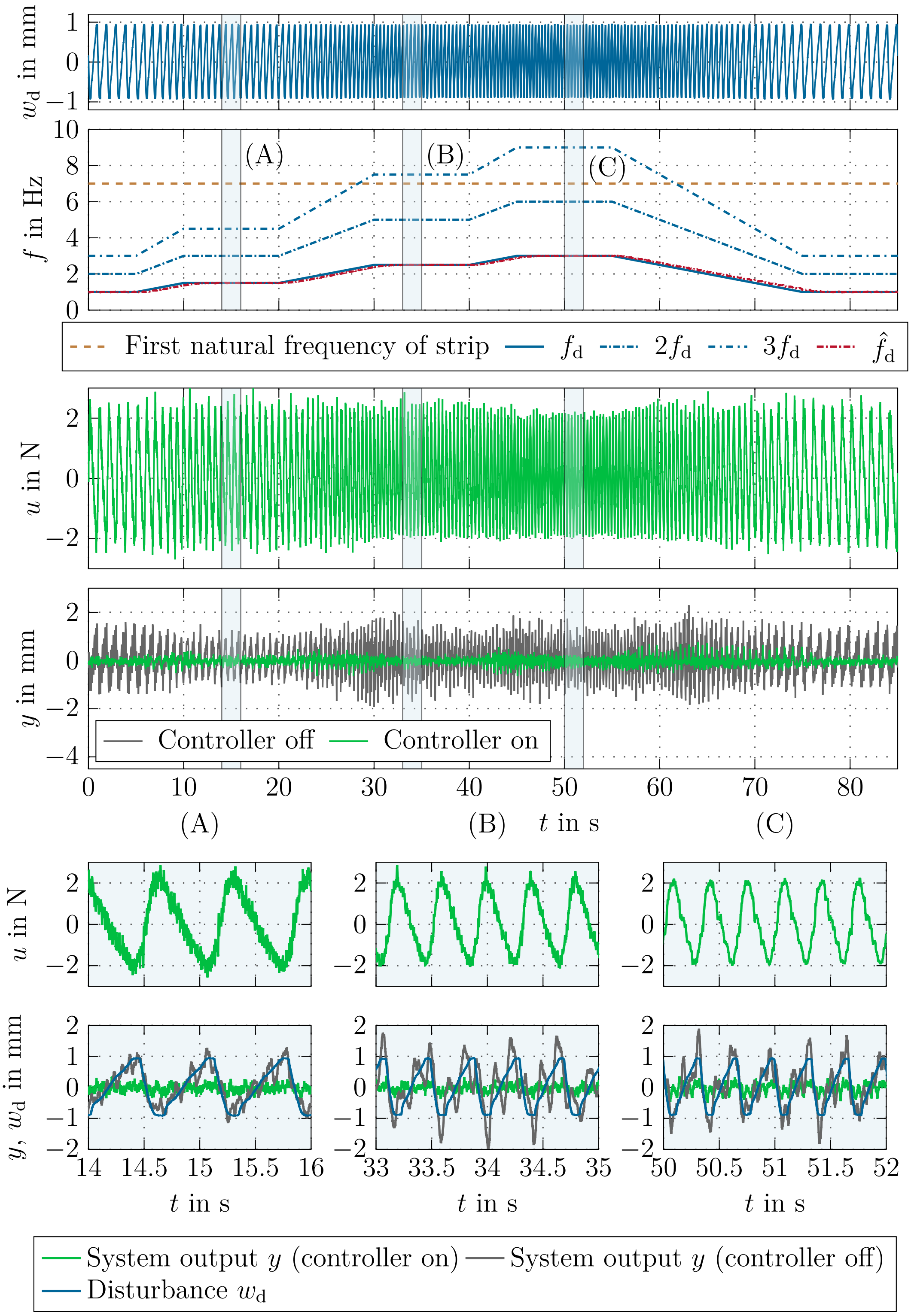

Figure 5.16: Measurement results for a periodic disturbance with higher harmonics and a slowly varying frequency.

5.6.4 Conclusions and outlook

This chapter deals with active rejection control of an unknown multi-harmonic (periodic) disturbance at an unmeasured position of a vibrating steel strip. A pair of electromagnets was custom made to apply the desired control force to the steel strip. A single distance sensor was used as only measurement for the developed control method. The main findings of this chapter can be summarized as follows:

- A method for the rejection of unknown periodic disturbances including higher harmonics was developed for a non-collocated sensor-actuator setup and practically validated on an experimental test rig.
- The control task is complicated by the fact that the disturbance, the controlled system output, the electromagnetic actuator, and the distance sensor are all located at different positions along the strip.
- A calibrated quasi-static relation between the electromagnetic force, the transverse strip displacement, and the coil currents (top and bottom magnet) was used to apply control forces in both directions to the strip. The desired currents were realized by subordinate PI controllers.
- The control method works well even without a force sensor for measuring the electromagnetic force or an extra distance sensor for measuring the transverse strip displacement at the position of the magnets.
- Using the electromagnets with an offset current allows a partial compensation of the nonlinear electromagnetic force characteristics.
- The proposed control method is not limited to steel strips. For non-magnetic metals, a different type of actuator may be used to apply the control force.
- Based on the explicit discrete-time solution of the dynamic system, an extended Kalman filter (EKF) was designed. Also, a more efficient implementation of the EKF was proposed based on the implicit Euler integration method.
- The design of the laboratory experiment mimics the conditions observed in the industrial hot-dip galvanizing line.

CHAPTER 6

Conclusions and outlook

6.1 Summary

This thesis deals with the development of model-based control concepts for industrial hot-dip galvanizing lines to improve the flatness of the transverse strip profile at the gas wiping dies compared to the state-of-the-art methods. A flattened transverse strip profile at this position is a prerequisite to establish a uniform zinc coating with the minimum required thickness. The objective here is to lower the operating costs of the process, i.e., to reduce the zinc consumption.

The first part of the work is concerned with the analysis of the steady-state and dynamic behavior of steel strips in industrial hot-dip galvanizing lines. To this end, a dynamic mathematical model of the transverse strip shape was developed. It takes into account the electromagnetic forces of a strip stabilizer and the transverse loads exerted on the strip through the impinging air jets from the nozzles of the cooling elements. The electromagnetic forces exerted on the strip were calculated based on a validated finite-element model and stored in look-up tables for several configurations. The electromagnetic force characteristics of an actuator pair mainly depends on the strip thickness, the pole-shoe-to-strip distances (air gaps), the coil currents, and the BH-curve of the strip material. In order to model the transverse loads of the impinging air jets of the cooling elements in the tower, a laboratory flow simulator was built and used to measure the force characteristics of a single impinging air jet on a plate. A simulation study was conducted to analyze the influence of the air coolers on the stability of the strip transport through the cooling tower. The mathematical model also considers the elasto-plastic deformation history of the incoming strip, i.e., the residual membrane strains and residual curvatures of the strip, and the boundary conditions at the pot roll. Different boundary conditions at the pot and the tower roll, the geometrical nonlinearity of the strip, and the elasto-plastic deformation history were thoroughly analyzed. A beam model of the bending line was presented, which can be used to calculate the elasto-plastic deformation history of the strip based on the configuration of the tension leveler in the zinc pot. Also, an estimator of the residual curvature in lateral direction of the strip was developed that uses only the measurements of the strip stabilizer and nominal parameters of the current production. To study the dynamic behavior of the strip, free vibration experiments were conducted at the industrial plant. The effects of an external viscous damping and an internal Kelvin-Voigt damping were analyzed for setups with and without the zinc pot. Moreover, the influence of the liquid zinc pot on the dynamics of the strip was investigated.

In the second part of this work and based on the validated model of the industrial plant, new model-based control concepts were developed in order to improve the flatness of the transverse strip profile at the gas wiping dies. An optimization-based feedforward controller was designed and tested in a simulation study, where the results were compared to the state-of-the-art control approach (flat transverse strip profile at the electromagnets). The feedforward controller calculates position set-points for the strip in the electromagnetic stabilizer. Hence, the existing control structure can be used without any modifications. As an alternative, a different controller to regulate the strip position at the electromagnets can be used. Here, the electromagnetic force serves as control input. The feedforward controller can be augmented by a disturbance rejection method for the compensation of persistently exciting disturbances. The desired control force can be approximately realized by an inversion of the respective electromagnetic force characteristics. This yields the desired coil currents, which are realized by fast subordinate current controllers.

The last part of this work deals with a model-based disturbance rejection control for unknown multi-harmonic disturbances of the transverse strip displacement at an arbitrary position of a steel strip under tensile load. An experimental test rig was developed for this purpose which was inspired by the conditions in the industrial hot-dip galvanizing line, where persistently exciting disturbances, e.g., due to eccentric zinc pot rolls, are frequently observed. However, it is difficult to completely suppress such strip vibrations with those feedback control methods commonly used in hot-dip galvanizing plants. The control task is particularly challenging because, in general, the disturbance, the electromagnetic actuator, the sensor for measuring the transverse strip displacement, and the system output to be controlled (i.e., the strip displacement at the gas wiping dies) are all located at different positions along the strip. The method proposed in this work is based on a state-space description of an Euler-Bernoulli beam. A control concept was designed based on a combination of a linear quadratic regulator (LQR) and a disturbance feedforward concept that exploits the theory of invariant manifolds. The states of the strip, the disturbance, and the disturbance frequency were estimated by an extended Kalman filter (EKF). The damping parameters of the model were determined by means of free oscillation experiments. The dynamics of the subordinate current controllers turned out to be negligible. Hence, an inversion of the electromagnetic force characteristics was applicable to compensate for the input nonlinearity of the electromagnets. This force characteristics was measured and utilized for the feedforward control of the desired force. The developed control strategy was successfully tested on the experimental test rig.

6.2 Conclusions

As a preparation for the model-based control approach in this thesis, special effort was put into the development and validation of a dynamic model of the transverse strip shape in the industrial hot-dip galvanizing line. A suitable model should be accurate enough to capture the most important physical effects of the process. At the same time, such a model should be computationally undemanding to facilitate real-time control. The mechanical model of the transverse strip shape was validated with measurements from the industrial plant for steady-state and dynamic scenarios. It turned out that during the normal operation of the plant, a linear model is suitable for model-based control methods because the expected transverse strip displacements are usually small (due to a relatively high tensile load in the strip) and because the tensile load is kept constant by the strip tension controller. The influence of the air cooling jets in the tower as well as the geometrical nonlinearity of the strip are negligible in this case. The linear character of the mechanical system is particularly advantageous for the evaluation of steady-state and transient solutions of the mathematical model. The linearity property can also be exploited for model-based control approaches.

The damping behavior of the strips with and without the zinc pot was also analyzed based on measurements from the electromagnetic stabilizer and the tower sensors. It turned out that the damping of strip vibrations in the free oscillation experiments is dominated by external viscous damping. The internal Kelvin-Voigt material damping cannot be identified by such experiments. However, the internal Kelvin-Voigt material damping is of importance for the realistic decay of strip vibrations with higher frequencies. In the normal galvanizing process, where the strip traverses the zinc pot, the liquid zinc significantly increases the inertia of the strip movement near the pot.

A beam model was presented to calculate the elasto-plastic deformation history of the strip based on the configuration of the tension leveler in the zinc pot. However, it turned out that a simpler estimator of the residual curvature also accurately captures the elasto-plastic deformation history of the strip. This estimator was successfully validated for different test strips with measurements of the transverse strip profile in the cooling tower. Moreover, extra measurement equipment is not required for this method. The measured zinc coating profiles are also clearly correlated with the estimated transverse strip profile at the gas wiping dies in different scenarios. Hence, it can be argued that the validated plate model is accurate enough to capture the transverse strip profile at the gas wiping dies. Since a flat transverse strip profile at the gas wiping dies is a prerequisite to achieve a homogeneous zinc coating thickness, the validated model was used to develop a model-based feedforward control of this profile.

This optimization-based feedforward controller significantly improves the flatness of the transverse strip profile at the gas wiping dies. However, the results depend on the number of strip profile modes to be compensated by the feedforward controller. The compensation of higher strip profile modes at the gas wiping dies results in larger deflections of the transverse strip profile at the electromagnets and higher electromagnetic forces. Furthermore, the strip deformations at the electromagnets increase with the vertical distance between the gas wiping dies and the electromagnets. To limit the required electromagnetic forces, only the first few and usually dominant strip profile modes should be compensated. The computed position set-points can be realized by the subordinate position controllers of the electromagnetic strip stabilizer. A modification of the existing control structure is not required.

A disturbance rejection method was developed for the compensation of persistently exciting disturbances. In contrast to model-based methods for the steady-state case, e.g., the feedforward control of the transverse strip profile at the gas wiping dies, model-based methods for the dynamic case also rely on accurate damping parameters of the system. Moreover, such methods must be executable in real time. This makes a transfer of the model-based disturbance rejection method to the industrial plant more challenging. The proof of concept of the disturbance rejection method was conducted on the experimental test rig. The results demonstrate the feasibility and effectiveness of the proposed method. At first glance, the scenario in the experimental test rig seems to be simplified compared to the one in the industrial plant. However, one must consider that in contrast to the experimental test rig, the vertical distance between the gas wiping dies (system output) and the electromagnets is very short compared to the distance between the stabilization and the tower roll (this section defines the strip length). Hence, a simplified situation appears in the industrial hot-dip galvanizing line compared to the experimental test rig. Moreover, in the considered industrial plant, the distance sensor of the electromagnetic stabilizer is located in the center of the electromagnets, i.e., the sensor-actuator pairs are approximately collocated. Therefore, an estimation of the air gaps for the feedforward control of the electromagnetic force is not required.

The application of model-based control methods in the industrial hot-dip galvanizing line allows to indirectly improve the homogeneity of the zinc coating thickness via a flattened and constant strip profile at the gas wiping dies. Moreover, the developed feedforward controller can also react very fast to transient changes in the processing conditions because the zinc coating measurements with the significant transport delay are not required for this method. This is a novelty compared to methods reported in the literature. In this way, the zinc consumption and hence the operating costs can be significantly reduced.

6.3 Outlook

It is planned to apply a model-order reduction technique to the mathematical model of the transverse strip shape. This step should be carried out prior to the commissioning of the developed methods at the industrial hot-dip galvanizing line. All algorithms to be implemented in the industrial plant will be based on the reduced-size mathematical model to lower the associated computational workload.

It is planned to implement an online estimator of the residual curvature in the industrial hot-dip galvanizing line. Based on the estimated residual curvature, a pilot installation of the feedforward control concept will be commissioned at the industrial plant. As a first step, the state-of-the-art position controllers of the electromagnetic strip stabilizer (with the coil currents as control inputs) could be used. During a test phase, it can be analyzed if the tension leveler in the zinc pot can be removed without a loss of accuracy of the homogeneity of the zinc coating thickness. Clearly, a plant configuration without a tension leveler in the zinc pot would significantly reduce the investment and operating costs of the process.

As a second step, it is planned to replace the state-of-the-art position controller of the electromagnetic stabilizer with a self-developed position controller (the electromagnetic force is used as control input). The inverse electromagnetic force characteristics could be used to approximately realize the desired force. The linearity property allows to easily combine the feedforward control concept with the disturbance rejection control concept.

A follow-up research project deals with model-free concepts to improve the flatness of the transverse strip profile at a measured position. These concepts mainly focus on position and vibration control at the electromagnetic stabilizer, where measurements of the strip displacement are available.

APPENDIX A

Jacobian matrices

This appendix summarizes the analytical expressions required for the assembly of the Jacobian matrix in Section 2.1.7. An analytical form of the Jacobian matrix is preferred over a numerical approximation because of a better balance between accuracy and computational effort. The analytical Jacobian matrices of individual finite elements are derived in Section (A.1). They are assembled to the Jacobian matrix of the full system in Section (A.2).

A.1 Finite elements

A.1.1 In-plane system

The geometrically nonlinear term in (2.28) is considered for the finite element e. Splitting the integrals in (2.29k) and (2.29l) into m integrals of the form

$$\breve{\mathbf{f}}_e^{\mathrm{w}1} = \sum_{f=1}^{m} \tilde{\mathbf{f}}_{e,f}^{\mathrm{w}1} = \frac{A}{2} \sum_{f=1}^{m} \int_{\tilde{\Omega}_{e,f}} (\cdots) \mathrm{d}\tilde{x} \mathrm{d}\tilde{y} \tag{A.1a}$$

$$\breve{\mathbf{f}}_e^{\mathrm{w}2} = \sum_{f=1}^{m} \tilde{\mathbf{f}}_{e,f}^{\mathrm{w}2} = \frac{A}{2} \sum_{f=1}^{m} \int_{\tilde{\Omega}_{e,f}} (\cdots) \mathrm{d}\tilde{x} \mathrm{d}\tilde{y} \tag{A.1b}$$

yields the Jacobian matrix

$$\frac{\partial \tilde{\mathbf{f}}_{e,f}^{\mathrm{w}} \left(\tilde{\mathbf{t}}_{e,f}^{w} \right)}{\partial \tilde{\mathbf{t}}_{e,f}^{w}} = \left[\left(\tilde{\mathbf{f}}_{e,f}^{\partial \mathrm{w}1} \right)^{\mathrm{T}} \quad \left(\tilde{\mathbf{f}}_{e,f}^{\partial \mathrm{w}2} \right)^{\mathrm{T}} \right]^{\mathrm{T}} \tag{A.2a}$$

of (2.29j) with

$$\begin{aligned}\tilde{\mathbf{f}}_{e,f}^{\partial \mathrm{w}1} =& A\int_{\tilde{\Omega}_{e,f}} \left(\partial_x \bar{\mathbf{\Psi}}_e^u\right)\left[\partial_x w\left(\partial_x \mathbf{\Psi}_{e,f}^w\right)^{\mathrm{T}} + \nu \partial_y w \left(\partial_y \mathbf{\Psi}_{e,f}^w\right)^{\mathrm{T}}\right] \\ &+ \frac{1}{2}\left(\partial_y \bar{\mathbf{\Psi}}_e^u\right)(1-\nu)\left[\left(\partial_x \mathbf{\Psi}_{e,f}^w\right)^{\mathrm{T}}\partial_y w + \partial_x w\left(\partial_y \mathbf{\Psi}_{e,f}^w\right)^{\mathrm{T}}\right]\mathrm{d}\tilde{x}\mathrm{d}\tilde{y}\end{aligned} \quad \text{(A.2b)}$$

$$\begin{aligned}\tilde{\mathbf{f}}_{e,f}^{\partial \mathrm{w}2} =& A\int_{\tilde{\Omega}_{e,f}} \left(\partial_y \bar{\mathbf{\Psi}}_e^v\right)\left[\nu\partial_x w\left(\partial_x \mathbf{\Psi}_{e,f}^w\right)^{\mathrm{T}} + \partial_y w \left(\partial_y \mathbf{\Psi}_{e,f}^w\right)^{\mathrm{T}}\right] \\ &+ \frac{1}{2}\left(\partial_x \bar{\mathbf{\Psi}}_e^v\right)(1-\nu)\left[\left(\partial_x \mathbf{\Psi}_{e,f}^w\right)^{\mathrm{T}}\partial_y w + \partial_x w\left(\partial_y \mathbf{\Psi}_{e,f}^w\right)^{\mathrm{T}}\right]\mathrm{d}\tilde{x}\mathrm{d}\tilde{y}.\end{aligned} \quad \text{(A.2c)}$$

A.1.2 Out-of-plane system

Next, the geometrically nonlinear terms in (2.32) are considered for the finite element (e, f). The Jacobian matrix of the product $\tilde{\mathbf{K}}^{\mathrm{N}}_{e,f}\tilde{\mathbf{t}}^w_{e,f}$, see also (2.33g), reads as

$$\frac{\partial\left(\tilde{\mathbf{K}}^{\mathrm{N}}_{e,f}\left(\tilde{\mathbf{t}}^w_{e,f}, \check{\mathbf{t}}^{uv}_e\right)\tilde{\mathbf{t}}^w_{e,f}\right)}{\partial \tilde{\mathbf{t}}^w_{e,f}} = \tilde{\mathbf{K}}^{\mathrm{N},\partial\mathrm{w}}_{e,f} + \tilde{\mathbf{K}}^{\mathrm{N},\partial\mathrm{uv}}_{e,f} + \tilde{\mathbf{K}}^{\mathrm{N}}_{e,f} \quad \text{(A.3a)}$$

with

$$\begin{aligned}\tilde{\mathbf{K}}^{\mathrm{N},\partial\mathrm{w}}_{e,f} =& A\int_{\tilde{\Omega}_{e,f}} \left(\partial_x \bar{\mathbf{\Psi}}_{e,f}^w\right)\left[\partial_x w\left(\partial_x \mathbf{\Psi}_{e,f}^w\right)^{\mathrm{T}} + \nu \partial_y w \left(\partial_y \mathbf{\Psi}_{e,f}^w\right)^{\mathrm{T}}\right]\partial_x w \\ &+ \left(\partial_y \bar{\mathbf{\Psi}}_{e,f}^w\right)\left[\nu\partial_x w\left(\partial_x \mathbf{\Psi}_{e,f}^w\right)^{\mathrm{T}} + \partial_y w \left(\partial_y \mathbf{\Psi}_{e,f}^w\right)^{\mathrm{T}}\right]\partial_y w \\ &+ \left(\partial_x \bar{\mathbf{\Psi}}_{e,f}^w\right)\frac{1-\nu}{2}\left[\left(\partial_x \mathbf{\Psi}_{e,f}^w\right)^{\mathrm{T}}\partial_y w + \partial_x w\left(\partial_y \mathbf{\Psi}_{e,f}^w\right)^{\mathrm{T}}\right]\partial_y w \\ &+ \left(\partial_y \bar{\mathbf{\Psi}}_{e,f}^w\right)\frac{1-\nu}{2}\left[\left(\partial_x \mathbf{\Psi}_{e,f}^w\right)^{\mathrm{T}}\partial_y w + \partial_x w\left(\partial_y \mathbf{\Psi}_{e,f}^w\right)^{\mathrm{T}}\right]\partial_x w\mathrm{d}\tilde{x}\mathrm{d}\tilde{y}\end{aligned} \quad \text{(A.3b)}$$

and

$$\begin{aligned}\tilde{\mathbf{K}}^{\mathrm{N},\partial\mathrm{uv}}_{e,f} =& A\int_{\tilde{\Omega}_{e,f}} \left(\partial_x \bar{\mathbf{\Psi}}_{e,f}^w\right)\left[\frac{\partial(\partial_x u)}{\partial \tilde{\mathbf{t}}^w_{e,f}} + \nu\frac{\partial(\partial_y v)}{\partial \tilde{\mathbf{t}}^w_{e,f}}\right]\partial_x w \\ &+ \left(\partial_y \bar{\mathbf{\Psi}}_{e,f}^w\right)\left[\nu\frac{\partial(\partial_x u)}{\partial \tilde{\mathbf{t}}^w_{e,f}} + \frac{\partial(\partial_y v)}{\partial \tilde{\mathbf{t}}^w_{e,f}}\right]\partial_y w \\ &+ \left(\partial_x \bar{\mathbf{\Psi}}_{e,f}^w\right)\frac{1-\nu}{2}\left[\frac{\partial(\partial_y u)}{\partial \tilde{\mathbf{t}}^w_{e,f}} + \frac{\partial(\partial_x v)}{\partial \tilde{\mathbf{t}}^w_{e,f}}\right]\partial_y w \\ &+ \left(\partial_y \bar{\mathbf{\Psi}}_{e,f}^w\right)\frac{1-\nu}{2}\left[\frac{\partial(\partial_y u)}{\partial \tilde{\mathbf{t}}^w_{e,f}} + \frac{\partial(\partial_x v)}{\partial \tilde{\mathbf{t}}^w_{e,f}}\right]\partial_x w\mathrm{d}\tilde{x}\mathrm{d}\tilde{y}.\end{aligned} \quad \text{(A.3c)}$$

The term (A.3b) captures the direct influence of the geometrical nonlinearity on the Jacobian matrix and (A.3c) accounts for the indirect influence due to the coupling with the in-plane displacements. For the calculation of (A.3c), the solution of u and v is required, see Sections 2.1.7 and 2.1.8. In contrast, the Jacobian matrix of (2.33l) is evaluated using numerical methods.

A.2 Assembly

The derivative of (2.47) with respect to $\tilde{\mathbf{t}}$ can be written in the form

$$\frac{\partial \breve{\mathbf{t}}}{\partial \tilde{\mathbf{t}}} = -\left(\breve{\mathbf{K}} - V^2 \breve{\mathbf{H}}\right)^{-1} \frac{\partial \breve{\mathbf{f}}^{\mathrm{w}}\left(\tilde{\mathbf{t}}\right)}{\partial \tilde{\mathbf{t}}}, \tag{A.4}$$

where the term $\partial \breve{\mathbf{f}}^{\mathrm{w}}\left(\tilde{\mathbf{t}}\right)/\partial \tilde{\mathbf{t}}$ represents the assembly of (A.2) for the full system. The use of (2.39), (2.38), (2.22), (2.23), and (A.4) leads to uniquely defined expressions in the rectangular brackets of (A.3c). Finally, the second to last term in (2.54) follows from the assembly of (A.3a) for the full system.

Bibliography

[1] ANDRITZ Metals, *Hot dip galvanizing line no. 5, voestalpine AG, Austria*, `https://www.andritz.com/resource/blob/77380/80a71edeed68605d04572dcee6be66b5/me-hotdipgalvanizinglineno5-brochure-en-data.pdf`, Accessed: 2020-08-25, 2013.

[2] E. Elsaadawy, G. Hanumanth, A. Balthazaar, J. McDermid, A. Hrymak, and J. Forbes, "Coating weight model for the continuous hot-dip galvanizing process", *Metallurgical and Materials Transactions B: Process Metallurgy and Materials Processing Science*, vol. 38, no. 3, pp. 413–424, 2007.

[3] Y.-H. Kweon and H.-D. Kim, "Study on the wiping gas jet in continuous galvanizing line", *Journal of Thermal Science*, vol. 20, no. 3, pp. 242–247, 2011.

[4] N. Guelton, C. Lopès, and H. Sordini, "Cross coating weight control by electromagnetic strip stabilization at the continuous galvanizing line of ArcelorMittal Florange", *Metallurgical and Materials Transactions B*, vol. 47, no. 4, pp. 2666–2680, 2016.

[5] M. Niederer, S. Strommer, A. Steinboeck, and A. Kugi, "Nonlinear model predictive control of the strip temperature in an annealing furnace", *Journal of Process Control*, vol. 48, pp. 1–13, 2016.

[6] S. Strommer, M. Niederer, A. Steinboeck, and A. Kugi, "A mathematical model of a direct-fired continuous strip annealing furnace", *International Journal of Heat and Mass Transfer*, vol. 69, pp. 375–389, 2014.

[7] M. Niederer, S. Strommer, A. Steinboeck, and A. Kugi, "A simple control-oriented model of an indirect-fired strip annealing furnace", *International Journal of Heat and Mass Transfer*, vol. 78, pp. 557–570, 2014.

[8] Y. Kaseda and T. Masui, "Control of buckling and crossbow in strip processing lines", *Iron and Steel Engineer*, vol. 71, no. 9, pp. 14–20, 1994.

[9] T. Masui, Y. Kaseda, and K. Ando, "Warp control in strip processing plant", *ISIJ International*, vol. 31, no. 3, pp. 262–267, 1991.

[10] Y. Misaka and T. Masui, "Shape correction of steel strip by tension leveller", *Transactions ISIJ*, vol. 18, no. 8, pp. 475–484, 1978.

[11] T. Hira, H. Abe, and S. Azuma, "Analysis of sheet metal bending deformation behavior in processing lines and its effectiveness", *Kawasaki Steel Technical Report*, no. 19, pp. 54–62, 1988.

[12] M. Takeda and M. Watanabe, "Self-excited vibration of a plate supported by air pressure in a floating conveying machine", in *Proceedings of the ASME 2017 Pressure Vessels and Piping Conference*, vol. 4, Waikoloa, Hawaii, USA, 2017, pp. 1–10.

[13] S. Hui, H. Zhang, J. Ma, and P. Xu, "One-third sub-harmonic resonance analysis for the up-going strip emerging from the zinc pot", *Key Engineering Materials*, vol. 693, pp. 1247–1254, 2016.

[14] J. Li, Y.-H. Yan, X.-H. Guo, and Y.-Q. Wang, "Research on vibration control method of steel strip for a continuous hot-dip galvanizing line", *ISIJ International*, vol. 52, no. 6, pp. 1072–1079, 2012.

[15] M. Shigeki, I. Atsushi, S. Hideaki, N. Kazuhisa, and K. Keiichi, "Study on shape control and vibration absorber of strip in steel process line", *Mitsubishi Heavy Industries Ltd. Technical Review*, vol. 32, no. 3, pp. 5–8, 1995.

[16] M. Irle and A. Jordan, "EMG-eMASS - homogeneous zinc layer and high production speed via an electromagnetic strip stabilization", in *Proceedings of the 3rd International Steel Conference on new Developments in Metallurgical Process Technologies*, Düsseldorf, Germany, 2007, pp. 109–115.

[17] L. Marko, M. Saxinger, A. Steinboeck, and A. Kugi, "Magnetic actuator design for strip stabilizers in hot dip galvanizing lines", in *Proceedings of the IEEE Industry Applications Society Annual Meeting*, Portland, Oregon, USA, 2018, pp. 1–9.

[18] EMG-Automation, *EMG eMASS - the leading electro MAgnetic Strip Stabilisation*, `https://www.emg-automation.com/fileadmin/content/automation/qualitaetssichernde_systeme/dokumente/eMASS_WhitePaper_EN_01-2018.pdf`, Accessed: 2020-03-18.

[19] M. Baumgart, A. Steinboeck, M. Saxinger, and A. Kugi, "Elasto-plastic bending of steel strip in a hot-dip galvanizing line", *Acta Mechanica*, vol. 228, no. 7, pp. 2455–2470, 2017.

[20] L. Marko, M. Saxinger, A. Steinboeck, and A. Kugi, "Magnetic actuator design for strip stabilizers in hot-dip galvanizing lines: Examining rules and basic tradeoffs", *IEEE Industry Applications Magazine*, vol. 26, no. 2, pp. 54–63, 2020.

[21] C. Orth, "Auslegung und Aufbau eines Laborversuchs zur Untersuchung des Schwingungsverhaltens eines Stahlbandes in der Feuerverzinkung", Master's thesis, Automation and Control Institute (ACIN), TU Wien, 2020.

[22] U. Knechtelsdorfer, "MIMO shape control of a metal strip using electromagnets", Master's thesis, Automation and Control Institute (ACIN), TU Wien, 2017.

[23] M. Saxinger, A. Steinboeck, M. Baumgart, and A. Kugi, "Dynamical model of axially moving steel strips", *IFAC-PapersOnLine*, vol. 49, no. 20, pp. 190–195, 2016.

[24] M. Saxinger, A. Steinboeck, M. Baumgart, P. Kerschbaummayr, and A. Kugi, "Influence of air cooling jets on the steady-state shape of strips in hot dip galvanizing lines", *IFAC-PapersOnLine*, vol. 28, no. 17, pp. 143–148, 2015.

[25] M. Saxinger, A. Steinboeck, L. Marko, M. Baumgart, and A. Kugi, "Nonlinear dynamical model of an axially moving steel strip in a surface coating plant (in German)", *at-Automatisierungstechnik*, vol. 65, no. 8, pp. 546–560, 2017, (best paper award).

[26] M. Saxinger, A. Steinboeck, M. Baumgart, and A. Kugi, "Nichtlineares Bewegungsmodell für ein Stahlband in einer Oberflächenbeschichtungsanlage", in *Tagungsband GMA-Fachausschuss 1.30 "Modellbildung, Identifikation und Simulation in der Automatisierungstechnik"*, Anif/Salzburg, Austria, 2016, pp. 46–67.

[27] M. Baumgart, A. Steinboeck, M. Saxinger, and A. Kugi, "Elasto-plastic bending of steel strip in a hot-dip galvanizing line", in *Proceedings of the 3rd Polish Congress of Mechanics (PCM) and 21st International Conference on Computer Methods in Mechanics (CMM)*, Gdansk, Poland, 2015, pp. 55–56.

[28] M. Saxinger, L. Marko, A. Steinboeck, and A. Kugi, "Active rejection control for unknown harmonic disturbances of the transverse deflection of steel strips with control input, system output, sensor output, and disturbance input at different positions", *Mechatronics*, vol. 56, pp. 73–86, 2018, (best paper award).

[29] M. Saxinger, L. Marko, A. Steinboeck, and A. Kugi, "Non-collocated position control of steel strip with electromagnetic rejection of unknown multi-harmonic disturbances", *IFAC-PapersOnLine*, vol. 52, no. 15, pp. 430–435, 2019, (best young author award).

[30] M. Saxinger, L. Marko, A. Steinboeck, and A. Kugi, "Feedforward control of the transverse strip profile in hot-dip galvanizing lines", *Journal of Process Control*, vol. 92, pp. 35–49, 2020.

[31] C. Shin, J. Chung, and H. Hee Yoo, "Dynamic responses of the in-plane and out-of-plane vibrations for an axially moving membrane", *Journal of Sound and Vibration*, vol. 297, no. 3–5, pp. 794–809, 2006.

[32] Q. Nguyen and K.-S. Hong, "Transverse vibration control of axially moving membranes by regulation of axial velocity", *IEEE Transactions on Control Systems Technology*, vol. 20, no. 4, pp. 1124–1131, 2012.

[33] J. Chung and G. M. Hulbert, "A time integration algorithm for structural dynamics with improved numerical dissipation: The generalized-alpha method", *Journal of Applied Mechanics*, vol. 60, pp. 371–375, 1993.

[34] M. Géradin and D. Rixen, *Mechanical Vibrations: Theory and Application to Structural Dynamics*, 2nd ed. Chichester: Wiley, 1997.

[35] C. Shearer and C. Cesnik, "Modified generalized α method for integrating governing equations of very flexible aircraft", in *Proceedings of the 47th AIAA/ASME/ASCE/AHS/ASC Structures, Structural Dynamics, and Materials Conference*, Newport, Rhode Island, USA, 2006, pp. 1–21.

[36] J. Reddy, *Theory and Analysis of Elastic Plates and Shells*, 2nd ed. Boca Raton, London, New York: CRC Press, 2007.

[37] D. McIver, "Hamilton's principle for systems of changing mass", *Journal of Engineering Mathematics*, vol. 7, no. 3, pp. 249–261, 1973.

[38] A. Steinboeck, M. Saxinger, and A. Kugi, "Hamilton's principle for material and nonmaterial control volumes using Lagrangian and Eulerian description of motion", *Applied Mechanics Reviews*, vol. 71, no. 1, pp. 010802-1–010802-14, 2019.

[39] R. M. Bozorth, *Ferromagnetism*. New Jersey: Wiley Interscience, IEEE Press, 1993.

[40] D. Chen, "Adaptive control of hot-dip galvanizing", *Automatica*, vol. 31, no. 5, pp. 715–733, 1995.

[41] K.-T. Shin, H.-D. Park, and W.-K. Chung, "Synthesis method for the modelling and robust control of coating weight at galvanizing process", *ISIJ International*, vol. 46, no. 10, pp. 1442–1451, 2006.

[42] K. T. Shin and W. K. Chung, "A new model and control of coating process at galvanizing line", *IFAC Proceedings Volumes*, vol. 41, no. 2, pp. 9138–9143, 2008.

[43] F. A. Cuzzola and T. Parisini, "A multivariable control scheme for a hot dip galvanising line process", in *Proceedings of the IEEE International Conference on Control Applications*, Yokohama, Japan, 2010, pp. 938–943.

[44] N. Guelton and A. Lerouge, "Coating weight control on ArcelorMittal's galvanizing line at Florange works", *Control Engineering Practice*, vol. 18, no. 10, pp. 1220–1229, 2010.

[45] Z.-S. Pan, X.-H. Zhou, and P. Chen, "Development and application of a neural network based coating weight control system for a hot-dip galvanizing line", *Frontiers of Information Technology and Electronic Engineering*, vol. 19, no. 7, pp. 834–846, 2018.

[46] W. Jung, Y. Jang, S. Lim, and S. Won, "Active vibration and flatness control of a strip in a continuous galvanizing line using positive position feedback control", *ISIJ International*, vol. 53, no. 5, pp. 854–865, 2013.

[47] J.-Y. Choi, K.-S. Hong, and K.-J. Yang, "Exponential stabilization of an axially moving tensioned strip by passive damping and boundary control", *Journal of Vibration and Control*, vol. 10, no. 5, pp. 661–682, 2004.

[48] A. Preumont, *Vibration Control of Active Structures: An Introduction*, ser. Solid Mechanics and Its Applications. Netherlands: Springer, 2011.

[49] C. Vasques and J. Dias Rodrigues, "Active vibration control of smart piezoelectric beams: Comparison of classical and optimal feedback control strategies", *Computers and Structures*, vol. 84, no. 22-23, pp. 1402–1414, 2006.

[50] D. L. Trumper, M.-C. Weng, and R. J. Ritter, "Magnetic suspension and vibration control of beams for non-contact processing", in *Proceedings of the IEEE Conference on Control Applications*, vol. 1, Kohala Coast, Hawaii, USA, 1999, pp. 551–557.

[51] E. Omidi, S. Mahmoodi, and J. Shepard W.S., "Multi positive feedback control method for active vibration suppression in flexible structures", *Mechatronics*, vol. 33, pp. 23–33, 2016.

[52] R. Cannon and D. E. Rosenthal, "Experiments in control of flexible structures with noncolocated sensors and actuators", *Journal of Guidance, Control, and Dynamics*, vol. 7, no. 5, pp. 546–553, 1984.

[53] Q. Zhang, S. Shelley, and R. Allemang, "Active damping design of flexible structures based on SISO and SIMO noncollocated sensor-actuator velocity feedback", *Journal of Dynamic Systems, Measurement and Control, Transactions of the ASME*, vol. 113, no. 2, pp. 259–266, 1991.

[54] B. Yang and C. D. Mote, "Active vibration control of the axially moving string in the S domain", *Journal of Applied Mechanics, Transactions ASME*, vol. 58, no. 1, pp. 189–196, 1991.

[55] B. Gospodarič, D. Vončina, and B. Bučar, "Active electromagnetic damping of laterally vibrating ferromagnetic cantilever beam", *Mechatronics*, vol. 17, no. 6, pp. 291–298, 2007.

[56] S. Skogestad and I. Postlethwaite, *Multivariable Feedback Control: Analysis and Design*. Chichester: Wiley, 2005.

[57] L. Iorga, H. Baruh, and I. Ursu, "A review of H_∞ robust control of piezoelectric smart structures", *Applied Mechanics Reviews*, vol. 61, no. 1-6, pp. 0 408 021–04 080 215, 2008.

[58] Z.-C. Qiu and B. Ma, "Adaptive resonant vibration control of a piezoelectric flexible plate implementing filtered-X LMS algorithm", *International Journal of Acoustics and Vibrations*, vol. 19, no. 4, pp. 224–239, 2014.

[59] J.-E. Oh, S.-H. Park, J.-S. Hong, and J. Shin, "Active vibration control of flexible cantilever beam using piezo actuator and filtered-X LMS algorithm", *KSME International Journal*, vol. 12, no. 4, pp. 665–671, 1998.

[60] L. Sievers and A. von Flotow, "Comparison and extensions of control methods for narrow-band disturbance rejection", *IEEE Transactions on Signal Processing*, vol. 40, no. 10, pp. 2377–2391, 1992.

[61] G. De Nicolao, F. Lorito, and S. Strada, "On 'Comparison and extensions of control methods for narrow-band disturbance rejection'", *IEEE Transactions on Speech and Audio Processing*, vol. 2, no. 3, pp. 459–461, 1994.

[62] M. Bodson, "Rejection of periodic disturbances of unknown and time-varying frequency", *International Journal of Adaptive Control and Signal Processing*, vol. 19, no. 2-3, pp. 67–88, 2005.

[63] H. Shim, H. Kim, and C. C. Chung, "Design and experiment of add-on track following controller for optical disc drives based on robust output regulation", in *Proceedings of the 2004 American Control Conference*, vol. 2, Boston, Massachusetts, USA, 2004, pp. 1829–1835.

[64] W. Kim, H. Kim, C. C. Chung, and M. Tomizuka, "Adaptive output regulation for the rejection of a periodic disturbance with an unknown frequency", *IEEE Transactions on Control Systems Technology*, vol. 19, no. 5, pp. 1296–1304, 2011.

[65] H. Kim, H. Shim, and N. H. Jo, "Adaptive add-on output regulator for rejection of sinusoidal disturbances and application to optical disc drives", *IEEE Transactions on Industrial Electronics*, vol. 61, no. 10, pp. 5490–5499, 2014.

[66] M. Ficocelli and F. Amara, "Adaptive regulation of MIMO linear systems against unknown sinusoidal exogenous inputs", *International Journal of Adaptive Control and Signal Processing*, vol. 23, no. 6, pp. 581–603, 2009.

[67] G. Obregón-Pulido, B. Castillo-Toledo, and A. Loukianov, "A structurally stable globally adaptive internal model regulator for MIMO linear systems", *IEEE Transactions on Automatic Control*, vol. 56, no. 1, pp. 160–165, 2011.

[68] W.-H. Chen, "Disturbance observer based control for nonlinear systems", *IEEE/ASME Transactions on Mechatronics*, vol. 9, no. 4, pp. 706–710, 2004.

[69] J. Deutscher, "Output regulation for linear distributed-parameter systems using finite-dimensional dual observers", *Automatica*, vol. 47, no. 11, pp. 2468–2473, 2011.

[70] U. Knechtelsdorfer, M. Saxinger, M. Schwegel, A. Steinboeck, and A. Kugi, "A two-stage observer for the compensation of actuator-induced disturbances in tool-force sensors", *Mechanical Systems and Signal Processing*, vol. 146, pp. 106989-1–106989-12, 2021.

[71] D. Simon, *Optimal State Estimation: Kalman, H_∞, and Nonlinear Approaches*. New Jersey: John Wiley & Sons, 2006.

[72] A. Isidori, L. Marconi, and A. Serrani, *Robust Autonomous Guidance: An Internal Model Approach*, ser. Advances in Industrial Control. London: Springer, 2003.

[73] C. Byrnes and A. Isidori, "Output regulation for nonlinear systems: An overview", *International Journal of Robust and Nonlinear Control*, vol. 10, no. 5, pp. 323–337, 2000.

[74] H. Knobloch, A. Isidori, and D. Flockerzi, *Topics in Control Theory*, ser. DMV Seminar. Basel: Birkhäuser Verlag, 1993.

[75] F. Ziegler, *Mechanics of Solids and Fluids*, ser. Graduate Texts in Mathematics; 159. New York: Springer, 1995.

[76] M. Abramowitz and I. Stegun, *Handbook of Mathematical Functions: with Formulas, Graphs, and Mathematical Tables*, ser. Dover Books on Mathematics. New York: Dover Publications, 2012.

[77] M. Liu and D. Gorman, "Formulation of Rayleigh damping and its extensions", *Computers & Structures*, vol. 57, no. 2, pp. 277–285, 1995.

[78] O. Zienkiewicz, R. Taylor, and J. Zhu, *The Finite Element Method: Its Basis and Fundamentals*, 7th ed. Amsterdam: Elsevier, 2013.

[79] O.C. Zienkiewicz and K. Morgan, *Finite Elements and Approximation*. New York: Wiley, 1983.

[80] A. Steinboeck, M. Baumgart, G. Stadler, M. Saxinger, and A. Kugi, "Dynamical models of axially moving rods with tensile and bending stiffness", *IFAC-PapersOnLine*, vol. 48, no. 1, pp. 598–603, 2015.

[81] H. Khalil, *Nonlinear Systems*, 3rd ed., ser. Pearson Education. New Jersey: Prentice-Hall, 2002.

[82] P. Papalambros and D. Wilde, *Principles of Optimal Design: Modeling and Computation*. New York: Cambridge University Press, 2000.

[83] D. Luenberger and Y. Ye, *Linear and Nonlinear Programming*, 3rd ed., ser. International Series in Operations Research & Management Science. New York: Springer, 2008, vol. 116.

[84] W. Zhang and L.-Q. Chen, “Vibration control of an axially moving string system: Wave cancellation method”, *Applied Mathematics and Computation*, vol. 175, no. 1, pp. 851–863, 2006.

[85] L. Ljung, *System Identification - Theory for the User*, 2nd ed. New Jersey: Prentice-Hall, 2009.

[86] T. Rittenschober and K. Schlacher, “Observer-based self sensing actuation of piezoelastic structures for robust vibration control”, *Automatica*, vol. 48, no. 6, pp. 1123–1131, 2012.

[87] A. Isidori, *Nonlinear Control Systems*, ser. Communications and Control Engineering. London: Springer, 1995.

[88] K. Åström and B. Wittenmark, *Computer-Controlled Systems: Theory and Design*, 3rd ed. Upper Saddle River, New Jersey: Prentice Hall, 1997.

[89] R. H. Bartels and G. W. Stewart, “Solution of the matrix equation AX + XB = C [f4]”, *Communications of the ACM*, vol. 15, no. 9, pp. 820–826, 1972.

[90] M. Boutayeb and D. Aubry, “A strong tracking extended Kalman observer for nonlinear discrete-time systems”, *IEEE Transactions on Automatic Control*, vol. 44, no. 8, pp. 1550–1556, 1999.

[91] L. Marko, M. Saxinger, M. Bittner, A. Steinboeck, and A. Kugi, “Discrete-time repetitive control for multi-harmonic reference trajectories with arbitrary frequency”, in *Preprints of the 21st IFAC World Congress*, Berlin, Germany, 2020, pp. 1–6.

[92] E. Maslen, G. Schweitzer, H. Bleuler, M. Cole, P. Keogh, R. Larsonneur, R. Nordmann, Y. Okada, and A. Traxler, *Magnetic Bearings: Theory, Design, and Application to Rotating Machinery*. Berlin, Heidelberg: Springer, 2009.

[93] E. Kallenbach, R. Eick, P. Quendt, T. Ströhla, K. Feindt, and M. Kallenbach, *Elektromagnete: Grundlagen, Berechnung, Entwurf und Anwendung*. Wiesbaden: Vieweg + Teubner, 2008.

[94] R. P. Jastrzębski and R. Pöllänen, “Compensation of nonlinearities in active magnetic bearings with variable force bias for zero- and reduced-bias operation”, *Mechatronics*, vol. 19, no. 5, pp. 629–638, 2009.